DAHLGREN DIVISION
NAVAL SURFACE WARFARE CENTER
Dahlgren, Virginia 22448-5100

NSWCDD/TR-01/106

THE 2002 VERSION OF THE AEROPREDICTION CODE: PART I – SUMMARY OF NEW THEORETICAL METHODOLOGY

BY FRANK G. MOORE
AEROPREDICTION, INC.

THOMAS C. HYMER
NSWCDD

WEAPONS SYSTEMS DEPARTMENT

MARCH 2002

REPORT DOCUMENTATION PAGE	Form Approved OMB No. 0704-0188

1. AGENCY USE ONLY (Leave blank)	2. REPORT DATE	3. REPORT TYPE AND DATES COVERED
	March 2002	Final

4. TITLE AND SUBTITLE

The 2002 Version of the Aeroprediction Code: Part I – Summary of New Theoretical Methodology

5. FUNDING NUMBERS

6. AUTHOR(s)

Frank G. Moore, Thomas C. Hymer

7. PERFORMING ORGANIZATION NAME(S) AND ADDRESS(ES)

Commander
Naval Surface Warfare Center
Dahlgren Division (Code G23)
17320 Dahlgren Road
Dahlgren, VA 22448-5100

8. PERFORMING ORGANIZATION REPORT NUMBER

NSWCDD/TR-01/108

9. SPONSORING/MONITORING AGENCY NAME(S) AND ADDRESS(ES)

10. SPONSORING/MONITORING AGENCY REPORT NUMBER

11. SUPPLEMENTARY NOTES

12a. DISTRIBUTION/AVAILABILITY STATEMENT

Approved for public release; distribution is unlimited.

12b. DISTRIBUTION CODE

13. ABSTRACT (Maximum 200 words)

A new version of the aeroprediction code (APC), the AP02, has been developed to address the requirements arising from advanced weapon concepts. The AP02 was formed by adding significant new technology and several productivity improvements to the previous version of the APC, the AP98. New technology added included 6 and 8 fin aerodynamics, improved nonlinear aerodynamics, improved pitch damping predictions, improved power-on base drag estimates, base-bleed effect on base drag estimation, improved axial force of nonaxisymmetric bodies and trailing-edge flap capability. Other improvements and productivity enhancements include an aerodynamic smoother, ballistic and three degree-of-freedom simulation modules as well as refinements for the pre- and post-processor for inputs and outputs of the AP02. Comparison of the predicted aerodynamics of the AP02 to AP98 and experimental data showed the AP02 to be slightly better than the AP98 in most cases that both codes would handle. However, due to the additional new technology incorporated into the AP02, many new options are available in the AP02 that are not available in the AP98. Therefore, the AP02 is more robust and, on average, is slightly more accurate than the AP98 in predicting aerodynamics of weapons.

14. SUBJECT TERMS	15. NUMBER OF PAGES
aeroprediction code	226
	16. PRICE CODE

17. SECURITY CLASSIFICATION OF REPORT	18. SECURITY CLASSIFICATION OF THIS PAGE	19. SECURITY CLASSIFICATION OF ABSTRACT	20. LIMITATION OF ABSTRACT
UNCLASSIFIED	UNCLASSIFIED	UNCLASSIFIED	UL

FOREWORD

The first three versions of the aeroprediction code (APC), the AP72, AP74, and AP77, were all developed to meet guided and unguided projectile requirements in the seventies. The next four versions of the APC, the AP81, AP93, AP95, and AP98, were developed to meet tactical missile requirements. Missiles tend to fly faster, fly at higher altitudes, and at times, at higher angles of attack as compared to projectiles. During the nineties, several emerging projectile needs arose that the AP98 could not handle. To address these additional needs, various capabilities were incorporated into the AP98. The new capabilities included multi-fin capability, improved rocket motor-on and base-bleed capability, improved pitch-damping capability, capability for trailing-edge flaps, and improvements in axial force prediction for nonaxisymmetric bodies. In addition, the ability to generate range in a timely and cost effective manner was a need which was not available in AP98. This capability was achieved by combining the APC with trajectory models. As a result of the above set of needs and requirements, the AP02 was developed. Thus, the AP02 is the first version of the APC in 25 years that places projectile requirements at the forefront of needs. This report summarizes the new technology that has been developed over the past four years that will be a part of the AP02.

The work described in this report was supported by the Office of Naval Research (Mr. Gil Graff) through the Surface Weapons Systems Technology Program managed at the Naval Surface Warfare Center, Dahlgren Division (NSWCDD) by Mr. Robin Staton. Tasking from this program was provided by Mr. Roger Horman, Mr. John Fraysse, and Mr. Tim Spivak. Mr. George Long of the Standard Missile Program also provided some funding in past years. The authors express appreciation for support received in this work.

Approved by:

DANNY BRUNSON, Head
Weapons Systems Department

CONTENTS

CONTENTS (CONTINUED)

ILLUSTRATIONS

ILLUSTRATIONS (Continued)

ILLUSTRATIONS (Continued)

ILLUSTRATIONS (Continued)

ILLUSTRATIONS (Continued)

ILLUSTRATIONS (Continued)

ILLUSTRATIONS (Continued)

ILLUSTRATIONS (Continued)

ILLUSTRATIONS (Continued)

ILLUSTRATIONS (Continued)

TABLES

TABLES (CONTINUED)

TABLES (CONTINUED)

1.0 INTRODUCTION

The aeroprediction code (APC) has been developed over a 30-year period beginning in 1971. The objective of the APC development over this 30-year period has stayed the same–to predict aerodynamics cost effectively and with reasonable accuracy over the flight envelope and configuration geometries of interest to weapons designers. While the objective of the APC has stayed the same, the application uses, flight requirements, and configuration geometries have evolved over that time frame. The initial application was primarily accurate range of various unguided projectile design concepts at low angles of attack (AOA) and for Mach numbers less than 2.5. Now the application includes trim aerodynamics of guided weapons, aerodynamic design of guided weapons, structural loads and aerodynamic heating. Mach numbers as high as 15 have been encountered, AOA as high as 90 deg, and body geometries axisymmetric or nonaxisymmetric have been considered in the design process. Figure 1 summarizes the current objective, application, and flight requirements of the APC effort.

OBJECTIVE

PREDICT AERODYNAMICS COST EFFECTIVELY AND WITH REASONABLE ACCURACY OVER FLIGHT ENVELOPE OF INTEREST TO WEAPONS DESIGNERS

APPLICATION REQUIREMENT OF APC

- **INPUTS TO 3-DOF/TRIM PERFORMANCE MODELS**
- **AERODYNAMIC DESIGN (PRELIMINARY)**
- **PRELIMINARY STRUCTURAL LOADINGS**
- **CONVECTIVE HEAT TRANSFER INPUTS**

OVERALL FLIGHT REQUIREMENTS

MACH NUMBER:	**0-15**
ANGLE-OF-ATTACK:	**0-90°**
CONTROL DEFLECTION:	**±30°**
ROLL ORIENTATION:	**0°, 45°**
SETS OF FINS:	**0, 1, 2 REQUIRED; 3 DESIRED**
BODY GEOMETRY:	**AXISYMMETRIC REQUIRED; NONAXISYMMETRIC TREATMENT DESIRED**

FIGURE 1. OBJECTIVE AND REQUIREMENTS OF APC

Since the 2002 version (AP02) of the APC may be the last under Office of Naval Research sponsorship, a more extensive introduction will be given. This introduction will cover not only the rationale of the new technology that has been integrated into the 1998 version (AP98) of the APC to form the basis of the AP02, but will also go back and give a historical perspective on why the APC was started in 1971. In addition, a discussion of the new technology and products developed during the 30 plus years of development of the APC, which allowed the code to stay current with the operational and technical needs of the aerodynamics community, will be given.

1.1 HISTORICAL PERSPECTIVE OF AEROPREDICTION EFFORT

The aeroprediction effort was started in 1971 by the first author as a result of being asked by many engineers to provide aerodynamics for weapon concepts. The focus of these requests was for zero lift drag first and foremost and secondly for low AOA lift characteristics (normal force, center of pressure, and pitching moments). The first efforts to provide this information was based on empirical estimates using wind tunnel data reports, handbooks, and hand calculations using approximate methods. Pitts, et al[1] proved quite useful for the hand calculation of lift properties but was of no value in the more difficult to obtain zero-lift drag. In researching the literature, there were no reasonably accurate and computationally fast computer programs that could calculate total forces and moments for the configurations and flight regimes of interest at the time. The aircraft Datcom[2] could be used to provide hand calculations using the various methods included, but its accuracy was questionable, particularly for the body. Body aerodynamics are quite significant for weapons, as opposed to aircraft where the wing dominates. The GE "Spinner" code[3] was also available in the early 70's, but it was an all empirical code for spin stabilized projectiles. It was based on nose length, boattail length, and overall length. Hence, its use as a design tool was somewhat limited because it would give the same zero lift drag for a nose of given length, regardless of shape. Saffell, et al[4] had developed a missile-oriented high AOA code. However, the drag was computed by handbook techniques and slender body theory was used for lift and pitching moment. As a result, limited accuracy of the Reference 4 code could be expected.

The major reason that there were no fast, yet reasonably accurate codes available for body alone or wing-body aerodynamics was that there were no reasonably accurate approximate methods available to compute wave drag on blunt or truncated nose shapes at low to moderate supersonic Mach numbers. This low supersonic Mach number range is where unguided projectiles spent about 90 percent of their flight time; thus, accurate axial force was required to get accurate range. Therefore, the first author combined the Hybrid Theory of Van Dyke with Modified Newtonian Theory[5,6] to obtain accurate wave drag of typical projectiles. This new combined theory formed the basis of the first version of the APC published in 1972[5] and is referred to here as the AP72. The AP72 met an existing need at the time, as it gave quite accurate drag calculations of projectiles while only requiring one minute per case on a mainframe computer. The same information can be obtained today in less than a second using a personal computer.

Requests for copies of the AP72 code began coming in to Dahlgren from outside agencies as well as requests to extend the capability of the AP72 beyond body-alone cases. The requests for extensions of the code were presented to Naval Sea, Naval Air, and Office of Naval Research sponsors. Consequently, funding for continuous upgrades to the APC has been provided for the past 30 years. In addition to Navy funding, a small amount of funding has been provided by the Army and Air Force. NASA has also provided support through wind tunnel testing.

The first extension of the AP72 was to allow for the addition of two sets of lifting surfaces to the geometry (see Figure 2) so that guided, as well as unguided, projectiles could be considered. This version of the code is referred to as the AP74.[7,8,9] One of the most significant aspects of the AP74, in addition to a total force and moment code for guided projectiles, was the engineering approximations for interference lift of non-slender wings and the change in base drag as a result of the presence of wings.

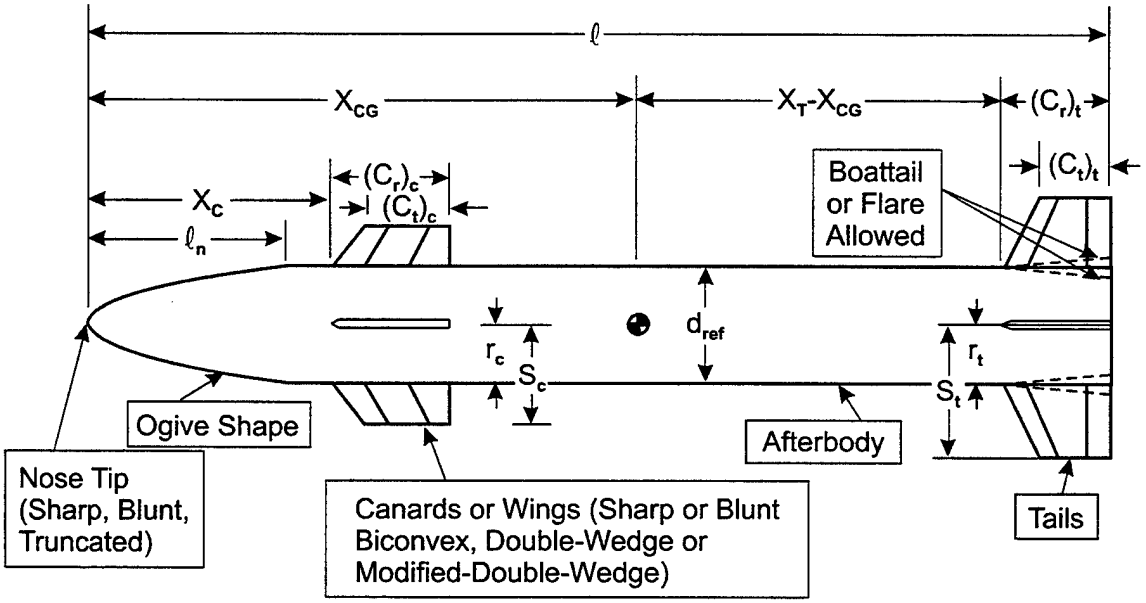

FIGURE 2. TYPICAL AXISYMMETRIC WEAPON CONFIGURATION GEOMETRY OPTIONS AND NOMENCLATURE

The next extension of the APC was to add dynamic derivatives (pitch damping, roll damping, and magnus moment) to the codes capability. The magnus moment was for spin stabilized projectiles only and was assumed to be zero for slowly spinning fin-stabilized rounds. This information could be used to perform dynamic stability analysis of various concepts and to determine how quickly a motion could be expected to damp out. This version of the code was referred to as the AP77.[10-15] The first three versions of the APC were all focused first and foremost on meeting projectile conceptual design requirements.

The next four versions of the APC were all aimed at meeting configuration and missile flight requirements. The first requirement was to extend the Mach number to 8. This Mach number limit was considered as an upper bound of where the perfect gas law could be applied.

A modified form of second-order-shock-expansion theory combined with Modified Newtonian Theory[16] was used as the pressure predictor on the body for Mach numbers greater than about 2. Improved transonic nose drag estimates were also designed[17] and incorporated into the AP81.[18-21] Real gas effects and aeroheating capability was added in the early 90's and the Mach number capability extended to 20 as well.[22-35] Additionally, several new approximate pressure predictors were developed and an improved base drag prediction model was derived. Finally, complete nonlinear aerodynamics were included for all lift components to allow aerodynamics to be estimated at AOA up to 30 deg. The first author introduced the "direct approach" for computing the aerodynamic nonlinearities in this version of the APC, which is referred to as the AP93. By "direct approach" to approximate aerodynamic nonlinearities it is meant that each normal force component associated with a configuration be broken down into a linear and a nonlinear term. The linear term is estimated by linear theory or slender body theory. The nonlinear term is estimated as "directly" as possible by subtracting the linear term from component wind tunnel data and then developing approximations to this nonlinear term based on freestream and geometry consideration. The AP93 theory and computer code was summarized in References 29 and 30.

The AOA capability was extended from 30 to 90 deg at the roll position of $\Phi = 0$ deg (fins in the plus "+" roll position as viewed from the rear) in 1995.[36-45] For the first time, a user friendly pre- and post-processor[37] was developed to reduce the set up time from hours to minutes for most geometries. The AP95 was summarized in References 37, 39, and 40.

The AP98 added significant new capabilities to the APC. First, nonlinear aerodynamics were extended to the $\Phi = 45$ deg roll position (fins in cross or "×" orientation). This technology again used the so called "direct approach" and is summarized in References 46 and 49-51. A method was developed to distribute structural loads (including the nonlinear terms) over the body and wing surface for structural engineers.[48,54] The nonlinear wing-tail interference model was extended to $\Phi = 45$ deg as well.[50] An improved method for axial force at high AOA was developed[52,56] and integrated into the APC. Finally, new technology[55,57,58] was developed to allow noncircular wing-body-tail configurations to be combined in the geometry mix (see Figure 3). All the technology integrated into AP98 is given in References 46-65 and is summarized in References 59-61.

The technology developed for the first seven versions of the APC (AP72, AP74, AP77, AP81, AP93, AP95, AP98) was spread out over a period of over 25 years and many of the references were not easily accessible. Furthermore, no summary document existed that could bring all the many different theories and empirical methods together in a single cohesive fashion. As a result, the first author published a book in 2000, Approximate Methods for Weapon Aerodynamics.[66] This book summarizes all the approximate methods currently in use in the AP98 and offers many sample calculations.

1.2 AP02 NEW TECHNOLOGY

The primary focus of this report is to summarize the new technology which has been integrated into the AP98 to form the basis of the AP02. As already mentioned, the first three

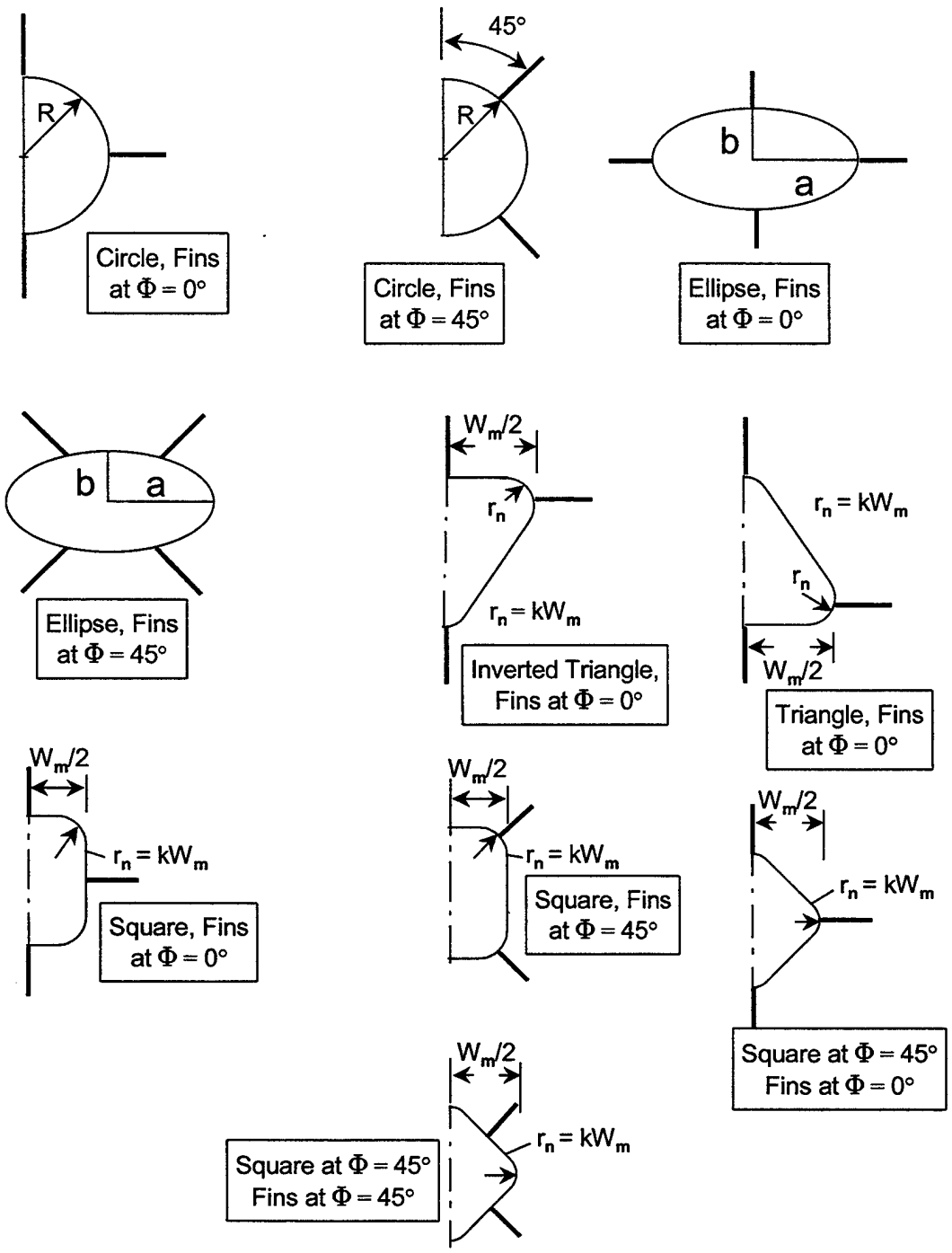

FIGURE 3. NONCIRCULAR CROSS-SECTION, WING-BODY CONFIGURATIONS FOR THE AEROPREDICTION CODE

versions of the APC focused on meeting guided and unguided projectile requirements (AP72, AP74, AP77) and the last four versions have focused on meeting missile requirements (AP81, AP93, AP95, AP98). During the past 20 plus years, many emerging projectile concepts have been investigated; however, many could not be considered in their entirety by the APC. The

APC could be used as the workhorse to do many of the aerodynamic calculations, but the projectile concepts had many design needs that could not be met with even the latest version of the APC, the AP98. These emerging projectile needs that form the basis of the AP02 are summarized in Figure 4.

Referring to Figure 4, the first requirement that we addressed for the projectile concepts was that of providing aerodynamics for concepts that consider 6 and 8 fins as alternatives to 2 or 4 fins, which the AP98 handled. The Extended Range Guided Munitions (ERGM) as well as other concepts, have considered multi-fins in the past. The present approach is to use the AP98 in conjunction with hand calculations to estimate multi-fin aerodynamics. New technology was developed[67,68] and integrated into the AP98 to automate this process.

The next problem area addressed for the projectiles was refinement of the nonlinear aerodynamic terms. The primary data base upon which these nonlinear terms were developed was the NASA/Tri Service Data Base.[69] The Reference 69 data base was developed using a constant value of r/s of 0.5, which is typical of many missiles. However, many guided projectiles have fins with fairly large semispans and can have r/s values as low as 0.2. A more recent data base[70] was provided to us where r/s was varied from 0.25, 0.33 and 0.5. This allowed us to refine our nonlinear aerodynamic terms for all normal force and interference effects. The new technology resulting from the refinement was documented[71-73] and integrated into the AP98.

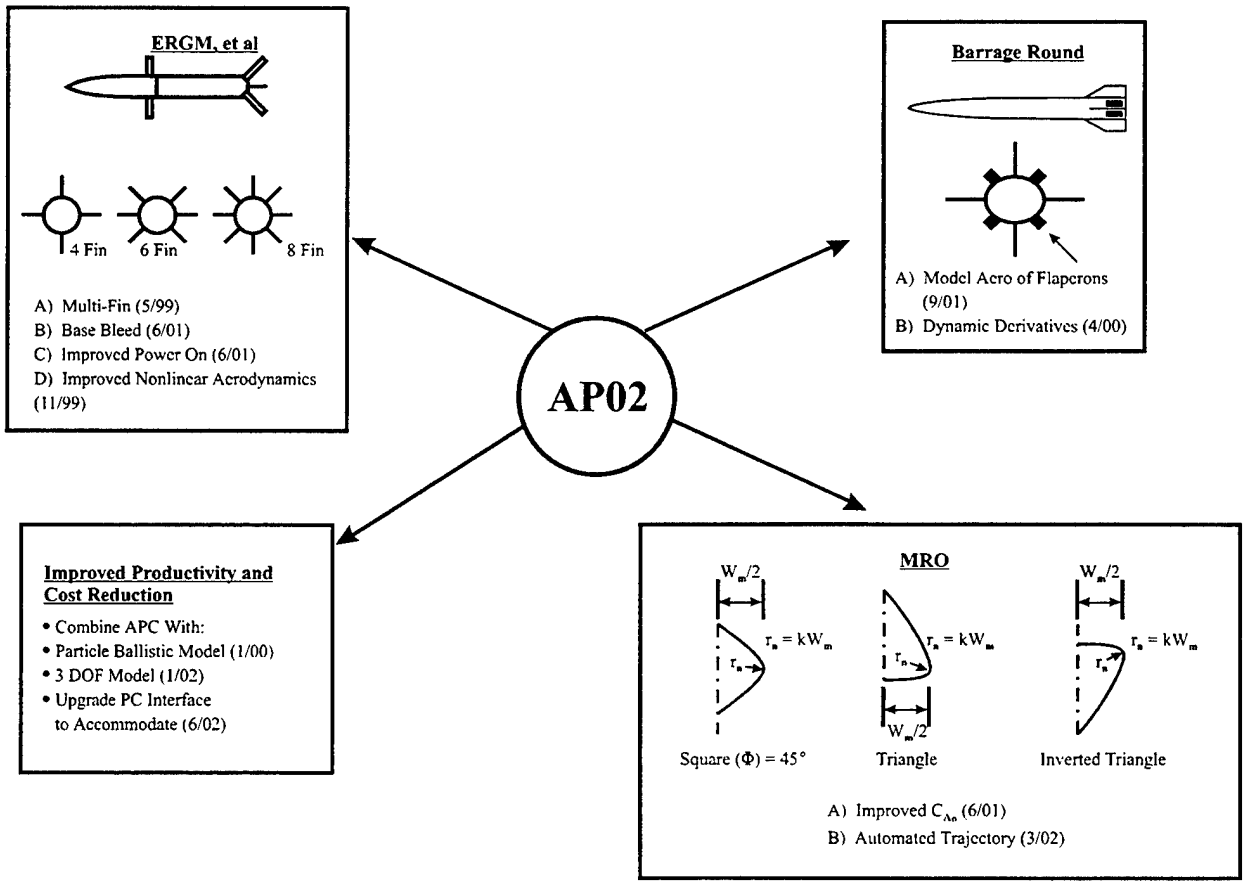

FIGURE 4. AP02 REQUIREMENTS

The third problem area indicated in Figure 4 for projectiles was dynamic derivatives. The dynamic derivatives had not been changed since 1977. Specifically, the limitations for the dynamic derivatives include the lack of a pitch damping term for the flare component of a projectile configuration. Also, the body alone pitch damping is based on an old empirical data base, and no nonlinear terms were included in this data base. The first two of these problem areas were addressed, improved upon, documented,[74,75] and integrated into the AP98 to be a part of the AP02. The third problem area, a lack of nonlinearities for the dynamic derivatives, was not addressed due to lack of a good generic data base that covered the flight regimes of interest. To develop a generic data base, analogous to References 69 or 70, was beyond the scope of present work.

The fourth problem area addressed for the projectile needs was that of improving the power-on base drag and providing a base bleed capability. The power-on base drag was incorporated in the AP81 and had not been changed since that time. This methodology was improved upon by making it more robust. In addition, a base bleed capability, which has been requested by projectile designers for over 10 years, was integrated into the APC and will also be a part of the AP02. The improved power-on base drag methodology was documented in References 76 and 77.

Another area indicated for improvement in Figure 4 to meet projectile requirements is that of improving the zero lift axial force for noncircular cross section bodies. Some weapon concepts, such as the Mission Responsive Ordnance, need the capability to reasonably and accurately predict axial force so a good trajectory estimate can be made. Some modifications to axial force for nonaxisymmetric bodies were made and incorporated into the AP98.[55] However, without adequate data, it was not clear if enough refinements in axial force had been made. A recent data base taken at the Aeroballistic Range Facility[78] at Eglin Air Force Base has allowed the axial force prediction for noncircular bodies to be refined. This refinement has not been formally documented and this report will serve to meet the formal documentation need.

The final aerodynamic requirement referred to in Figure 4 that the AP98 cannot meet is to calculate aerodynamics of concepts which use trailing-edge flaps for control. The Barrage Round is an example of a concept that considered trailing-edge flaps. Again technology was developed and documented[79] that will be a part of the AP02. This new technology can only be applied to the aft located set of lifting surfaces as presently configured for the AP02.

In addition to aerodynamic needs that were not met from a projectile requirements standpoint, improved productivity for one of the primary applications of the APC aerodynamics is addressed by the AP02. This application is to use aerodynamics generated by the AP02 as inputs to trajectory (either ballistic or trim mode) analysis. The AP98 process is to generate a set of aerodynamics, provide these to a flight dynamicist who will input the aerodynamics into a trajectory module and generate trajectories. In many cases, aerodynamic design changes are made as a result of this process and an interaction process between the aerodynamicist and flight dynamicist begins. The AP02 will contain a module for ballistic and a three degree-of-freedom code for trim aerodynamics. As a result, a personal computer can be used to rapidly make design changes and see the results in terms of range and flight performance. This automation of

incorporation of trajectories into the AP02 should provide significant airframe only in the design productivity improvements.

Figure 5 summarizes the APC evolution from its inception in 1972 to the present AP02 version that will soon be available.

1.3 SUMMARY OF AEROPREDICTION PRODUCTS PRODUCED

Since this version of the APC may be the last under ONR sponsorship, it is believed worthwhile to summarize the products produced for the money invested over the last 30 years. During that time frame, it is estimated a total of 5 to 6 million dollars (in fiscal year 2002 dollars a factor of 2 would be applied to the 5 or 6 million) has been invested in developing the 8 versions of the aeroprediction code. The products produced include computer codes, new technologies, training of new engineers, reports, and one book. Table 1A summarizes the first authors perspective on the new or improved methods that were developed during the 30-year time frame. These new technologies were documented in References 5-68, 71-77, and 79. The new technologies developed up through 1998 were then summarized in a book.[66] This report will summarize the new technologies developed since the AP98 was developed.

Table 1B summarizes the products produced from the 30-year technology effort. These products included 8 versions of the APC. The latest version that is in transition (AP98) has been transitioned to over 140 requesting organizations. This includes all major Department of Defense activities (both private and public) involved in the weapons business as well as several universities. It currently includes 80 publications and several more publications will be added to fully document the AP02. Some of the intangible products produced are the numerous young engineers who have been trained on the job with some version of the APC. Also, the cost savings to the many weapons programs that have used the APC in preliminary design is difficult to estimate.

At the request of several branch heads, the first author has just started providing training courses on APC theory and use. These courses are not paid for by the Navy technology sponsors, but by the agencies who send students to the classes. However, it is a means to continue to provide technical support to the aeroprediction effort and help the technical community to better use the APC with all its available options. It is also a means to train junior engineers on fundamental weapon aerodynamics and the use of the code.

2.0 AP02 NEW CAPABILITY

Section 1.2 discussed the new methods that have been developed to meet some of the needs of the projectile community and those that will be part of the AP02. These methods included multi-fin aerodynamics, improved nonlinear aerodynamics, improved pitch damping, improved axial force for nonaxisymmetric bodies, improved power-on base drag (including base bleed effects), trailing-edge flap technology, and trajectory models. In addition to these new

			FLIGHT CONDITIONS							
VERSION	**WEAPONS**	**AERODYNAMICS**	**MACH NO.**	**REAL GAS AVAILABLE**	**AOA RANGE**	**ROLL**	**TRAJECTORY AVAILABLE**	**NONLINEAR DISTRIBUTED LOADS AVAILABLE**	**COMPUTERS**	**EMERGING PROJECTILE NEEDS**
1972	AXISYMMETRIC UNGUIDED PROJECTILES	STATIC ONLY	0-3	NO	0-15°	Φ=0°	NO	NO	CDC	NO
1974	AXISYMMETRIC UNGUIDED PROJECTILES, ROCKETS, MISSILES	SAME	0-3	NO	SAME	SAME	NO	NO	CDC	NO
1977	SAME	STATIC AND DYNAMIC	0-3	NO	SAME	SAME	NO	NO	CDC, IBM	NO
1981	SAME	SAME	0-8	NO	0-15° (LIMITED CONF AT HIGHER α)	SAME	NO	NO	CDC, IBM, VAX	NO
1993	SAME	SAME	0-20	YES	0-30°	SAME	NO	NO	CDC, IBM, VAX SILICON GRAPHICS	NO
1995	SAME	SAME	SAME	YES	0-90°	SAME	NO	NO	INTERACTIVE PC	NO
1998	AXISYMMETRIC & ASYMMETRIC MISSILES, ROCKETS	SAME	SAME	YES	SAME	Φ=0°, 45°	NO	YES	INTERACTIVE PC, WINDOWS 98 ONLY	NO
2002	SAME PLUS MULTI-FIN	SAME	SAME	YES	SAME	SAME	YES	YES	IMPROVED INTERACTIVE PC, WINDOWS 98, 2000 & NT	YES

FIGURE 5. EVOLUTION OF AEROPREDICITON CODE IN TERMS OF MAJOR NEW ADDED CAPABILITY

TABLE 1A. NEW TECHNOLOGY DEVELOPED IN ENGINEERING AEROPREDICTION AREA

1.	New method for computing wave drag on blunt bodies for Mach numbers $1.2 \leq M \leq 2.5$
2.	New semiempirical method for estimating base drag
3.	First Aeroprediction Code (coined the term aeroprediction in 1973 and it is widely used in the community today)
4.	Engineering methods for treating lift and interference of non slender wings with linear theory and slender body theory
5.	Empirical method to estimate base drag due to angle of attack and tail fins
6.	Improved method of second-order-shock-expansion theory for blunt bodies
7.	Improved methods for dynamic derivatives
8.	Semiempirical method for transonic wave drag and normal force prediction
9.	New empirical method for magnus prediction due to boattails
10.	New optimization method for design of bodies for minimum drag
11.	A new method for calculating aerodynamics on nonaxisymmetric bodies at low supersonic Mach numbers
12.	Extended second order shock expansion theory to include real gas effects
13.	New pressure prediction methods developed for blunt bodies and to include angle of attack effects
14.	New approximate method for computing heat transfer coefficients
15.	Improved body alone nonlinear lift prediction
16.	New wing-alone, wing-body, and body-wing interference lift methods developed for angle of attack effects
17.	New wing-body interference method due to control deflection
18.	New base drag data base
19.	Improved empirical base drag prediction method
20.	Improved wing-tail interference method
21.	Method to distribute nonlinear loads over wings and body for structural application
22.	Improved method for nonlinear axial force prediction
23.	Improved method for aerodynamics of noncircular cross-section bodies
24.	Simplified method for multi-fin weapon aerodynamics
25.	Improved methods for power-on base drag prediction
26.	Improved method for aerodynamics of trailing-edge flaps

TABLE 1B. PRODUCTS AND TRANSITIONS PRODUCED FROM THE ENGINEERING AEROPREDICTION TECHNOLOGY

1.	Eight (8) versions of the AP Code 1972, 1974, 1977, 1981, 1993, 1995, 1998, 2002
2.	Numerous transitions of various versions of code. 1998 version transitioned to over 140 agencies
3.	87 publications with several more planned • 37 NSWCDD Technical Reports • 28 Papers at recognized meetings • 21 Journal articles • 1 Book
4.	Intangible Products • Training provided to numerous young engineers • Cost savings to numerous weapons programs due to productivity enhancements and cost effective accuracy of APC

technologies integrated into the AP02, we have incorporated an aerodynamic smoother at boundary points where different methods are used to calculate aerodynamics. We have also upgraded the pre- and post-processor interface to the Fortran computer code that allows aerodynamics to be obtained several times faster than using the older method of inputs to the Fortran code. Each of these new methods are discussed in detail in References 67, 68, 71-77, and 79. Each of the new capabilities will be summarized in this report. For more details on each new method and for more detailed validation with experiment, the reader is referred to the above references.

After the new or improved methods added to the AP98 (which will comprise the AP02) are summarized, it is believed useful to briefly discuss the methods in the AP98 that will remain unchanged. In fact, most of the theoretical and empirical methods currently in use in the AP98 will remain unchanged. The reader is referred to Reference 59 for a brief summary of the AP98 methods and to Reference 66 for a more detailed summary of the AP98 theory.

2.1 MULTI-FIN AERODYNAMICS CAPABILITY

Work discussed in this section of the report was documented in References 67 and 68 and the reader is referred to these references for the details of the multi-fin aerodynamics capability. The work of those two references will be briefly summarized here.

Typical weapon configuration design and control alternatives, for which aerodynamics are desired, are shown in Figure 6. These configurations define the general requirements to be considered in the analytical development methodology for multi-fin configurations. In general, one can have a body-tail configuration that is either guided or unguided. If it is unguided, four, six, or eight tail fins can be assumed. Should other needs become apparent in the future, additional fin alternatives could be considered.

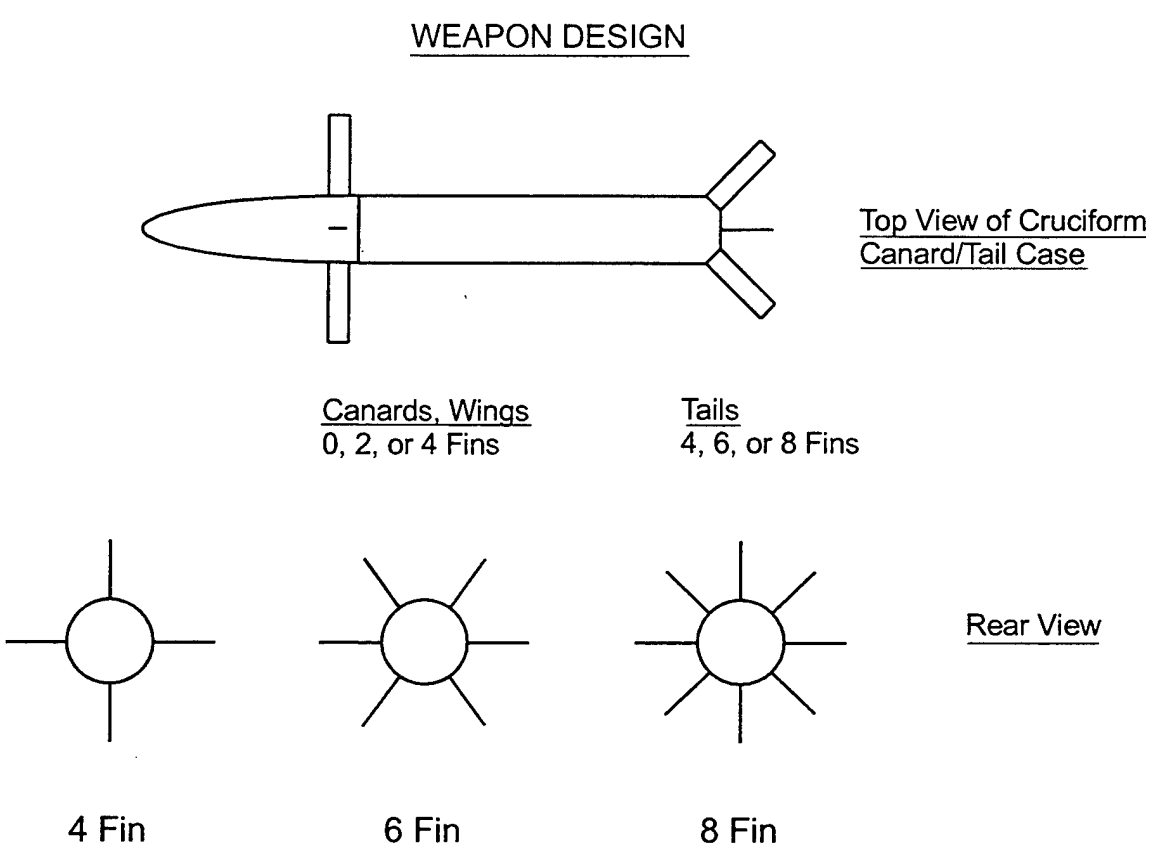

FIGURE 6. TYPICAL WEAPON DESIGN AND CONTROL ALTERNATIVES

Canard or wing-body-tail configurations have more options for control than body-tail. The control can be from the canards or wings, in which case there will be two or four canards (wings) present and either four, six, or eight tail surfaces. Here, the tail surfaces are used exclusively for stability. For the tail control option, the forward set of lifting surfaces can have 2, 4, 6, or 8 fins; but again, the tail controls are assumed to be cruciform. In effect, the above alternative design and control constraints are placed on the aerodynamics methodology from a practical standpoint.

The above set of requirements had to do with the practical configurations for which aerodynamics are desired. A second set of requirements in the analytical methodology development had to do with the methodology development approach in the APC. This latter set

of requirements is driven by the APC logic and how to most cost-effectively integrate multi-fin computations into a code set up for 2- or 4-fin alternatives. The APC logic requirement thus leads one to define factors by which the 2- or 4-fin aerodynamics can be multiplied so as to make the minimum amount of changes to the APC.

The multi-fin aerodynamics we are interested in include the effect on axial force, normal force, center of pressure, roll damping moment, and pitch damping moment. Magnus moment is presently assumed to be zero for fin-stabilized weapons because of low spin rates (this assumption may be inaccurate if the spin rate is greater than a few cycles per second). Each of these aerodynamics will be considered individually.

Based on past experience with calculations of axial force of two fins versus four fins, we have found reasonable accuracy by taking the axial force coefficient of a single fin and multiplying it by the number of fins of interest. No interference effect between the body and fins, other than the base pressure, has been observed. Hence, this assumption will be made for the axial force of weapons with more than four fins. That is

$$C_A = C_{A_{BODY}} + \left(C_{A_{SF}}\right)(NF) \tag{1}$$

However, it should be pointed out that as the number of fins increases from four to eight, the probability of mutual interference between fins increases. This is particularly true for highly blunt fin leading edges. Nevertheless, for the time being, Equation (1) will be assumed.

It will also be assumed that the center of pressure of the total normal force contribution of multi-fins is the same as that of four fins. The total normal force contribution of the fins includes the normal force of the fins in presence of the body, plus the additional normal force on the body as a result of the fins being present.

For roll damping moments, the present methodology in the AP98 assumes the fins go to the centerline of the body, the roll damping of planar fins is computed using linear theory, the number of fins is accounted for by slender body theory (SBT), and body interference effects are accounted for by Figure 7. Figure 7 is taken from Reference 80; it basically says that for two- or four-fin cases, the wing-body roll damping is nearly independent of r/s (where r is the body radius and s is the body radius plus the wing semispan) for values up to 0.4. After that, the roll damping goes to the body-alone value in a nearly linear fashion as r/s approaches 1.0. Also, SBT says that the value of roll damping of eight, six, and four fins compared to that of two fins is 2.3, 2, and 1.62, respectively. These factors are used in conjunction with the roll damping moment of the fin alone and the interference factors of Figure 7 to compute roll damping of multi-fin configurations. The only assumption made here is that for six or eight fins, the curve of Figure 7 for four fins can be used directly. This assumption is based on the fact that SBT shows little difference between two- and four-fin wing-body roll damping as a function of r/s, as seen in Figure 7.

As far as pitch damping moment is concerned, the computational procedure is similar to that of the roll damping. The wings are assumed to extend to the centerline of the body, the pitch

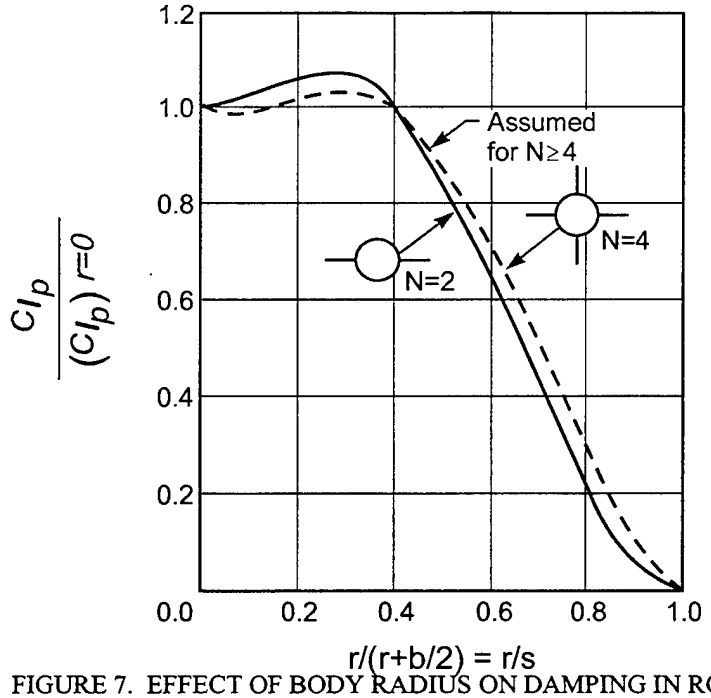

FIGURE 7. EFFECT OF BODY RADIUS ON DAMPING IN ROLL FOR FIXED SPAN (TAKEN FROM REFERENCE 67)

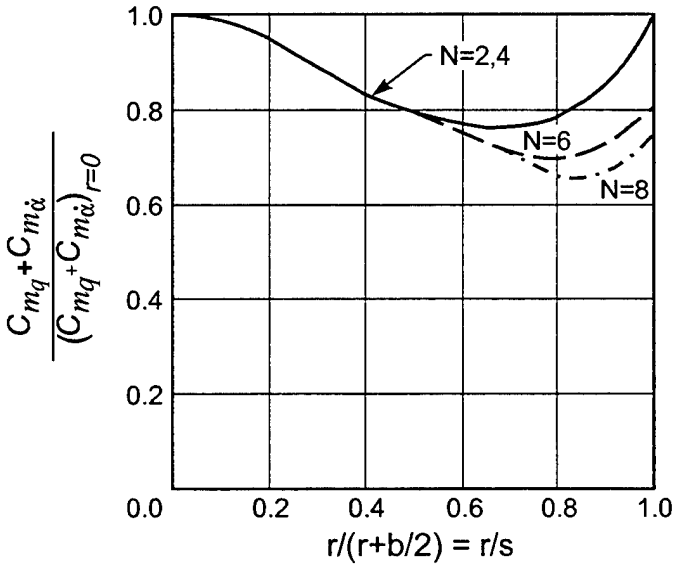

FIGURE 8. EFFECT OF BODY RADIUS ON DAMPING IN PITCH FOR FIXED SPAN WINGS

damping of planar wings is computed using linear theory, and then the method of Bryson[81] is used to account for the interference effects of the body in the presence of the wing. Since the wings are assumed to extend to the centerline of the body and the number of wings will be accounted for by the factor of the normal force of the wing alone, this wing-body interference factor will be less than one. Figure 8 gives the SBT interference results for pitch damping

moment for two, four, six, and eight wings. As seen in Figure 8, increasing the number of fins from two to eight has very little effect for small values of r/s (r/s $\leq$ 0.4), but wing-body interference has an increasing effect for all fins as r/s approaches 0.6 to 0.8.

SBT states that the normal force of six and eight fins is, respectively, 1.5 and 2.0 times that of four fins. Experience has shown these factors to be high in general, particularly as AOA increases. Since the AP98 has all the nonlinearities for the normal force contributions of the wing, body, and interference terms, it seems logical to assume

$$\left[C_{N_{W(B)}}, C_{N_{B(W)}}, C_{N_{T(V)}}\right]_{6,8\,Fin} = (F_6, F_8)\left[C_{N_{W(B)}}, C_{N_{B(W)}}, C_{N_{T(V)}}\right]_{4\,Fin} \tag{2}$$

where the factors F_6 and F_8 must be determined. They are the factors by which we multiply the cruciform fin normal force components for six- and eight-fin configurations, respectively. These factors are the SBT factors of 1.5 and 2.0 previously mentioned. However, the SBT values will be replaced with values appropriate for a given aspect ratio wing at a given AOA and Mach number. While the factors will be determined explicitly for the wing-body plus the body-wing contributions to normal force, they will also be assumed to apply to the tail downwash $C_{N_{T(V)}}$ and pitch damping moment for the time being. Computational Fluid Dynamics (CFD) methods were used to calculate the factors F_6 and F_8 of Equation (2).

Two CFD codes were used in the computational process. They are the ZEUS[82] and GASP[83] codes. The ZEUS code is a full Euler solver; the GASP code is a full Navier-Stokes solver with a subsonic Euler solver option. The ZEUS code uses a marching solution to the Euler equations. This means the flow along the axial plane must be supersonic in order for the code to have hyperbolic flow conditions throughout the computational region. This region encompasses the bow shock to the rear of the body.

Results for the factors F_6 and F_8 obtained from use of the CFD code in conjunction with extrapolations of CFD results in some cases is given in Table 2. Table 2, along with Equations (1) and (2), Figures 7 and 8, and the SBT factors for roll and pitch damping is the process the AP02 will use for estimating aerodynamics of 6 and 8 fin configurations based on the aerodynamics of 4 fin cases.

2.2 AERODYNAMIC SMOOTHER

The APC uses many different methods to predict aerodynamics at a given Mach number and AOA. At Mach numbers 1.2, 2.0, and 6.0, where one method ends and another method takes over, discontinuities in aerodynamics can be encountered. The discontinuities are the result of different methods being used on either side of M_∞ = 1.2, 2.0, or 6.0. The problem does not appear to be significant at M = 1.2, but at 2.0 and 6.0, these fictitious discontinuities can be misleading to an unsuspecting user of the APC when they plot the aerodynamics as a function of Mach number. As an illustration of this problem, consider Figure 9. Figure 9 is an example of a 12-caliber, axisymmetric body, tangent ogive-cylinder configuration with a nose length of 3 calibers. It has aspect ratio 2.0 cruciform delta fins oriented in the Φ = 0 deg roll orientation

TABLE 2. APPROXIMATED VALUES OF THE FACTORS F_6 AND F_8 OBTAINED FROM SMOOTHED VALUES OF THE ZEUS AND GASP CODE COMPUTATIONS AND ENGINEERING JUDGEMENT

AR	α	F_6 MACH NUMBER					F_8 MACH NUMBER				
		0.6	1.5	2.0	3.0	4.5	0.6	1.5	2.0	3.0	4.5
.25	0	1.26	1.37	1.27	1.19	1.22	1.90	1.42	1.4	1.27	1.30
	15	1.00	1.00	1.10	1.19	1.35	1.45	1.03	1.17	1.27	1.46
	30	1.00	1.00	1.00	1.19	1.22	1.00	1.00	1.01	1.27	1.32
	45	1.00	1.00	1.00	1.00	1.00	1.00	1.00	1.00	1.00	1.00
	60	1.00	1.00	1.00	1.00	1.00	1.00	1.00	1.00	1.00	1.00
	75	1.00	1.00	1.00	1.00	1.00	1.00	1.00	1.00	1.00	1.00
	90	1.00	1.00	1.00	1.00	1.00	1.00	1.00	1.00	1.00	1.00
.50	0	1.35	1.25	1.20	1.30	1.47	2.00	1.36	1.28	1.35	1.72
	15	1.06	1.10	1.15	1.29	1.50	1.50	1.18	1.24	1.40	1.83
	30	1.00	1.00	1.07	1.28	1.36	1.00	1.08	1.16	1.41	1.60
	45	1.00	1.00	1.00	1.00	1.00	1.00	1.00	1.04	1.06	1.20
	60	1.00	1.00	1.00	1.00	1.00	1.00	1.00	1.00	1.00	1.00
	75	1.00	1.00	1.00	1.00	1.00	1.00	1.00	1.00	1.00	1.00
	90	1.00	1.00	1.00	1.00	1.00	1.00	1.00	1.00	1.00	1.00
1.0	0	1.40	1.22	1.35	1.42	1.50	1.92	1.27	1.58	1.96	2.00
	15	1.15	1.13	1.23	1.32	1.50	1.69	1.38	1.38	1.80	2.00
	30	1.07	1.00	1.00	1.21	1.38	1.43	1.28	1.15	1.64	2.00
	45	1.02	1.00	1.00	1.10	1.13	1.20	1.05	1.00	1.48	1.61
	60	1.00	1.00	1.00	1.00	1.00	1.00	1.00	1.00	1.32	1.25
	75	1.00	1.00	1.00	1.00	1.00	1.00	1.00	1.00	1.16	1.00
	90	1.00	1.00	1.00	1.00	1.00	1.00	1.00	1.00	1.00	1.00
2.0	0	1.42	1.50	1.50	1.50	1.50	1.92	1.77	1.97	1.92	1.90
	15	1.31	1.41	1.27	1.39	1.50	1.70	1.95	1.75	1.77	2.00
	30	1.17	1.00	1.03	1.27	1.45	1.47	1.65	1.57	1.62	2.10
	45	1.03	1.00	1.00	1.14	1.23	1.25	1.32	1.27	1.47	1.95
	60	1.00	1.00	1.00	1.00	1.00	1.02	1.00	1.02	1.32	1.62
	75	1.00	1.00	1.00	1.00	1.00	1.00	1.00	1.00	1.17	1.32
	90	1.00	1.00	1.00	1.00	1.00	1.00	1.00	1.00	1.00	1.00

with the leading edge located 7.8 calibers from the nose tip. The moments are taken about the center of gravity.

The static aerodynamics shown in Figure 9 are axial force, normal force, and pitching moment coefficients along with the center of pressure. Mach numbers for which the AP98 was executed were 0.6, 0.9, 1.2, 1.5, 1.99, 2.01, 2.4, 2.95, 3.95, 5.99, 6.0, and 10. The point where second-order Van Dyke (SOVD) ends and second-order shock expansion (SOSE) takes over was selected to be 2.0. The point where conventional second-order shock expansion ends and a modified form of shock expansion theory (MSOSE) takes over is automatically set at 6.0 in the AP98. Hence, M = 1.99 data is from SOVD, M = 2.01 and 5.99 data are from SOSE, and M = 6.0 data is from MSOSE. Notice on the C_A plot that there is a discontinuity between SOVD and SOSE at M = 2.0. Also notice on the C_N plot that there is a discontinuity at both M = 2.0 and 6.0. For pitching moment and center of pressure, discontinuities occur only at M = 6.0. The discontinuities in Figure 9 appear small, but some cases considered in the past have shown discontinuities larger than these.

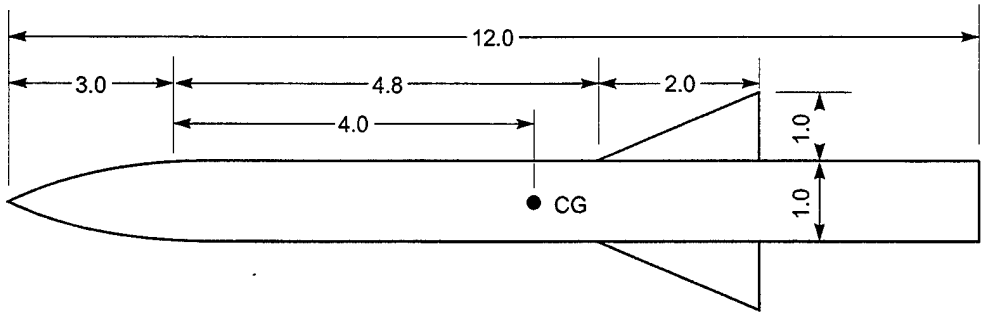

Body Tail Configuration (Dimensions in Calibers with 1 Calibers = 3.0 in.)

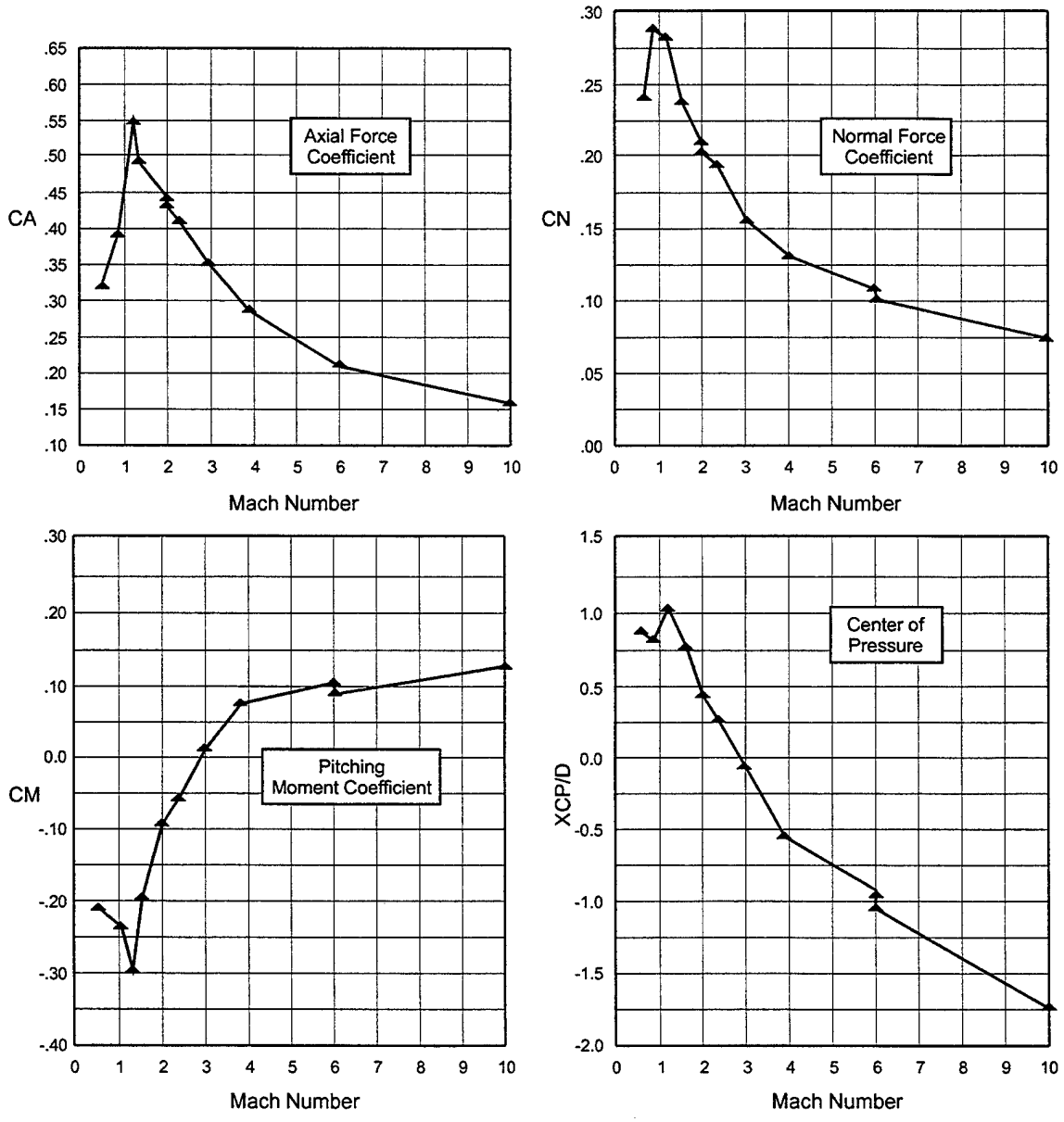

FIGURE 9. STATIC AERODYNAMICS OF A BODY-TAIL CONFIGURATION ILLUSTRATING DISCONTINUITIES AROUND M = 2.0 AND 6.0 (α = 1 DEG, Φ = 0 DEG)

While the numbers in this particular example, due to the different aerodynamic methods, are less then 5 percent of the totals, the user of the APC is left with the question of which number to use. Experience has shown in comparison to data that an average of the two numbers is probably better than using either of the estimates alone. As a result, an aerodynamic smoother was developed that is based on an average of the values given by SOSE and SOVD at M = 2.0 and an average of SOSE and MSOSE at M = 6.0. The smoother linearly goes to the SOVD value at M = 1.5 and to the SOSE value of the particular coefficient at M = 2.5. Likewise, the value of the aerodynamic coefficient at M = 5.0 is based fully on SOSE. At M = 7.0, it is based on MSOSE. The average value of the two methods is used at M = 6.0.

The mathematics of the aerodynamic smoother at M = 2.0 and M = 6.0 are defined by Equations (3) and (4).

Smoother at M = 2.0

$$(C_i)_{M=1.5} = (C_i)_{SOVD}; (C_i)_{M=2.5} = (C_i)_{SOSE} \tag{3A}$$

$1.5 \le M < 2.0$

$$(C_i)_M = (C_i)_{SOVD} + 2(M-1.5)(\Delta C_i)_{M=2.0} \tag{3B}$$

$2.0 \le M \le 2.5$

$$(C_i)_M = (C_i)_{SOSE} + 2(M-2.5)(\Delta C_i)_{M=2.0} \tag{3C}$$

where $(\Delta C_i)_{M=2.0} = ((C_i)_{SOSE} - (C_i)_{SOVD})/2$

Smoother at M = 6.0

$$(C_i)_{M=5.0} = (C_i)_{SOSE}; (C_i)_{M=7.0} = (C_i)_{MSOSE} \tag{4A}$$

$5.0 \le M < 6.0$

$$(C_i)_M = (C_i)_{SOSE} + (M-5.0)(\Delta C_i)_{M=6.0} \tag{4B}$$

$6.0 \le M < 7.0$

$$(C_i)_M = (C_i)_{MSOSE} + (M-7.0)(\Delta C_i)_{M=6.0} \tag{4C}$$

where $(\Delta C_i)_{M=6.0} = ((C_i)_{MSOSE} - (C_i)_{SOSE})/2$

The term C_i of Equations (3) and (4) represents any of the static aerodynamic coefficients. Figure 10 is a qualitative view of what Equations (3) and (4) are doing in terms of modifying the values of the AP98 so as to eliminate the discontinuities shown in Figure 9.

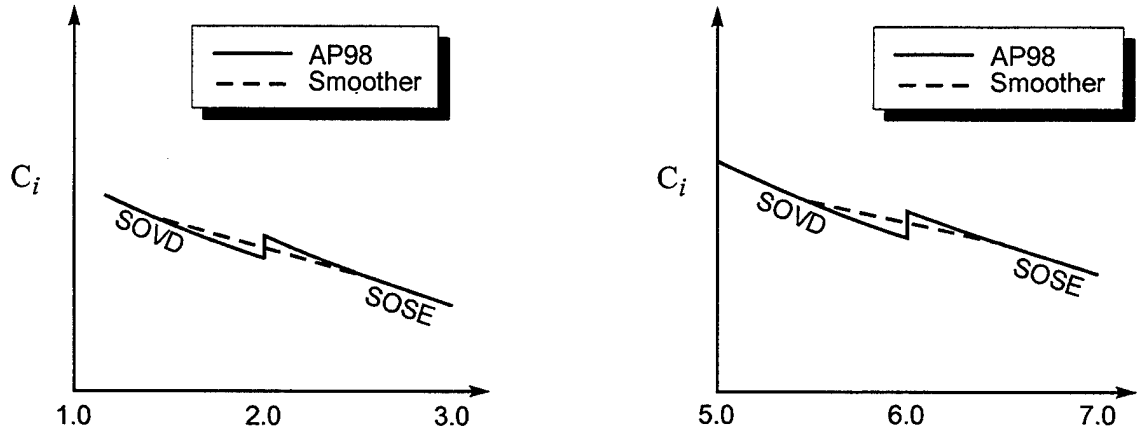

FIGURE 10. USE OF AERODYNAMIC SMOOTHER TO ELIMINATE DISCONTINUITY IN VALUE OF C_i AT M = 2 AND 6

Figure 11 shows the new values of normal force coefficient and center of pressure for the configuration of Figure 9 using the aerodynamic smoother. Note that the discontinuities of Figure 9 are no longer present in Figure 11 as a result of the aerodynamic smoother. The smoother only eliminates the discontinuity in the value of the aerodynamic coefficient. It does not require that the slope of the aerodynamic coefficients (i.e., dC_i/dM) be continuous in a mathematical sense.

2.3 IMPROVED NONLINEAR AERODYNAMICS

The APC is a semiempirical code which predicts low AOA aerodynamics primarily based on linearized, slender body and local slope theories and computes the nonlinear terms empirically based on several large component wind tunnel data bases.[69,70,84,85] To illustrate the semiempirical approach, it is convenient to write the total normal force coefficient equation for a wing-body-tail configuration as defined by Pitts,[1] et al. That is

$$\begin{aligned} C_N = C_{N_B} &+ \left[\left(K_{W(B)} + K_{B(W)}\right)\alpha + \left(k_{W(B)} + k_{B(W)}\right)\delta_W \right]\left(C_{N_\alpha}\right)_W \\ &+ \left[\left(K_{T(B)} + K_{B(T)}\right)\alpha + \left(k_{T(B)} + k_{B(T)}\right)\delta_T \right]\left(C_{N_\alpha}\right)_T + C_{N_{T(V)}} + C_{N_{B(V)}} \end{aligned} \tag{5}$$

Each of the terms in Equation (5) are composed of a linear and a nonlinear term. Reference 1 only considered the linear term; more recent semiempirical codes include nonlinearities as well (see References 59, 86, and 87 for examples).

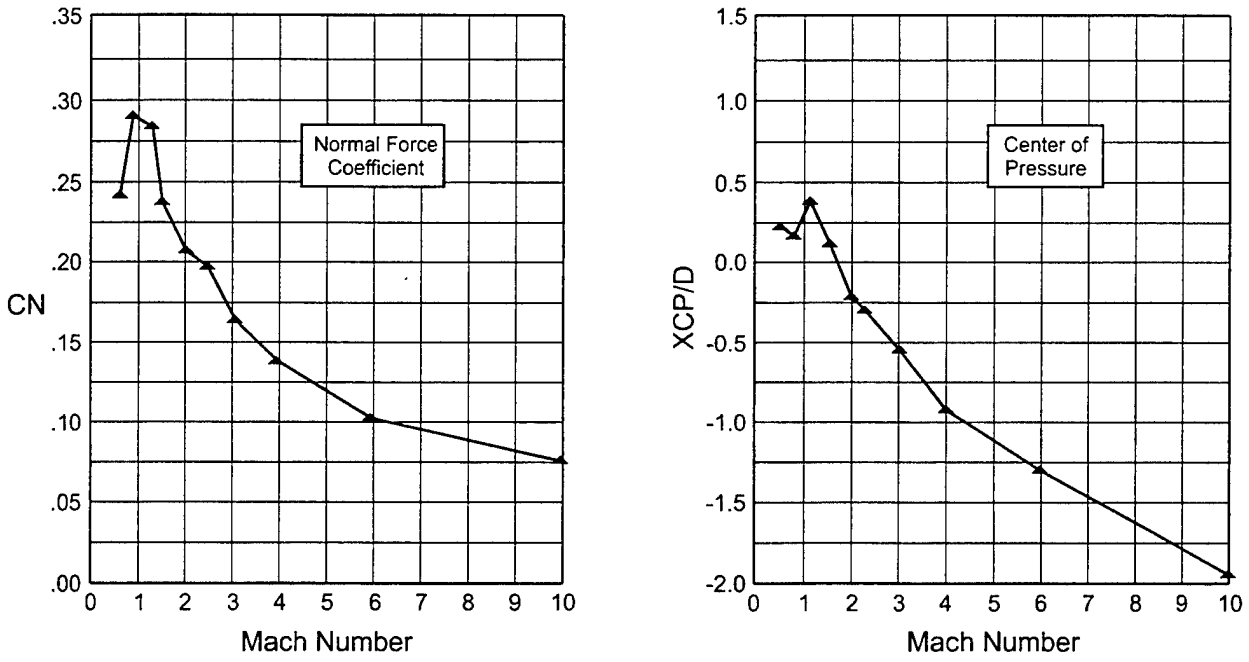

FIGURE 11. NORMAL FORCE COEFFICIENT AND CENTER OF PRESSURE FOR CONFIGURATION OF FIGURE 9 USING AERODYNAMIC SMOOTHER

The nonlinear terms of the AP98 were based primarily on data bases[69,84,85] where r/s was a constant (see Figure 2 for nomenclature) value of 0.5. A more recent missile component data base[70] varies r/s from 0.25, 0.33, and 0.5. This more recent data base, which includes wing-alone, body-alone, and wing-body data should allow refinement in the nonlinear terms that are used in the AP98 to model Equation (5) and the companion center of pressure representation. Figure 12 shows the comparisons of the configurations tested in the References 69 and 70 data bases.

In comparing the AP98 to the Reference 70 data base, it was found that there was good agreement between theory and data. The average error on normal force and center of pressure was about 7 percent and 2 percent of the body length, respectively.[71] Although these comparisons are within the desired accuracy levels of ±10 percent and ±4 percent of body length for normal force and center of pressure, respectively, there were some areas where the AP98 accuracy compared to the Reference 70 data base seemed to warrant improvement. These areas were body-alone normal-force coefficient for $M_\infty > 2.75$, body-alone center of pressure in the transonic Mach number region, and the treatment of the linear term of the body-alone normal-force coefficient above $\alpha = 30$ deg. For the wing-alone and total configuration aerodynamics, some slight changes appeared to be needed in the wing-alone aerodynamics and wing-body interference factors.

In some later undocumented work, several fine tuning changes were found to be needed for the nonlinear interference terms for control deflection of Equation (5). Hence, this section of the report summarizes the changes previously documented[71-73] for the nonlinear aerodynamic terms for the wing- and body-alone and the wing-body and body-wing interference due to AOA.

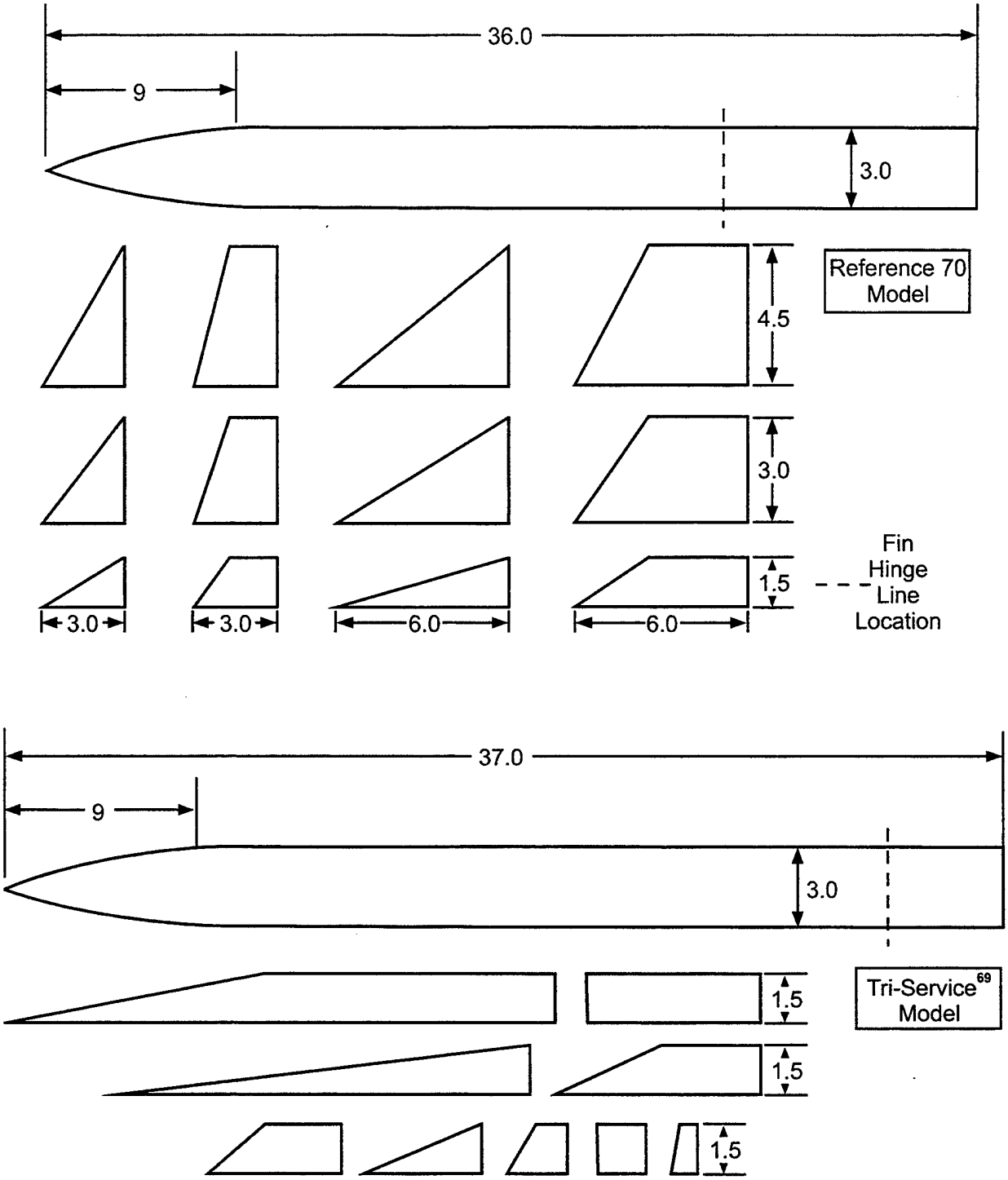

FIGURE 12. SCALED GEOMETRY COMPARISON WITH TRI-SERVICE MODEL[69] AND REFERENCE 70 MODEL (ALL DIMENSIONS IN INCHES)

In addition, some late refinements for the wing-body and body-wing interference due to control deflection that were not formally documented will be documented at this time.

2.3.1 Body Alone Modifications

In comparing the AP98 to the body-alone wind tunnel data of Reference 70, good agreement in center of pressure and normal force were obtained. Average errors of normal force were less than 6 percent and center of pressure less than one-fourth caliber or 2 percent of the body length. These average errors were calculated using optimum values of the critical crossflow Mach number and Reynolds number, which is quite important for $M_\infty \leq 1.2$ comparisons. Reynolds number Re_c was a constant 3.3×10^5, and M_{N_C} varied from 0 at $M_\infty = 0.6$ to 0.06 at $M_\infty = 0.9$. Also, error values were calculated at each 5-deg AOA at all Mach numbers where data were available. This gave a total of 40 data points, sufficiently large to get a good statistical average error.

In viewing the individual comparisons, it was clear that a couple of minor problems existed which, if corrected, could somewhat improve these average errors. The first one has to do with the current body-alone methodology for implementing compressibility effects into the nonlinear normal-force term. The present methodology for the body-alone aerodynamics in the normal plane is

$$C_{N_B} = C_{N_L} + \eta C_{d_c} \sin^2 \alpha (A_P / A_{ref}) \tag{6}$$

$$X_{CP} = \left[(X_{CP})_L C_{N_L} + (X_{CP})_{NL} C_{N_{NL}} \right] / C_{N_B} \tag{7}$$

$$C_{M_B} = -C_{N_B} (X_{CP} - X_0) \tag{8}$$

In addition, an empirical table of center of pressure shifts was used for the body-alone to partially account for physics not adequately accounted for in the determination of center of pressure. These physics include the following: transonic flow where shock waves can stand on the body, that the linear theory center of pressure does not stay constant as is presently assumed, and that the center of pressure moves in a parabolic fashion (vs a weighted average as represented by Equation (7)] from its value at $\alpha = 0$ to the centroid of the planform area at a high AOA, for example, 45 deg.

Three slight changes in the Reference 59 methodology are being implemented as a result of comparisons of the Reference 70 data base. The first has to do with the value of η, which is the normal force of a circular cylinder of given length-to-diameter ratio to that of a circular cylinder of given length. Likewise, η_0 is the value of η at $M_N = 0$. At present,

$$\eta = \left[(1 - \eta_0)/1.8 \right] M_N + \eta_o \quad \text{for} \quad M_N < 1.8 \tag{9}$$

$$\eta = [(1-\eta_0)/1.8]M_N + \eta_o \quad \text{for} \quad M_N < 1.8$$
$$\eta = 1 \quad \text{for} \quad M_N \geq 1.8 \tag{9}$$

Also, η is automatically set to one if $M_\infty \geq 2.75$. This last condition, where η is automatically set to one, appears to not be necessary. In other words, Equation (9) is allowed to completely determine the value of η. This change mainly affects normal-force results for conditions just above the cutoff Mach number of 2.75.

The second change implemented as a result of the Reference 70 data base has to do with the empirical table for the center of pressure shifts. Some slight changes were implemented that mainly affect results in the transonic region at lower AOAs. The Reference 70 data base had Mach 0.9 data available, which allowed the results of Reference 59 to be somewhat improved. These modified results are provided in Table 3. They result in some slight improvement in the average center of pressure error for the AP98 from about 0.25 to 0.2 caliber. The 0.2 caliber error is an average error of about 1.6 percent of the body length.

The third body-alone change has to do with the way the linear and nonlinear terms of Equation (6) are treated as α increases above 30 deg. The AP98 methodology assumes

$$C_{N_L} = (C_{N_\alpha})\alpha, \quad \alpha \leq 30$$
$$C_{N_L} = (C_{N_L})_{\alpha=30}[1-(\alpha-30)/60], \quad 30 < \alpha \leq 90 \tag{10}$$

TABLE 3. SHIFT IN BODY-ALONE CENTER OF PRESSURE AS A FUNCTION OF MACH NUMBER AND AOA (AS A FRACTION OF BODY LENGTH)

M \ α	0	10	20	30	40	50	60	70	80	90
0.00	0.00	0.025	0.02	0.000	-0.025	-0.040	-0.040	-0.030	-0.010	0.00
0.20	0.00	0.025	0.02	0.005	-0.025	-0.040	-0.045	-0.030	-0.010	0.00
0.40	0.00	0.03	0.025	0.005	-0.025	-0.040	-0.050	-0.030	-0.015	0.00
0.60	0.00	0.03	0.025	0.00	-0.035	-0.055	-0.070	-0.050	-0.030	0.00
0.80	0.00	0.030	0.020	-0.025	-0.050	-0.070	-0.070	-0.050	-0.015	0.00
0.90	0.00	0.030	0.020	-0.02	-0.050	-0.070	-0.070	-0.040	-0.015	0.00
1.00	0.00	0.02	-0.01	-0.02	-0.040	-0.040	-0.040	-0.030	-0.005	0.00
1.15	0.00	0.02	-0.01	-0.02	-0.020	-0.025	-0.030	-0.025	-0.005	0.00
1.30	0.00	0.02	-0.01	-0.01	-0.010	-0.010	-0.010	-0.005	0.000	0.00
1.50	0.00	0.02	-0.01	0.000	0.000	0.000	-0.010	-0.005	0.000	0.00
2.00	0.00	0.02	0.02	0.020	0.015	0.010	0.005	0.000	0.000	0.00
2.50	0.00	0.02	0.02	0.02	0.015	0.010	0.005	0.000	0.000	0.00
5.99	0.00	0.02	0.02	0.02	0.015	0.010	0.005	0.000	0.000	0.00
≥6.00	0.00	0.02	0.02	0.02	0.015	0.01	0.005	0.000	0.000	0.00

In reality, the linear term does not decay in the fashion of Equation (10), but is probably more parabolic in nature. Therefore, a better representation of the physics is assumed to be

$$
\begin{aligned}
C_{N_L} &= \left(C_{N_\alpha}\right)\alpha, \quad \alpha \le 30 \text{ deg} \\
C_{N_L} &= \left(C_{N_L}\right)_{\alpha=30}, \quad 30 \text{ deg} < \alpha \le 45 \text{ deg} \\
C_{N_L} &= \left(C_{N_L}\right)_{\alpha=30}\left[1-(\alpha-45)/45\right] \\
45 \text{ deg} &< \alpha \le 90 \text{ deg}
\end{aligned}
\tag{11}
$$

Figures 13 and 14 compare the AP98 methodology to the AP02, which includes the three body-alone changes discussed. Figure 13 is the Reference 70 data base and Figure 14 is the Reference 69 data base. Results are shown only for Mach numbers above 2.75 because this is

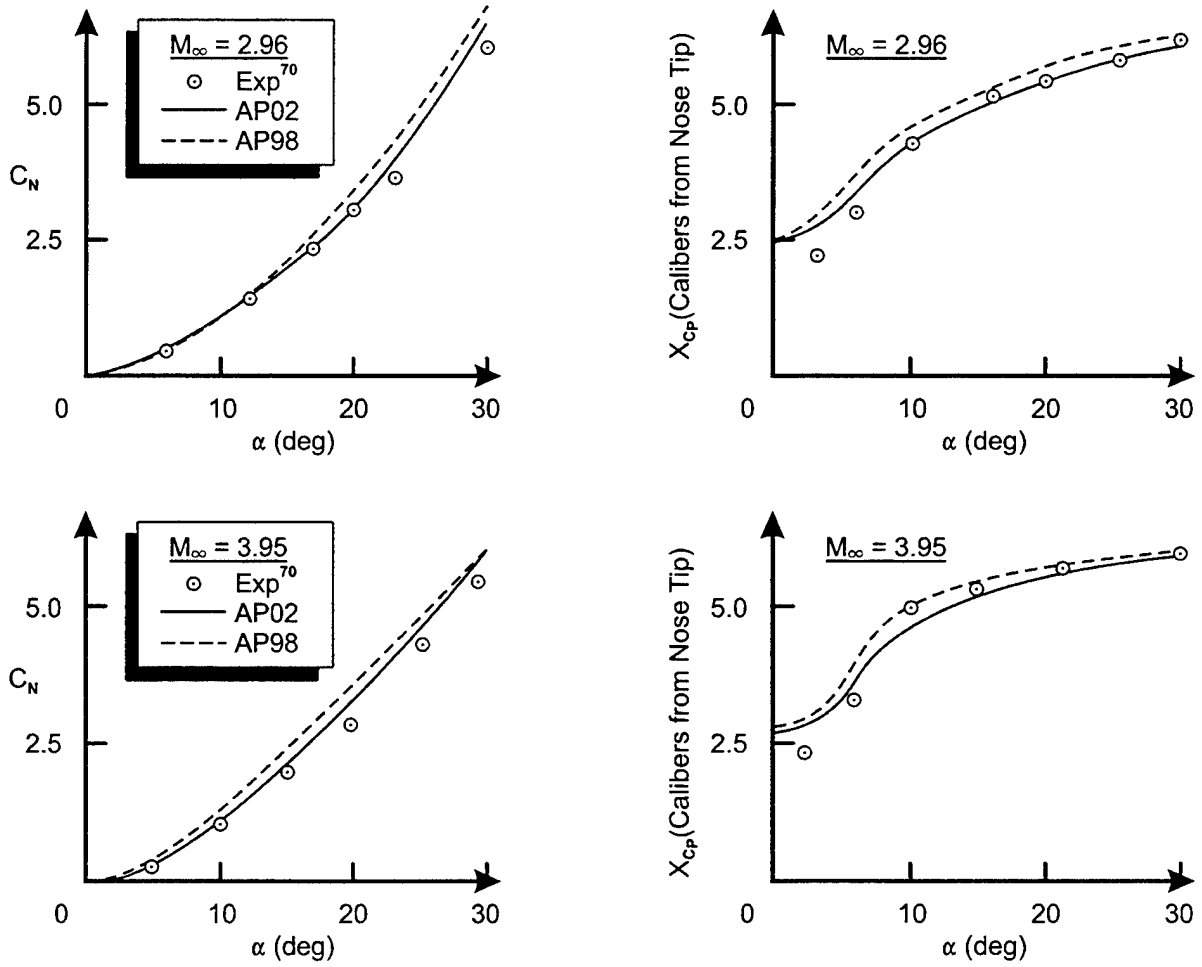

FIGURE 13. COMPARISON OF MODIFIED BODY-ALONE AERODYNAMICS METHOD TO EXPERIMENT FOR REF. 70 MODEL OF FIG. 12

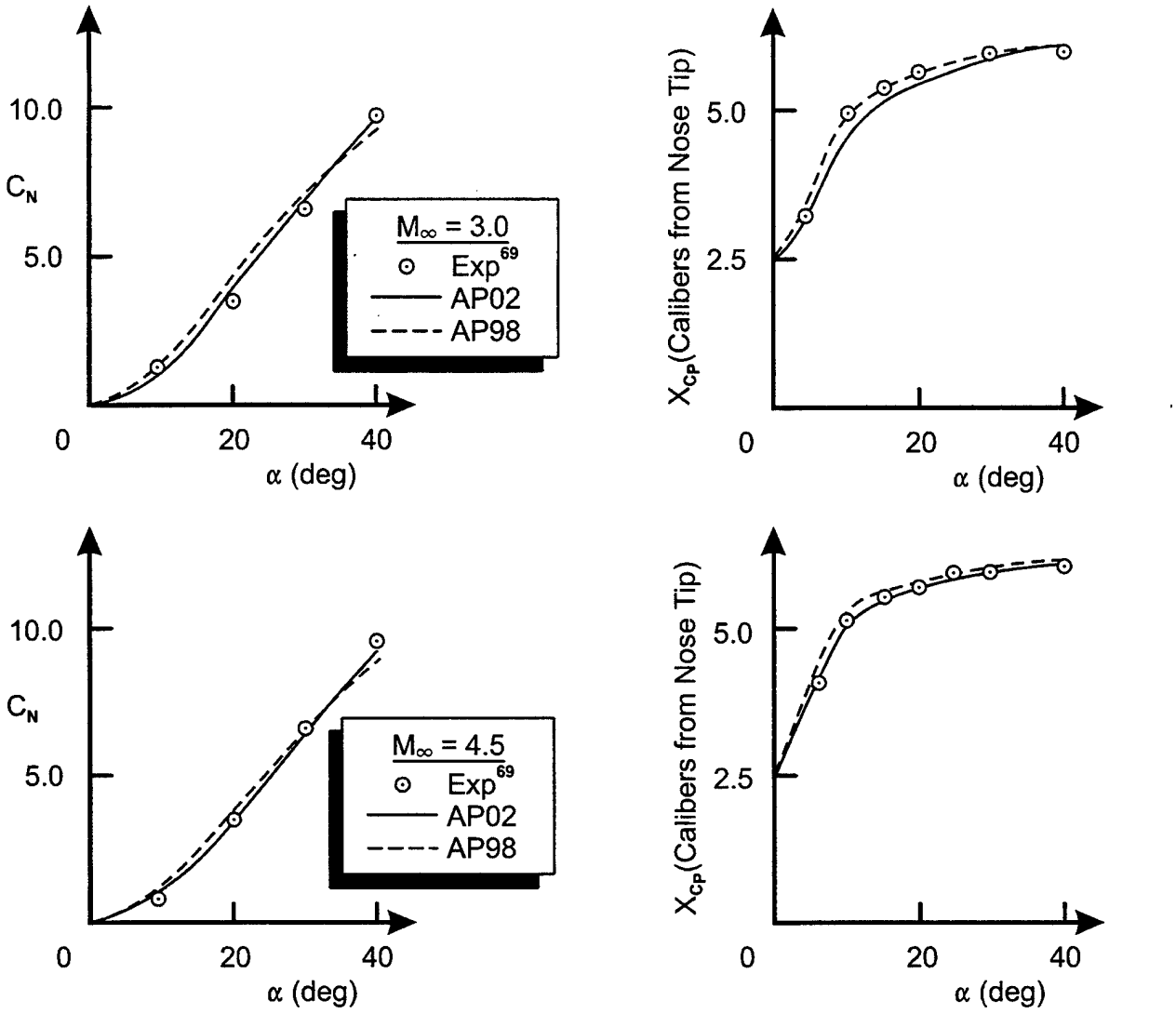

FIGURE 14. COMPARISON OF MODIFIED BODY-ALONE AERODYNAMICS METHOD TO EXPERIMENT FOR REFERENCE 69 MODEL OF FIGURE 12

2.3.2 Wing-Alone Modifications

The wing-alone methodology of Reference 59 assumed the wing-alone normal-force could be predicted from a fourth-order equation in AOA. That is, assuming no wing camber,

$$C_{N_W} = a_1\alpha_w + a_2\alpha_w^2 + a_3\alpha_w^3 + a_4\alpha_w^4 \tag{12A}$$

$$a_2 = 34.044(C_N)_{\alpha=15\,deg} - 4.824(C_N)_{\alpha=35\,deg} + 0.426(C_N)_{\alpha=60\,deg} - 6.412a_1 \tag{12B}$$

$$a_3 = -88.240(C_N)_{\alpha=15\,deg} + 23.032(C_N)_{\alpha=35\,deg} - 2.322(C_N)_{\alpha=60\,deg} + 11.464a_1 \tag{12C}$$

$$C_{N_W} = a_1\alpha_w + a_2\alpha_w^2 + a_3\alpha_w^3 + a_4\alpha_w^4 \quad (12A)$$

$$a_2 = 34.044(C_N)_{\alpha=15\,deg} - 4.824(C_N)_{\alpha=35\,deg} + 0.426(C_N)_{\alpha=60\,deg} - 6.412a_1 \quad (12B)$$

$$a_3 = -88.240(C_N)_{\alpha=15\,deg} + 23.032(C_N)_{\alpha=35\,deg} - 2.322(C_N)_{\alpha=60\,deg} + 11.464a_1 \quad (12C)$$

$$a_4 = 53.219(C_N)_{\alpha=15\,deg} - 17.595(C_N)_{\alpha=35\,deg} + 2.661(C_N)_{\alpha=60\,deg} - 5.971a_1 \quad (12D)$$

The term a_1 of Equation (12) is the value of wing-alone lift curve slope at $\alpha = 0$ given by linear theory. The terms $(C_N)_{\alpha = 15\ deg}$, $(C_N)_{\alpha = 35\ deg}$, and $(C_N)_{\alpha = 60\ deg}$ are values of wing-alone normal-force coefficients at α = 15, 35, and 60 deg, respectively, defined by the data bases of References 84, 85, and 86. Above α_w of 60 deg, extrapolation of the aerodynamics at α_w of 60 deg is used. For more details of the method, the reader is referred to Reference 42.

The center of pressure of the wing-alone and wing-body normal-force is assumed to vary in a quadratic fashion between its linear theory value near $\alpha = 0$ and the centroid of the planform area at α = 60 deg. If A and B are the centers of pressure of the linear and nonlinear normal-force terms (in percent of mean geometric chord), and $\alpha_W = \alpha + \delta$, then the center of pressure of the wing-body or wing-alone lift is

$$(X_{CP})_{WB} = (X_{CP})_W = A + (1/36)|\alpha_W|(B - A) + (1/5400)\alpha_W^2(A - B) \quad (13)$$

Equation (13) is the methodology used for the roll position of 0 deg. For the roll position of 45 deg, an equation for a center of pressure shift was derived from Reference 71 to account for the difference in load on the windward and leeward planes. This shift is added to Equation (13) for the roll position of Φ = 45 deg and is

$$(\Delta X_{CP})_{WB} = -\{r + [b/(c_r + c_t)](c_r/2 - c_t/3)\}\cos\Phi^2 \sin(2\alpha)(0.8\alpha/65); \alpha \le 65\,deg \quad (14A)$$

$$= -0.8\{r + [b/(c_r + c_t)](c_r/2 - c_t/3)\}\cos\Phi^2 \sin(2\alpha); \alpha > 65\,deg \quad (14B)$$

Equations (14a) and (14b) contain a correction to the original center of pressure shift derived in Reference 46. This change is the square of the cos Φ term in Equation (14), whereas in Reference 46 the cos (Φ) term was to the first power. The reason for the square is the fact that the cos (Φ) term does two things. First, it rotates the normal force to a plane normal to the body axis as opposed to being normal to the wing. Second, the cos (Φ) term rotates the radius vector to the lateral center of pressure of the wing from the Φ roll position to the horizontal plane. Reference 46 omitted this last rotation, causing a slightly more forward center of pressure shift at roll than was warranted.

As already mentioned, one of the keys to the Reference 59 method was the development of the wing-alone normal-force coefficient tables for values of α_w of 15, 35, and 60 deg. The

NASA/MDAC[70] wing-alone data base had, in principle, a couple of advantages over the databases used to develop the wing-alone tables at α = 15, 35, and 60 deg used in the wing-alone prediction methodology of the AP98 (Reference 59). First of all, the Reference 70 data base measured wing-alone data for the α = 0-90 deg and from M_∞ = 0.6 to 4.0. The data bases comprising the tables in Reference 59 consisted of several different sets of data (see References 84, 85, and 86) to cover the Mach number range of interest. In some cases, data from References 84, 85, and 86 was available only to 60-deg AOA, and in some data bases the data tended to give a stall effect at higher AOA, rendering it unusable. On the other hand, data from Reference 70 was more limited in wing planforms considered than in some of the other data bases (References 84, 85, and 86).

As a result of the new data base from Reference 70, it was decided to compare the Reference 70 data base to the AP98 tables as well as the Reference 84 data, which the author still believes is the best wing-alone data base available. Comparisons were made as a function of AOA, aspect ratio, Mach number, and taper ratio. Figures 15 and 16 compare the results of the Reference 84 data base and the recent NASA/MDAC[70] data base at Mach numbers of 1.6 and 4.0, respectively, for fins 7 and 8 of Reference 70. Fin 7 is of aspect ratio 1.0 with taper ratio 0, and has a semispan of 1.5 inches, whereas fin 8 is of aspect ratio 2, taper ratio 0, and semispan 3.0 inches. Figures 15 and 16 also show the results from the AP98 method and revisions to the wing-alone tables to be incorporated in the AP02. Several points are worthy of note. First, at both M_∞ = 1.6 and 4.0, the Reference 70 and 84 data are in excellent agreement for fin 8 up to AOA of 40-45 deg. Above α = 45 deg, the Reference 70 data stalls. Also, the Reference 70 data is consistently about 10 percent lower than the Reference 84 data for fin 7 at M_∞ = 1.6 and 4.0. It is theorized that because the Reference 70 data were taken with a splitter plate and Reference 84 with a sting, the differences in the data are due to the measurement. It is suspected that for the lower semispan, boundary-layer buildup ahead of the fin on the splitter plate is the source of the 10 percent lower value of C_{N_W} of Reference 70 data compared to Reference 84. In other words, for small-span wings, the lower dynamic pressure due to the boundary layer near the root chord has more of an effect than for the larger-span wings. This effect is magnified for small taper ratios because the wing cross-sectional area is the largest at the root chord. It is not known why the flow stalls above about 45 deg for the splitter plate results. However, this stall effect was the case for most of the Reference 70 results. As a result of these two phenomena, it was decided to use considerable judgement before using any of the Reference 70 results for the 1.5-inch semispan or for any span above α = 45 deg. The final point to be made in viewing Figures 15 and 16 is that the revised values of C_{N_W}, which will be incorporated into the AP02, are closer to the Reference 84 data than the AP98. The AP98 had intentionally increased the values of C_{N_W} to somewhat account for the Reference 84 data having been taken on fairly thick wings to accommodate many pressure taps. It was theorized that these thick wings would unrealistically lower C_{N_W}. The revised data decreases this thickness penalty and is, therefore, much closer to the Reference 84 data. Other values of revised wing-alone normal-force coefficients are given in Table 4.

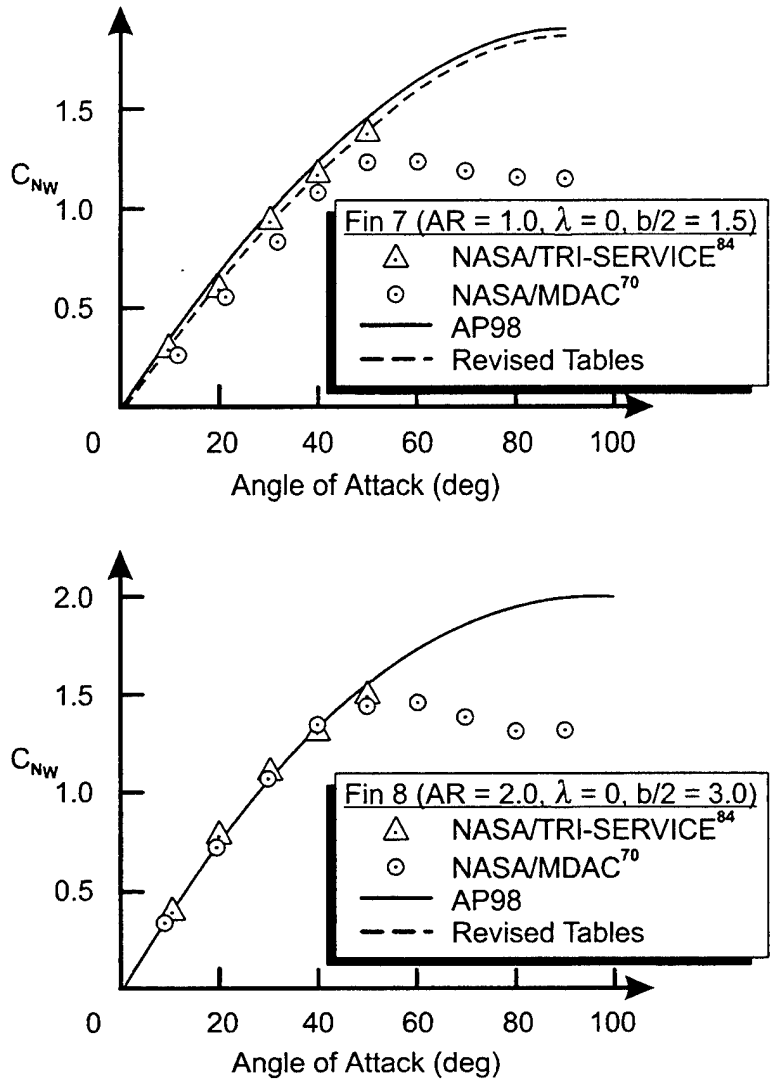

FIGURE 15. COMPARISON OF NASA/MDAC[70] WING-ALONE DATABASE TO THAT OF REFERENCE 84 ($M_\infty = 1.6$)

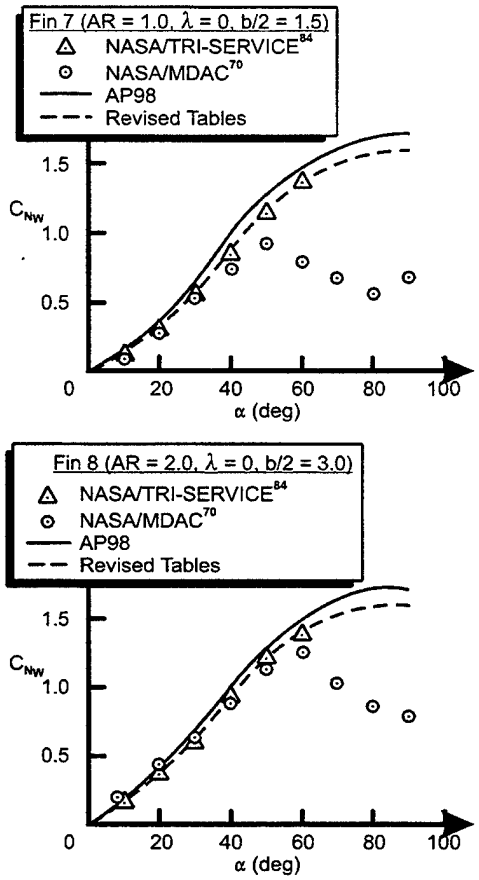

FIGURE 16. COMPARISON OF NASA/MDAC[70] WING-ALONE DATABASE TO THAT OF REFERENCE 84 ($M_\infty = 4.0$)

2.3.3 Refinements for Wing-Body and Body-Wing Interference Factor Nonlinearities Due to Angle of Attack

This part of the report considers refinements in the empirical factors used to model the nonlinearities in the wing-body and body-wing interference factors due to AOA. Also, the focus here will be on the roll orientation of $\Phi = 0$ deg (fins in plus + roll orientation). The $\Phi = 0$ deg roll emphasis is driven by the Reference 70 data base only having $\Phi = 0$ deg data available. However, when changes are made in the empirical constants for $\Phi = 0$ deg, changes in the $\Phi = 45$ deg roll will also be considered. To better understand the interference lift components, it is instructive to examine Equation (5).

The first term in Equation (5) is the normal-force of the body-alone, including the linear and nonlinear components; the second term is the contribution of the wing (or canard), including interference effects and control deflection; the third term is the contribution of the tail, including interference effects and control deflection; and the last terms are the negative downwash effect on the tail or body due to wing-shed or body-shed vortices. The K's represent the interference of the configuration with respect to AOA, and the k's represent the interference with respect to

TABLE 4A. VALUES OF $(C_{N_w})_{\alpha=15°}$

ASPECT RATIO	TAPER RATIO	MACH NUMBER									
		0	0.6	0.8	1.0	1.2	1.6	2.0	3.0	4.5	≥6.0
≤0.1	0.0	.18	.18	.18	.225	.24	.24	.21	.17	.14	.11
	0.5	.19	.19	.19	.225	.24	.24	.21	.17	.14	.11
	1.0	.19	.19	.19	.225	.24	.24	.21	.17	.14	.11
0.5	0.0	.28	.29	.30	.32	.32	.32	.30	.24	.18	.16
	0.5	.39	.41	.415	.43	.43	.45	.38	.30	.22	.19
	1.0	.34	.34	.36	.42	.42	.43	.37	.30	.22	.19
1.0	0.0	.43	.44	.46	.50	.54	.46	.42	.32	.22	.18
	0.5	.47	.50	.55	.65	.66	.58	.45	.34	.24	.21
	1.0	.46	.48	.52	.58	.60	.54	.45	.35	.26	.22
2.0	0.0	.55	.59	.65	.72	.70	.62	.50	.34	.27	.23
	0.5	.56	.59	.66	.76	.80	.68	.54	.40	.30	.27
	1.0	.65	.66	.71	.75	.80	.67	.54	.40	.29	.27
≥4.0	0.0	.65	.66	.71	.79	.83	.70	.59	.39	.31	.26
	0.5	.69	.71	.75	.88	.91	.75	.69	.45	.32	.29
	1.0	.69	.71	.75	.88	.91	.75	.67	.45	.31	.29

control deflection. Each of these interference factors is estimated by slender body or linear theory. As such, they are independent of AOA.

The terms considered for refinements in this section of the report are $K_{W(B)}$, $K_{B(W)}$, $K_{T(B)}$, and $K_{B(T)}$. These four interference factors are defined in the general form

$$K = K_{\substack{SBT \\ LT}} + \Delta K(M_\infty, \alpha, AR, \lambda) \qquad (15)$$

The first term of Equation (15) is defined by linear theory or slender body theory; the second term is defined by utilizing several large wind tunnel data bases to back out the nonlinearities as a function of Mach number, AOA, aspect ratio, and taper ratio. The general nonlinear trend of those two interference terms is shown in Figure 17. This general trend is basically the same for both the $\Phi = 0$ and $\Phi = 45$ deg roll orientations. However, the five tables of data that define the empirical constants in the equations of Figure 17 are different for $\Phi = 0$ and $\Phi = 45$ deg for both $K_{W(B)}$ and $K_{B(W)}$. As already discussed, for cruciform missiles, SBT gives no roll independence for low AOA values of $K_{W(B)}$ and $K_{B(W)}$.

As seen in Figure 17, $K_{W(B)}$ in general can deviate slightly from SBT or LT near AOA of 0 deg. It then decreases until it reaches a minimum value and then approaches a value of 1.0 at

TABLE 4B. VALUES OF $(C_{N_W})_{\alpha=35°}$

ASPECT RATIO	TAPER RATIO	MACH NUMBER									
		0	0.6	0.8	1.0	1.2	1.6	2.0	3.0	4.5	≥6.0
≤0.1	0.0	1.13	1.13	1.13	1.03	.92	.76	.65	.59	.53	.50
	0.5	.97	1.0	1.0	1.0	.95	.86	.75	.69	.60	.56
	1.0	.97	1.0	1.0	1.0	.97	.91	.8	.74	.65	.62
0.5	0.0	1.10	1.1	1.1	1.03	1.01	.95	.85	.72	.66	.62
	0.5	1.10	1.13	1.16	1.28	1.25	1.12	.95	.80	.72	.70
	1.0	1.06	1.08	1.13	1.19	1.22	1.15	1.0	.82	.70	.68
1.0	0.0	1.23	1.23	1.24	1.25	1.19	1.10	.99	.82	.72	.70
	0.5	1.26	1.28	1.30	1.33	1.40	1.20	1.0	.85	.78	.75
	1.0	1.22	1.24	1.26	1.29	1.36	1.20	1.08	.90	.78	.74
2.0	0.0	.99	1.01	1.13	1.20	1.28	1.18	1.05	.90	.76	.72
	0.5	1.00	1.07	1.18	1.31	1.41	1.28	1.18	.98	.84	.80
	1.0	.98	1.05	1.17	1.23	1.34	1.26	1.13	.97	.85	.80
≥4.0	0.0	.97	1.05	1.17	1.20	1.33	1.20	1.10	.95	.82	.78
	0.5	1.03	1.08	1.22	1.30	1.40	1.30	1.22	1.02	.89	.85
	1.0	1.03	1.09	1.21	1.3	1.4	1.3	1.22	1.02	.89	.85

TABLE 4C. VALUES OF $(C_{N_W})_{\alpha=60°}$

ASPECT RATIO	TAPER RATIO	MACH NUMBER									
		0	0.6	0.8	1.0	1.2	1.6	2.2	3.0	4.5	≥6.0
≤0.5	0.0	1.10	1.11	1.15	1.26	1.33	1.37	1.45	1.4	1.35	1.3
	0.5	1.34	1.35	1.4	1.45	1.52	1.56	1.48	1.43	1.39	1.36
	1.0	1.29	1.30	1.32	1.37	1.47	1.52	1.48	1.44	1.39	1.36
1.0	0.0	1.44	1.46	1.49	1.53	1.56	1.61	1.57	1.44	1.37	1.34
	0.5	1.40	1.42	1.45	1.53	1.58	1.70	1.59	1.48	1.42	1.38
	1.0	1.33	1.34	1.35	1.44	1.62	1.72	1.58	1.47	1.40	1.37
2.0	0.0	1.32	1.33	1.36	1.48	1.59	1.74	1.68	1.47	1.38	1.35
	0.5	1.30	1.31	1.37	1.48	1.63	1.8	1.76	1.56	1.46	1.43
	1.0	1.30	1.31	1.37	1.48	1.63	1.76	1.73	1.53	1.46	1.43
≥4.0	0.0	1.27	1.28	1.37	1.50	1.64	1.80	1.70	1.49	1.4	1.37
	0.5	1.31	1.32	1.40	1.5	1.64	1.8	1.77	1.56	1.5	1.46
	1.0	1.31	1.32	1.40	1.5	1.64	1.78	1.75	1.55	1.48	1.45

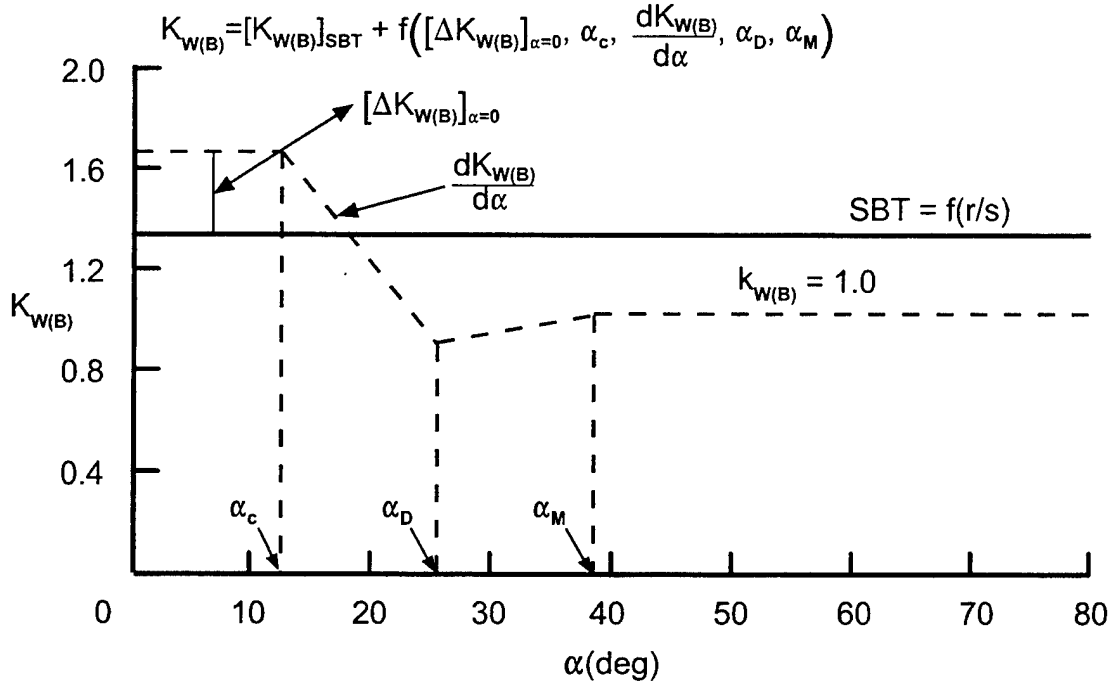

FIGURE 17A. GENERIC REPRESENTATION OF $K_{W(B)}$ WITH AOA

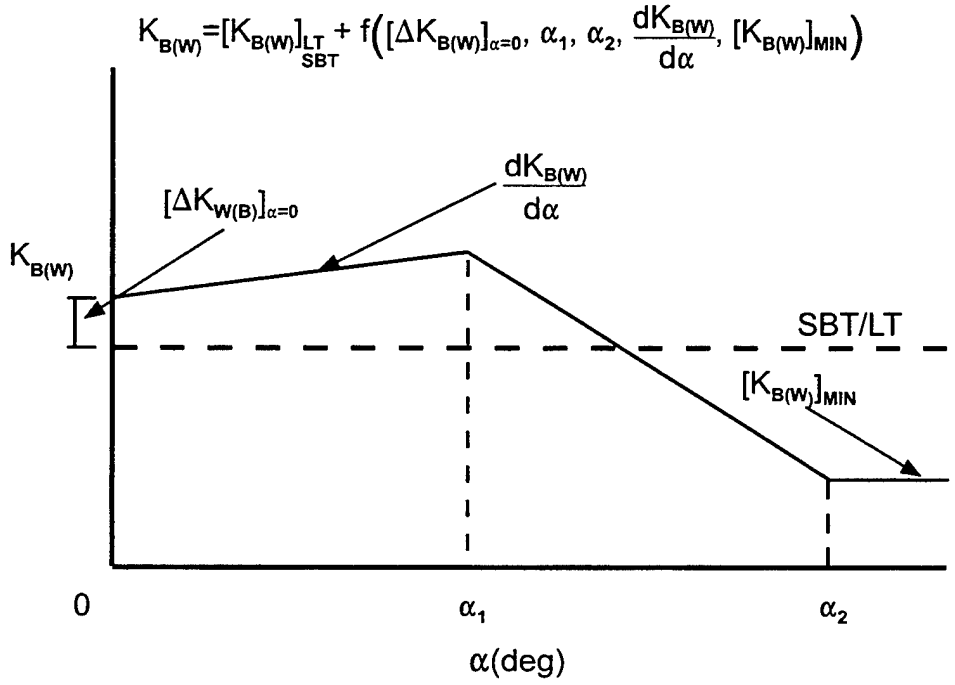

FIGURE 17B. GENERIC REPRESENTATION OF $K_{B(W)}$ WITH AOA

high AOA. On the other hand, $K_{B(W)}$ can either increase or decrease past AOA of 0 deg. Eventually, it also decreases until it reaches some minimum value at high AOA. The physics of what occurs in this nonlinear behavior and the details of the interference factor nonlinearities are

given in References 39 and 46. For ease of reference for the reader, a brief discussion of the physics of the flow that underlies Figure 17 is provided.

In examining the nonlinear models for $K_{W(B)}$ and $K_{B(W)}$ of Figure 17, it is instructive to try to correlate the mathematical models with the physics of the flow. The wing-body interference factor is somewhat easier to understand than the body-wing interference. The wing-body experimental data show that at low Mach number, SBT slightly underpredicts the experimental data. As AOA is increased, $K_{W(B)}$ starts decreasing and in some cases decreases below its wing-alone value. As AOA increases, $K_{W(B)}$ approaches its wing-alone value. As Mach number increases, the positive interference lift on the wing, caused by the presence of the body, is lost faster and faster as AOA increases. That is, the wing-alone solution is recovered much faster at high Mach number as AOA increases, than at low Mach number. This is believed to be the result of the Newtonian Impact mechanism where, at high Mach number, the momentum of the air particle is lost almost entirely upon direct impact on a surface as opposed to wrapping around the surface and carrying some of the momentum with it, as at low Mach numbers.

The $K_{B(W)}$ model contains body vortex effects, nose- and wing-to-wing shock effects, as well as the usual added dynamic pressure of the body caused by the presence of the wing. While some of the trends in Figure 17 can be rationalized, others cannot except in light of these combination effects. The alternative to simultaneously modeling several physical phenomena is to try to estimate the effects of the body vortices and nose- and wing-shock interactions and subtract them from the experimental data for the configuration tested and then add them back in analytically for another configuration of interest. This process not only complicates the methodology, but adds additional inherent errors because these effects cannot be easily and accurately estimated. The present approach neglects some of the scale effects caused by the position of the wing on the body. However, this error is probably smaller than the results of analytically approximating the other effects, subtracting them, and then adding them again for a different geometrical configuration.

In general, $K_{B(W)}$ actually increases with AOA at low Mach numbers to a certain point, where it starts decreasing analogous to $K_{W(B)}$. However, a certain amount of lift or force enhancement is gained all the way to $\alpha = 90$ deg for low Mach numbers as shown in Figure 17. This phenomenon is assumed to occur all the way to $M = 6.0$ based on extrapolated data from the point where experimental data end, which is AOA of 25 to 40 deg depending on Mach number, to $\alpha = 90$ deg shown in Figure 17.

Additional higher AOA data above $\alpha = 40$ deg is needed for both $K_{W(B)}$ and $K_{B(W)}$ to modify the assumed extrapolations of the models for $K_{W(B)}$ and $K_{B(W)}$ at high AOA. However, until additional data are available, the approximate nonlinear models for $K_{W(B)}$ and $K_{B(W)}$ can be used to estimate aerodynamics for engineering use. This statement will be validated for a limited set of flight conditions in a later section.

The way the nonlinearities are treated for the second term of Equation (15) is by using five tables for $\Delta K_{W(B)}$ and five tables for $\Delta K_{B(W)}$. Also, these tables are different for $\Phi = 0$ and

45 deg roll orientation. These tables define the parameters shown in Figure 17. The definition of these 10 parameters is as follows:

$[\Delta K_{W(B)}]_{\alpha=0}$ = difference between SBT and data at $\alpha = 0$

α_C = angle of attack where $K_{W(B)}$ starts decreasing

$\frac{d K_{W(B)}}{d\alpha}$ = rate of decrease of $K_{W(B)}$ between $\alpha = \alpha_C$ and $\alpha = \alpha_D$

α_D = angle of attack where $K_{W(B)}$ reaches an initial minimum

α_M = angle of attack where $K_{W(B)}$ reaches a constant value

$[\Delta K_{B(W)}]_{\alpha=0}$ = difference between SBT/LT and data at $\alpha = 0$

$\frac{dK_{B(W)}}{d\alpha}$ = rate of change of $K_{B(W)}$ between $\alpha = 0$ and $\alpha = \alpha_1$

α_1 = angle of attack where $dK_{B(W)}/d\alpha$ changes sign

α_2 = angle of attack where $K_{B(W)}$ reaches a constant

$[K_{B(W)}]_{MIN}$ = constant value of $K_{B(W)}$ above $\alpha = \alpha_2$ as a percent of linear theory or slender body theory

The mathematical models for $K_{W(B)}$ and $K_{B(W)}$ are once again defined based on SBT/LT and the empirical data for the constants previously defined. The specific equations for $K_{W(B)}$ are

$$K_{W(B)} = \left[K_{W(B)}\right]_{SBT} + \left[\Delta K_{W(B)}\right]_{\alpha=0}; \alpha \le \alpha_C \tag{16A}$$

$$= \left[K_{W(B)}\right]_{SBT} + \left[\Delta K_{W(B)}\right]_{\alpha=0} + \left|\left(|\alpha| - \alpha_C\right)\right| \frac{dK_{W(B)}}{d\alpha}; \alpha_C < \alpha \le \alpha_D \tag{16B}$$

$$= 1 - \left(\frac{\alpha_M - |\alpha|}{\alpha_M - \alpha_D}\right)\left(1 - \left[K_{W(B)}\right]_{\alpha=\alpha_D}\right); \alpha_D < \alpha \le \alpha_M \tag{16C}$$

$$K_{W(B)} = \left[K_{W(B)}\right]_{\alpha=\alpha_M}; \alpha > \alpha_M \tag{16D}$$

The specific mathematical model for $K_{B(W)}$ is given by Equations (17A) through (17C).

For $\alpha \leq \alpha_1$,

$$K_{B(W)} = \left[K_{B(W)}\right]_{\substack{LT \\ SBT}} + \left[\Delta K_{B(W)}\right]_{\alpha=0} + |\alpha| \frac{dK_{B(W)}}{d\alpha} \tag{17A}$$

For $\alpha_1 < \alpha \leq \alpha_2$,

$$K_{B(W)} = \left[K_{B(W)}\right]_{\alpha=\alpha_1} + \left(\frac{\alpha_1 - \alpha}{\alpha_2 - \alpha_1}\right)\left\{\left[K_{B(W)}\right]_{\alpha=\alpha_1} - \left[K_{B(W)}\right]_{MIN}\right\} \tag{17B}$$

For $\alpha > \alpha_2$,

$$K_{B(W)} = \left[K_{B(W)}\right]_{MIN} \tag{17C}$$

Tables 5 through 14 give the revised set of values for the 10 empirical constants of Figure 17 for the $\Phi = 0$ deg roll orientation and Tables 15 through 25 give values of these same constants for $\Phi = 45$ deg roll.

The revised values of the empirical constants in Tables 5 through 25 were derived primarily based on comparing the AP98 (including the revisions of Sections 2.1 and 2.2 of this report) to the wing-body data base of Reference 70. The empirical constants were then adjusted on a case-by-case basis to improve the overall predictions of theory to data. Some tables were hardly changed from those of Reference 59. Other tables, such as Tables 11 and 22, were significantly changed.

TABLE 5. DATA FOR $[\Delta K_{W(B)}]_{\alpha=0}$ AT $\Phi = 0$ DEG

		MACH NUMBER										
ASPECT RATIO	TAPER RATIO	≤0.1	0.6	0.8	1.2	1.5	2.0	2.5	3.0	3.5	4.5	≥5.0
≤0.25	0, 0.5, 1.0	0	.25	.25	.15	0	0	0	0	0	0	0
0.5	0.5	.05	.05	.05	.05	0	0	0	0	0	0	0
1.0	0.5	.25	.15	.05	0	0	0	0	0	0	0	0
≥2.0	0.5	.20	.1	0	0	0	0	0	0	0	0	0
0.5	0	.30	.35	.2	.18	0	0	0	0	0	0	0
1.0	0	.35	.29	.16	.06	0	0	0	0	0	0	0
≥2.0	0	.27	.29	.10	.10	0	0	0	0	0	0	0
0.5	1.0	.05	.05	.05	.05	0	0	0	0	0	0	0
1.0	1.0	.25	.15	.05	0	0	0	0	0	0	0	0
≥2.0	1.0	.20	.1	0	.10	0	0	0	0	0	0	0

TABLE 6. DATA FOR α_C (deg) AT Φ = 0 DEG

MACH NUMBER												
ASPECT RATIO	TAPER RATIO	≤0.1	0.6	0.8	1.2	1.5	2.0	2.5	3.0	3.5	4.5	≥5.0
≤0.25	0, 0.5, 1.0	30.0	22.0	22.0	10.0	0	0	0	0	0	0	0
0.5	0.5	30.0	17.3	11.5	10.0	0	0	0	0	0	0	0
1.0	0.5	30.0	20.0	15.0	10.0	0	0	0	0	0	0	0
≥2.0	0.5	20.0	15.0	10.0	15.0	0	0	0	0	0	0	0
0.5	0	20.0	12.0	10.0	10.0	0	0	0	0	0	0	0
1.0	0	40.0	20.0	15.0	10.0	0	0	0	0	0	0	0
≥2.0	0	10.0	20.0	15.0	15.0	0	0	0	0	0	0	0
0.5	1.0	30.0	17.3	10.0	10.0	0	0	0	0	0	0	0
1.0	1.0	30.0	15.0	12.5	10.0	0	0	0	0	0	0	0
≥2.0	1.0	10.0	15.0	15.0	15.0	0	0	0	0	0	0	0

TABLE 7. DATA FOR $\left[K_{W(B)}\right]_{\alpha=\alpha_D}$ AT Φ = 0 DEG

MACH NUMBER												
ASPECT RATIO	TAPER RATIO	≤0.1	0.6	0.8	1.2	1.5	2.0	2.5	3.0	3.5	4.5	≥5.0
≤0.25	0, 0.5, 1.0	1.0	1.0	1.0	1.0	1.0	1.0	1.0	1.0	1.0	1.0	1.0
0.5	0.5	1.0	1.0	1.0	1.0	1.0	1.0	.95	1.0	.97	1.0	1.0
1.0	0.5	1.0	1.0	1.0	1.0	1.0	1.0	1.0	1.0	1.0	1.0	1.0
≥2.0	0.5	1.0	1.0	1.0	1.0	1.0	1.0	1.0	1.0	1.0	1.0	1.0
0.5	0	1.0	1.0	1.0	1.05	.90	.90	.90	.90	.90	.90	1.0
1.0	0	1.0	1.0	1.0	.95	1.0	1.0	1.0	1.0	1.0	1.0	1.0
≥2.0	0	1.0	1.0	.95	1.0	1.0	1.0	1.0	1.0	1.0	1.0	1.0
0.5	1.0	1.0	1.0	1.0	1.0	1.0	1.0	1.05	1.15	1.13	1.15	1.0
1.0	1.0	1.0	1.0	1.0	.95	.95	.95	1.0	1.0	1.0	1.0	1.0
≥2.0	1.0	1.0	1.0	1.0	1.0	1.0	1.0	1.0	.93	.90	.95	1.0

TABLE 8. DATA FOR α_D (deg) AT $\Phi = 0$ DEG

MACH NUMBER												
ASPECT RATIO	TAPER RATIO	≤0.1	0.6	0.8	1.2	1.5	2.0	2.5	3.0	3.5	4.5	≥5.0
≤0.25	0, 0.5, 1.0	80.0	40.0	38.0	35.0	35.0	35.0	30.0	25.0	20.0	15.0	15.0
0.5	0.5	70.0	33.0	31.4	27.5	30.0	16.8	17.8	17.0	15.0	15.0	14.0
1.0	0.5	60.0	32.5	44.0	22.0	20.0	22.5	17.5	18.0	10.0	17.0	15.0
≥2.0	0.5	45.0	35.0	44.0	40.0	25.0	16.5	17.0	16.0	10.0	12.0	15.0
0.5	0	70.0	30.0	30.0	21.2	25.0	15.0	14.0	15.0	15.0	12.0	11.5
1.0	0	65.0	31.0	39.0	20.0	18.0	21.5	16.0	17.0	11.0	13.0	13.0
≥2.0	0	50.0	35.0	35.0	30.0	25.0	20.0	17.7	17.0	12.0	12.6	11.5
0.5	1.0	70.0	33.0	34.2	26.0	30.0	14.2	17.0	13.4	11.8	12.2	11.5
1.0	1.0	60.0	33.0	40.0	21.0	20.0	22.0	17.0	16.0	9.0	14.0	12.0
≥2.0	1.0	45.0	35.0	35.0	40.0	25.0	18.0	15.0	15.5	12.0	12.6	11.5

TABLE 9. DATA FOR α_M (deg) AT $\Phi = 0$ DEG

MACH NUMBER												
ASPECT RATIO	TAPER RATIO	≤0.1	0.6	0.8	1.2	1.5	2.0	2.5	3.0	3.5	4.5	≥5.0
≤0.25	0, 0.5, 1.0	80.0	45.0	45.0	40.0	44.0	38.0	50.0	46.0	50.0	50.0	46.0
0.5	0.5	80.0	33.0	31.4	40.0	50.0	17.0	40.0	17.0	40.0	15.0	14.0
1.0	0.5	80.0	33.0	45.0	45.0	50.0	50.0	50.0	36.0	33.0	17.0	17.0
≥2.0	0.5	80.0	43.0	45.0	45.0	50.0	50.0	50.0	36.0	33.0	17.0	17.0
0.5	0	80.0	30.0	30.0	40.0	50.0	48.0	50.0	50.0	50.0	50.0	50.0
1.0	0	80.0	31.0	40.0	50.0	42.0	50.0	50.0	50.0	44.0	40.0	40.0
≥2.0	0	80.0	43.0	45.0	45.0	50.0	50.0	50.0	50.0	50.0	50.0	35.0
0.5	1.0	80.0	33.0	34.2	50.0	31.0	50.0	50.0	50.0	50.0	50.0	50.0
1.0	1.0	80.0	33.0	40.0	50.0	42.0	50.0	50.0	50.0	44.0	40.0	40.0
≥2.0	1.0	80.0	43.0	45.0	45.0	25.0	18.0	15.0	36.0	33.0	37.0	30.0

TABLE 10. DATA FOR $[\Delta K_{B(W)}]_{\alpha=0}$ AT $\Phi = 0$ DEG

MACH NUMBER												
ASPECT RATIO	TAPER RATIO	≤0.1	0.6	0.8	1.2	1.5	2.0	2.5	3.0	3.5	4.5	≥5.0
≤0.25	0, 0.5, 1.0	0.0	0.0	0.0	0.0	0.0	0.0	0.0	0.0	0.0	0.0	0.0
0.5	0.5	0.0	-.28	-.15	.16	.15	.05	0.0	0.0	0.0	0.0	0.0
1.0	0.5	0.0	-.20	-.20	.15	.10	.15	0.0	0.0	0.0	0.0	0.0
≥2.0	0.5	0.0	-.20	-.07	.1	.18	.10	0.0	0.0	0.0	0.0	0.0
0.5	0	0.0	-.33	-.30	.28	.20	.10	.08	0.0	0.0	0.0	0.0
1.0	0	0.0	-.24	-.25	.05	.2	.05	0.0	0.0	0.0	0.0	0.0
≥2.0	0	0.0	-.20	0.0	.17	0.0	0.0	0.0	0.0	0.0	0.0	0.0
0.5	1.0	0.0	-.28	-.15	.13	.15	.10	0.0	0.0	0.0	0.0	0.0
1.0	1.0	0.0	-.20	-.20	.22	.10	.05	0.0	0.0	0.0	0.0	0.0
≥2.0	1.0	0.0	-.20	-.07	.17	.20	.10	.15	0.0	0.0	0.0	0.0

TABLE 11. DATA FOR $dK_{B(W)}/d\alpha$ (per deg) AT $\Phi = 0$ DEG

MACH NUMBER												
ASPECT RATIO	TAPER RATIO	≤0.1	0.6	0.8	1.2	1.5	2.0	2.5	3.0	3.5	4.5	≥5.0
≤0.25	0, 0.5, 1.0	0.0	0.0	0.0	0.0	0.0	0.0	-.006	-.008	-.010	-.020	-.024
0.5	0.5	.003	.023	.023	-.009	-.018	-.020	-.015	-.014	-.015	-.016	-.020
1.0	0.5	.003	.012	.006	-.0075	-.014	-.016	-.013	-.014	-.015	-.020	-.020
≥2.0	0.5	.003	.006	0.0	0.0	0.0	-.008	-.012	-.014	-.015	-.016	-.020
0.5	0	.003	.035	.028	0.0	0.0	0.0	-.004	-.014	-.015	-.016	-.020
1.0	0	.003	.020	.0225	-.0075	-.011	-.012	-.013	-.014	-.015	-.020	-.020
≥2.0	0	.003	.008	.006	0.0	0.0	-.008	-.012	-.014	-.015	-.016	-.020
0.5	1.0	.003	.038	.033	-.003	-.010	-.020	-.015	-.014	-.015	-.016	-.020
1.0	1.0	.003	.007	.005	-.0075	-.014	-.016	-.015	-.016	-.016	-.020	-.020
≥2.0	1.0	.003	.006	0.0	0.0	0.0	-.008	-.012	-.014	-.015	-.016	-.020

TABLE 12. DATA FOR α_1 (deg) AT $\Phi = 0$ DEG

		MACH NUMBER										
ASPECT RATIO	TAPER RATIO	≤0.1	0.6	0.8	1.2	1.5	2.0	2.5	3.0	3.5	4.5	≥5.0
≤0.25	0, 0.5, 1.0	15.0	21.1	16.5	45.0	37.0	30.0	23.3	20.5	18.0	15.0	10.0
0.5	0.5	30.0	22.2	16.7	62.0	43.0	40.0	25.0	25.0	25.0	20.0	20.0
1.0	0.5	30.0	25.0	20.0	70.0	20.0	0.00	10.0	10.0	10.0	10.0	10.0
≥2.0	0.5	30.0	20.0	20.0	40.0	30.0	30.0	30.0	24.0	20.4	26.0	26.0
0.5	0	30.0	15.0	15.0	25.0	25.0	20.0	20.0	10.0	27.0	20.0	20.0
1.0	0	30.0	25.0	20.0	70.0	20.0	0.00	10.0	10.0	10.0	10.0	10.0
≥2.0	0	30.0	25.0	20.0	40.0	30.0	30.0	30.0	32.0	30.0	20.0	20.0
0.5	1.0	30.0	17.0	15.5	48.5	43.0	40.0	25.0	26.5	21.6	20.0	20.0
1.0	1.0	30.0	25.0	20.0	70.0	20.0	0.00	10.0	10.0	10.0	10.0	10.0
≥2.0	1.0	30.0	20.0	40.0	40.0	48.0	47.0	32.0	26.0	20.0	26.0	26.0

TABLE 13. DATA FOR α_2 (deg) AT $\Phi = 0$ DEG

		MACH NUMBER										
ASPECT RATIO	TAPER RATIO	≤0.1	0.6	0.8	1.2	1.5	2.0	2.5	3.0	3.5	4.5	≥5.0
≤0.25	0, 0.5, 1.0	90.0	75.0	65.0	63.4	60.0	55.0	52.5	40.0	47.5	45.0	42.5
0.5	0.5	90.0	75.0	65.0	62.0	43.0	41.0	42.5	25.0	42.0	40.0	40.0
1.0	0.5	90.0	75.0	75.0	80.0	40.0	50.0	40.0	30.0	30.0	30.0	30.0
≥2.0	0.5	90.0	75.0	75.0	80.0	90.0	90.0	42.0	40.0	40.0	40.0	40.0
0.5	0	90.0	75.0	75.0	80.0	49.0	47.8	42.5	43.0	26.5	40.0	40.0
1.0	0	90.0	75.0	75.0	80.0	40.0	50.0	40.0	40.0	30.0	30.0	30.0
≥2.0	0	90.0	75.0	75.0	80.0	90.0	90.0	41.0	40.0	40.0	43.0	43.0
0.5	1.0	90.0	75.0	53.2	48.7	43.0	41.0	42.5	26.5	43.5	40.0	40.0
1.0	1.0	90.0	75.0	74.0	72.0	40.0	50.0	40.0	40.0	30.0	30.0	30.0
≥2.0	1.0	90.0	75.0	75.0	80.0	90.0	90.0	45.0	30.0	40.0	43.0	43.0

TABLE 14. DATA FOR $[K_{B(W)}]_{MIN}$ AS A FRACTION OF SLENDER BODY THEORY AT $\Phi = 0$ DEG

M_∞	$[K_{B(W)}]_{MIN}$
0	0.5
3.8	0.5
4.9	0.25
6.0	0

TABLE 15. DATA FOR $[K_{W(B)}]_{\alpha=0}$ AT $\Phi = 45$ DEG

MACH NUMBER												
ASPECT RATIO	TAPER RATIO	≤0.1	0.6	0.8	1.2	1.5	2.0	2.5	3.0	3.5	4.5	≥5.0
≤0.25	0, 0.5, 1.0	0.00	0.00	0.00	0.00	0.00	0	0	0	0	0	0
0.5	0.5	0.00	0.00	0.00	-0.13	0.00	0	0	0	0	0	0
1.0	0.5	0.10	0.00	0.00	0.00	-0.10	0	0	0	0	0	0
≥2.0	0.5	0.10	0.00	0.00	0.00	0.00	0	0	0	0	0	0
0.5	0	0.00	0.00	0.00	0.00	0.00	0	0	0	0	0	0
≥2.0	0	0.00	0.00	0.00	0.00	-0.18	0	0	0	0	0	0
0.5	1.0	0.00	0.00	0.00	0.00	0.00	0	0	0	0	0	0
≥2.0	1.0	0.05	0.00	0.00	0.00	0.00	0	0	0	0	0	0
1.0	0	0.35	0.15	0.05	0.00	-0.10	0	0	0	0	0	0
1.0	1.0	0.10	0.00	0.00	0.00	-0.10	0	0	0	0	0	0

TABLE 16. DATA FOR α_C AT Φ = 45 DEG

MACH NUMBER												
ASPECT RATIO	TAPER RATIO	≤0.1	0.6	0.8	1.2	1.5	2.0	2.5	3.0	3.5	4.5	≥5.0
≤0.25	0, 0.5, 1.0	0.0	22.0	22.0	0.0	0.0	0	0	0	0	0	0
0.5	0.5	15.0	11.5	11.0	10.0	0.0	0	0	0	0	0	0
1.0	0.5	15.0	13.3	0.0	6.5	0.0	0	0	0	0	0	0
≥2.0	0.5	10.0	10.0	0.0	6.5	2.2	0	0	0	0	0	0
0.5	0	30.0	15.0	11.5	10.0	0.0	0	0	0	0	0	0
≥2.0	0	10.0	10.0	0.0	6.5	0.0	0	0	0	0	0	0
0.5	1.0	15.0	11.0	11.0	10.0	0.0	0	0	0	0	0	0
≥2.0	1.0	10.0	10.0	0.0	6.5	1.5	0	0	0	0	0	0
1.0	0	40.0	13.3	0.0	6.5	0.0	0	0	0	0	0	0
1.0	1.0	15.0	13.3	0.0	6.5	0.0	0	0	0	0	0	0

TABLE 17. DATA FOR $\left[K_{W(B)}\right]_{\alpha=\alpha_D}$ AT Φ = 45 DEG

MACH NUMBER												
ASPECT RATIO	TAPER RATIO	≤0.1	0.6	0.8	1.2	1.5	2.0	2.5	3.0	3.5	4.5	≥6.0
≤0.25	0, 0.5, 1.0	1.0	1.0	1.00	1.00	1.00	1.00	1.00	1.00	1.00	1.00	1.0
0.5	0.5	1.0	1.0	1.00	0.90	0.90	1.00	0.95	1.00	0.97	1.00	1.0
1.0	0.5	1.0	1.0	1.00	0.95	1.00	1.00	1.00	1.00	1.00	1.00	1.0
≥2.0	0.5	1.0	1.0	0.95	0.95	1.00	1.00	1.00	1.00	1.00	1.00	1.0
0.5	0	1.0	1.0	1.00	1.00	0.90	0.90	0.90	0.90	0.90	0.90	1.0
≥2.0	0	1.0	1.0	0.95	1.00	1.00	1.00	1.00	1.00	1.00	1.00	1.0
0.5	1.0	1.0	1.0	1.00	1.00	1.00	1.00	1.00	1.00	1.00	1.00	1.0
≥2.0	1.0	1.0	1.0	1.00	1.00	1.00	1.00	1.00	0.93	0.90	0.95	1.0
1.0	0	1.0	1.0	1.00	0.95	1.00	1.00	1.00	1.00	1.00	1.00	1.0
1.0	1.0	1.0	1.0	1.00	0.95	0.95	0.95	1.00	1.00	1.00	1.00	1.0

TABLE 18. DATA FOR α_D AT Φ = 45 DEG

MACH NUMBER												
ASPECT RATIO	TAPER RATIO	≤0.1	0.6	0.8	1.2	1.5	2.0	2.5	3.0	3.5	4.5	≥6.0
≤0.25	0, 0.5, 1.0	20.0	40.0	38.0	35.0	30.0	25.0	16.3	15.1	13.9	13.1	10.0
0.5	0.5	59.0	33.0	30.0	25.6	25.0	15.0	15.0	10.0	15.0	15.0	10.0
1.0	0.5	49.0	38.0	32.0	26.0	24.0	17.0	15.0	14.4	10.0	10.0	10.0
≥2.0	0.5	39.0	31.5	30.0	28.0	25.0	16.5	15.0	14.4	10.0	13.0	10.0
0.5	0	59.0	35.5	33.0	39.5	29.5	15.0	25.0	15.0	15.0	10.0	10.0
≥2.0	0	39.0	31.5	30.0	28.0	24.7	17.0	13.5	11.4	10.0	10.0	10.0
0.5	1.0	59.0	35.5	33.0	25.6	29.5	15.0	15.0	15.0	12.0	13.0	10.0
≥2.0	1.0	39.0	31.5	30.0	28.0	23.3	14.0	16.0	15.0	11.8	12.0	10.0
1.0	0	59.0	38.5	32.5	36.0	27.1	17.2	21.0	11.4	10.0	10.0	10.0
1.0	1.0	49.0	38.5	32.5	26.0	26.4	16.0	15.3	15.0	11.8	10.0	10.0

TABLE 19. DATA FOR α_M AT Φ = 45 DEG

MACH NUMBER												
ASPECT RATIO	TAPER RATIO	≤0.1	0.6	0.8	1.2	1.5	2.0	2.5	3.0	3.5	4.5	≥6.0
≤0.25	0, 0.5, 1.0	35.0	45.0	45.0	40.0	44.0	43.0	38.0	28.0	25.0	29.0	20.0
0.5	0.5	65.0	33.0	30.0	49.0	52.0	40.0	40.0	30.0	25.0	25.0	20.0
1.0	0.5	55.0	38.0	47.0	49.5	66.0	48.5	45.0	41.0	40.0	10.0	20.0
≥2.0	0.5	45.0	31.5	40.0	56.0	57.0	45.0	45.0	41.0	40.0	28.0	20.0
0.5	0	65.0	35.5	33.0	65.0	48.0	50.0	46.0	30.0	30.0	50.0	20.0
≥2.0	0	45.0	31.5	40.0	56.0	55.0	58.5	49.8	44.2	41.5	28.5	20.0
0.5	1.0	65.0	35.5	33.0	49.0	52.0	40.0	28.0	24.0	21.0	13.0	20.0
≥2.0	1.0	45.0	31.5	40.0	56.0	49.5	44.0	40.0	33.0	32.0	28.0	20.0
1.0	0	70.0	38.5	49.0	63.0	60.0	60.5	49.8	44.2	41.5	40.0	20.0
1.0	1.0	55.0	38.5	49.0	49.5	60.0	47.5	40.0	33.0	32.0	20.0	20.0

TABLE 20. DATA FOR $\left[K_{W(B)}\right]_{\alpha=\alpha_M}$ AT $\Phi = 45$ DEG

MACH NUMBER												
ASPECT RATIO	TAPER RATIO	≤0.1	0.6	0.8	1.2	1.5	2.0	2.5	3.0	3.5	4.5	≥6.0
≤0.25	0, 0.5, 1.0	0.80	0.95	1.0	1.0	1.0	1.0	1.0	1.0	1.0	1.0	1.0
0.5	0.5	0.85	0.95	1.0	1.0	1.0	1.0	1.0	1.0	1.0	1.0	1.0
1.0	0.5	0.85	0.90	1.0	1.0	1.0	1.0	1.0	1.0	1.0	1.0	1.0
≥2.0	0.5	0.85	0.90	1.0	1.0	1.0	1.0	1.0	1.0	1.0	1.0	1.0
0.5	0	0.85	0.95	1.0	1.0	1.0	1.0	1.0	1.0	1.0	1.0	1.0
≥2.0	0	0.85	0.95	1.0	1.0	1.0	1.0	1.0	1.0	1.0	1.0	1.0
0.5	1.0	0.85	0.95	1.0	1.0	1.0	1.0	1.0	1.0	1.0	1.0	1.0
≥2.0	1.0	0.85	0.90	1.0	1.0	1.0	1.0	1.0	1.0	1.0	1.0	1.0
1.0	0	0.90	0.95	1.0	1.0	1.0	1.0	1.0	1.0	1.0	1.0	1.0
1.0	1.0	0.85	0.90	1.0	1.0	1.0	1.0	1.0	1.0	1.0	1.0	1.0

TABLE 21. DATA FOR $[\Delta K_{B(W)}]_{\alpha=0}$ AT $\Phi = 45$ DEG

MACH NUMBER												
ASPECT RATIO	TAPER RATIO	≤0.1	0.6	0.8	1.2	1.5	2.0	2.5	3.0	3.5	4.5	≥6.0
≤0.25	0, 0.5, 1.0	0.0	0.0	0.00	0.00	0.0	0	0	0	0	0	0
0.5	0.5	0.0	-0.12	-0.10	0.00	0.0	0	0	0	0	0	0
1.0	0.5	0.0	-0.07	-0.25	0.00	0.0	0	0	0	0	0	0
≥2.0	0.5	0.0	-0.23	-0.18	0.00	0.0	0	0	0	0	0	0
0.5	0	0.0	-0.12	0.00	0.00	0.0	0	0	0	0	0	0
≥2.0	0	0.0	-0.23	-0.18	0.00	0.0	0	0	0	0	0	0
0.5	1.0	0.0	-0.12	0.00	0.00	0.0	0	0	0	0	0	0
≥2.0	1.0	0.0	-0.23	-0.18	0.00	0.0	0	0	0	0	0	0
1.0	0	0.0	-0.05	-0.25	0.00	0.0	0	0	0	0	0	0
1.0	1.0	0.0	-0.07	-0.25	0.00	0.0	0	0	0	0	0	0

TABLE 22. DATA FOR $dK_{B(W)}/d\alpha$ (PER DEG) AT $\Phi = 45$ DEG

MACH NUMBER												
ASPECT RATIO	TAPER RATIO	≤0.1	0.6	0.8	1.2	1.5	2.0	2.5	3.0	3.5	4.5	≥6.0
≤0.25	0, 0.5, 1.0	-0.0050	-0.00557	-0.0200	-0.0215	-0.0250	-0.022	-0.022	-0.025	-0.030	-0.04	-0.04
0.5	0.5	-0.006	-0.006	-0.024	-0.030	-0.032	-0.047	-0.035	-0.0330	-0.0620	-0.060	-0.06
1.0	0.5	-0.0030	0.00000	0.000	-0.024	-0.020	-0.020	-0.02	-0.02	-0.02	-0.02	-0.02
≥2.0	0.5	0.0030	0.00670	0.005	-0.0150	-0.02	-0.0300	-0.045	-0.054	-0.060	-0.062	-0.065
0.5	0	-0.0020	-0.020	-0.027	-0.039	-0.040	-0.053	-0.035	-0.040	-0.050	-0.060	-0.06
≥2.0	0	0.0030	0.00670	0.005	-0.0150	-0.02	-0.0300	-0.045	-0.054	-0.060	-0.062	-0.065
0.5	1.0	0.0015	-0.006	-0.025	-0.030	-0.032	-0.040	-0.0275	-0.0400	-0.060	-0.060	-0.06
≥2.0	1.0	0.0030	0.00670	0.005	-0.0150	-0.02	-0.0300	-0.045	-0.054	-0.060	-0.062	-0.065
1.0	0	0.003	0.0	0.0	-0.024	-0.02	-0.02	-0.02	-0.02	-0.02	-0.02	-0.02
1.0	1.0	-0.003	0.0	0.0	-0.024	-0.02	-0.02	-0.02	-0.02	-0.02	-0.02	-0.02

TABLE 23. DATA FOR α_1 (DEG) AT $\Phi = 45$ DEG

MACH NUMBER												
ASPECT RATIO	TAPER RATIO	≤0.1	0.6	0.8	1.2	1.5	2.0	2.5	3.0	3.5	4.5	≥6.0
≤0.25	0, 0.5, 1.0	10.0	15.0	15.0	15.0	10.0	10.0	10.0	10.0	10.0	10.0	10.0
0.5	0.5	10.0	57.0	20.0	23.0	23.0	15.0	20.0	15.0	10.0	10.0	10.0
1.0	0.5	10.0	10.0	20.0	25.0	30.0	30.0	15.0	17.5	15.0	15.0	15.0
≥2.0	0.5	10.0	15.0	15.0	15.0	10.0	10.0	10.0	12.0	10.0	10.0	10.0
0.5	0	10.0	24.0	33.0	23.0	19.0	20.0	22.5	15.0	10.0	10.0	10.0
≥2.0	0	10.0	15.0	15.0	15.0	10.0	10.0	10.0	12.0	10.0	10.0	10.0
0.5	1.0	10.0	62.0	24.0	25.0	25.0	16.0	20.0	15.0	10.0	10.0	10.0
≥2.0	1.0	10.0	15.0	15.0	15.0	10.0	10.0	10.0	12.0	10.0	10.0	10.0
1.0	0	10.0	10.0	20.0	25.0	30.0	30.0	15.0	17.5	15.0	15.0	15.0
1.0	1.0	10.0	10.0	20.0	25.0	30.0	30.0	15.0	17.5	15.0	15.0	15.0

TABLE 24. DATA FOR α_2 (DEG) AT $\Phi = 45$ DEG

MACH NUMBER												
ASPECT RATIO	TAPER RATIO	≤0.1	0.6	0.8	1.2	1.5	2.0	2.5	3.0	3.5	4.5	≥6.0
≤0.25	0, 0.5, 1.0	35.0	55.0	50.0	50.0	45.0	40.0	35.0	32.5	30.0	27.5	25.0
0.5	0.5	75.0	65.0	55.0	43.0	40.0	38.0	44.0	44.0	36.0	30.0	20.0
1.0	0.5	75.0	35.0	30.0	30.0	60.0	60.0	62.0	80.0	80.0	80.0	80.0
≥2.0	0.5	75.0	65.0	30.0	30.0	30.0	60.0	62.0	80.0	42.0	45.0	45.0
0.5	0	75.0	60.0	50.0	52.0	40.0	35.0	44.0	50.0	36.0	30.0	20.0
≥2.0	0	75.0	65.0	30.0	30.0	30.0	60.0	62.0	80.0	42.0	45.0	45.0
0.5	1.0	75.0	65.0	55.0	42.0	40.0	38.0	44.0	40.0	36.0	30.0	20.0
≥2.0	1.0	75.0	65.0	30.0	30.0	30.0	60.0	62.0	80.0	42.0	45.0	45.0
1.0	0	75.0	50.0	30.0	30.0	60.0	60.0	62.0	80.0	80.0	80.0	80.0
1.0	1.0	75.0	35.0	30.0	30.0	60.0	60.0	62.0	80.0	80.0	80.0	80.0

TABLE 25. DATA FOR $[K_{B(W)}]_{MIN}$ (FRACTION OF SBT/LT) AT $\Phi = 45$ DEG

MACH NUMBER												
ASPECT RATIO	TAPER RATIO	≤0.1	0.6	0.8	1.2	1.5	2.0	2.5	3.0	3.5	4.5	≥6.0
≤0.25	0, 0.5, 1.0	0.25	0.25	0.25	0.12	0.12	0.12	0.12	0.12	0.12	0.12	0
0.5	0.5	0.25	0.25	0.25	0.12	0.12	0.12	0.12	0.12	0.12	0.12	0
1.0	0.5	0.25	0.25	0.25	0.12	0.12	0.12	0.12	0.12	0.12	0.12	0
≥2.0	0.5	0.25	0.25	0.25	0.12	0.12	0.12	0.12	0.12	0.12	0.12	0
0.5	0	0.25	0.25	0.25	0.12	0.12	0.12	0.12	0.12	0.12	0.12	0
≥2.0	0	0.25	0.25	0.25	0.12	0.12	0.12	0.12	0.12	0.12	0.12	0
0.5	1.0	0.25	0.25	0.25	0.12	0.12	0.12	0.12	0.12	0.12	0.12	0
≥2.0	1.0	0.25	0.25	0.25	0.12	0.12	0.12	0.12	0.12	0.12	0.12	0

2.3.4 Wing-Body and Body-Wing Interference Due to Control Deflection

Reference 71 used a more recent wind tunnel data base informally provided by Jerry Allen of NASA/LARC to improve upon the nonlinear constants used for the wing-alone, body-alone and wing-body interference factors due to AOA. Neither interference factors due to control deflection, nor the wing-tail interference model, were considered in Reference 71 refinements. Those factors are not considered because the informal data from NASA/LARC was for an undeflected wing-body configuration with no tail present.

More recently, some other unpublished wind tunnel data has been provided to the author from Steve Malyevac of the Naval Surface Warfare Center at Dahlgren, Virginia. The new data provided by Mr. Malyevac contained control deflection data and more importantly, the configuration had canards and tails. Also, data was available in the Mach range 0.5 to 1.2, in addition to the supersonic region up to Mach 3.0.

The subsonic and transonic data was particularly useful since when the author originally defined the wing-tail interference model,[45] data was available primarily at $M_\infty = 2$, 3, and 4,[88] with only one data point at $M = 1.1$.[89] As a result of this scarcity of subsonic and transonic wing-tail interference data, many engineering guesses and extrapolations were made[39] in the development of the nonlinear wing-tail interference model. Also, since the wing-body interference model due to control deflection was developed,[39,46] additional wind tunnel data reports have become available.

The purpose of this section and the next section of the report is to refine upon the wing-body interference factors for control deflection and the wing-tail interference methodology. These refinements will be based on the informal wind tunnel data base provided by Mr. Malyevac and additional validations completed based on other wind tunnel data reports. Therefore, these next two sections will serve as formal documentation for changes made to the

wing-body interference methodology due to control deflection and the wing-tail interference methodology.

The nonlinear form of the wing-body and body-wing interference due to control deflection was defined in References 39 and 46 by

$$k_{W(B)} = C_1(M)\left[k_{W(B)}\right]_{SBT} + C_2\left(|\alpha_W|, M\right) \tag{18}$$

$$k_{B(W)} = C_3\left(M, |\alpha_W|\right)\left[k_{B(W)}\right]_{SBT} \tag{19}$$

The parameters C_1, C_2, and C_3 of Equations (18) and (19) were derived based on numerical experiments of the AP95[39] and AP98[59] compared to data. References 39 and 46 used the above approach of numerical experiments because many of the fins in the data base upon which the nonlinear coefficients for wing-body interference due to AOA were derived were small. The small fin size made it difficult to get accurate measurements of the nonlinear interference terms represented by Equations (18) and (19). By using total force and moment data from data bases to estimate the nonlinear variation of $k_{W(B)}$ and $k_{B(W)}$ with Mach number and total AOA, one can estimate the combined effect of Equations (18) and (19) reasonably well. However, one cannot break down the physical effects easily between Equations (18) and (19).

Refinements to the constants C_1, C_2, and C_3 of Equations (18) and (19) were made more recently based on additional numerical experiments with existing data bases as well as numerical experiments with new data bases. Tables 26 and 27 give the revised semiempirical nonlinear control deflection models for the roll positions of $\Phi = 0$ and 45 deg, respectively.

In examining the constants and model of Table 26, several physical phenomena occur that are modeled in a semiempirical sense by Equations (18) and (19). These phenomena are qualitatively shown in Figure 18A. At low Mach number, Figure 18A indicates the SBT gives a low value of $k_{W(B)}$ for small values of α_W. At a value of α_W of about 40 deg, the controls lose effectiveness as a result of a combination of stall and blow-by effects due to the separation between the wing and body. At an α_W of about 70 deg, the controls have lost most effectiveness. At Mach numbers greater than about 4, the controls initially generate less effectiveness than is generated by SBT for values of α_W up to about 10 to 40 deg. The controls then become more effective because of nonlinear compressibility effects. On the other hand, at an α_W of around 45 to 50 deg, the controls once again begin to lose effectiveness, presumably because of shock interactions and blow-by effects. For Mach numbers in between subsonic and high supersonic, $k_{W(B)}$ has behavior in between the two extremes illustrated in Table 26.

A lot of similarity is seen when comparing the nonlinear control deflection models for $\Phi = 0$ and 45 deg roll in Tables 26 and 27. The constants for the $\Phi = 45$ deg are slightly different than those for $\Phi = 0$ deg and the values of α_W where the nonlinearities begin are somewhat different. However, by and large, Equation (18) holds for both the $\Phi = 0$ and 45 deg roll cases. It should be pointed out that in Reference 30, mostly linear variations of $k_{W(B)}$ with α_W were used. However, these were improved upon for the $\Phi = 45$ deg case with cubic fits of

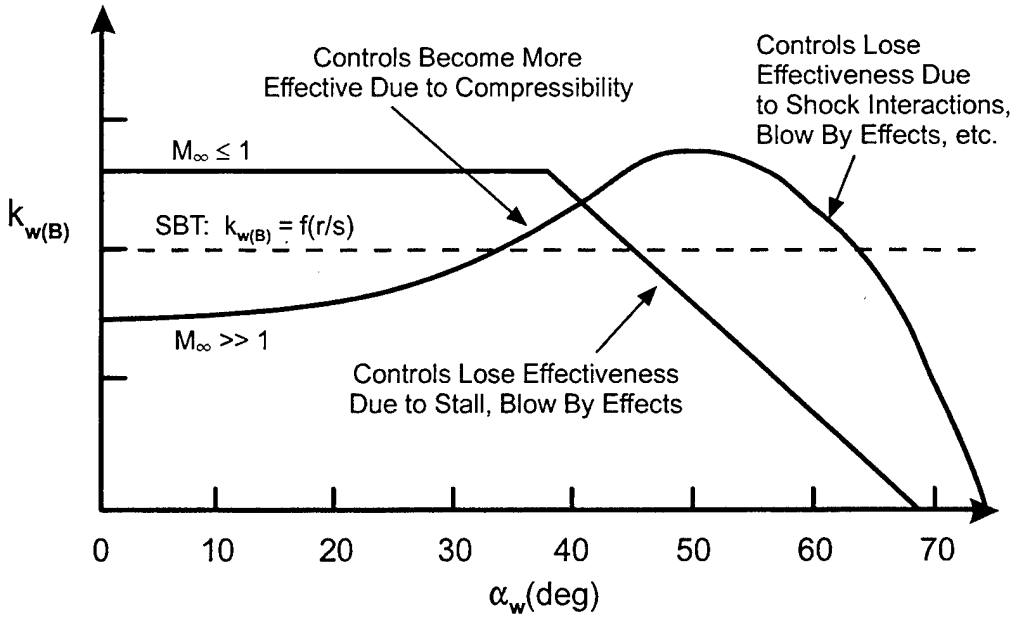

FIGURE 18A. QUALITATIVE TREND OF WING-BODY INTERFERENCE DUE TO CONTROL DEFLECTION AS FUNCTION OF M_∞, α_W

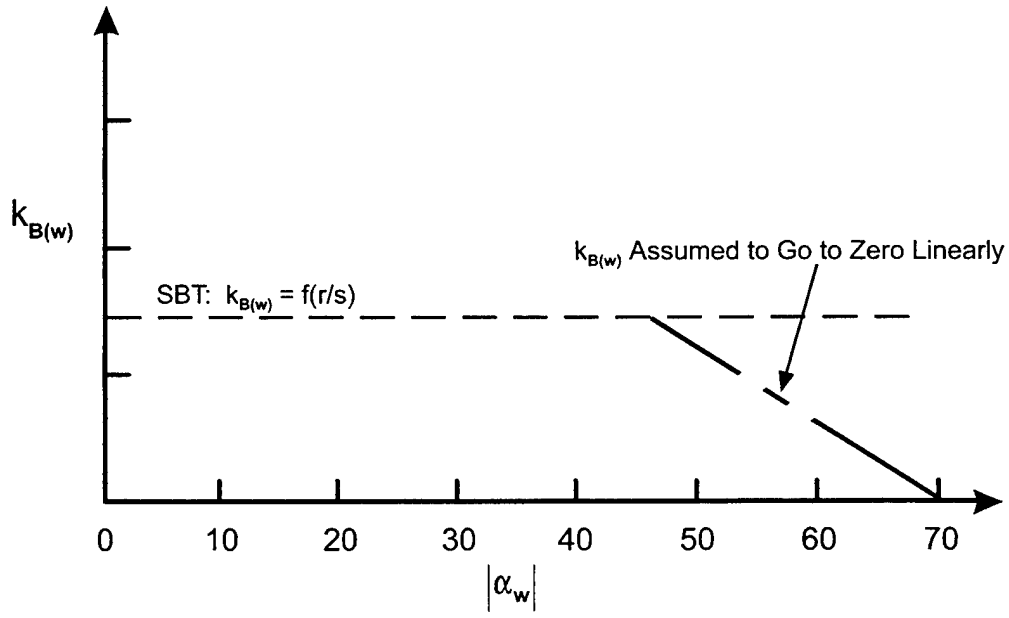

FIGURE 18B. QUALITATIVE TREND OF BODY-WING INTERFERENCE DUE TO CONTROL DEFLECTION AS FUNCTION OF α_W

TABLE 26. SEMIEMPIRICAL NONLINEAR CONTROL DEFLECTION MODEL (Φ = 0 DEG)

MACH NUMBER	NONLINEAR MODEL
$M_\infty \leq 0.8$	If $\lvert\alpha_W\rvert \leq 40.0 \rightarrow k_{W(B)} = 1.1\,[k_{W(B)}]_{SBT}$ If $\lvert\alpha_W\rvert > 40.0 \rightarrow k_{W(B)} = 2.04 - \lvert\alpha_W\rvert/40$ If $\lvert\alpha_W\rvert \geq 80.0 \rightarrow k_{W(B)} = 0.04$
$M_\infty = 1.1$	If $\lvert\alpha_W\rvert \leq 15.0 \rightarrow k_{W(B)} = [k_{W(B)}]_{SBT}$ If $\lvert\alpha_W\rvert > 15.0 \rightarrow k_{W(B)} = 1.15 - 0.9\,\lvert\alpha_W\rvert/65$ If $\lvert\alpha_W\rvert \geq 80.0 \rightarrow k_{W(B)} = 0.04$
$M_\infty = 1.5$	If $\lvert\alpha_W\rvert \leq 10.0 \rightarrow k_{W(B)} = [k_{W(B)}]_{SBT}$ If $\lvert\alpha_W\rvert > 10.0 \rightarrow k_{W(B)} = [k_{W(B)}]_{SBT} - 0.005\,(\lvert\alpha_W\rvert - 10.0)$ If $\lvert\alpha_W\rvert \geq 70.0 \rightarrow k_{W(B)} = 0.64 - 0.6\,(\lvert\alpha_W\rvert - 70.0)/35$; $[k_{W(B)}]_{min} = 0.04$
$M_\infty = 2.0$	If $\lvert\alpha_W\rvert \leq 10.0 \rightarrow k_{W(B)} = 0.9\,[k_{W(B)}]_{SBT}$ If $\lvert\alpha_W\rvert > 10.0 \rightarrow k_{W(B)} = 0.9\,[k_{W(B)}]_{SBT} - 0.003\,(\lvert\alpha_W\rvert - 10.0)$ If $\lvert\alpha_W\rvert \geq 70.0 \rightarrow k_{W(B)} = 0.67 - 0.63\,(\lvert\alpha_W\rvert - 70.0)/35$; $[k_{W(B)}]_{min} = 0.04$
$M_\infty = 2.35, 2.87$	If $\lvert\alpha_W\rvert \leq 40.0 \rightarrow k_{W(B)} = 0.9\,[k_{W(B)}]_{SBT}$ If $\lvert\alpha_W\rvert > 40.0 \rightarrow k_{W(B)} = 0.9\,[k_{W(B)}]_{SBT} + 0.005\,(\lvert\alpha_W\rvert - 40.0)$ If $\lvert\alpha_W\rvert > 70.0 \rightarrow k_{W(B)} = 1 - 0.96\,(\lvert\alpha_W\rvert - 70.0)/35$
$M_\infty = 3.95$	If $\lvert\alpha_W\rvert \leq 20.0 \rightarrow k_{W(B)} = 0.8\,[k_{W(B)}]_{SBT}$ If $\lvert\alpha_W\rvert > 20.0 \rightarrow k_{W(B)} = 0.8\,[k_{W(B)}]_{SBT} + 0.007\,(\lvert\alpha_W\rvert - 20.0)$ If $\lvert\alpha_W\rvert > 70.0 \rightarrow k_{W(B)} = 1.1 - 1.06\,(\lvert\alpha_W\rvert - 70.0)/35$
$M_\infty = 4.6$	If $\lvert\alpha_W\rvert \leq 20.0 \rightarrow k_{W(B)} = 0.75\,[k_{W(B)}]_{SBT}$ If $\lvert\alpha_W\rvert > 20.0 \rightarrow k_{W(B)} = 0.75\,[k_{W(B)}]_{SBT} + 0.013\,(\lvert\alpha_W\rvert - 20.0)$ If $\lvert\alpha_W\rvert > 70.0 \rightarrow k_{W(B)} = 1.36 - 1.32\,(\lvert\alpha_W\rvert - 70.0)/35$
$0 \leq M_\infty \leq \infty$	$k_{B(W)} = [k_{B(W)}]_{SBT}$ for $\lvert\alpha_W\rvert \leq 70$ deg $k_{W(B)} = [k_{B(W)}]_{SBT} + [1 - (\lvert\alpha_W\rvert - 70)/20]$; $70 < \lvert\alpha_W\rvert < 90$ $k_{W(B)} = 0$ for $\lvert\alpha_W\rvert > 90$ deg

TABLE 27. SEMIEMPIRICAL NONLINEAR CONTROL DEFLECTION MODEL (Φ = 45 DEG)

MACH NUMBER	NONLINEAR MODEL
$M_\infty \le 0.8$	If $\lvert\alpha_W\rvert \le 40.0 \rightarrow k_{W(B)} = 1.1\ [k_{W(B)}]_{SBT}$ If $\lvert\alpha_W\rvert > 40.0 \rightarrow k_{W(B)} = 2.04 - \lvert\alpha_W\rvert/40$ If $\lvert\alpha_W\rvert > 80.0 \rightarrow k_{W(B)} = 0.04$
$M_\infty = 1.1$	If $\lvert\alpha_W\rvert \le 15.0 \rightarrow k_{W(B)} = [k_{W(B)}]_{SBT}$ If $\lvert\alpha_W\rvert > 15.0 \rightarrow k_{W(B)} = 1.15 - 0.9\ \lvert\alpha_W\rvert/65$ $[k_{W(B)}]_{min} = 0.04$
$M_\infty = 1.5$	If $\lvert\alpha_W\rvert \le 35.0 \rightarrow k_{W(B)} = 0.95\ [k_{W(B)}]_{SBT}$ If $\lvert\alpha_W\rvert > 35.0 \rightarrow k_{W(B)} = [-(8.06 \times 10^{-5})(\lvert\alpha_W\rvert - 35.0)^3 + 0.002(\lvert\alpha_W\rvert - 35.0)^2$ $- 0.0295(\lvert\alpha_W\rvert - 35.0) + 0.94]\ [k_{W(B)}]_{SBT}$ If $\lvert\alpha_W\rvert > 55.0 \rightarrow k_{W(B)} = 0.48 - 0.44(\lvert\alpha_W\rvert - 55.0)/35.0$ If $\lvert\alpha_W\rvert > 90.0 \rightarrow k_{W(B)} = 0.04$
$M_\infty = 2.0$	If $\lvert\alpha_W\rvert \le 32.5 \rightarrow k_{W(B)} = 0.95\ [k_{W(B)}]_{SBT}$ If $\lvert\alpha_W\rvert > 32.5 \rightarrow k_{W(B)} = [(-0.000008(\lvert\alpha_W\rvert - 32.5)^3 - 0.00091(\lvert\alpha_W\rvert - 32.5)^2$ $+ 0.01(\lvert\alpha_W\rvert - 32.5) + 0.95]\ [k_{W(B)}]_{SBT}$ If $\lvert\alpha_W\rvert > 55.0 \rightarrow k_{W(B)} = 0.59 - 0.55(\lvert\alpha_W\rvert - 55.0)/35.0$ If $\lvert\alpha_W\rvert > 90.0 \rightarrow k_{W(B)} = 0.04$
$M_\infty = 2.35$	If $\lvert\alpha_W\rvert \le 30.0 \rightarrow k_{W(B)} = 0.95\ [k_{W(B)}]_{SBT}$ If $\lvert\alpha_W\rvert > 30.0 \rightarrow k_{W(B)} = [0.000043(\lvert\alpha_W\rvert - 30.0)^3 - 0.0029(\lvert\alpha_W\rvert - 30.0)^2$ $+ 0.039(\lvert\alpha_W\rvert - 30.0) + 0.9]\ [k_{W(B)}]_{SBT}$ If $\lvert\alpha_W\rvert > 40.0 \rightarrow k_{W(B)} = 0.90 - 0.86(\lvert\alpha_W\rvert - 78.0)/38.0$ If $\lvert\alpha_W\rvert > 78.0 \rightarrow k_{W(B)} = 0.04$
$M_\infty = 2.87$	If $\lvert\alpha_W\rvert \le 30.0 \rightarrow k_{W(B)} = 0.9\ [k_{W(B)}]_{SBT}$ If $30 < \lvert\alpha_W\rvert \le 50.0 \rightarrow k_{W(B)} = [0.000065(\lvert\alpha_W\rvert - 30.0)^3 - 0.004(\lvert\alpha_W\rvert - 30.0)^2$ $+ 0.057(\lvert\alpha_W\rvert - 30.0) + 0.9]\ [k_{W(B)}]_{SBT}$ If $\lvert\alpha_W\rvert > 50.0 \rightarrow k_{W(B)} = 0.91 - 0.87(\lvert\alpha_W\rvert - 50.0)/28.0$ If $\lvert\alpha_W\rvert > 78.0 \rightarrow k_{W(B)} = 0.04$
$M_\infty = 3.95$	If $\lvert\alpha_W\rvert \le 35.0 \rightarrow k_{W(B)} = 0.88\ [k_{W(B)}]_{SBT}$ If $35 < \lvert\alpha_W\rvert \le 48.0 \rightarrow k_{W(B)} = [-0.000088(\lvert\alpha_W\rvert - 35.0)^3 + 0.00017(\lvert\alpha_W\rvert - 35.0)^2$ $+ 0.016(\lvert\alpha_W\rvert - 35.0) + 0.88]\ [k_{W(B)}]_{SBT}$ If $48 < \lvert\alpha_W\rvert \le 80.0 \rightarrow k_{W(B)} = 0.82 - 0.78(\lvert\alpha_W\rvert - 48.0)/32.0$ If $\lvert\alpha_W\rvert > 80.0 \rightarrow k_{W(B)} = 0.04$
$M_\infty = 4.6$	If $\lvert\alpha_W\rvert \le 35.0 \rightarrow k_{W(B)} = 0.83\ [k_{W(B)}]_{SBT}$ If $35 < \lvert\alpha_W\rvert \le 50.0 \rightarrow k_{W(B)} = [0.000047(\lvert\alpha_W\rvert - 35.0)^3 - 0.0046(\lvert\alpha_W\rvert - 35.0)^2$ $+ 0.074(\lvert\alpha_W\rvert - 35.0) + 0.83]\ [k_{W(B)}]_{SBT}$ If $50 < \lvert\alpha_W\rvert \le 77.0 \rightarrow k_{W(B)} = 1.06 - 1.02(\lvert\alpha_W\rvert - 50.0)/27.0$ If $\lvert\alpha_W\rvert > 77.0 \rightarrow k_{W(B)} = 0.04$
$0 \le M_\infty \le \infty$	$k_{B(W)} = [k_{B(W)}]_{SBT} - \dfrac{\lvert\delta_W\rvert}{30.0}\ 0.75\ [k_{B(W)}]_{SBT}$ for $\lvert\delta_W\rvert \le 30$ $k_{W(B)} = 0.25\ [k_{B(W)}]_{SBT}$ for $\lvert\delta_W\rvert > 30$ $k_{B(W)} = 0.25\ [k_{B(W)}]_{SBT}\ [1 - (\lvert\alpha_W\rvert - 50)/5]$ for $\lvert\alpha_W\rvert > 50$ $k_{W(B)} = 0$ for $\lvert\alpha_W\rvert > 55$ deg

control deflection data as seen in Table 27. As such, all nonlinear effects are included in the variations of $k_{W(B)}$ as a function of Mach number and $|\alpha + \delta|$.

Figure 18B assumes that $k_{B(W)}$ can be represented by SBT up to some value of $|\alpha_W|$, at which point it decays to zero. For $\Phi = 0$ deg, the value for $|\alpha_W|$ is 70 deg. For $\Phi = 45$ deg roll, the model for $k_{B(W)}$ is based on $|\delta|$ only and begins decaying at $|\delta| = 0$. It reaches a minimum $k_{B(W)}$ of 25 percent of SBT at $|\delta| = 30$. For $30 \le |\delta| \le 50$, the value of $k_{B(W)}$ remains constant. It then decays to zero at $|\delta_W| = 55$ deg.

It should also be noted that $k_{W(B)}$ and $k_{B(W)}$ of Table 27 are multiplied by 1.414 to indicate that all four fins are assumed to be deflected by an equal amount in the $\Phi = 45$ deg roll position. Finally, for Mach numbers in between the values on Table 26 and 27, linear interpolation is used.

2.3.5 Nonlinear Wing–Tail Interference Model

The nonlinear wing-tail interference normal-force component is defined by

$$C_{N_{T(V)}} = \frac{A_W \left(C_{N_\alpha}\right)_W \left(C_{N_\alpha}\right)_T \left[K_{W(B)}\alpha + Fk_{W(B)}\delta_W\right]}{2\pi \left(AR\right)_T \left(f_W - r_W\right) A_{REF}} \left(s_T - r_T\right)\left[i_1 \cos\Phi + i_4 \sin\Phi\right] \quad (20)$$

Each of the normal-force and interference terms in Equation (20) utilizes the complete nonlinear form,[39,46,59] as opposed to its linear theory or slender body representation. Equation (20) can also be written as

$$C_{N_{T(V)}} = \left[C_{N_{T(V)}}\right]_\alpha + \left[C_{N_{T(V)}}\right]_\delta \quad (21)$$

Reference 39 defined the first term of Equation (21) for $\Phi = 0$ as

$$\left[C_{N_{T(V)}}\right]_\alpha = A + B\alpha + C\alpha^2 + D\alpha^3 \quad (22)$$

where the constants A, B, C, and D are functions of SBT and experimental data and are defined by

$$A = 0$$

$$B = \left[\left(\frac{dC_{N_{T(V)}}}{d\alpha}\right)_{\alpha=0}\right]_{SBT} E_1$$

$$C = \frac{-B - D\,\alpha_N^2}{\alpha_N}$$

$$D = \frac{E_2\,\alpha_N - B\alpha_N\alpha_F + B\alpha_F^2}{\alpha_N\alpha_F^3 - \alpha_F^2\alpha_N^2}$$

The parameters in the constants B, C, and D are defined as follows:

α_{N_0} = Value from Figure 19A

α_F = (Value from Figure19B) $\times \frac{\alpha_N}{100}$

E_1 = Value from Figure 19C

E_2 = (Value from Figure 19D) $\times \left(\left[C_{N_{T(V)}}\right]_{SBT}\right)_{\alpha=\alpha_F}$

For $\Phi = 45$ deg, Reference 45 defined the $\left[C_{N_{T(V)}}\right]_\alpha$ term as

$$\left[C_{N_{T(V)}}\right]_\alpha = G_1\left[C_{N_{T(V)}}\right]_{SBT} \tag{23}$$

where G_1 is given in Figure 20. The modifications to the parameters α_F, E_1, E_2, and G at $\Phi = 0$ and $\Phi = 45$ deg in Figures 19 and 20, as a result of the recent improvements, are indicated as AP02. The AP98[59] indicates the values of these parameters prior to the recent refinements in the wing-tail interference model.

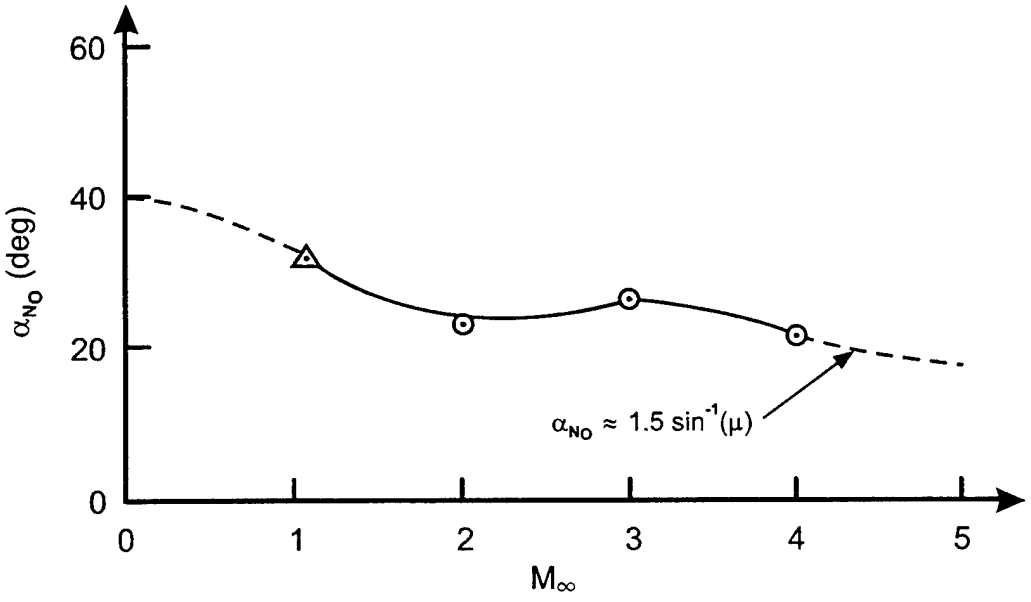

FIGURE 19A. AOA WHERE WING-TAIL INTERFERENCE IS NEGLIGIBLE

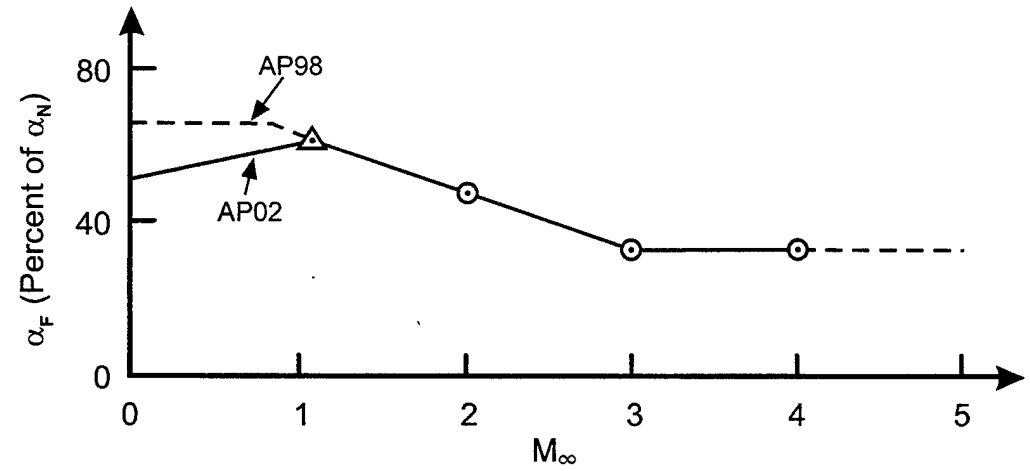

FIGURE 19B. AOA WHERE WING-TAIL INTERFERENCE IS A MAXIMUM (PERCENT OF α_N)

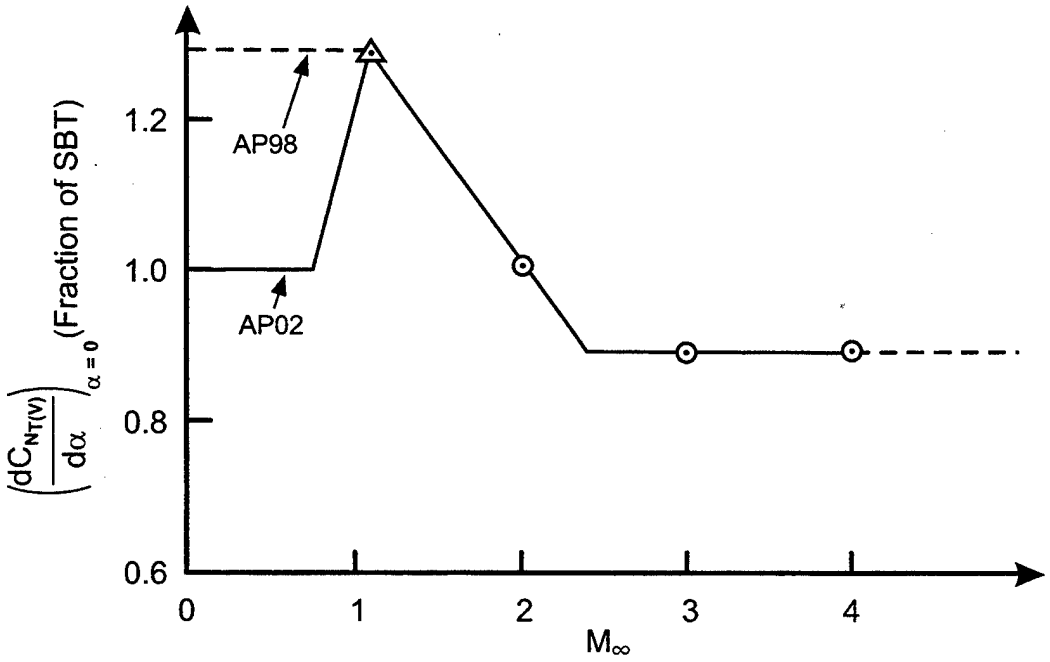

FIGURE 19C. INITIAL SLOPE AT $\alpha = 0$ OF WING-TAIL INTERFERENCE AS A FUNCITON OF M_∞

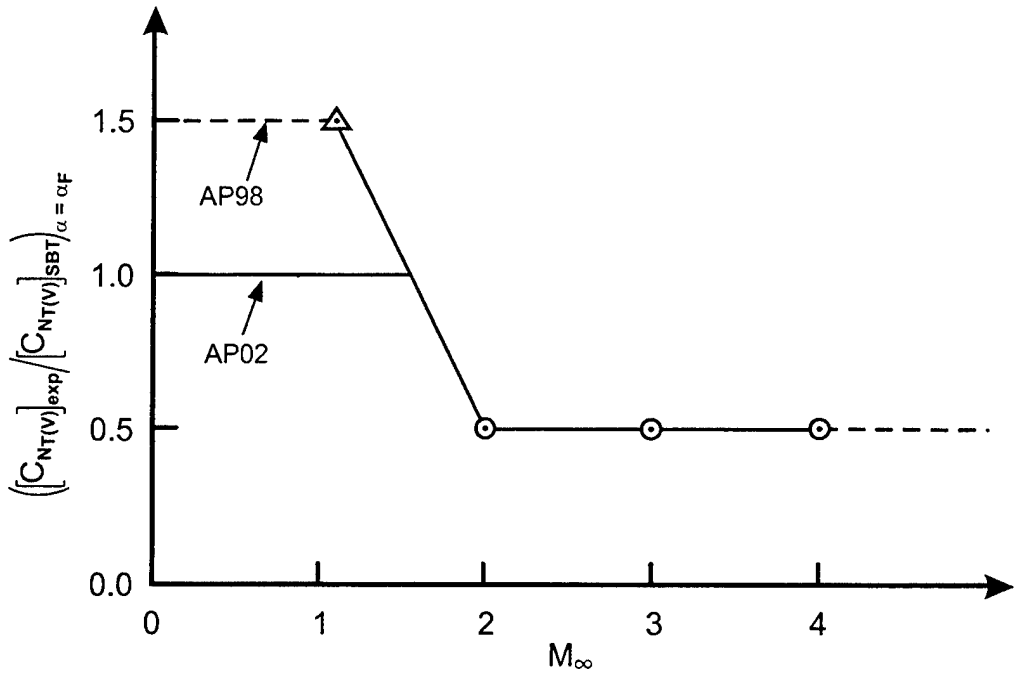

FIGURE 19D. SLENDER BODY THEORY PREDICTION OF WING-TAIL INTERFERENCE AT AOA WHERE $[C_{N_{T(V)}}]_{EXP}$ REACHES A MAXIMUM AS A FRACTION OF EXPERIMENTAL DATA

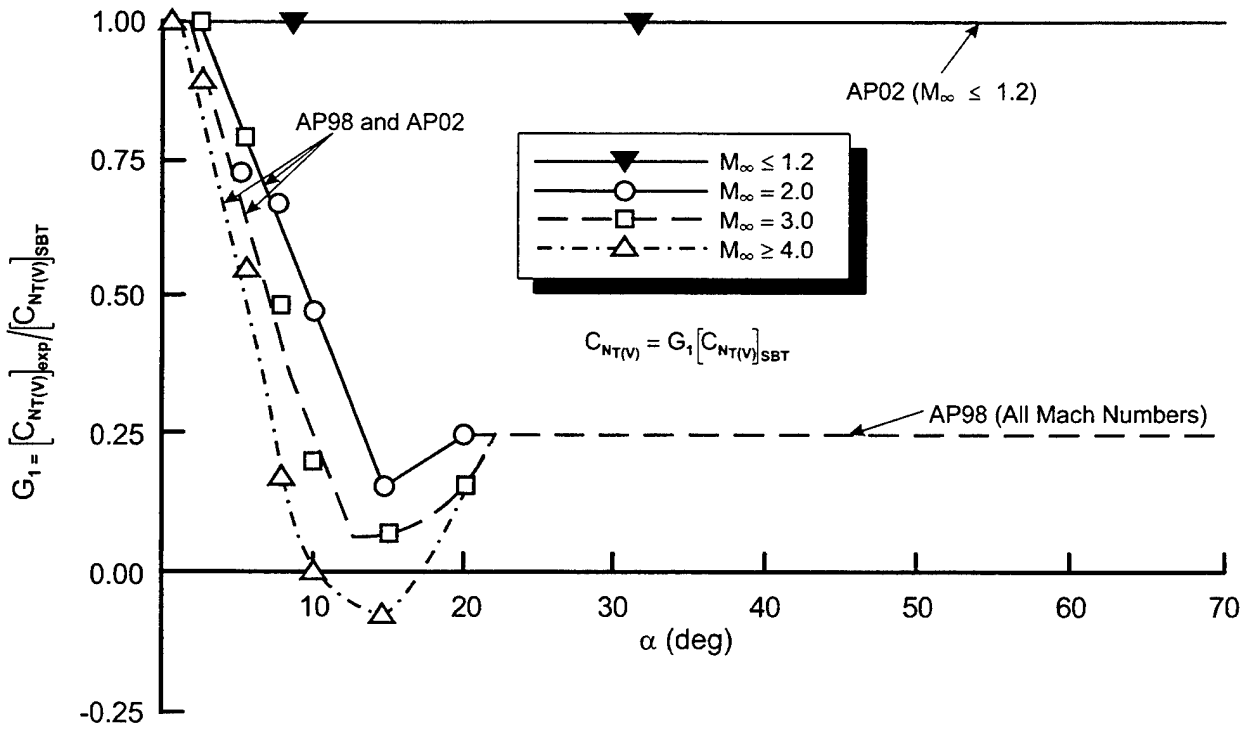

FIGURE 20. WING-TAIL INTERFERENCE MODEL FOR NO CONTROL DEFLECTION AT $\Phi = 45$ DEG

Equations (22) and (23) define the first term of Equation (21). In addition to Equations (23) and (24), an upper limit on the amount of lift loss on the tail will remain in effect for large wing areas (i.e. $A_W/A_{ref} \geq 5.5$).

The value of A_W/A_{ref} of 5.5 corresponds to the wing area ratio in Reference 2. This upper limit is defined by the following methodology:

For $M \leq 1.5$

$$\frac{\left|C_{N_{T(V)}}\right|_\alpha}{C_{N_T}} = 1.0\,;\ \alpha \leq 5$$

$$\frac{\left|C_{N_{T(V)}}\right|_\alpha}{C_{N_T}} = 1.0 - 0.04125\,(\alpha - 5);\ \alpha > 5 \qquad (24A)$$

For $1.5 < M \leq 2.5$

$$\frac{\left|C_{N_{T(V)}}\right|_\alpha}{C_{N_T}} = 0.9 - 0.025\alpha\,;\ \alpha \leq 10$$

$$\frac{\left|C_{N_{T(V)}}\right|_\alpha}{C_{N_T}} = 0.65 - 0.0235\,(\alpha - 10);\ \alpha > 10 \qquad (24B)$$

For $M > 2.5$

$$\frac{\left|C_{N_{T(V)}}\right|_\alpha}{C_{N_T}} = 0.8 - 0.025\alpha \qquad (24C)$$

where α is AOA in degrees. Equation (24A) says that at $\alpha = 0$ deg, the maximum lift loss on the tail due to AOA is limited to 100 percent of the tail lift, regardless of the size of the wings. The percent lift loss then decreases linearly with AOA as defined by Equations (24A) – (24C).

Admittedly, this is conservative (overpredicts $C_{N_{T(V)}}$) for values of $A_W/A_{REF} < 5.5$ and is simply a judgement based on numerical experiments for values of $A_W/A_{REF} > 5.5$. It does accomplish the objective of making the wing-tail interference with no control deflection more closely approximate data than available approaches.[45]

Before moving to the wing-tail interference methodology for the second term of Equation (21), a comment would be valuable on the Figure 19 results, which basically compare

SBT to data. First of all, it is clear that at low AOA, SBT underpredicts $C_{N_{T(V)}}$ for low Mach number and overpredicts it at high Mach number, for the Reference 88 configuration. The point of optimum prediction appears to be around Mach 2 (see Figure 19C). Second, the $C_{N_{T(V)}}$ term decays much faster at high AOA than does SBT. This is increasingly true as Mach number increases. This again highlights the Newtonian Impact assumptions at high Mach number where any vortices in the leeward plane are completely dominated by the dynamic pressure in the windward plane. Figures 19A and 19B illustrate this fact, showing that AOA where $C_{N_{T(V)}}$ is negligible gets smaller as M_∞ increases; also, the maximum magnitude as a percent of SBT gets smaller with increasing M_∞.

To define the second term of Equation (21), the wing-tail interference component due to a wing control deflection, a parameter "F" has been defined. This parameter "F" is used to control the value of the wing-tail interference resulting from a control deflection of the forward lifting surface. "F" was determined by numerical experiments comparing theory to data for various weapon configurations under various freestream conditions. Values of the parameter "F" are given in Tables 28 and 29 for the roll positions of $\Phi = 0$ and 45 deg, respectively. Many of the values for "F" in Tables 28 and 29 are substantially different than those used in the AP98 defined in References 46 and 59.

TABLE 28. EMPIRICAL PARAMETER "F" USED IN WING-TAIL INTERFERENCE MODEL ($\Phi = 0$ DEG)

MACH NUMBER	PARAMETER "F"
$M_\infty \leq 1.2$	$F = 0.8$
$M_\infty = 1.5$	If $\lvert\alpha_W\rvert \leq 20.0 \rightarrow F = 0.8$ If $\lvert\alpha_W\rvert > 20.0 \rightarrow F = 0.8 + 0.1\ (\lvert\alpha_W\rvert - 20.0)$ $F_{max} = 1.0$
$M_\infty = 2.0$	If $\lvert\alpha_W\rvert \leq 40.0 \rightarrow F = 0.8$ If $\lvert\alpha_W\rvert > 40.0 \rightarrow F = 0.8 + 0.01\ (\lvert\alpha_W\rvert - 40.0)$ $F_{max} = 1.0$
$M_\infty = 2.3$	If $\lvert\alpha_W\rvert \leq 40.0 \rightarrow F = 0.8$ If $\lvert\alpha_W\rvert > 40.0 \rightarrow F = 0.8 + 0.10\ (\lvert\alpha_W\rvert - 40.0)$ $F_{max} = 2.0$
$M_\infty = 2.87$	If $\lvert\alpha_W\rvert \leq 40.0 \rightarrow F = 0.9$ If $\lvert\alpha_W\rvert > 40.0 \rightarrow F = 0.9 + 0.12\ (\lvert\alpha_W\rvert - 40.0)$ $F_{max} = 3.0$
$M_\infty = 3.95$	If $\lvert\alpha_W\rvert \leq 40.0 \rightarrow F = 0.9$ If $\lvert\alpha_W\rvert > 40.0 \rightarrow F = 0.9 + 0.15\ (\lvert\alpha_W\rvert - 40.0)$ $F_{max} = 4.0$
$M_\infty \geq 4.60$	If $\lvert\alpha_W\rvert \leq 35.0 \rightarrow F = 0.9$ If $\lvert\alpha_W\rvert > 35.0 \rightarrow F = 0.9 + 0.20\ (\lvert\alpha_W\rvert - 35.0)$ $F_{max} = 6.0$

TABLE 29. EMPIRICAL PARAMETER "F" USED IN WING-TAIL INTERFERENCE MODEL (Φ = 45 DEG)

MACH NUMBER	PARAMETER "F"
$M_\infty \le 1.2$	$F = 0.7$
$M_\infty = 1.5$	If $\lvert\alpha_W\rvert \le 20.0 \rightarrow F = 0.7$ If $\lvert\alpha_W\rvert > 20.0 \rightarrow F = 0.7 - 0.02\,(\lvert\alpha_W\rvert - 20.0)$ $F_{min} = 0.2$
$M_\infty = 2.0$	If $\lvert\alpha_W\rvert \le 20.0 \rightarrow F = 0.75$ If $\lvert\alpha_W\rvert > 20.0 \rightarrow F = 0.75 - 0.015\,(\lvert\alpha_W\rvert - 20.0)$ $F_{min} = 0.4$
$M_\infty = 2.3$	If $\lvert\alpha_W\rvert \le 30.0 \rightarrow F = 0.85$ If $\lvert\alpha_W\rvert > 30.0 \rightarrow F = 0.85 + 0.01\,(\lvert\alpha_W\rvert - 30.0)$ $F_{max} = 1.0$
$M_\infty = 2.87$	If $\lvert\alpha_W\rvert \le 40.0 \rightarrow F = 0.7$ If $\lvert\alpha_W\rvert > 40.0 \rightarrow F = 0.7 + 0.02\,(\lvert\alpha_W\rvert - 40.0)$ $F_{max} = 1.0$
$M_\infty = 3.95$	If $\lvert\alpha_W\rvert \le 25.0 \rightarrow F = 0.7$ If $\lvert\alpha_W\rvert > 25.0 \rightarrow F = 0.7 + 0.02\,(\lvert\alpha_W\rvert - 25.0)$ $F_{max} = 2.0$
$M_\infty \ge 4.0$	If $\lvert\alpha_W\rvert \le 30.0 \rightarrow F = 0.6$ If $\lvert\alpha_W\rvert > 30.0 \rightarrow F = 0.6 + 0.02\,(\lvert\alpha_W\rvert - 30.0)$ $F_{max} = 1.8$

In examining Tables 28 and 29, it is seen that the value of "F" is generally less than one for smaller values of $\lvert\alpha_W\rvert$. This implies the wing-tail interference prediction from linear theory and SBT are too high. However, as Mach number and $\lvert\alpha_W\rvert$ increase, the value of "F" increases for both the Φ = 0 and 45 deg roll positions. It is postulated that this increase in "F" is due to a combination of internal shock interactions having a larger impact on the second term of Equation (21) than linear theory predicts.

2.3.6 Axial Force Coefficient Due to Control Deflection

The axial force coefficient due to deflection for the AP98[59] is estimated by

$$(C_A)_{\delta_W} = \left(C_{N_{W(B)}} \sin\delta_W\right) f(M, \delta_W) \tag{25}$$

$$(C_A)_{\delta_T} = \left(C_{N_{T(B)}} + C_{N_{T(V)}}\right) \sin\delta_T \; f(M, \alpha_T) \tag{26}$$

where f(M, α_W) and f(M, α_T) are 1.0 when α and δ are of the same sign but are defined empirically as having a value between 0 and 1.0 when α and δ are of opposite signs. Reference 56 gives the details of the values of f(M, α_W) or f(M, α_T) for both $\Phi = 0$ and 45 deg roll positions when α and δ are of opposite signs. The slightly lower revised values of C_{N_W} discussed in Section 2.3.2 and given in Reference 71, had an adverse impact of prediction of axial force coefficient at higher Mach number when α and δ were of the same sign. It is speculated that the AP98 had compensating errors that offset one another. That is, increased normal force when α and δ were of the same sign was compensated for by an f(M, α_W) of one, when actually this value of f(M, α_W) should be slightly greater than one. This higher value of f(M, α_W) is required due to the internal shock interactions that become stronger as Mach number and AOA increases.

As a result of the decrease in accuracy of axial force when α and δ are the same sign, a new table of f(M, α_W) was generated to partially account for the internal shock interaction physical phenomena. This table of data for f(M, α_W) when α and δ are of the same sign is given in Table 30. For values of Mach number or α_W in between values shown in Table 30, linear interpolation is used.

2.4 IMPROVED PITCH DAMPING WITH EMPHASIS ON CONFIGURATIONS WITH FLARES

The next area that new technology has been added to the AP98, which will be a part of the AP02, is improvement in aerodynamics of flared configurations, particularly the pitch damping derivative. Figure 21 illustrates the typical geometrical parameters associated with a flare. The two most important parameters are the flare length and angle (the flare angle can also be expressed in terms of the flare base to forward or reference diameter).

The problem of inaccurate aerodynamic predictions for flared configurations from the APC first came to the author's attention a couple of years ago in the form of pitch damping moment coefficient predictions for a flared projectile concept at a AIAA meeting. The increased interest in the use of flares for stability in recent years, particularly for higher Mach numbers (see References 90-92 for example), has also led the author to feel that improvements in the aerodynamic predictions of flared projectiles were needed.

As a result of the increased interest in flared projectiles for higher Mach number applications, the authors decided to take another look at the APC to determine its weak areas with respect to flared shaped projectiles. Several problem areas were identified. First of all, for the static aerodynamics, no particular attention was given for flared projectiles for $M_\infty < 1.2$. For $M_\infty \geq 1.2$, low AOA aerodynamics are computed by theoretical methods such as Second-Order-VanDyke (SOVD) or Second-Order-Shock-Expansion-Theory (SOSET) and reasonable estimates of static aerodynamics (C_A, C_N, x_{CP}) can be obtained from the APC. For $M_\infty < 1.2$, the capability to compute static aerodynamics needs to be incorporated into the code.

TABLE 30. VALUES OF EMPIRICAL PARAMETER f(M, α_W) WHEN α, δ ARE OF SAME SIGN

		Φ = 0 DEG	Φ = 45 DEG
M_∞	α_W	f(M, α_W)	f(M, α_W)
≤1.5	0-90 DEG	1.0	1.0
2.87	0-40 DEG	1.0	1.0
2.87	45	1.03	1.0
2.87	50	1.11	1.05
2.87	55	1.15	1.08
2.87	≥60	1.13	1.08
≥4.6	0-30 DEG	1.0	1.0
≥4.6	35	1.09	1.0
≥4.6	40	1.11	1.04
≥4.6	45	1.16	1.06
≥4.6	50	1.15	1.10
≥4.6	55	1.14	1.12
≥4.6	≥60 DEG	1.13	1.08

The second problem uncovered in the APC was for the dynamic derivative, $C_{M_q} + C_{M_{\dot{\alpha}}}$, or pitch damping moment coefficient. No capability exists at any Mach number in the APC for pitch damping moment of flared projectile shapes. In fact, based on recent CFD calculations of projectiles without a flare,[93,94] it was found that the pitch damping moment of configurations without flares needed improvement as well. Table 31 summarizes the problems in predicting aerodynamics of flared projectile shapes using the AP98.

TABLE 31. AP98 WEAK AREAS IN PREDICTING AERODYNAMICS OF FLARED CONFIGURATIONS

a) C_A, C_N, X_{CP} not available for $M_\infty < 1.2$ for flare
b) Body alone $C_{M_q} + C_{M_{\dot{\alpha}}}$ needs improvement for $M_\infty \geq 1.2$ (no flare)
c) No pitch damping contribution for flare in AP98 at any M_∞

Each of the three weak areas listed in Table 31 will be individually discussed in this section of the report. The discussion will be in terms of modifications that will be made to the AP98 to allow more accurate computations of aerodynamics of flared projectiles. These modifications will then be part of the next release of the APC which will be the AP02 in 2002. More details of the work described in this section can be found in Reference 75.

2.4.1 Static Aerodynamics of Flared Projectiles

The wave component of axial force for configurations with small flare angles ($\theta_f < 15$ deg) can be calculated approximately with the perturbation theory of Wu and Aoyoma[95] that was designed for boattails, except the angle is reversed in sign. There was a sign error in the AP98, but when this error was corrected, approximate estimates of wave drag for $M_\infty < 1.2$ could be computed from the Reference 95 method. For $M_\infty < 0.9$, the wave drag component is assumed to be zero. Base drag and skin-friction drag were already being computed within the accuracy desired using the AP98 so no changes in the methodology for these aerodynamic terms were made.

The normal force and pitching moment coefficients and center of pressure for the flares are not predicted at all for $M_\infty < 1.2$. Furthermore, numerical methods do not exist in the AP98 to allow calculations of C_N, C_M and x_{CP} for $M_\infty < 1.2$. Also, as will be discussed later in the pitch damping computations for flares, C_N, C_M and x_{CP} for a flare will be needed at all Mach numbers.

To compute $\left(C_{N_\alpha}\right)_f$ and $(x_{CP})_f$, one of several options are available. The first is to utilize the available values in the APC. Unfortunately, these values are only available for $M_\infty \geq 1.2$ where pressures are computed and integrated over the body surface. Also, the logic of the APC is such that this would require considerable changes to allow these calculations to be performed and brought forward into another subroutine. The second option would be to exercise the APC twice, once with a flare and once without and subtract the C_{N_α}'s and C_{M_α}'s to obtain the flare normal force coefficient derivative and its center of pressure. Again, this is not a very desirable alternative since the APC must be exercised twice to get a single number. A third option, which appears more attractive, is to exercise the APC code offline, compute values of $\left(C_{N_\alpha}\right)_f$ and $(x_{CP})_f$ for $M_\infty \geq 1.2$ and store these in a table lookup as a function of geometric and freestream parameters. For $M_\infty < 1.2$, SBT can be used to approximate values of $\left(C_{N_\alpha}\right)_f$ and $(x_{CP})_f$. The fourth and most attractive option is to use available cone tables[96] or approximate conical formulas to compute $\left(C_{N_\alpha}\right)_f$, use SBT to approximate the center of pressure of the flare and $\left(C_{N_\alpha}\right)_f$ for $M_\infty < 1.2$, and to include these parameters in a table lookup as a function of geometry and Mach number. This last option can be used since we are assuming the flare is a conical frustrum or can be approximated by a conical frustrum. The last option is the one that will be used in the AP98 upgrade as it has the advantage of being at least as accurate as current computations in the APC due to use of an exact cone solution from Reference 96. Also, this approach offers the opportunity to obtain results in a straightforward and direct way from the APC as opposed to more costly approaches of logic change in the APC or cycling through the APC twice to obtain results for the flare alone.

The C_{N_α} results for the total cone of Reference 96 must be corrected to include only the frustrum portion of the cone and also put in the appropriate reference area format. Referring to Figure 21, the percent of conical shape that is a flare is:

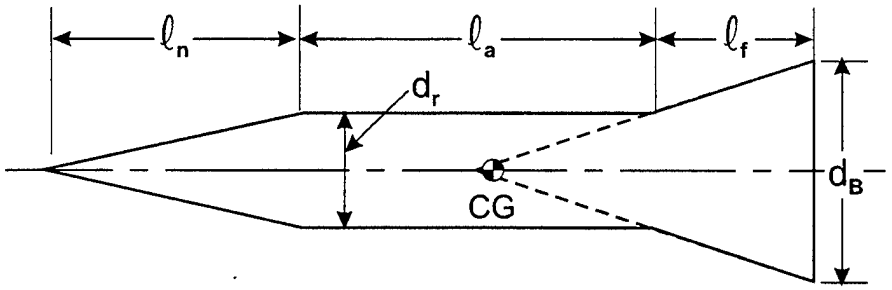

A. Cone-Cylinder-Flare Configuration

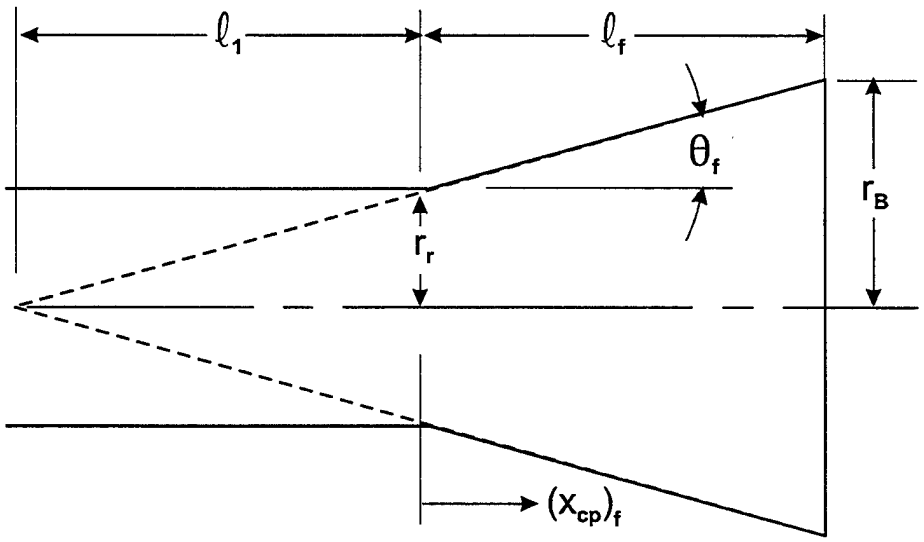

B. Expanded View of Flare

FIGURE 21. TYPICAL FLARE CONFIGURATION WITH THE SIGNIFICANT GEOMETRICAL PARAMETERS

$$\frac{A_f}{A_C} = \frac{\pi\left[r_B^2 - r_r^2\right]}{\pi r_B^2} = 1 - \left(\frac{r_r}{r_B}\right)^2 \tag{27}$$

Now the value of C_{N_α} obtained from Reference 96 is based on the cone base area. Hence, Equation (27) must be multiplied by A_B/A_r to place it in the same reference area as other C_{N_α} components for the total configuration of Figure 21. Thus, to relate the value of the C_{N_α} from Reference 96 for a cone of given angle at a given Mach number to that of a flare we have

$$\left(C_{N_\alpha}\right)_f = \left(C_{N_\alpha}\right)_C \left[1-\left(\frac{r_r}{r_B}\right)^2\right]\left(\frac{r_B}{r_r}\right)^2$$

or

$$\left(C_{N_\alpha}\right)_f = \left(C_{N_\alpha}\right)_C \left[\left(\frac{r_B}{r_r}\right)^2 - 1\right] \tag{28}$$

Equation (28) is valid at all Mach numbers and for all geometries. However, $\left(C_{N_\alpha}\right)_C$ is available from Reference 96 for conditions where the flow is supersonic and the shock wave is attached to the conical tip. For conditions where these two assumptions are not met, SBT will be assumed in conjunction with interpolation. SBT gives

$$\left(C_{N_\alpha}\right)_C = 2.0 \tag{29}$$

The SBT value of $\left(C_{N_\alpha}\right)_C$ will be assumed for $M_\infty \leq 0.8$. The value of $\left(C_{N_\alpha}\right)_C$ from Reference 96 can be used for low AOA calculations of most reasonable flares down to M_∞ of about 1.2. Linear interpolation between SBT and Reference 96 will be used for $0.8 < M_\infty < 1.2$.

In examining Equation (28), it is seen that the C_{N_α} for a flare can get quite large if the flare is long or if the flare is short but has a large flare angle. This is why use of a flare is quite popular at higher Mach numbers, where the C_{N_α} for a fin substantially decreases with Mach number increase.

The SBT center of pressure for a cone is the same as that from exact theory. The center of pressure is at 2/3 of the cone length. However, for a conical frustrum, the center of pressure in general will vary between 0.5 ℓ_f and 2/3 ℓ_f, depending on the flare angle. For flare angles approaching 0, the value of $(x_{CP})_f$ approaches 0.5 ℓ_f whereas for large flare angles, $(x_{CP})_f$ approaches 2/3 ℓ_f. Referring to Figure 21, the center of pressure of the flare using SBT can be shown to be[74]

$$\left(\bar{x}_{CP}\right)_f = \frac{2}{3}\left(\frac{1}{1-r_r/r_B}\right)\left[\frac{1-(r_r/r_B)^3}{1-(r_r/r_B)^2}\right] - \frac{r_r/r_B}{1-r_r/r_B} \tag{30}$$

Results of Equation (30) are computed and plotted in Figure 22 as a function solely of the parameter r_r/r_B. As seen in the figure, when the body consists of a cone ($r_r = 0$), then the center of pressure is at 2/3 of the cone or flare length (which are one and the same). On the other hand, when the flare angle goes to zero so that $r_r/r_B = 1.0$, the center of pressure goes to $x_{CP}/\ell_f = 0.5$. For most typical flare lengths and angles, x_{CP}/ℓ_f will vary from about 0.54 to 0.60.

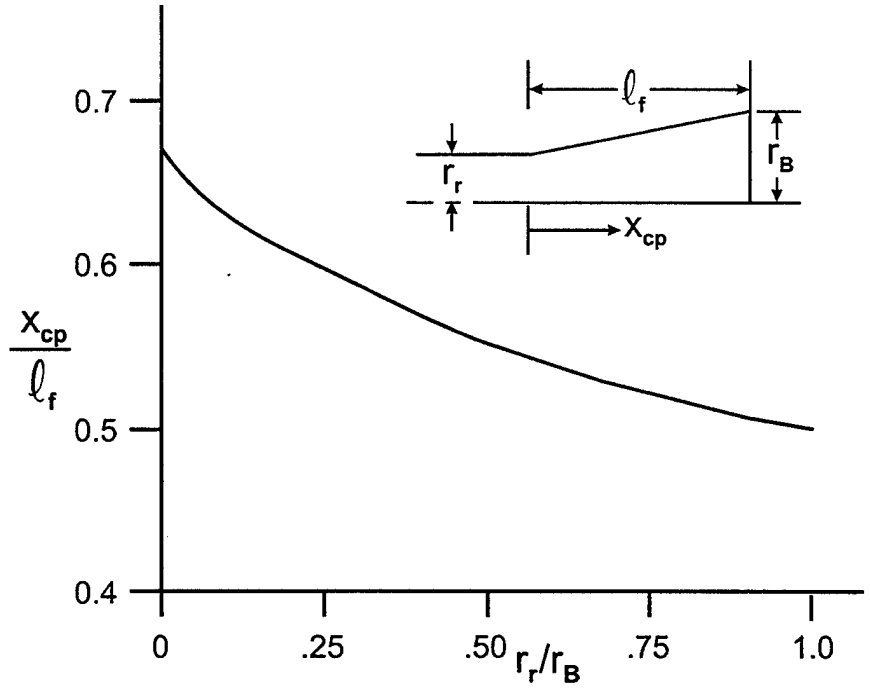

FIGURE 22. SLENDER BODY THEORY CENTER OF PRESSURE OF FLARE

Equation (30) results can be changed to body diameters by multiplying Equation (30) by ℓ_f/d to obtain:

$$\left(\frac{x_{CP}}{\ell_f}\right)\left(\frac{\ell_f}{d}\right)=\frac{(x_{CP})_f}{d} \tag{31}$$

The combination of Equations (28)-(31) give the C_{N_α} and x_{CP} for flares at all Mach numbers. C_N is simply

$$C_{N_f}=(C_{N_\alpha})_f\,\alpha \tag{32}$$

for small angles of attack. Since most flare configurations are designed to fly at small angles of attack, Equations (31) and (32) determine two of the desired static aerodynamic terms for a flare. The pitching moment coefficient of the flare about some reference location is then

$$C_{M_f}=-\left(\frac{x_{CP}-x_{CG}}{d}\right)C_{N_f} \tag{33}$$

2.4.2 Body Alone Pitch Damping Moment

The body alone dynamic derivatives are all computed based on an empirical model developed by Whyte,[97] called "Spinner." The version that is incorporated into the AP98 is basically the same version as initially included in the APC series in 1977. The technology of Reference 97 was based on curve fits of data using standard spin stabilized rounds. The curve fits have key parameters of length, boattail length, and Mach number for the dynamic derivative predictions. Magnus force and moments are also estimated at both 1 and 5 deg AOA to incorporate some nonlinearity due to AOA in the Magnus moment. The data bases upon which the empirical curve fits were based were primarily limited to about 5.5 calibers and Mach numbers less than 5.0 (newer versions of Spinner may now be available which remove these limits). However, length was considered in a linear sense for roll damping moment and one of the data bases had length as a parameter for pitch damping moments as well.

Since the late 1960's and early 1970's, the Army Research Laboratory (ARL) at Aberdeen, Maryland has developed a very good CFD capability to compute both static and dynamic derivatives of projectiles, with and without flares. References 90, 91, 93, and 94 are some of the reports generated by ARL using CFD. As a result of these many CFD computations, and comparison to data, one can now fine tune the older "Spinner" Model[97] to be more representative of a broader class of configurations.

In comparing the AP98 (in essence the "Spinner" model) predictions of pitch damping moment to ballistic range data and CFD predictions of References 90, 91, 93, and 94, it became apparent that a problem existed. The Spinner results appeared to be reasonable for $M_\infty \leq 1.2$ but overpredicted $C_{M_q} + C_{M_{\dot{\alpha}}}$ as Mach number increased. The higher the Mach number, the worse the predictions became. On the other hand, the errors followed a fairly smooth pattern, allowing a correction to be derived based on CFD results from References 90, 91, 93, and 94.

The modified pitch damping moment coefficient for bodies without a flare present is therefore

$$C_{M_q} + C_{M_{\dot{\alpha}}} = \left(C_{M_q} + C_{M_{\dot{\alpha}}}\right)_S F_1 \tag{34}$$

where $\left(C_{M_q} + C_{M_{\dot{\alpha}}}\right)_S$ is the value obtained from the AP98[59] which basically uses Reference 97. F_1 is an empirical decay factor for Mach number derived using the AP98 and References 90, 91, 93, and 94. Here, F_1 is a function of Mach number and total length of the projectile and is defined by the following model.

a) $\underline{\ell/d \leq 5.0}$

$$F_1 = 1.0 \qquad ; M_\infty \leq 1.2$$

$$F_1 = 0.0043\,M_\infty^2 - 0.151\,M_\infty + 1.175; \qquad (35)$$

$$1.2 < M_\infty \leq 5.0$$

$$F_1 = 0.53 \qquad ; M_\infty > 5.0$$

b) $\underline{\ell/d = 8}$

$$F_1 = 1.0 \qquad ; M_\infty \leq 2.0$$

$$F_1 = 0.0031\,M_\infty^2 - 0.0884\,M + 1.164; \qquad (36)$$

$$2.0 < M_\infty \leq 5.0$$

$$F_1 = 0.8 \qquad ; M_\infty > 5.0$$

c) $\underline{5 < \ell/d < 8}$

$$F_1 = F_1\,(\ell/d = 5) - \left(\frac{\ell/d - 5}{3}\right)\left[F_1\,(\ell/d = 5) - F_1\,(\ell/d = 8)\right] \qquad (37)$$

d) $\underline{\ell/d \geq 12}$

$$F_1 = 1.0 \qquad ; M_\infty \leq 2.0$$

$$F_1 = 0.0011\,M_\infty^2 - 0.111\,M_\infty + 1.178; \qquad (38)$$

$$2 < M_\infty \leq 5.0$$

$$F_1 = 0.9 \qquad ; M_\infty > 5.0$$

e) $\underline{8 < \ell/d < 12}$

$$F_1 = F_1\,(\ell/d = 8) - \left(\frac{\ell/d - 8}{4}\right)\left[F_1\,(\ell/d = 8) - F_1\,(\ell/d = 12)\right] \qquad (39)$$

2.4.3 Pitch Damping Moment of Bodies With Flares

A typical body configuration with a flare present is shown in Figure 21. As already mentioned, the AP98 code does not calculate a value of additional pitch damping due to the presence of a flare. The approximate method used here to represent the flare is basically to use the Reference 98 approach where

$$\left(C_{M_q} + C_{M_{\dot{\alpha}}}\right)_f = -2\left(C_{N_\alpha}\right)_f \left(\frac{x_{CP} - x_{CG}}{d}\right)_f^2 \tag{40}$$

Equation (40) was used in Reference 98 to approximate the pitch damping moment coefficient of a wing, but here the flare replaces the wing planform area. $\left(C_{N_\alpha}\right)_f$ of Equation (40) is defined by Equation (28). $(x_{CP})_f / d$ of Equation (40) is defined by Equations (30) and (31) and Figure 22. Finally, since Equation (28) already includes the approximate reference areas, Equation (40) is appropriate as it stands. Equation (40) only includes that portion of the flare area external to the cylindrical part of the body (see Equation (27)). This is because the body alone pitch damping moment discussed earlier already includes the cylindrical part of the afterbody.

2.5 IMPROVED POWER-ON BASE DRAG PREDICTION INCLUDING BASE BLEED EFFECTS

The approach used in the AP98 to predict the effect of the rocket engine burning on the base drag of weapons was integrated into the aeroprediction code in the late 1970's and has not been upgraded since that time. The method utilized was basically an extension of the Brazzel[99,66] technique. The Brazzel technique was for solid rockets, which had an exit Mach number of 1.0 or greater. It required knowledge of some of the details of the rocket such as chamber pressure, exit area to nozzle throat area, specific heat ratio of the exit gas, and location of the nozzle exit with respect to the base of the missile or projectile. This approach has been shown to give reasonable estimates of power-on base drag for a limited range of flight conditions when these parameters (P_C/P_∞, A_j/A_t, γ_j, x_j/d_r) are known.

While the approach by Brazzel has its strengths, it also has several weaknesses when approached from an aerodynamics viewpoint. First, it was limited to jet momentum flux ratios (RMF) of about 2.5 or less. Many of the world's rockets have values of this parameter much higher and therefore the method of Brazzel needs extending to higher values of RMF. This was done and documented in Reference 66. Another problem with the Brazzel technique from an aerodynamicist's viewpoint is the required knowledge of the engine parameters. These parameters are required in order to perform conceptual design tradeoffs of various rockets for total drag when the engine is burning. As a result of this desire for conceptual trade studies where some account of engine–on base drag is considered, other simplified procedures are needed for base drag prediction. This report will address two other options to calculate power–on base drag. Another limitation of the Brazzel method is its limitation to supersonic flow at the nozzle exit. While the exit supersonic flow requirement is not a severe limitation for most rocket

engines, it is a severe limitation for projectile configurations that use base bleed for base drag reduction. As a result of this shortcoming, a method developed by Danberg[100] for predicting base drag for small values of the bleed injection parameter (I) will be made more general. A final limitation of the Brazzel method is that it was derived based on freestream Mach number data of 1.5 and greater. Therefore, it needs to be extended to at least the transonic Mach number regime.

It is the purpose of this section of the report to develop the methodology to overcome the shortcomings of both the Brazzel and Danberg methods for predicting power-on base pressure coefficient. The modifications to the Brazzel[99,66] and Danberg[100] methods will be incorporated into the aeroprediction code for power-on base drag prediction and be a part of the next release to the public, which will be in 2002 (AP02). The power-on base drag modifications will also be incorporated into the personal computer interface for the AP02 so as to allow the various power-on options to be considered in a very user friendly mode.

2.5.1 Power-on Base Drag for $M_j \geq 1.0$

Since the power-on base drag prediction method of the aeroprediction code is based on an extension of the method of Brazzel, et al,[99,66] it is appropriate to briefly summarize Brazzel's method. Figure 23A shows the nomenclature that is used for the rocket engine parameters. The Brazzel and Henderson method defines the base pressure as

$$\frac{P_B}{P_\infty} = 0.047(5 - M_\infty)\left[2(x_j/d_B) + (x_j/d_B)^2\right] + \left[\frac{T_j}{T_j^*}\right]\left[0.19 + 1.28\left(\frac{RMF}{1+RMF}\right)\right]\left[\frac{3.5}{1+2.5(d_B/d_r)^2}\right] \tag{41}$$

where $RMF = \dfrac{\gamma_j P_j d_j^2 M_j^2}{\gamma_\infty P_\infty d_r^2 M_\infty^2}$ (42)

$$\frac{T_j}{T_j^*} = \frac{\frac{\gamma_j + 1}{2}}{1 + \frac{\gamma_j - 1}{2} M_j^2} \tag{43}$$

x_j/d_B is the distance the nozzle exit extends past the base in calibers and RMF is the jet momentum flux ratio.

Brazzel's method was built around two fundamental assumptions that he was able to develop based on analysis of experimental data for jet exit Mach numbers 1.0 to 3.8. The first

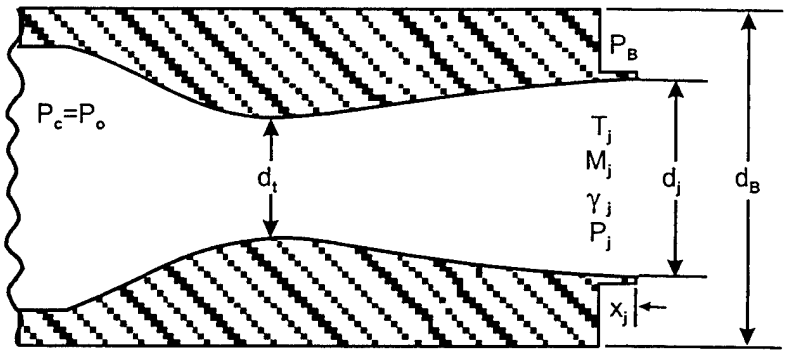

A. Rocket Engine Parameters

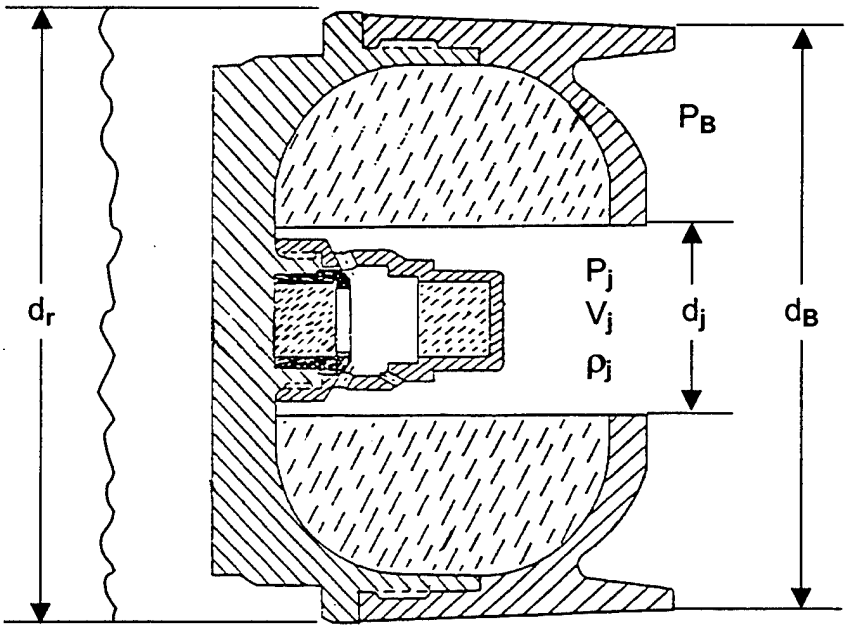

B. A Typical Projectile Base Bleed Configuration[3]

FIGURE 23. NOMENCLATURE FOR POWER-ON CONDITIONS FOR ROCKETS AND BASE BLEED CONCEPTS

assumption is that freestream Mach number and nozzle diameter are accounted for by the momentum flux term defined by Equation (42). The second assumption was that jet exit Mach number could be described by the ratio of the jet static temperature for a given jet Mach number to that at a jet exit Mach number of 1.0. This relationship is defined by Equation (43).

In reality, the Brazzel method was geared primarily to accounting for base drag for sustainer rocket motors that typically have values of thrust coefficient of 0.2 to about 3.0 and fly supersonically. However, as the mass flow ratio or thrust coefficient get large or the freestream Mach number is transonic, the Brazzel method produces increasingly erroneous results for many cases. This behavior of Equation (41) is illustrated in Figure 24, which correlates base pressure predictions on a cylindrical afterbody for a jet exit Mach number of one $\left(T_j / T_j^* = 1.0\right)$. Note

that the Brazzel correlation fits the data taken from References 99, 101, 102, and 103 quite well for RMF values up to almost 0.5. Above values of 0.5, the data of Figure 24 is more scattered, particularly for RMF values above about 1.5.

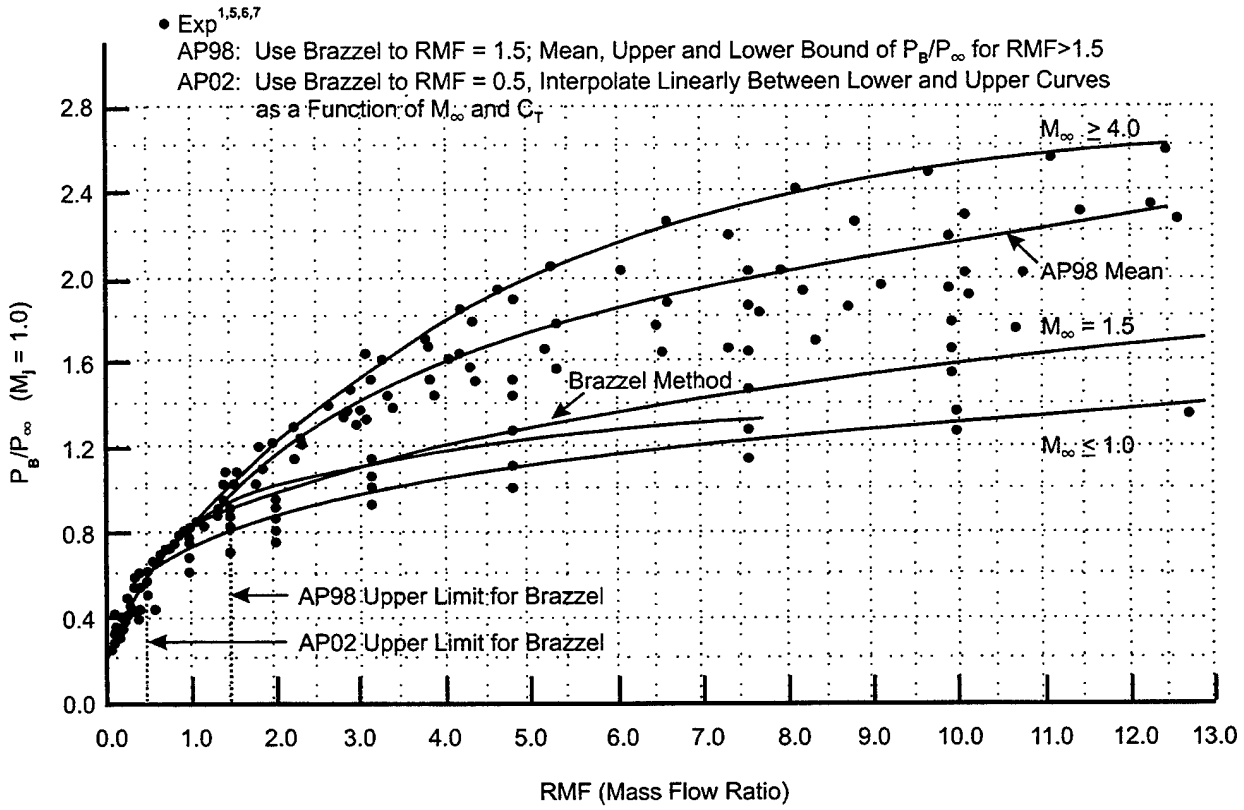

FIGURE 24. CORRELATION OF AVERAGE BASE PRESSURE FOR SOME CONDITIONS AT EXIT

Brazzel indicated he had little data for high thrust ratios to use in the method development. The method of References 66 and 27, and included in the AP98,[59] uses the method of Brazzel for RMF values up to 1.5 and then the empirical curve fits that bracket most of the data of Figure 24 in terms of upper and lower values along with a mean value. This mean value is shown in Figure 24. However, in examining the data of Figure 24 more closely, it was found that for higher values of C_T, P_B/P_∞ was primarily dependent on freestream Mach number with little dependence on jet exit Mach number or jet exit diameter. Apparently, for high thrust levels such as would occur on a high impulse sustainer or a booster rocket motor, one of the main correlation parameters for P_B/P_∞ is M_∞. Thus, the AP02 will modify the current methodology for power-on base drag prediction of Reference 27 for RMF values greater than 0.5 so that P_B/P_∞ will be correlated with freestream Mach number, as opposed to giving the user an upper, lower, and mean value of P_B/P_∞ for all freestream Mach numbers. The discussion of power-on base drag prediction will be broken down by thrust or momentum flux ratio level.

We will first of all consider the lower values of RMF or C_T which are more representative of a lower thrust sustainer engine. For these values of RMF, we will use the

Brazzel method given by Equations (41) through (43). To utilize the Brazzel method, we must obtain values of RMF either through direct input or through calculation based on known engine quantities. The parameters that are normally known in a rocket engine are the chamber pressure, P_C, the nozzle throat and exit area and the ratio of specific heats for the gas of interest. We can use this information to determine the quantities M_j and RMF through the following process. We will first of all assume isentropic flow throughout the nozzle. This means there are no strong shock waves in the nozzle, only weak expansion or compression waves. This means that the chamber pressure, which is the total pressure, since velocity is zero in the chamber, is constant throughout the nozzle. Then, using this information, along with isentropic flow relations for flow through a nozzle, the jet exit Mach number and pressure relationships can be defined. The reader is referred to Reference 76 for the details of this process. Reference 76 documents the methods discussed in this report in more detail and also gives more example cases as well.

Now knowing P_j/P_∞, A_j/A_{ref}, M_j/M_∞ and γ_j/γ_∞, we can compute the jet momentum flux ratio from Equation (42). Finally, knowing x_j/x_B as a defined physical parameter and T_j/T_j^* from Equation (43), the base pressure ratio for power on can be computed from Equation (41).

The base pressure coefficient is defined by

$$C_{P_B} = \frac{2}{\gamma M_\infty^2}\left[\frac{P_B}{P_\infty} - 1\right] \tag{44}$$

where P_B/P_∞ comes from Equation (41). Finally, the base drag coefficient for power on conditions is

$$C_{A_B} = -C_{P_B}\left[\left(\frac{d_B}{d_r}\right)^2 - \left(\frac{d_j}{d_r}\right)^2\right] \tag{45}$$

Notice that Equation (45) subtracts out that part of the base area attributed to the jet exit diameter, where the pressure is P_j, not P_b. P_j is used in the calculation of jet thrust coefficient through the relationship

$$C_T = 2\,RMF + \left(\frac{d_j}{d_r}\right)^2 \frac{2}{\gamma_\infty M_\infty^2}\left(\frac{P_j}{P_\infty} - 1\right) \tag{46}$$

RMF and P_j/P_∞ of Equation (46) come from Equation (42) and the isentropic flow relationships discussed earlier and defined in more detail in Reference 76. The total axial force coefficient is then

$$C_A = C_{A_W} + C_{A_f} + C_{A_B} - C_T \tag{47}$$

As mentioned earlier, Equation (41) is limited to low to moderate values of jet momentum flux ratio (RMF ≤ 0.5). Many rockets, including some in the Navy, have values of RMF much higher than 0.5. As a result, the method of Brazzel, et al,[99] was extended to higher values of RMF using data later taken by Craft and Brazzel,[101] Henderson,[102] and Deep, et al.[103]

The method that will be part of the AP02 will have several changes from that in the AP98. First, the method of Brazzel will be used up to values of RMF of 0.5 versus 1.5 as currently stated in the AP98. Next, for values of RMF > 0.5, a more robust empirical relationship was derived for P_b/P_∞ than Equation (41). This empirical relationship was based on Equation (41), but extended Equation (41) to more appropriately fit the data of Figure 24 and other experimental cases for high values of thrust. The method is defined by Equation (48).

$$P_b/P_\infty = \left[\frac{T_j}{T_j^*}\right]^N \left[C_1(C_T, M_\infty) + C_2(M_\infty)\left(\frac{RMF}{1+RMF}\right)\right] f(d_B/d_r) + 0.047(5-M_\infty)\left[2(x_j/d_B) + (x_j/d_B)^2\right] \quad (48A)$$

where

$$N = \frac{12-C_T}{11.0}, \quad 1.0 \le C_T < 12$$
$$= 0, \quad C_T \ge 12$$
$$= 1, \quad C_T < 1.0$$

C_1 (C_T, M_∞) and C_2 (M_∞) of Equation (48A) are found from Table 32 by linearly interpolating based on a given value of C_T and M_∞. Also, for Mach numbers below about 1.5, it was found that T_j/T_j^* should have limiting lower values. This limiting lower value is defined by

$$(T_j/T_j^*)_{min} = 0.7 - (M_\infty - 1.2)\frac{(0.7 - T_j/T_j^*)}{0.3} \quad \text{for } 1.2 \le M_\infty < 1.5$$
$$(T_j/T_j^*)_{min} = 0.7 \text{ for } M_\infty < 1.2 \quad (48B)$$

For values of Mach number above 1.5, T_j/T_j^* retains the value computed from Equation (43). The boattail term $f(d_B/d_r)$ of Equation (48A) was also found to be dependent on thrust coefficient. For low to moderate values of C_T on a boattailed configuration, $f(d_B/d_r)$ follows the form of Equation (41). That is

$$f(d_B/d_r)=\frac{3.5}{1+2.5(d_B/d_r)^2};C_T\le 6.0 \tag{48C}$$

For higher values of C_T, Equation (48C) is replaced by

$$f(d_B/d_r)=1+\left(\frac{12-C_T}{6}\right)\left[\frac{3.5}{1+2.5(d_B/d_r)^2}-1\right]$$

$$\text{for } 6\le C_T\le 12.0 \tag{48D}$$

$$f(d_B/d_r)=1 \text{ for } C_T>12.0$$

If the configuration has a flare, then $f(d_B/d_r)$ follows the form:

$$f(d_B/d_r)=\frac{3.5}{1+2.5(d_B/d_r)^2} \qquad ;C_T\le 25$$

$$=1+\frac{75-C_T}{50}\left[\frac{3.5}{1+2.5(d_B/d_r)^2}-1\right];25<C_T\le 75 \tag{48E}$$

$$=1 \qquad ;C_T>75$$

Equations (48C) and (48D) indicate that for lower thrust levels, the base pressure is raised by a boattail, lowering base drag. However, for high values of C_T, the base pressure ratio is nearly independent of boattail and the base drag reduction comes purely from a base area reduction. Equation (48) reduces to the method of Brazzel at RMF $\le$ 0.5 but will give higher values than the Brazzel method for higher M_∞. At transonic Mach numbers, it can give values of P_b/P_∞ lower than the Brazzel method, due to the fact that Mach numbers as low as 0.9 have been included in Figure 24 and Table 32 whereas the Brazzel method was originally derived for Mach numbers of 1.5 and greater. Also note that for C_T values greater than 12, the exit Mach number dependence

TABLE 32. EMPIRICAL MODEL AND PARAMETERS TO DEFINE POWER ON BASE PRESSURE

$$P_B/P_\infty = \left(\frac{T_j}{T_j^*}\right)^N \left[C_1(C_T, M_\infty) + C_2(M_\infty)\left(\frac{RMF}{1+RMF}\right)\left(\frac{RMF}{1+RMF}\right)\right] f(d_B/d_r) + f(x_j/d)$$

where
$$N = \frac{12-C_T}{11} \quad , \quad 1.0 \le C_T < 12$$
$$= 0 \quad , \quad C_T \ge 12.0$$
$$= 1 \quad , \quad C_T < 1.0$$

and $f(x_j/d) = .047(5-M_\infty)\left[2(x_j/d_B) + (x_j/d_B)^2\right]$

$$\left(T_j/T_j^*\right)_{min} = 0.7 - (M_\infty - 1.2)\left(\frac{0.7 - T_j/T_j^*}{0.3}\right) \quad ; \quad 1.2 \le M_\infty \le 1.5$$
$$= 0.7 \quad ; \quad M_\infty < 1.2$$
$$\left(T_j/T_j^*\right)_{min} = \frac{\frac{\gamma_j+1}{2}}{1+\frac{\gamma_j-1}{2}M_j^2} \quad ; \quad M_\infty > 1.5$$

<u>If $d_B/d_r < 1.0$</u>

$$f(d_B/d_r) = \frac{3.5}{1+2.5(d_B/d_r)^2} \quad ; \quad C_T \le 6.0$$
$$= 1 + \frac{12-C_T}{6}\left[\frac{3.5}{1+2.5(d_B/d_r)^2} - 1\right] \quad ; \quad 6 \le C_T \le 12$$
$$= 1 \quad ; \quad C_T > 12.0$$

<u>If $d_B/d_r > 1.0$</u>

$$f(d_B/d_r) = \frac{3.5}{1+2.5(d_B/d_r)^2} \quad ; \quad C_T \le 25.0$$
$$= 1 + \frac{75-C_T}{50}\left[\frac{3.5}{1+2.5(d_B/d_r)^2} - 1\right] \quad ; \quad 25 \le C_T \le 75$$
$$= 1 \quad ; \quad C_T > 75$$

TABLE 32. EMPIRICAL MODEL AND PARAMETERS TO DEFINE POWER ON BASE PRESSURE (CONTINUED)

M_∞	C_1 (C_T, M_∞)					C_2 (M_∞, C_T)	
	C_T					C_T	
	≤1.0	2.0	20	40	≥70	≤1.0	≥2.0
≤0.9	0.19	0.16	-0.06	0.02	0.0	1.24	1.24
1.0	0.19	-0.085	-0.06	0.02	0.0	1.28	1.37
1.25	0.19	-0.085	-0.01	0.02	0.0	1.28	1.47
1.65	0.19	-0.175	-0.06	0.04	0.0	1.28	1.70
2.0	0.19	-0.30	-0.20	0.02	0.0	1.28	1.90
2.5	0.19	-0.45	-0.23	0.01	0.0	1.28	2.30
3.0	0.19	-0.55	-0.22	-0.03	0.0	1.28	2.50
≥4.0	0.19	-0.65	-0.10	-0.04	0.0	1.28	2.7

of Equation (48) goes away. While Equation (48) is believed to be an improvement over the AP98 methodology[59] and the Brazzel technique,[99,66] it still lacks complete robustness in terms of nozzle exit geometry.

Another problem associated with the method outlined by Equations (41) – (48) and Figure 24 for computing power-on base drag is the fact that for many users of the aeroprediction code, information other than P_C may be available for a given rocket. Users would like the option for computing power-on base drag, given a value of thrust and either P_C/P_∞, P_j/P_∞, or M_j. Hence, for cases where thrust and P_C/P_∞ are known, the process to calculate P_b/P_∞ is the same as Equations (41) – (47), except Equation (48) is substituted for Equation (41). If thrust and P_j/P_∞ are given, then from Equation (46),

$$RMF = \frac{1}{2}\left[C_T - \left(\frac{d_j}{d_r}\right)^2 \frac{2}{\gamma_\infty M_\infty^2}\left(\frac{P_j}{P_\infty} - 1\right)\right] \tag{49A}$$

Then utilizing Equation (42)

$$M_j = \sqrt{\frac{RMF\,\gamma_\infty\,P_\infty\,d_r^2\,M_\infty^2}{\gamma_j\,P_j\,d_j^2}} \tag{49B}$$

Likewise, if thrust and M_j are known, then utilizing Equations (42), (46), and (47) we obtain

$$\frac{P_j}{P_\infty} = \frac{C_T + \frac{2}{\gamma_\infty M_\infty^2}\left(\frac{d_j}{d_r}\right)^2}{\frac{2}{\gamma_\infty M_\infty^2}\left(\frac{d_j}{d_r}\right)^2 \left[1+\gamma_j M_j^2\right]} \tag{50A}$$

RMF can then be computed from Equation (42).

Finally, if thrust and P_C/P_∞ are given, then utilizing Equation (50A) and isentropic flow relations, we obtain:

$$\frac{P_C}{P_\infty} = \frac{\left[C_T + \frac{2}{\gamma_\infty M_\infty^2}\left(\frac{d_j}{d_r}\right)^2\right]\left[1+\frac{\gamma_j - 1}{2} M_j^2\right]^{\frac{\gamma_j}{\gamma_j - 1}}}{\frac{2}{\gamma_\infty M_\infty^2}\left(\frac{d_j}{d_r}\right)^2 \left[\gamma_j M_j^2 + 1\right]} \tag{50B}$$

All terms in Equation (50B) are known except M_j. M_j can be found by a numerical iterative solution of Equation (50B).

Of course, C_T is defined by

$$C_T = \frac{2T}{\gamma_\infty P_\infty M_\infty^2 A_{ref}} \tag{51}$$

C_{P_B}, C_{A_B}, and C_A are then obtained through use of Equations (44), (45), and (47), respectively.

A third alternative for rocket engine effects on base drag and total weapon performance is where you know nothing about the rocket engine, except you know you want to parametrically trade off power-on base drag as a function of weapon performance. For this option, we define

$$C_{A_B} = -K\left(C_{A_B}\right)_{\text{power off}} \tag{52}$$

where K varies from −1.5 to 2.5. While it is true this alternative of base drag that allows a variation in C_{A_B} from 1.5 to $-2.5\,C_{A_B}$ is just an approximation based on no real rocket engine, the range of values are reasonable boundaries of what one should expect for power-on effects on base drag.

2.5.2 Base Bleed

Base bleed is an alternative considered for use, primarily in unguided projectiles, to decrease base drag. The concept works on the basis of burning a small amount of propellant in the base of a projectile. This burning generates an exhaust gas which is typically subsonic and incompressible and raises the temperature and pressure in the base area, thus lowering the base drag. Figure 23B is an example of a base bleed configuration taken from Reference 100. There have been numerous references in the literature over the past 40 years or so that address the base bleed problem. Some of the more notable references are discussed in Reference 100. However, as noted by Danberg[100], many of these references investigated the effects of base bleed or base pressure in wind tunnel tests where fairly high values of the non-dimensional injection parameter were used. This parameter is defined by

$$I = \frac{\dot{m}_j}{\rho_\infty V_\infty A_{ref}} \tag{53}$$

and is the ratio of the mass flow out of the bleed exit to that in a stream tube of area equal to the cross sectional area of the body. Danberg[100] noted that many tests were for values of I = .01 to .04 for cold air whereas the practical case for projectiles is I ≅ .001 to .005 with hot gas. These low values of I for projectiles are due to the fact that only so much propellant can be carried in the projectile cavity (see Figure 23B), and if a high value of I is used, the time over which the base drag reduction occurs will be very short. A slower burn, lower velocity exhaust gas, and hence lower value of I is thus more practical, even though the optimum value of I is about .01 to .03 for minimum base drag based on the cold gas tests of References 104 and 105.

Assuming values of I of .001 to .005 allows some simplifications in the base pressure estimation process. This is because for values of $I \le 0.005$, the base pressure is approximately a linear variation with I. This linearity of base pressure for low values of I is shown by References 105, 106, and 107.

Danberg[99] used the conclusion of near linearity of P_b/P_∞ as a function of I for $I < 0.005$ to derive a semiempirical relationship to predict base pressure. Since the purpose of including base bleed in the APC is to allow application primarily to unguided projectiles and since the range of practical interest of base bleed for projectiles is fairly low, a slightly modified method of Danberg will be adopted for use in the APC. Danberg's method defines the base pressure as

$$\frac{P_B}{P_\infty} = \left(\frac{P_B}{P_\infty}\right)_{I=0} + \frac{\sigma I}{1+\beta\sigma I} \tag{54A}$$

$$\text{where } \sigma = \frac{d(P_b/P_\infty)}{dI} = \left[-5.395 + 0.0172T_j\right]M_\infty + \left[4.610 - 0.0146T_j\right]M_\infty^2 + \left[-0.566 + 0.00446T_j\right]M_\infty^3 \tag{54B}$$

and

$$\beta = 15.1 - 46.3\left(M_\infty - 0.71\right) \tag{54C}$$

T_j of Equation (54B) must be in degrees Rankine. Also, if β is less than 2.6, it should be set to 2.6 according to Danberg. Also, an upper limit of P_B/P_∞ of 1.0 will be included in the modified Danberg theory. Notice that Equation (54B) has some nonlinearity brought into the method through the second term. Danberg used a combination of computational fluid dynamics calculations for forebody wave and skin friction drag, in conjunction with total axial force from ballistic range data, to back out the base axial force term. Knowing C_{A_B}, the base pressure for no base bleed can be calculated from

$$\left(\frac{P_b}{P_\infty}\right)_{I=0} = \frac{\gamma_\infty M_\infty^2}{2} C_{P_B} + 1 \tag{55}$$

Equation (55) is then used as the first term of Equation (54A). The present approach differs from Danberg's approach in that $(P_b/P_\infty)_{I=0}$ will be defined based on the present method in the APC.[28] In this approach, a mean base pressure coefficient curve has been defined based on an extensive data base taken over many years. This mean base pressure coefficient curve is shown in Figure 25. Thus, for a given freestream Mach number, one determines a value of $(P_b/P_\infty)_{I=0}$ from Equation (55). Then for a given value of exit temperature, T_j, freestream Mach number and injection parameter I, the base pressure can be calculated directly from Equation (54A). Base pressure coefficient is then calculated from Equation (44).

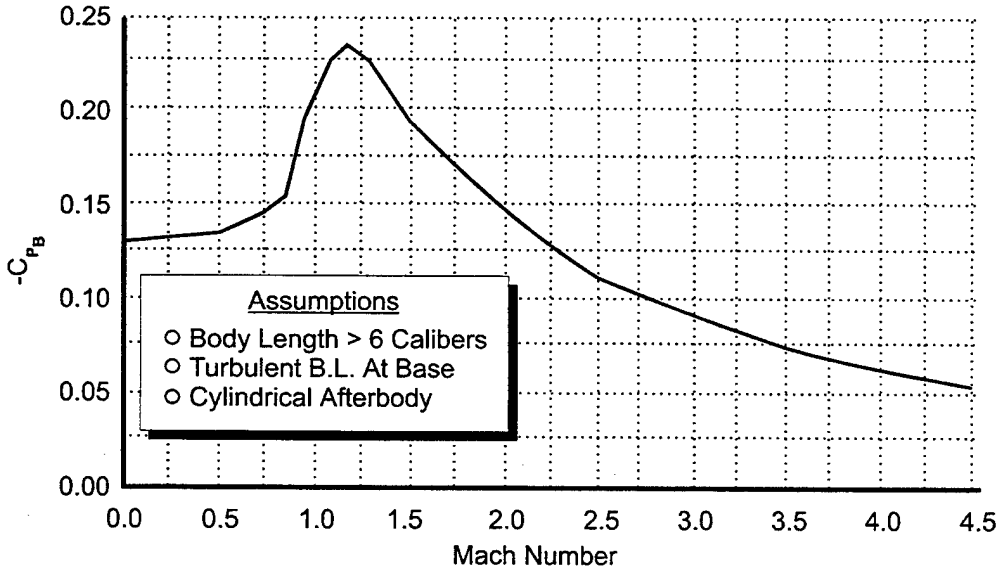

FIGURE 25. MEAN BODY-ALONE BASE PRESSURE COEFFICIENT USED IN AP98[59]

For the base bleed methodology, Danberg assumed that $P_j = P_B$ in his analysis. Hence, for base bleed, we do not subtract the area of the exit from the axial force calculations as we did for rocket motors (see Equation (45)). The base axial force coefficient for base bleed conditions is thus

$$C_{A_B} = -C_{P_B}\left(\frac{d_B}{d_r}\right)^2\left(\frac{d_B}{d_r}\right)^i \quad \begin{matrix} ; i = 0 \text{ for flare} \\ ; i = 1 \text{ for boattail} \end{matrix} \tag{56}$$

To summarize the new methodology which will be incorporated into the 2002 version of the APC, we will use a slightly modified method of Danberg where base pressure is defined by Equations (53)-(55) and Figure 25 and base axial force by Equation (56). Equation (54A) requires an input value of freestream Mach number, exit temperature in degrees Rankine, and a value of the Injection parameter I. For most accuracy, I should be less than 0.005, but values of I as high as 0.01 can be assumed, but with larger errors in the prediction process.

2.5.3 Modified Base Drag Prediction Model

The base drag prediction model currently in use in the AP98 is described in References 27 and 28. This model accounts approximately for the effects of Mach number, AOA, fin thickness, fin location, fin local AOA, power-on/off, and boattail or flare. The method described in this report will only affect the value of the power-on base pressure coefficient of the body-alone. It will be assumed that this new value of body-alone base pressure coefficient will replace that value currently used in the AP98. Then the effects of fins and AOA will be unchanged from that in Reference 27 and 28.

2.6 IMPROVED ZERO-LIFT AXIAL FORCE FOR NONCIRCULAR BODIES

The approach used in the AP98 for calculating drag of the nonaxisymmetric body configurations is based on the formation of an equivalent axisymmetric body of the same cross sectional area. A correction is made in the skin friction component where

$$\left(C_{A_f}\right)_{NC} = \left[\frac{(Cir)_{NC}}{2\pi r_{eq}}\right]\left(C_{A_f}\right)_{eq} \tag{57}$$

However, wave drag and base drag are based on the equivalent body which assumes an equal area distribution.

To check out the assumptions of drag of nonaxisymmetric bodies, Eglin Air Force Base conducted a series of ballistic range tests at the Aeroballistic Range Facility (ARF). These test results are documented in Reference 78. Table 33 gives the physical characteristics of the models tested and Figure 26 shows a schematic of the models. The models tested included 3 and

4 fin circular and elliptical configurations with a/b = 1.25 and 1.67, and 4 fin square and 3 fin triangular cases. As seen in Table 33, 11 to 18 shots of each configuration was tested, all with a constant cross sectional area and an equivalent diameter of 17 mm. All configurations were 137.5 mm in length with 37.4 mm tangent ogive nose and 100.1mm afterbody.

TABLE 33. MODEL PHYSICAL PROPERTIES

Configuration	Circular 4 Fin	Circular 3 Fin	0.8 Elliptical 4 Fin	0.6 Elliptical 4 Fin	Blended Elliptical 4 Fin	Square 4 Fin	Triangular 3 Fin
Diameter (d), mm	17	17	17	17	17	17	17
Length (L), mm	137.5	137.5	137.5	137.5	137.5	137.5	137.5
Mass, g	844	835	880	916	912	853	824
I_x, gram-cm^2	36.0	34.6	38.0	42.3	39.8	38.4	40.5
I_y, gram-cm^2	1270	1230	1355	1290	1410	1304	1230
C.G. location (X_{CG}), mm from nose	58.6	58.6	62.5	64.8	63.5	59.5	59.5
Number of ARF Trials	15	15	17	15	11	13	18

There were two reasons for testing 3 and 4 fin circular configurations as baselines. First, in principle, by subtracting the 3 fin from the 4 fin circular and multiplying the result by four, one could obtain the body-alone and fin-alone drag. In reality, it is difficult to do this with the accuracy desired due to not having multiple fit ARF data points at the same Mach numbers for 3 and 4 fin cases. The second reason for testing 3 and 4 fin circular was to compare to the elliptical, square, and triangular cases in a direct sense. The 4 fin circular can be compared directly with the 4 fin elliptical and square cross-sections and the 3 fin circular to the 3-fin triangular. Since the circular and elliptical, circular and square, and circular and triangular cross-sections all have the same number of fins present, the difference in the zero-lift axial force coefficient can be attributed to the body cross sectional shape. This difference can then be used to define an empirical factor to modify the AP02 circular body drag predictions for noncircular bodies.

The fins were all located flush with the base and had a semi-span of 9.91 mm with a root and tip chord of 20.07 mm. The fin thickness was a constant 0.508 mm and the leading and trailing edges were 100% truncated. Again, Figure 26 shows a schematic of the configurations tested along with the Eglin Air Force Base Test Objectives.

Before we develop an empirical correction to the axial force of nonaxisymmetric bodies, we will first compare the predictions of the AP02 to the ARF data for the various configurations. The first case considered is the 4 fin circular configuration case and comparison of the AP02 axial force calculations to the ARF multiple data point data is shown in Figure 27. The ARF multiple point data is where several trajectories are matched at a single Mach number. Three boundary layer options are considered in the AP02 calculations. These are a smooth model with

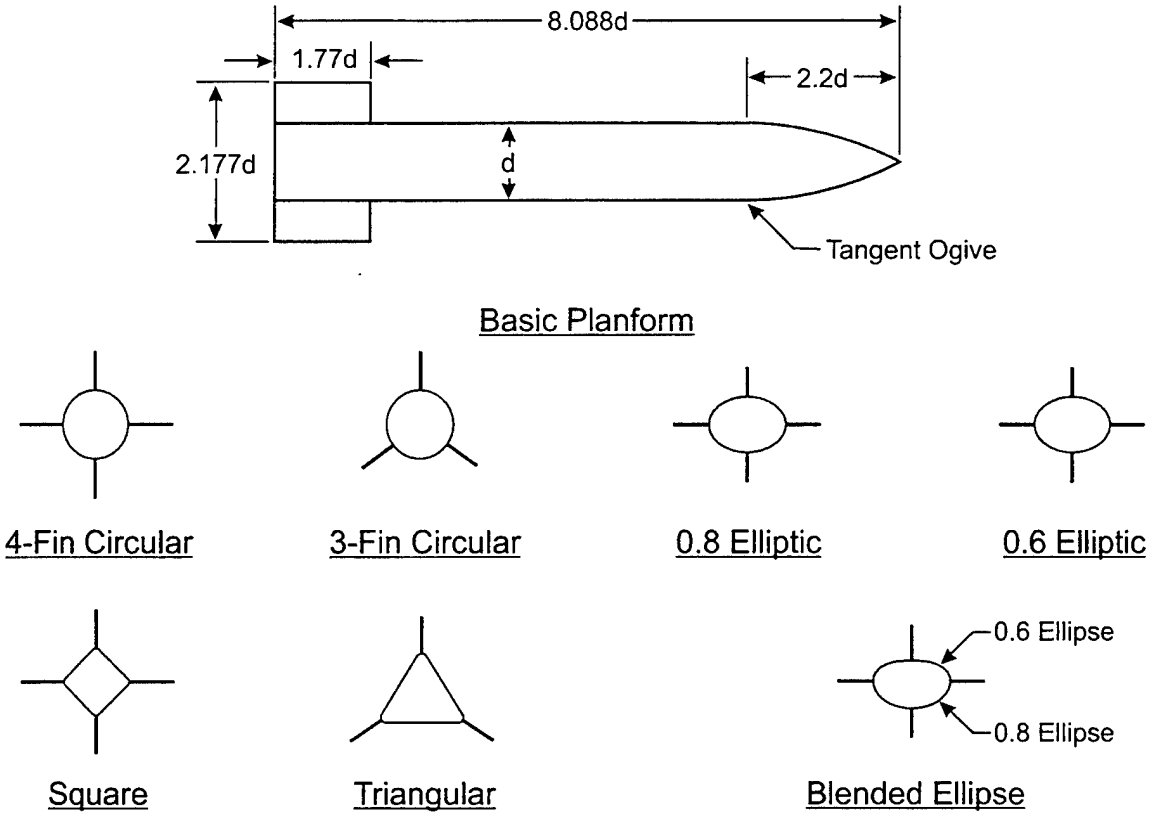

FIGURE 26. MODEL CROSS SECTION CONFIGURATIONS

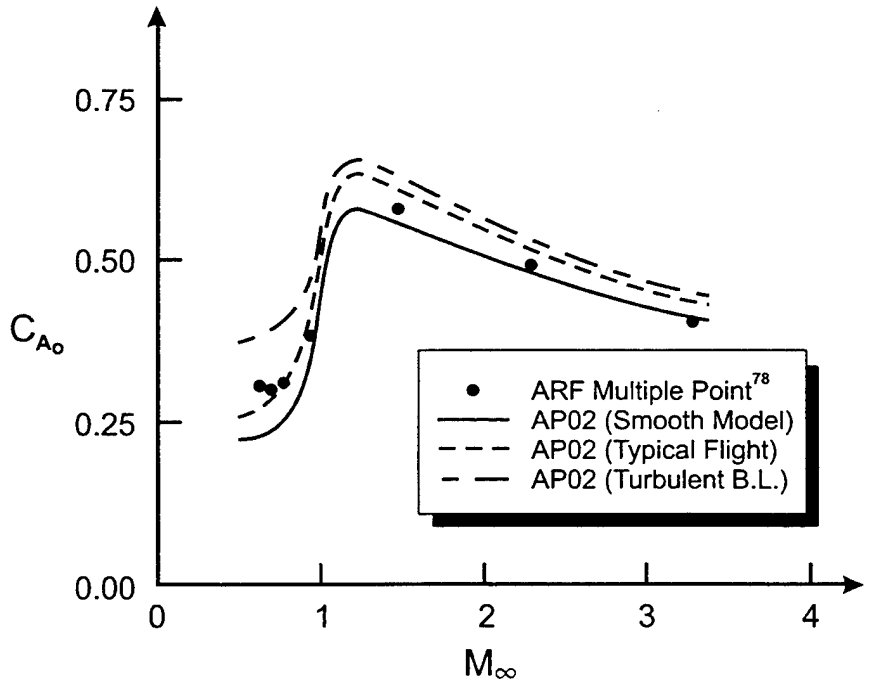

FIGURE 27. COMPARISON OF AP02 PREDICTIONS WITH VARIOUS BOUNDARY LAYER OPTIONS TO ARF DATA FOR 4 FIN CIRCULAR CONFIGURATION

no boundary layer trip at sea level conditions (assumes $R_{NT} = 4 \times 10^6$), typical flight configuration (assumes $R_{NT} = 1 \times 10^6$), and all turbulent flow. Since the models were polished surfaces, it is expected the smooth model option or the typical flight configuration would best represent the ARF data. As seen in Figure 27, the smooth model option is best for $M \geqq 1.5$. As Mach number decreases, the transitional Reynolds number also decreases based on comparison to data, and at transonic and subsonic Mach numbers, a transition Reynolds number (R_{NT}) of typical flight models is more realistic. At any rate, we will use the smooth model boundary layer option when comparing the AP02 to the nonaxisymmetric body axial force coefficients of the ARF data as a first approximation.

Figure 28 compares the smooth model boundary layer option of the AP02 to ARF circular, elliptical with a/b = 1.25, and elliptical with a/b = 1.67 results. As seen in the figure, experimental and theoretical results indicate for modest values of a/b, circular and elliptical results are nearly identical for axial force coefficient. Although the theory does have a slight variation of elliptical from circular, the differences are too small to see in the plot. These results are similar to those given by Jorgensen[108] as well. Hence, no change will be made to the AP02 elliptical axial force computations based on Figure 28. As already noted, it is difficult to model the drag over the entire Mach number range with a constant transition Reynolds number. Based on Figure 27 and 28, it is estimated that the transition Reynolds number varies between 0.5×10^6 at $M \leqq 0.5$ to 4.0×10^6 at $M \geqq 2.00$. Since Figure 28 calculations were done with $R_{NT} = 4.0 \times 10^6$, the higher Mach number comparison of AP02 and ARF data are much better than the lower Mach number comparisons.

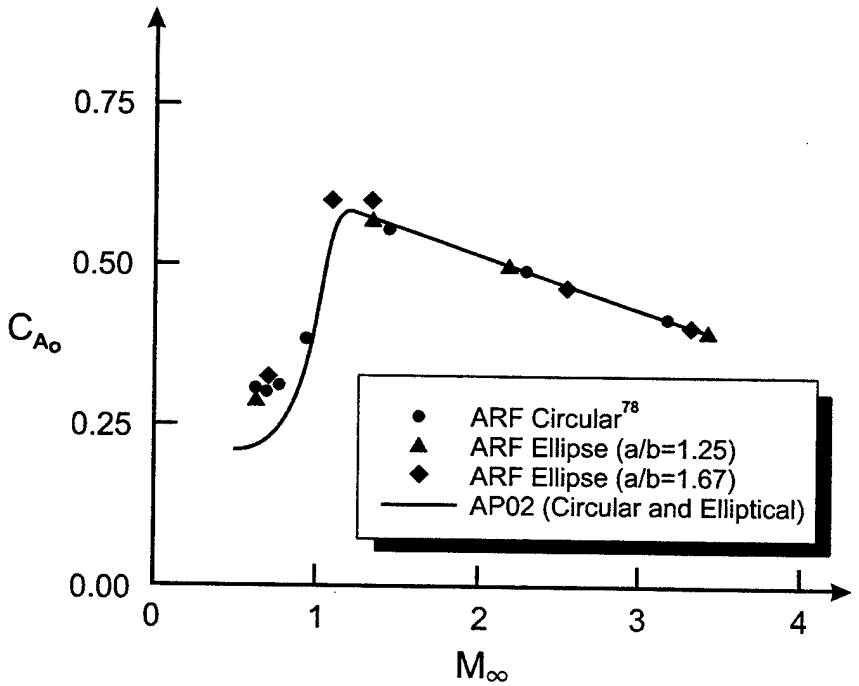

FIGURE 28. COMPARISON OF AP02 CALCULATIONS TO ARF DATA

Figure 29 compares the AP02 predictions for the axial force of the circular and square cross sections to the ARF data. The ARF data shows a consistently higher drag for the square than the circular cross section. An approximate correction to the AP02 will be made to the body wave drag and base drag terms to account for the ARF flight differences. The modified equation for the AP02 zero yaw axial force for the square is

$$(C_A)_{sq} = (C_{A_f})_C \left[\frac{(Cir)_{sq}}{2\pi r_{eq}}\right] + (C_{A_W} + C_{A_B})_{eq} [1 + .08(1 - 2k)] \tag{58}$$

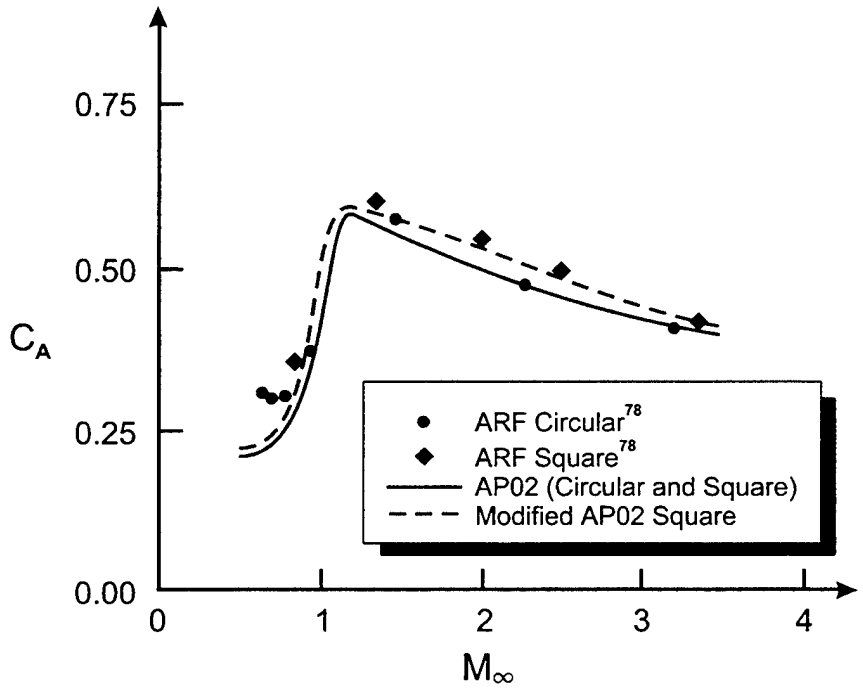

FIGURE 29. COMPARISON OF AP02 AND MODIFIED AP02 CALCULATIONS TO ARF DATA (CIRCULAR AND SQUARE SHAPES)

In Equation (58), $(Cir)_{sq}$ is the circumference of the square compared to the circumference of the equivalent circular cylinder and $k = r_n W_M$. k is a measure of the corner roundness. $k = 0.5$ means the square goes to a circle so Equation (58) resorts back to the circular cross section values. Also, Equation 58 applies to only the body-alone axial force components.

Figure 30 compares the AP02 predictions for the 3 fin circular and 3 fin triangular shapes to the ARF data for the same shapes. Again, the AP02 differences for the circular and triangular axial force predictions are approximately the same whereas the ARF data shows the triangular shape having a slightly higher axial force coefficient for moderate supersonic Mach numbers and lower. Since the data implies the triangular and circular shapes give about the same values of axial force coefficient at higher Mach numbers, only the base drag term will be modified in the modified AP02 computations. This is because base drag goes to zero as Mach number gets very high. The modified value of AP02 for the triangular shape of Figure 5 is computed based on

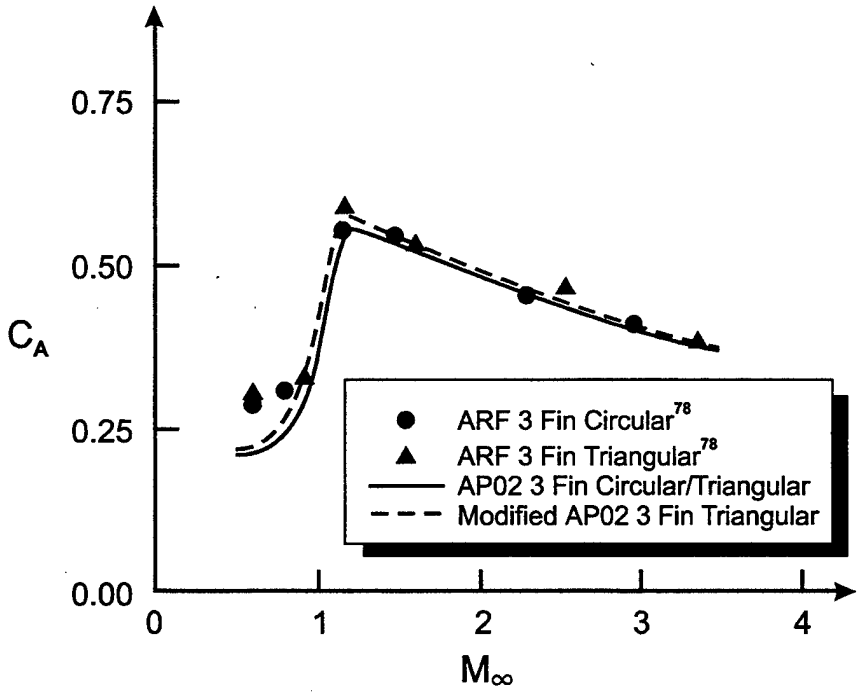

FIGURE 30. COMPARISON OF AP02 AND MODIFIED AP02 CALCULATIONS TO ARF DATA (3 FIN CIRCULAR AND 3 FIN TRIANGULAR SHAPES)

Equation (59)

$$(C_A)_{TR} = (C_{A_f})_C \left[\frac{(Cir)_{TR}}{2\pi r_{eq}}\right] + (C_{A_B})_{eq} [1 + .07(1 - 2k)] + (C_{A_W})_{eq} \tag{59}$$

As seen in Figure 30, the modified AP02 results are more in line with ARF data.

In summary, the ARF data has provided a means to modify the zero-lift axial force coefficient for noncircular cross-sectional shapes. It was found no modifications to the present AP02 calculations for C_A were needed for elliptical shapes whereas a slight increase in C_A in the AP02 was required for square and triangular shapes. The square shapes increased the circular shape body-alone wave and base drag by about 8 percent for sharp corners. The triangular shapes increased the body alone circular base drag by 7 percent for sharp corners.

2.7 TRAILING-EDGE FLAP TECHNOLOGY

One idea that has been considered to meet lower cost, lower volume, and lower maneuverability control requirements for guided projectiles is to deflect a part of a wing or tail surface as opposed to the entire surface. The portion of the tail surface considered for deflection is at the tail or wing trailing edge. Figure 31 is an illustration of a typical concept being considered where a part of the trailing edge portion of the tail fin is being considered for the control surface as opposed to the entire tail surface. As seen in Figure 31, this projectile concept

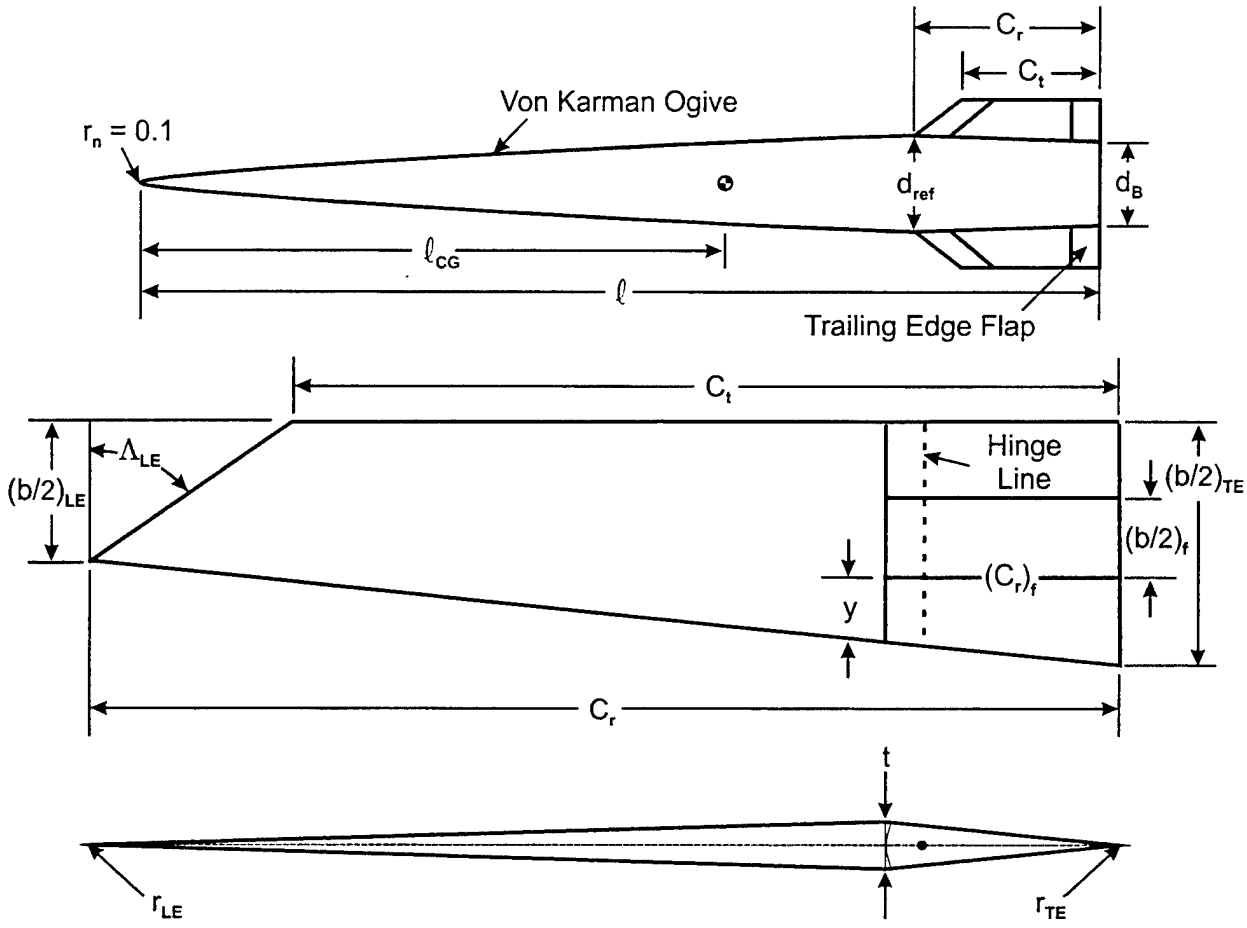

Enlarged View of Fin Planform and Root Cross Section

FIGURE 31. PROJECTILE CONCEPT WHERE TAIL TRAILING EDGE FLAP IS DEFLECTED FOR CONTROL

is very low drag, and given a high initial velocity, can produce a fairly long range, even without a rocket motor. For long ranges, winds and other ballistic errors can produce sizeable miss distances without some sort of corrective device. While the large tail fins of the Figure 31 concept are needed for stability at a high velocity launch, deflecting the entire tail fin a significant amount to eliminate the ballistic errors is not needed. Only a fraction of tail surface is required to provide adequate maneuverability if the deflection occurs over a sustained period of time. The small deflected surface area can also result in a much lower volume, weight, and cost for the control system. As seen in Figure 31, the amount of area of the trailing edge can vary depending on the requirements. Shown in the figure is a variable semispan, root chord, and hinge line for the trailing edge flap.

The most recent version of the NSWC APC (AP98[59]) distributed to users is not capable of computing aerodynamics on a concept such as that shown in Figure 31 when the trailing edge flaps are deflected. The objective of this section of the report is to summarize the methodology developed in Reference 109 that allows the 2002 version of the APC (AP02) to compute aerodynamics on a configuration where some portion of the rear part of the aft lifting surface

(either wing or tail) can be deflected to provide control. In developing this trailing edge flap aerodynamic predictive methodology, considerations of the cost to integrate the new methodology into the APC were a prime driver in the method chosen.

In reviewing the literature to determine approaches to use for calculating the aerodynamics of trailing edge flaps, the general approach that came the closest to that desired for use in the future AP02 is that adopted for the Missile Datcom[87]. In that approach, an equivalent value of deflection for the entire wing or tail surface is determined to reflect a given flap deflection. In other words

$$\delta_W = f(\delta_f) \tag{60}$$

The equivalent value of δ_W was determined offline using methods in the airplane DATCOM[2] at subsonic speeds and the method of Goin[110] at supersonic speeds. The advantage of an approach such as Equation (60) for codes such as Missile Datcom[87] or AP98[59] is that this is the least costly and most straightforward approach to incorporate the computation of aerodynamics of trailing edge flaps into an existing computer code. The low cost is because codes such as AP98[59] or Missile Datcom[87] are generally already set up logic-wise to compute the aerodynamics of a configuration where one set of fins are deflected. Hence, if one can define what that wing deflection is in terms of some flap deflection, the codes[59,87] can be exercised to provide a set of aerodynamics that simulate a configuration with a trailing edge flap deflected by a given amount.

While the approach used by the Missile Datcom [Equation (60)] to compute aerodynamics of trailing edge flaps is the same approach that will be adopted for use here, the methods that will be used for the AP02 will differ from those[2,110] used in the Missile Datcom[87]. There are several reasons for this. First, the method of Goin[110] has too many limitations. Some of these limitations include requirements for supersonic leading and trailing edges of the flap hinge line, viscous effects are not accounted for, and the method does not include nonlinearities due to large flap deflections or AOAs. Second, while the method of Reference 2 takes into account some of the viscous and nonlinear effects that Reference 110 does not account for, the method itself is inconsistent with that of Reference 110.

The objective here is to derive an improved method to compute aerodynamics of trailing edge flaps that utilize the Equation (60) approach. The method should be similar for both subsonic and supersonic freestream Mach numbers, should not be limited to supersonic leading and trailing edges, should account (at least empirically) for viscous effects, and should account for nonlinearities associated with large flap deflections or AOAs. From a practical standpoint, the weapons that will use the trailing edge flaps for control will typically fly at fairly small trim AOAs (less than 10 deg). However, flap deflections as large as ±30 deg are not unreasonable in order to achieve the appropriate trim AOA desired. Also, from a practical standpoint, most applications the author is aware of will be below $M_\infty = 2.0$. However, the method should be general enough to be applied over the Mach number range of applicability of the AP98 or AP02, which is 0 to 20. On the other hand, the method will not be validated over this large Mach number range due to limited experimental data and lack of funding to perform extensive Navier Stokes computations.

To most efficiently implement the methodology for computing the aerodynamics of a weapon concept that is controlled by trailing edge flaps, we seek the definition of the equivalent wing deflection that yields the same normal force, pitching moment, and trim AOA as that obtained by deflecting the trailing edge flaps. In mathematical terms,

$$N_{W(B)} + N_{B(w)} = N_f \, f_1 \tag{61}$$

$$M_{W(B)} + M_{B(W)} = N_f \, f_1 \left[(X_{CP})_f - X_{ref} \right] \tag{62}$$

$$(\alpha_{TR})_W = (\alpha_{TR})_f \tag{63}$$

In reality, if Equations (61) and (62) are satisfied, Equation (63) will automatically be satisfied. We then must define the relationships that allow Equations (61) and (62) to be satisfied.

Notice that in Equations (61) and (62), the wing-body normal force and pitching moments are equated to the normal force and pitching moment coefficients of the flap alone with no interference effects present, times an empirical constant. There are a couple of reasons for this. First, when the entire wing is deflected, it will have carryover normal force onto the wing. This means the equivalent control deflection of the entire wing will be lower than if no carryover normal force were present. Second, while there will be some interference carryover normal force onto the flap from the wing or body, this extra normal force can be lumped into an empirical term, f_1, which will be defined later.

Equation (61) can be expanded as

$$(C_{N_\alpha})_W \left[k_{W(B)} + k_{B(W)} \right] \delta_W = (C_{N_\alpha})_f \, f_1 \, \delta_f \tag{64}$$

The empirical factor, f_1, of Equation (64) accounts for several physical phenomena. These include boundary layer buildup and separation of the flow ahead of the flap on the wing surface; flap thickness effects; effects of the slot created between the wing and flap when the flap is deflected; and interference effects of the flap onto the body or wing or the wing or body onto the flap. The factor f_1 will be determined empirically based on experimental data for wings which have trailing edge flaps. Figure 32 attempts to pictorially and mathematically show the representation of a trailing edge flap deflection by deflecting the full wing.

To determine f_1, we equate the right hand side of Equation (64) to the change in normal force coefficient at some AOA due to a control deflection δ_f. That is

$$f_1 = \frac{(\Delta C_N)_f}{(C_{N_\alpha})_f \, \delta_f \, f_2} \tag{65}$$

$(\Delta C_N)_f$ of Equation (65) is the additional normal force coefficient created by a flap deflection δ_f. $(C_{N_\alpha})_f$ is the theoretical normal force coefficient slope for the flap of given aspect ratio and

Physical Representation

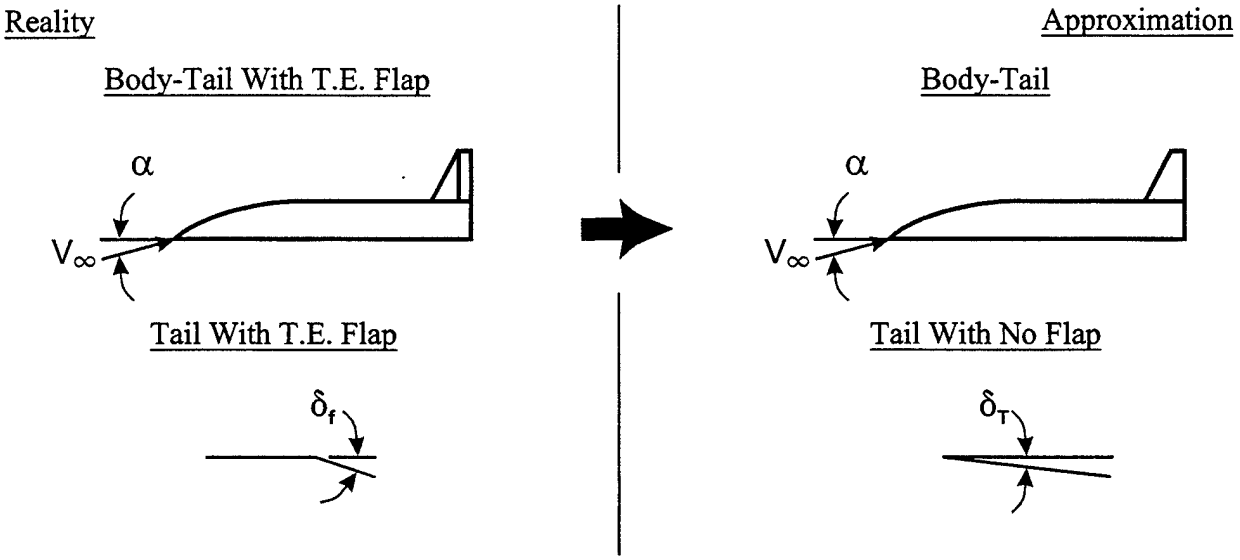

Mathematical Representation

$(C_{N_\alpha})_f f_l \delta_f$	=	$\delta_T (C_{N_\alpha})_T (k_{T(B)} + k_{B(T)})$
(Normal force coefficient of flap deflected an amount δ_f)	=	(Normal force coefficient of tail deflected on amount δ_T)

Physics f_l Accounts for

- Boundary layer buildup and separation ahead of flap
- Slot between wing and flap
- Interference effects of wing/body on flap and vice versa due to flap deflection

- Viscous effects completely different (boundary layer, no separation bubble)
- No slot present
- Interference effects automatically included

FIGURE 32. PHYSICAL AND MATHEMATICAL REPRESENTATION OF TRAILING EDGE FLAP DEFLECTION BY FULL WING DEFLECTION

taper ratio at a given Mach number and AOA. This theoretical value is determined by the methods in the AP02 for a flap only (no wing ahead of it). The AP02 methods include linearized theories at low AOA or control deflection combined with empirical approaches at higher AOA.

These methods in the AP98 or AP02 are fairly general and can calculate aerodynamics on supersonic or subsonic leading edge wings or flaps at low AOA. Also, aerodynamics can be computed for Mach numbers 0 to 20 and AOAs to 90 deg. Hence, the theoretical methodology for computing $(C_{N_\alpha})_f$ is fairly general. The value of $(C_{N_\alpha})_f$ is actually computed using a secant slope for a given AOA. This value of $(C_{N_\alpha})_f$ is then multiplied by the given flap deflection, δ_f, as seen in Equation (65). The numerator of Equation (65) is based on experimental data, which accounts for various physical phenomena of a flap in conjunction with a wing, which a wing alone does not have. Hence, the empirical factor f_1 is generated by the ratio of experimental data for a flap on a wing to a theoretical wing alone solution.

The factor f_2 in the denominator of Equation (65) is used to account for the fact that the theory in the AP02 which defines the lift curve slope of an entire wing deflected an amount δ at a given AOA may not accurately predict the increment in normal force generated by a flap. The factor f_2 is expected to be near one at supersonic speeds. However, at subsonic speeds, wind tunnel data suggests the theoretical predictions of additional normal force generated by a flap are higher than what the theory suggests. This inaccuracy of the theory arises from using the secant slope for $(C_{N_\alpha})_f$ versus using the local slope at a given value of α. At supersonic speeds, use of the secant slope does not appear to be a problem. However, subsonically, the C_N versus α curve levels out at around 25 to 30 deg AOA, so an additional increase in α brings increasingly less increase in C_N. Using a secant slope for $(C_{N_\alpha})_f$ versus the local tangent gives a value of $(C_{N_\alpha})_f$ too large and therefore a value of f_1 too low. The parameter f_2 therefore corrects for this weakness. One could change the overall AP02 code to use local versus secant slopes. However, this would be a very costly and time consuming process, and it was much more cost effective to define the factor f_2 to take care of this correction for the trailing edge flap technology.

In Equation (65), it is assumed both the numerator and denominator are based on the same reference area A_{ref}. If $(C_{N_\alpha})_f$ is calculated based on a wing-alone solution for the flap, then Equation (65) must be multiplied by A_{ref}/A_f to have consistent reference areas.

To define the empirical factor f_1, two data bases will be used.[111,129] Reference 111 contains data for a canard-body-tail configuration (see Figure 33) with trailing edge flaps. Data is available for Mach numbers 1.5 to 4.63, AOAs -2 to about 30 deg (except for $M_\infty = 1.5$ where some data is available only to about 15 deg AOA), and control deflections 0 to -30 deg. Unfortunately, no positive values of δ_f were available in Reference 111, possibly because a negative value of δ_f is required for trim to occur when α is positive.

Reference 129 contains data for low Mach number ($M_\infty = 0.3$ to 0.5) for several different configurations. These configurations included an elliptical and circular cylinder-shaped body with either a delta or sweptback rectangular wing. The wings could have either a leading or trailing edge flap. The configuration of most interest here is the delta wing with trailing edge flaps on a circular cylinder body (see Figure 34). Data is available to 40 deg AOA for flap deflections of ± 10 and ± 30 deg. Hence, Reference 129 will complement the supersonic data of Reference 111.

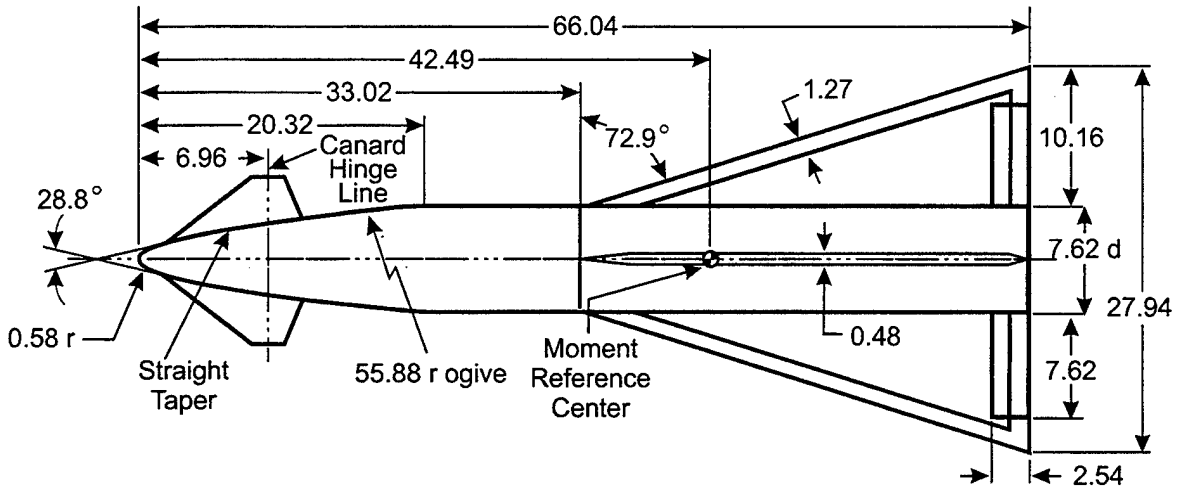

FIGURE 33. DRAWING OF THE MODEL USED FOR SUPERSONIC TESTS[111]
(ALL LINEAR DIMENSIONS IN CENTIMETERS)

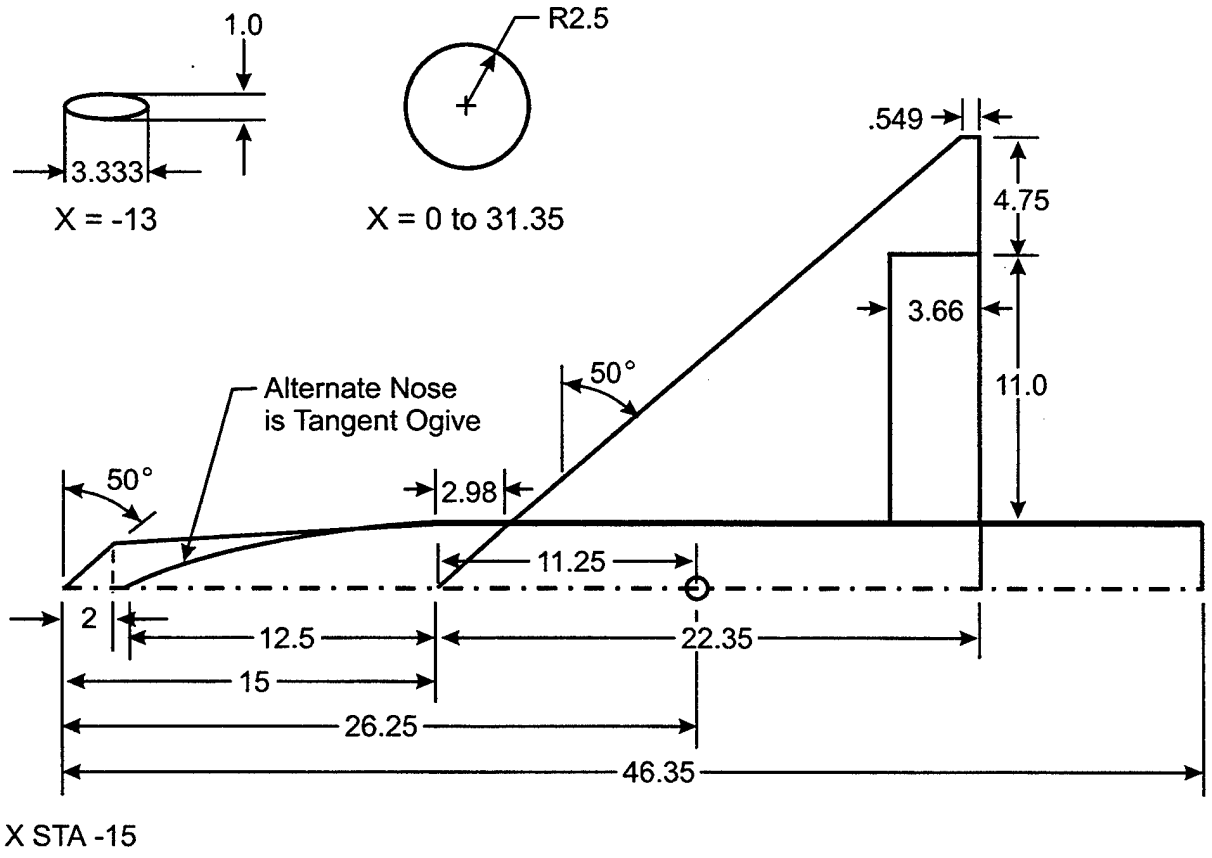

FIGURE 34. DELTA WING PLANFORM USED FOR SUBSONIC TESTS[129]
(ALL DIMENSIONS IN INCHES)

For Mach numbers in between M_∞ = 0.4 and M_∞ = 1.5, the following procedure will apply for computing f_1. For Mach numbers below M_∞ = 0.8, the value of f_1 computed at M_∞ = 0.4 will be assumed to apply. For Mach numbers between M_∞ = 1.5 and 0.8, linear interpolation will be used to compute f_1 based on the values of f_1 at M_∞ = 1.5 and 0.8.

Figures 35 and 36 give the values of f_1 determined by using References 111 and 129 to find values of $(\Delta C_N)_f$ and Reference 59 to compute a value of $(C_{N_\alpha})_f$ at a given AOA. Figure 35 is when α and δ are of opposite signs, which is the practical case for trim when the aft located control surface is deflected. Figure 35 applies for $M_\infty \geq 1.5$ and for values of α and δ of the same sign when α is numerically small. No data has been found to ascertain the validity of Figure 35 when α and δ are the same sign and α is greater than a small value. For $M_\infty > 4.63$, the value of f_1 at M_∞ = 4.63 will be assumed. Figure 35 also holds for values of δ_f up to −30 deg, based on Reference 111 data.

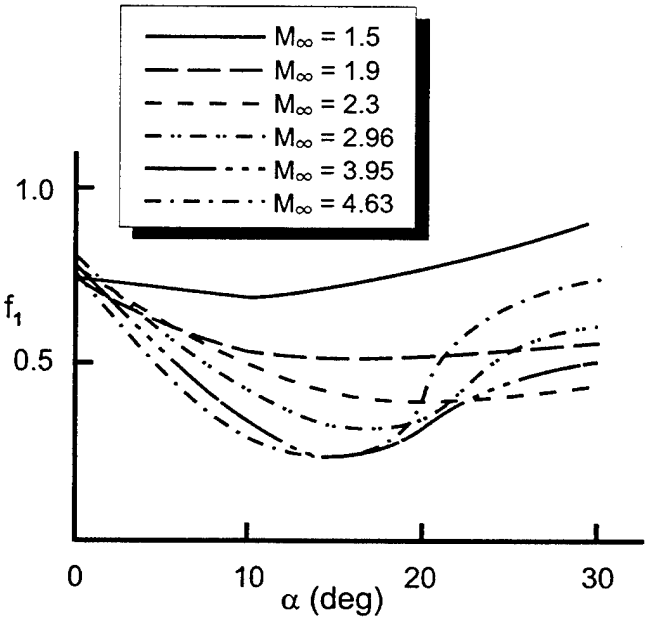

FIGURE 35. VALUE OF PARAMETER f_1 AT SUPERSONIC SPEEDS BASED ON REFERENCE 111 DATA AND AP98

Figure 36 gives values of f_1 for M_∞ = 0.4 for values of α up to 30 deg and for values of δ_f of ±30 deg. Figure 36 values of f_1 utilize the values of f_2 from Figure 37. Figure 37A presents the most practical case for tail-located trailing edge flaps since α and δ_f must be of opposite signs for trim to occur. Figures 37B and 37C present results for f_2 when α and δ_f are of the same sign. Figure 37B is for δ_f = 10 deg and Figure 37C is for δ_f = 30 deg. Linear interpolation of Figures 37B and 37C will occur for values of δ_f other than 10 or 30 deg.

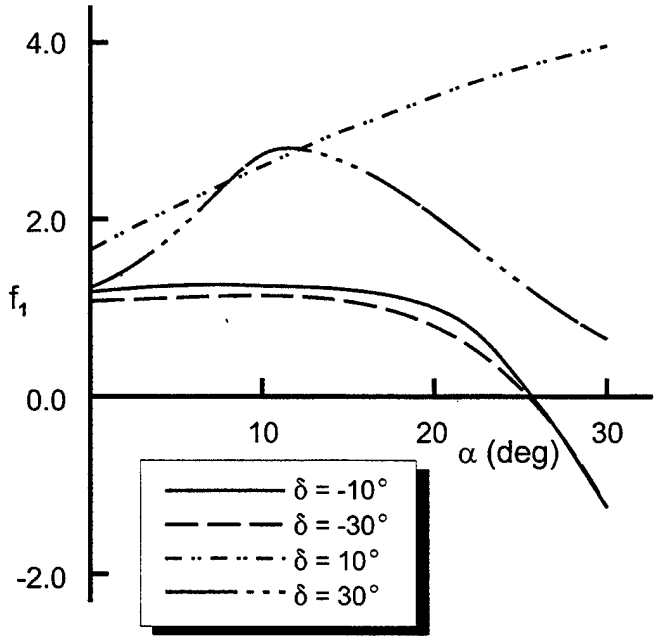

FIGURE 36. VALUE OF PARAMETER f_1 AT SUBSONIC SPEEDS BASED ON REFERENCE 129 DATA AND AP98

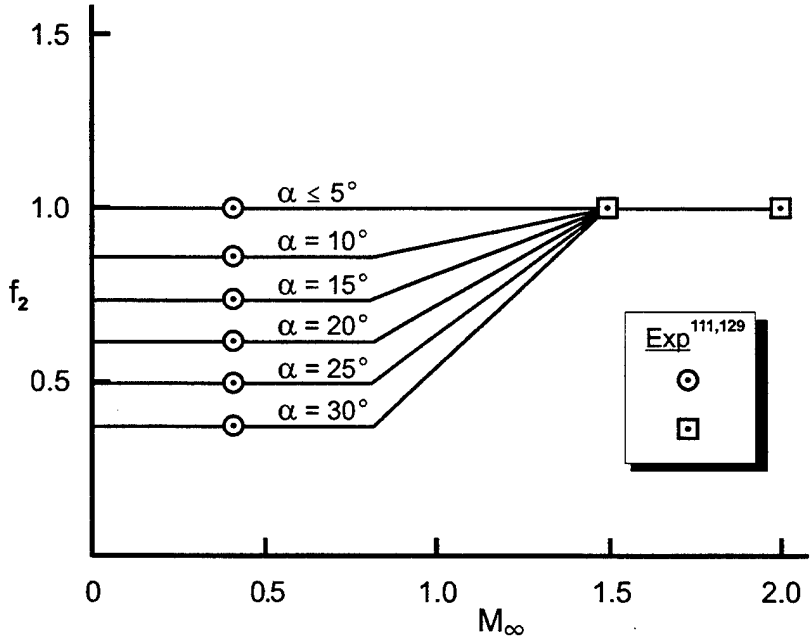

FIGURE 37A. FACTOR WHICH CORRECTS FOR USE OF SECANT VERSUS TANGENT IN NORMAL FORCE CURVE SLOPE (α AND δ OF OPPOSITE SIGNS)

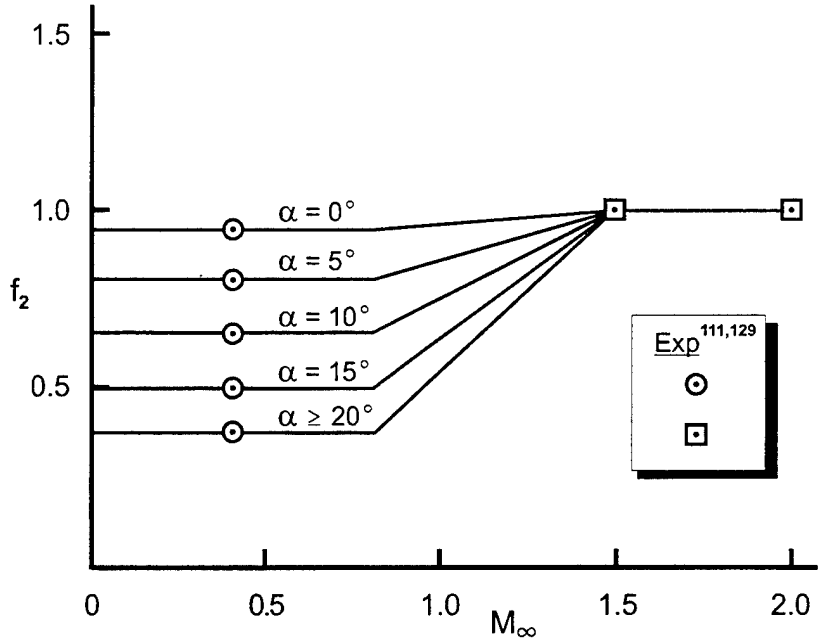

FIGURE 37B. FACTOR WHICH CORRECTS FOR USE OF SECANT VERSUS TANGENT IN NORMAL FORCE CURVE SLOPE (δ_f = 10 DEG)

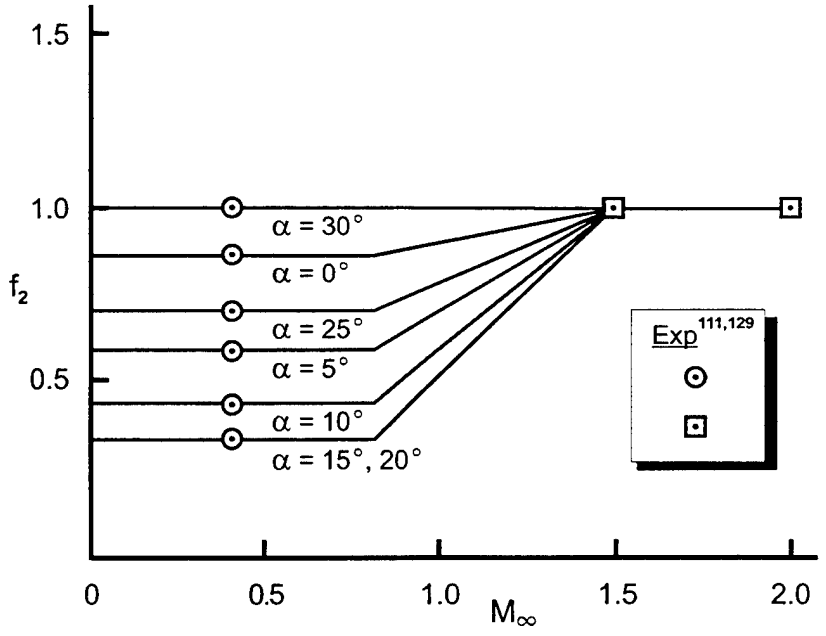

FIGURE 37C. FACTOR WHICH CORRECTS FOR USE OF SECANT VERSUS TANGENT IN NORMAL FORCE CURVE SLOPE (δ_f = 30 DEG)

Knowing f_1 from Figures 35 or 36, Equation (64) can be rewritten as

$$\delta_W = \left[\frac{\left(C_{N_\alpha}\right)_f f_1}{\left(C_{N_\alpha}\right)_W \left(k_{W(B)} + k_{B(W)}\right)} \right] \delta_f \tag{66}$$

The way Equation (66) is utilized within the AP02 is as follows:

1. For a given flap size, $\left(C_{N_\alpha}\right)_f$ is computed from the wing-alone solution in the AP02 at a given M_∞, α, AR, and λ. This value of $\left(C_{N_\alpha}\right)_f$ is then related to A_{ref} versus A_f.

2. f_1 is then computed via table lookup for a given value of α, M_∞, and δ_f (if the flow is subsonic).

3. For a given wing size, compute $\left(C_{N_\alpha}\right)_W$ from the wing-alone solution in the AP02 at a given M_∞, α, AR, and λ. This value of $\left(C_{N_\alpha}\right)_W$ must again be referenced to A_{ref}.

4. Compute values of $k_{W(B)}$ and $k_{B(W)}$ at a given α using the nonlinear control methodology in the AP02. This methodology uses SBT as a basis for low AOA estimates and wind tunnel data at high AOA to modify these estimates.

5. For a given value of δ_f, an effective value of δ_W can now be computed based on Equation (66). This value of δ_W is the amount the entire wing is deflected to approximate the additional normal force of a wing due to a trailing edge flap deflection of an amount δ_f.

Equation (66) defines the equivalent fin deflection to give the same normal force that deflecting the rear part of the fin an amount δ_f would give. The normal force coefficient of the flap or fin is computed from Equation (67). That is

$$\left(\Delta C_N\right)_f = f_1 \left(C_{N_\alpha}\right)_f \delta_f \tag{67}$$

The question that we must now address is the pitching moment for the flap. By deflecting the entire wing an amount δ_W defined by Equation (66), the pitching moment for the wing will be based on the center of pressure of the entire wing, not that due to the flap. Therefore, to obtain the correct pitching moment for the flap, where the entire wing is deflected, a change in the center of pressure must be calculated.

Most trailing edge flaps under consideration have a fairly high aspect ratio with a fairly small root chord. The initial thought by the authors was to assume the center of pressure of the normal force generated by the trailing edge flap would be similar to that on a high aspect ratio wing alone. That is, for subsonic flow, the center of pressure would be around the quarter chord location and then transition to the half chord location around $M_\infty = 2.0$. However, in comparing this assumed location to the experimental data of References 111 and 129, it was clear this

assumption on center of pressure location was not correct. It is believed the reason for the center of pressure assumption not being correct is that the flap cannot be treated as a wing in isolation at most Mach numbers. At a Mach number of 1.5, the assumption of ¼ chord transitioning to ½ chord supersonically was a good assumption (see Figure 38). However, at other Mach numbers, assuming the center of pressure of the flap normal force could be treated similar to a high aspect ratio wing in isolation became increasingly erroneous as seen by the experimental data of Figure 38. In giving the behavior of the experimental data in Figure 38 some thought, the authors believe that the physics of the flow can explain the Figure 38 experimental data. That is, as Mach number increases and the trailing edge flap is deflected, a shock is created ahead of the leading edge of the flap. This shock in turn creates a high pressure region on the wing where the flap is attached. This high pressure region is the reason for the experimental center of pressure of the flap normal force actually lying ahead of the leading edge of the flap as seen by Figure 38. The dashed line in Figure 38 is the new assumed center of pressure of the flap normal force as a function of Mach number. Notice that in Figure 38, $\left[(X_{CP})_f / C_r\right]_{avg}$ represents the average center of pressure over the AOA range from 0 to 30 deg as a fraction of the root chord of the flap.

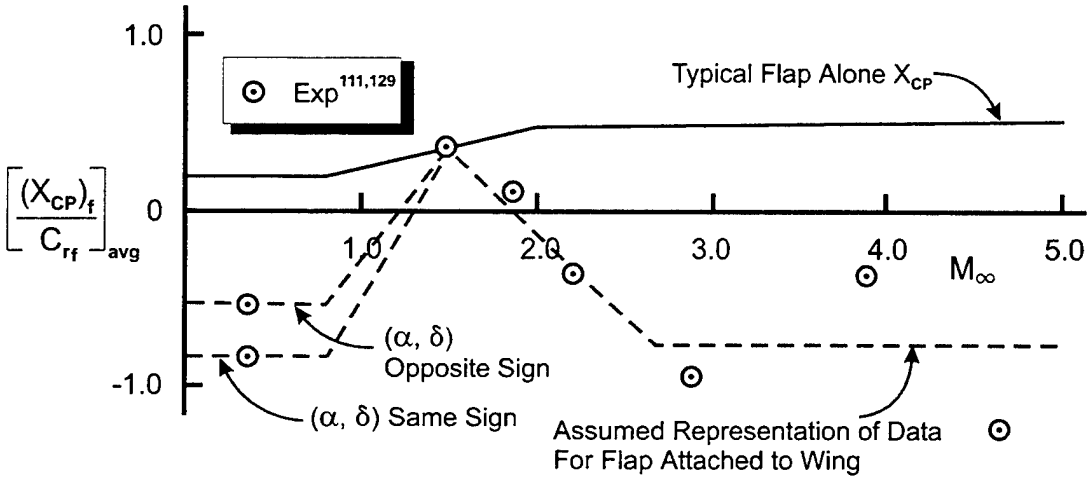

FIGURE 38. FLAP ALONE AND TRAILING EDGE FLAP ATTACHED TO WING AVERAGE CENTER OF PRESSURE OVER ANGLE OF ATTACK RANGE OF 0 TO 30 DEG FOR VARIOUS MACH NUMBERS

At a subsonic Mach number of 0.4, the center of pressure also lies ahead of the flap. If the flap deflection has the same sign as the AOA, this center of pressure location is about 0.7 chord lengths ahead of the flap leading edge. If the flap deflection is of opposite sign to the AOA, the center of pressure is about 0.4 chord lengths ahead of the flap leading edge. For Mach numbers 0 to 0.8, it is assumed these values of 0.4 and 0.7 chord lengths hold constant. For Mach numbers 0.8 to 1.5, it is assumed the location of the flap center of pressure varies linearly between the values at $M_\infty = 0.8$ and 1.5.

The physics which cause the center of pressure to move ahead of the flap are believed to be different for the subsonic and supersonic cases. Supersonically, it is believed viscous effects

as well as the shock structure are the dominant features. However, subsonically, it is believed the flap deflection rearranges the pressure distribution on the wing ahead of the flap as well as the viscous effects, which are present at all Mach numbers. The rearrangement of the pressure distribution on the wing ahead of the flap occurs because in subsonic flow, disturbances in the flow can feed forward, whereas supersonically they cannot, except through the boundary layer.

From a practical standpoint, the effect of the flap center of pressure shift diminishes its effectiveness somewhat in generating trim AOA. This is because the center of pressure of the normal force actually lies in front of the flap at most Mach numbers, decreasing the moment somewhat and hence the trim AOA. On the other hand, if the flap is located near the base of a fairly long body, a one to four inch shift in the center of pressure forward can be fairly small in terms of the overall moment arm. The amount of normal force created does not seem to be affected by the forward shift in center of pressure for trailing edge flaps.

The center of pressure of the trailing edge flap is therefore

$$\frac{(X_{CP})_f}{\ell_{ref}} = \frac{(X_{LE})_W + C_{r_w} - C_{r_f} f_3 - X_{ref}}{\ell_{ref}} \tag{68}$$

The term f_3 of Equation (68) is based on the empirically defined dotted lines of Figure 38. That is

$$\begin{aligned}
f_3 &= +1.5 \text{ for } M_\infty \le 0.8 \text{ and } (\alpha, \delta) \text{ opposite signs} \\
&= +1.8 \text{ for } M_\infty \le 0.8 \text{ and } (\alpha, \delta) \text{ same signs} \\
f_3 &= 2.53 - 1.29\, M_\infty \text{ for } 0.8 < M_\infty \le 1.5 \text{ and} \\
&\quad (\alpha, \delta) \text{ opposite signs} \\
&= 3.17 - 1.71\, M_\infty \text{ for } 0.8 < M_\infty \le 1.5 \text{ and} \\
&\quad (\alpha, \delta) \text{ same signs} \\
f_3 &= -0.84 + 0.96\, M_\infty \text{ for } 1.5 < M_\infty \le 2.7 \\
&= 1.75 \qquad \text{for} \qquad M_\infty > 2.7
\end{aligned} \tag{69}$$

Using Equations (68) and (69), the change in pitching moment created by the fact the wing is deflected to simulate the trailing edge flap deflection is then

$$(\Delta C_M)_f = -\frac{(\Delta C_N)_f}{\ell_{ref}} \{ [(X_{CP})_f - (X_{CP})_W] + [(X_{CP})_W - X_{CG}] \} \tag{70}$$

Equation (70) represents the pitching moment coefficient of any configuration where the trailing edge flap deflection is approximated by deflecting the full wing. The first term of Equation (70) represents the difference in the center of pressure between the flap and wing whereas the second term represents the center of pressure of the wing normal force term relative to a reference location which is taken to be the center of gravity of the vehicle. Of course, the center of

pressure of the wing is computed in the AP02 using linear theory methods at low AOA and transitions to the centroid of the wing planform area at high AOA.

The major focus in the analysis for estimating the aerodynamics of trailing edge flaps has been to determine an equivalent tail deflection which will give normal force and pitching moments equal to those when the flap is deflected. No mention of axial force has been made to this point. The axial force coefficient will be different for an equivalent wing deflection based on a flap deflection δ_f. The flap deflection will generate an additional axial force term due to the fact δ_f will be generally much larger than δ_W. An approximate relation which can be used to calculate the increment in axial force coefficient that results from estimating the aerodynamics based on a wing deflection of δ_W versus a flap deflection of δ_f is

$$(\Delta C_A)_f \cong \Delta(C_N)_f \left[\sin|\delta_f| - \sin|\delta_W|\right] \tag{71}$$

$(\Delta C_N)_f$ of Equation (21) is the additional normal force contribution due to the flap. Sin $|\delta_f|$ takes the component of this normal force term in the axial direction. Sin $|\delta_W|$ subtracts off the component of axial force of the wing since this is automatically included in the AP02 calculations; to leave this term in the calculations would mean doubly accounting for the wing deflection axial force contribution.

2.8 TRAJECTORY MODELS

The evaluation of the flight performance of today's projectiles and missiles is typically a two step, iterative process. First, the aerodynamic coefficients for the airframe must be determined over the anticipated envelope of flight conditions. This is accomplished through wind tunnel testing or by using software that will predict the aerodynamics. Second, the aerodynamic coefficients are inserted into a trajectory model so that the aerodynamic forces acting upon the missile may be determined for any flight condition. The trajectory model is then executed and the results are analyzed.

In the above process, the first step is usually performed by an aerodynamicist, while the second step is performed by a flight dynamicist. If the flight dynamicist is not satisfied by the flight performance predicted by the trajectory model, he may make changes to the airframe. These changes will in turn effect the aerodynamics, thereby requiring the aerodynamicist to create a new set of aerodynamic data to be inserted into the trajectory model. This iterative process continues until an airframe is found which optimizes some desired aspect of the flight performance.

Depending upon the flight regime over which the aerodynamics are to be computed, a set of trim aerodynamics may take on the order of 1 to 2 man-days to generate. The term "trim" means that the aerodynamic coefficients correspond to a state in which the pitching moment coefficient (C_M) is equal to zero. As an example, a set of trim aerodynamics was found for a wing-body-tail configuration for angles of attack (α) ranging from 0 to 30 deg in 5 deg increments. Also, there were two center of gravity (cg) locations and 4 Mach numbers (M) to be

evaluated. This means that there were 56 trim points to be found. The work was performed using AP98. Although AP98 executes fairly rapidly, it does not directly provide trim aerodynamics. Instead, the user must generate plots of pitching moment vs fin deflection (δ) at a given Mach number and AOA. Then the user must "eyeball" the results until the trim point is found to be within some desired accuracy. This may entail several iterations until the $C_M = 0$ point is bounded and is displayed on a scale large enough to ensure accuracy. It took an experienced AP98 user approximately 10 hr to accomplish the task. Of the 10 hr, only about 15 min were required to set up the missile configuration in AP98.

Note that the run matrix of 56 points is a very modest one. For example, the effect of altitude upon trim axial force coefficient $(C_A)_{TRIM}$ was disregarded. Also, the intervals between Mach numbers and angles of attack were fairly coarse. The center of gravity corresponded to the full and empty fuel states only. To predict flight performance more accurately, a correspondingly more detailed set of aerodynamics must be provided. The generation of aerodynamic tables, especially trim aerodynamics, can be tedious and time consuming.

The insertion of aerodynamics into the trajectory model also requires some amount of time. The actual amount of time will depend upon the amount of aerodynamic data to be inserted as well as the experience level of the flight dynamicist. For example, it took about 2 hr to insert the aforementioned set of trim aerodynamics into a trim 3 degree-of-freedom (3 DOF) model. This time also included the compilation and execution of the code. In this case, the flight dynamicist was experienced with the particular trajectory model. Obviously, the insertion of aerodynamic data would take considerably longer had the users not been familiar with the trajectory model.

The total amount of time to generate a set of aerodynamics, insert the aerodynamics into a trajectory model, and run the trajectory model for this example was approximately 12 hr and required 2 people. Each person was experienced in performing his part of the task. Also, each person was available to do the work when required. That is, there was no delay when the aerodynamicist transitioned the aerodynamic data to the flight dynamicist. In summary, one iteration from aerodynamicist to flight dynamicist for the example case cited took approximately 12 hr. This is relatively quick turn around time since the aerodynamics were sparse (in terms of Mach numbers and control deflections selected) and the people doing the work were experienced and available.

The process discussed in the preceding paragraph was for one iteration only. If the performance of the concept was adequate, that would probably complete the initial phase of the design and aerodynamic and performance assessment of the concept in question. However, in most cases, several design iterations are required to see the effect on the aerodynamics and performance of each design change. Thus, the time involved to generate the trim aerodynamics and perform performance assessments is a minimum of 12 hr times the number of concepts investigated. Combining the aeroprediction code with trajectory models for automatic trajectory generation of a given design concept thus has potential for a large cost savings. When the cost savings is multiplied by the many users of the APC, the cost savings becomes even larger.

The remainder of this section of the report will discuss the combination of trajectory models with the AP02. This combination will then allow one user to do the work of both the aerodynamicist and the flight dynamicist in the preliminary design of a weapon and in performance analysis. More specifically, this report will discuss the joining of an upgraded 1998 APC with a 2 DOF ballistics model (TRAMOD[112]) and a trim 3 DOF model (MEM[113]) to form the 2002 APC. By using the AP02 code, the aforementioned example case can be performed in 1 hr, versus 12 hr, for each design iteration. More details of what will be presented in this section of the report can be found in Reference 114.

2.8.1 TRAMOD - A 2 DOF Ballistics Model[112]

The TRAMOD code is used to simulate point mass ballistic trajectories of gun launched projectiles. It contains the following primary features:

DEGREES OF FREEDOM: There are two degrees of freedom: downrange and altitude. A third degree of freedom, the cross range translation (or drift), is not included in the equations of motion. Instead, the drift due to spin and yaw of repose are computed with closed form equations. In this sense, the TRAMOD is a quasi 3 DOF ballistic model. On the other hand, cross range due to the effects of crosswinds are accounted for in the equations of motion.

COORDINATE FRAME: The equations of motion are integrated in a flat earth system. The X component is aligned along the downrange direction, the Y component is to the right in the cross range direction, and the Z component is up, completing a left-handed coordinate system. A closed form equation is solved at the end of execution of the TRAMOD code to adjust the range for curved earth effects. An option is provided to include Coriolis effects should the user desire.

ATMOSPHERE: There are three options for describing the atmospheric properties. The users may choose from the Navy Standard Atmosphere (NAST), the International Civil Aviation Organization Atmosphere (ICAO), or the actual observed local atmospheric conditions may be entered.

INTERGRATION SCHEME: The code uses a 4^{th} order Runge Kutta method for integration. The integration time step may be specified by the user.

AERODYNAMICS: The user must supply an input file which contains a drag coefficient (CD) as a function of Mach number at sea level.

THRUST, WEIGHT, CG: Thrust (T) is not allowed. There is no provision to allow for continuously varying weight or cg; however, staging is allowed.

GUIDANCE: All trajectories are ballistic. The AOA is zero throughout the flight.

The mathematical model which defines the equations of motion of the TRAMOD code is given by:

$$\ddot{x} = -D(\dot{x} - W_x)/MV - C_x \tag{72}$$

$$\ddot{y} = -D(\dot{y} - W_y)/MV - C_y \tag{73}$$

$$\ddot{z} = -D(\dot{z})/MV - g - C_z \tag{74}$$

where

$$D = \frac{1}{2}\rho_\infty V_\infty^2 A_{ref} C_D$$

$$V_\infty = \sqrt{\dot{x}^2 + \dot{y}^2 + \dot{z}^2}$$

$$C_x = A_y \dot{z} - A_z \dot{y}$$

$$C_y = A_z \dot{x} - A_x \dot{z}$$

$$C_z = A_x \dot{y} - A_y \dot{x}$$

$$A_x = -2\Omega \cos(\theta_L)\cos(\theta_e)$$

$$A_y = 2\Omega \cos(\theta_L)\sin(\theta_e)$$

$$A_z = -2\Omega \sin(\theta_L)$$

$$\text{Drift} = k\int_O^T (x_T - x_t)/V_t dt \tag{75}$$

k = drift constant defined by user input

Equations (72) – (74) are integrated using a standard fourth-order Runge-Kutta integration scheme. The reason the TRAMOD is defined as 2-D versus 3-D is that the motion in the x-y plane caused by spin and yaw of response is not included directly in the equation of motion. Only crosswinds are accounted for in the y equation of motion, Equation (73). However, drift is approximated by Equation (75) where k is a user defined drift constant, x_T is the final range, and x_t, V_t are the initial range and velocity at the beginning of the drift calculation. For more details of the TRAMOD model or integration of this model with APC, the reader is again referred to References 112 and 114, respectively.

2.8.2 MEM – A 3 DOF Trim Model[113]

The MEM code is used to simulate and optimize trajectories of a tactical missile. It contains the following primary features:

DEGRESS OF FREEDOM: There are three translational degrees of freedom.

COORDINATE FRAME: The equations of motion are integrated in a North, East, Down coordinate frame, (SIM frame), which is defined at launch as a function of latitude and longitude. The attitude of the frame remains constant relative to an earth centered inertial (ECI) frame throughout the simulation. The code utilizes a round earth model which may be used in either a rotating or non-rotating mode.

ATMOSPHERE: The 1962 US Standard Atmosphere Tables are used.

INTEGRATION SCHEME: The code uses a 4^{th} order Runge Kutta method for integration. The integration time step is .25 sec.

AERODYNAMICS: The code determines the aerodynamic forces acting upon the weapon via linear interpolation inside of tables of aerodynamic coefficients. Aerodynamic coefficients include C_A and normal force coefficient (C_N) as a function of Mach number, AOA, and center of gravity location.

THRUST, WEIGHT, CG: These parameters are computed from tables by using linear interpolations.

GUIDANCE: Because the MEM is used as a tool for analyzing and optimizing missile performance, there are various types of guidance schemes that have been used. Kappa guidance is used most often for the midcourse trajectory.

For more information about MEM code, see Reference 113. For more information on combining the MEM code with the APO2, the reader is referred to Reference 114.

The mathematical model used in the MEM code is given by:

$$\ddot{x}_W = \frac{T - D_0}{m}\cos\alpha\cos\beta + \ddot{y}_B \sin\beta + \ddot{z}_B \sin\alpha\cos\beta \tag{76}$$

$$\ddot{y}_W = -\left(\frac{T - D_0}{m}\right)\cos\alpha\sin\beta + \ddot{y}_B \cos\beta - \ddot{z}_B \sin\alpha\sin\beta \tag{77}$$

$$\ddot{z}_W = -\left(\frac{T - D_0}{m}\right)\sin\alpha + \ddot{z}_B \cos\alpha \tag{78}$$

where

$\ddot{y}_B, \ddot{z}_B$ = achieved normal accelerations in the body y and z axes.
m = the mass of the missile
D_0 = the zero AOA drag
α, β = angle of attack and yaw, respectively
T = thrust
$T = T_{SL} + A_e P_{SL} (1.0 - P_C)$

where

A_e = the exit area of the nozzle
P_{SL} = the sea level pressure
P_C = the current normalized atmospheric pressure
T_{SL} = the sea level thrust

Equations (76) – (78) are defined in the wind axis system based on thrust, drag, missile instantaneous mass, and achieved normal acceleration in the y and z body axis given some commanded acceleration inputs. The commanded acceleration inputs are defined using one of several guidance laws, some current state, and some target state. Fourth-order Runge Kutta is used as the integration scheme for Equations (75) – (78). Again, for more details of the MEM model and implementation into the APC, the reader is referred to References 113 and 114, respectively.

3.0 SUMMARY OF AERODYNAMIC METHODS

Section 2 of this report summarized the new methods that will be included in the AP02 that were not available in the AP98. Reference 59 summarizes the methods that were part of the AP98 so the reader is referred to that reference for the details of the AP98 methods. Suffice it to say that the AP98 is based on modified versions of slender body, linear theory, or second-order perturbation theories at low AOA and empirical methods at high AOA. The low AOA theoretical methods gives the APC a good foundation to predict aerodynamics for various geometries and for various flight conditions up to AOA of about 10 deg. The empirical methods that were developed based on several large data bases extend the low AOA methods all the way to 90 deg AOA.

A summary of the theoretical methods that make up the AP02 are shown in Tables 34 - 37. Table 34 gives the body-alone methods, Table 35 provides the wing and interference methods, Table 36 shows the dynamic derivatives, and Table 37 provides the trajectory options which are part of the AP02. The highlighted (italic print) methods in Tables 34 - 37 represent the new theories that are part of the AP02 that were not included in the AP98.

Figure 5 shows the evolution of the APC from its initial version, the AP72, to the latest version to be released, the AP02. As seen in Figure 5, the AP02 is the only version of the APC that provides a trajectory option, multi-fin capability, and addresses several emerging projectile requirements.

TABLE 34. AP02 METHODS FOR BODY-ALONE AERODYNAMICS

COMPONENT/ MACH NUMBER REGION	SUBSONIC $M_\infty < 0.8$	TRANSONIC $0.8 \le M_\infty \le 1.2$	LOW SUPERSONIC $1.2 \le M_\infty \le 1.8$	MOD/HIGH SUPERSONIC $1.8 \le M_\infty \le 1.8$	HYPERSONIC $M_\infty > 6.0$
NOSE WAVE DRAG	EMPIRICAL	SEMIEMPIRICAL BASED ON EULER SOLUTIONS	SECOND-ORDER VAN DYKE PLUS MNT	SOSET PLUS IMNT	SOSET PLUS IMNT MODIFIED FOR REAL GASES
BOATTAIL OR FLARE WAVE DRAG	- - -	WU AND AOYOMA	SECOND-ORDER VAN DYKE	SOSET	SOSET FOR REAL GASES
SKIN FRICTION DRAG	VAN DRIEST II				
BASE DRAG • *POWER-OFF* • *POWER-ON* • *BASE BLEED*	*IMPROVED EMPIRICAL METHOD* • *EMPIRICAL* • *MODIFIED BRAZZEL METHOD* • *MODIFIED DANBERG METHOD*				
AXIAL FORCE AT α	EMPIRICAL METHOD				
AEROHEATING INFORMATION	- - -			SOSET PLUS IMNT FOR REAL GASES	
INVISCID LIFT AND PITCHING MOMENT	EMPIRICAL	SEMIEMPIRICAL BASED ON EULER SOLUTIONS	TSIEN FIRST-ORDER CROSSFLOW	SOSET	SOSET FOR REAL GASES
VISCOUS LIFT AND PITCHING MOMENT	IMPROVED ALLEN AND PERKINS CROSSFLOW				
NONAXISYMMETRIC BODY AERO • *LIFTING PROPERTIES* • *AXIAL FORCE*	• *MODIFIED JORGENSEN* • *MODIFIED AXISYMMETRIC BODY*				
NONLINEAR ST. LOADS AVAIL. ($\Phi = 0, 45°$)	NO		YES		

TABLE 35. AP02 METHODS FOR WING-ALONE AND INTERFERENCE AERODYNAMICS

COMPONENT/ MACH NUMBER REGION	SUBSONIC $M_\infty < 0.8$	TRANSONIC $0.8 \le M_\infty \le 1.2$	LOW SUPERSONIC $1.2 \le M_\infty \le 1.8$	MOD/HIGH SUPERSONIC $1.8 \le M_\infty \le 6.0$	HYPERSONIC $M_\infty > 6.0$
WAVE DRAG		EMPIRICAL	LINEAR THEORY PLUS MNT	SHOCK EXPANSION (SE) PLUS MNT ALONG STRIPS	SE PLUS MNT FOR REAL GASES ALONG STRIPS
SKIN FRICTION DRAG	VAN DRIEST II				
TRAILING EDGE SEPARATION DRAG	EMPIRICAL				
BODY BASE PRESSURE CAUSED BY TAIL FINS	EMPIRICAL				
INVISCID LIFT AND PITCHING MOMENT					
• LINEAR	• LIFTING SURFACE THEORY	• EMPIRICAL	• 3DTWT	• 3DTWT	• 3DTWT
• NONLINEAR	• EMPIRICAL				
WING-BODY, BODY-WING INTERFERENCE ($\Phi = 0, 45°$)					
• LINEAR	• SLENDER BODY THEORY OR LINEAR THEORY MODIFIED FOR SHORT AFTERBODIES				
• *NONLINEAR*	• *IMPROVED EMPIRICAL*				
WING-BODY, INTERFERENCE DUE TO δ ($\Phi = 0, 45°$)					
• LINEAR	• SLENDER BODY THEORY				
• *NONLINEAR*	• *IMPROVED EMPIRICAL*				
WING-TAIL INTERFERENCE ($\Phi = 0, 45°$)	LINE VORTEX THEORY WITH MODIFICATIONS FOR $K_{W(B)}$ TERM AND NONLINEARITIES				
AEROHEATING	NONE PRESENT			SE PLUS MNT	SE PLUS MNT REAL GASES
NONAXISYMMETRIC BODY AERO ($\Phi = 0, 45°$)	IMPROVED NELSON METHOD				
NONLINEAR ST. LOADS AVAIL. ($\Phi = 0, 45°$)	NO		YES		
6, 8 FIN AERO • *LINEAR* • *NONLINEAR*	• *SLENDER BODY THEORY* • *SEMIEMPIRICAL (CFD + DATA)*				
TRAILING EDGE FLAPS ON TAILS	*SEMIEMPIRICAL (SEEK TAIL DEFLECTION FOR EQUAL NORMAL FORCE)*				

TABLE 36. AP02 METHODS FOR DYNAMIC DERIVATIVES

COMPONENT/ MACH NUMBER REGION	SUBSONIC $M_\infty < 0.8$	TRANSONIC $0.8 \le M_\infty \le 1.2$	LOW SUPERSONIC $1.2 \le M_\infty \le 1.8$	MOD/HIGH SUPERSONIC $1.8 \le M_\infty \le 6.0$	HYPERSONIC $M_\infty > 6.0$
BODY ALONE • *NO FLARE* • *WITH FLARE*	• *EMPIRICAL* • *SEMIEMPIRICAL*				
WING AND INTERFERENCE ROLL DAMPING MOMENT	LIFTING SURFACE THEORY	EMPIRICAL	LINEAR THIN WING THEORY		
WING MAGNUS MOMENT	ASSUMED ZERO				
WING AND INTERFERENCE PITCH DAMPING MOMENT	LIFTING SURFACE THEORY	EMPIRICAL	LINEAR THIN WING THEORY		

TABLE 37. TRAJECTORY CAPABILITY WITHIN APC

SIMULATION MODE	AP72 – AP98	AP02
PARTICLE BALLISTIC	NONE	*YES*
3 DOF	NONE	*YES*

4.0 RESULTS AND DISCUSSION

The results and discussion section of the report will focus primarily on validating the new elements of technology that have been added to the AP98 that make up the new AP02. Focusing on the newer elements of technology discussed in Section 2 of the report still requires use of the elements of the AP98 that have not been modified. To point out the differences between the AP02 and AP98, both results will be shown compared to experiment when available. In some cases, such as 6 and 8 fin aerodynamics, trailing-edge flaps, or base bleed, this is not possible since the AP98 does not have these capabilities available.

4.1 IMPROVED NONLINEAR AERODYNAMICS

To compare the improved nonlinear aerodynamics generated by the AP02 to the AP98 and experiment, six cases will be considered. In addition to these six cases, comparison of the AP02 to the AP98 and the generic wind tunnel data bases of Reference 69 and 70 will be summarized. The References 69 and 70 data bases are based on Figure 12 configurations.

A summary of the comparison of normal force coefficient predictions by the AP02 and AP98 to the References 69 and 70 data bases is given in Table 38. The Tri-Service data base[69] consisted of Mach numbers 0.6, 0.8, 1.2, 1.5, 2.0, 2.5, 3.0, 3.5, and 4.5 with AOA up to 25 to

40 deg (depending on Mach number) and for $\Phi = 0$ and 45 deg roll. The highest aspect ratio fins (AR = 4) of the Tri-Service data base were very small, so the data associated with those fins was not included in Table 38. Also, the aspect ratio 2.0 fin data of Reference 69 was only included for Mach numbers 1.5 and greater for the same reason of small fin planform. The Reference 70 data base consisted of Mach numbers 0.6, 0.9, 1.2, 1.6, 2.0, 2.3, 2.96, and 3.95 for AOA from 0 to 20 or 30 deg (depending on Mach number), but at the roll position of $\Phi = 0$ deg only.

The Table 38 errors were measured at α = 10, 15, 20, 25 and 30 deg where data was available. The error in Table 38 is defined by

$$\text{Error}(\%) = \frac{\left|C_{N_{exp}} - C_{N_{Theory}}\right|}{C_{N_{exp}}} \times 100 \tag{79}$$

The errors in Table 38 are then broken down by Mach number and then summed and averaged for all Mach numbers. The average normal force coefficient error of 3.8 percent in Table 38 is about 2-3 percent lower than for the AP98. In other words, incorporation of the Reference 70

TABLE 38. AVERAGE NORMAL FORCE ERRORS OF AP02 COMPARED TO COMBINED DATA BASES[69,70]

MACH NO.	NO. POINTS	AVERAGE ERROR (PERCENT)
0.6	89	5.5
0.8-0.9	95	7.2
1.2	102	3.7
1.5-1.6	172	2.6
2.0	168	3.3
2.3-2.5	166	2.8
2.96-3.0	167	3.6
3.5-3.95	163	4.2
4.5	108	3.2
TOTALS	1230	3.8

data base, which focused on variations in r/s, has allowed the average normal force errors to be reduced by about 40 percent when comparing the AP02 to the AP98 and the data bases upon which the nonlinear aerodynamic terms were based.

No average error on center of pressure was made because of time constraints. However, suffice it to say that the average center of pressure error for the AP98 on the NASA Tri-Service data base was less than 2 percent of the body length.[59] Improvements made in normal force should only improve these already excellent predictions. Likewise, no improvements in axial

force were sought, as we were satisfied with the power-off predictions of axial force from the AP98.

While the average accuracy comparisons of C_N to experiment of Tables 38 is impressive for a semiempirical code, the true measure of success is based on the ability to accurately predict aerodynamics on a wide variety of configurations outside the data bases upon which the empirical nonlinearities were derived. The first case considered is taken from Reference 115 and is a model of an older version of the SEASPARROW missile. A fairly extensive data base exists for this configuration. The configuration is shown in Figure 39, where the wings or tail surfaces can be used for control.

This configuration has a length of about 18 calibers with a tangent ogive nose 2.25 calibers in length. It has wings and tails of fairly high aspect ratios of 2.8 and 2.6, respectively. Data was taken at Mach numbers of 1.5 to 4.63 for AOAs to 40 deg and control deflections of 0 and 10 deg (at M of 1.5 and 2.0) and 0 to 20 deg (at M of 2.35 to 4.63). The data was taken at a Reynolds number of 2.5×10^6/ft and boundary layer trips were also used. The model had a hollow camber, and camber axial force measurements were given separately in Reference 115. These results were added to the forebody axial force measurements to compare with the AP98 and AP02.

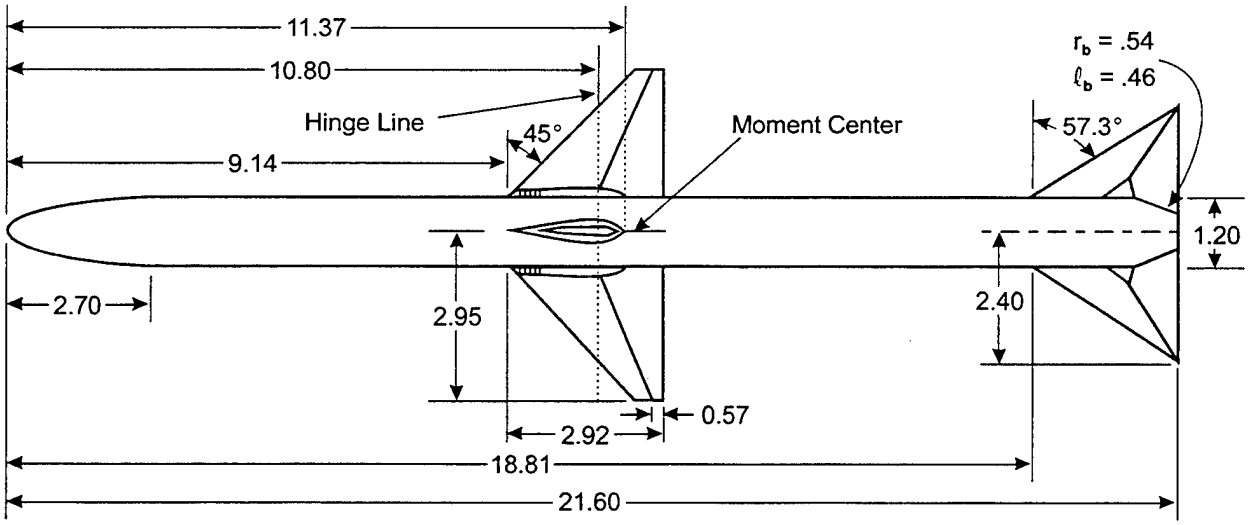

FIGURE 39. WING-BODY-TAIL CONFIGURATION USED IN VALIDATION PROCESS (ALL DIMENSIONS IN INCHES)

Figure 40 shows the comparisons of the AP98 and AP02 to the data of Reference 115 for $\Phi = 0$ deg and $\Phi = 45$ deg and for the wing control configuration. Figures 40A and 40B give C_A, C_N, and C_M for $M_\infty = 1.5$ at $\delta_W = 0$ and $\delta_W = 10$ deg at $\Phi = 0$ deg. In general, both the AP98 and AP02 give good comparisons to data. Figures 40C and 40D give similar results for $M_\infty = 2.87$, and Figures 40E and 40F, for $M_\infty = 4.6$. Overall, for this configuration, at $\Phi = 0$ deg roll, the AP02 and AP98 are about equal in overall accuracy comparisons with the AP02 being slightly more accurate. The worst case errors are for center of pressure at higher Mach number and AOA

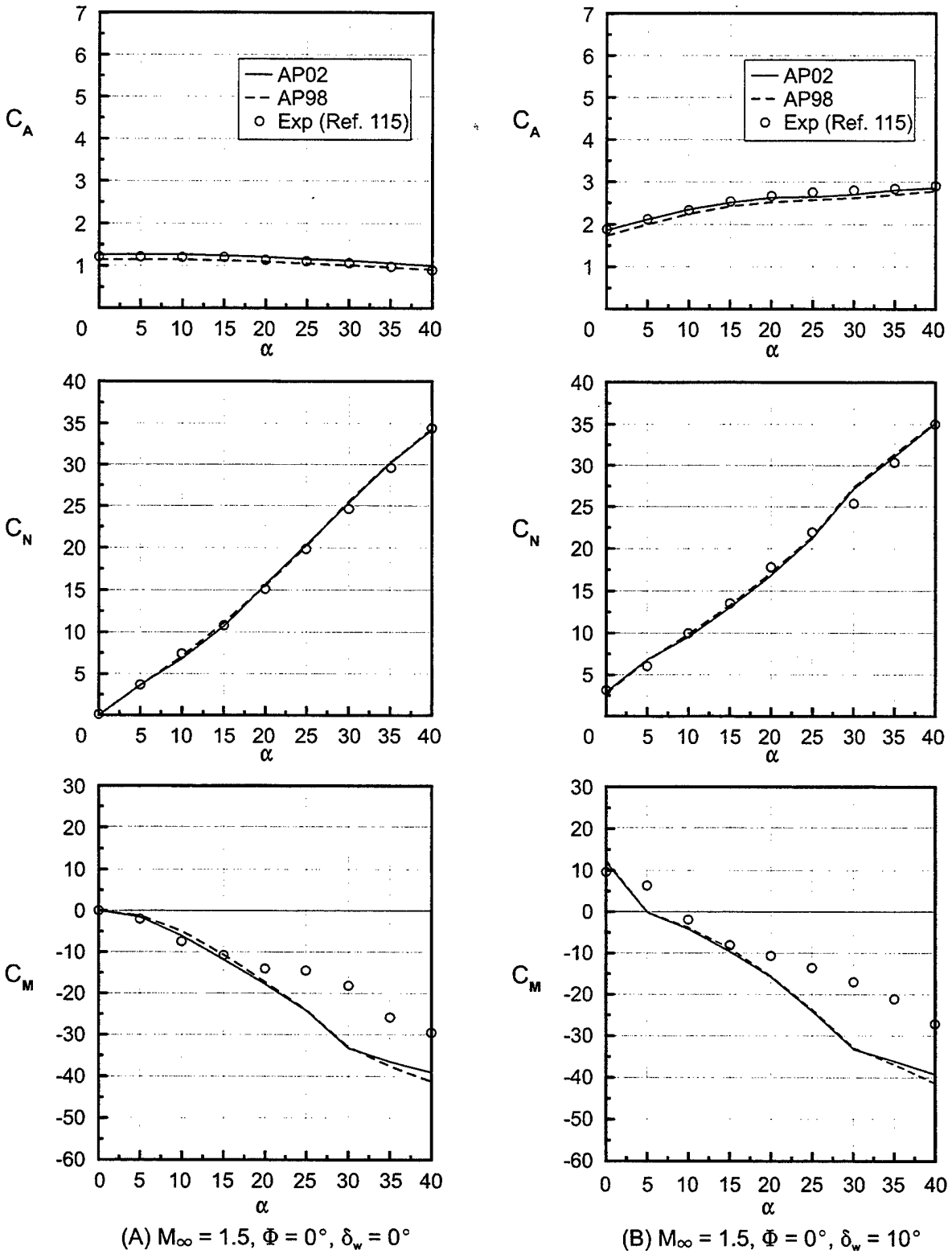

FIGURE 40. COMPARISON OF EXPERIMENT AND THEORY FOR C_A, C_N AND C_M FOR FIGURE 39 WING CONTROL CASE

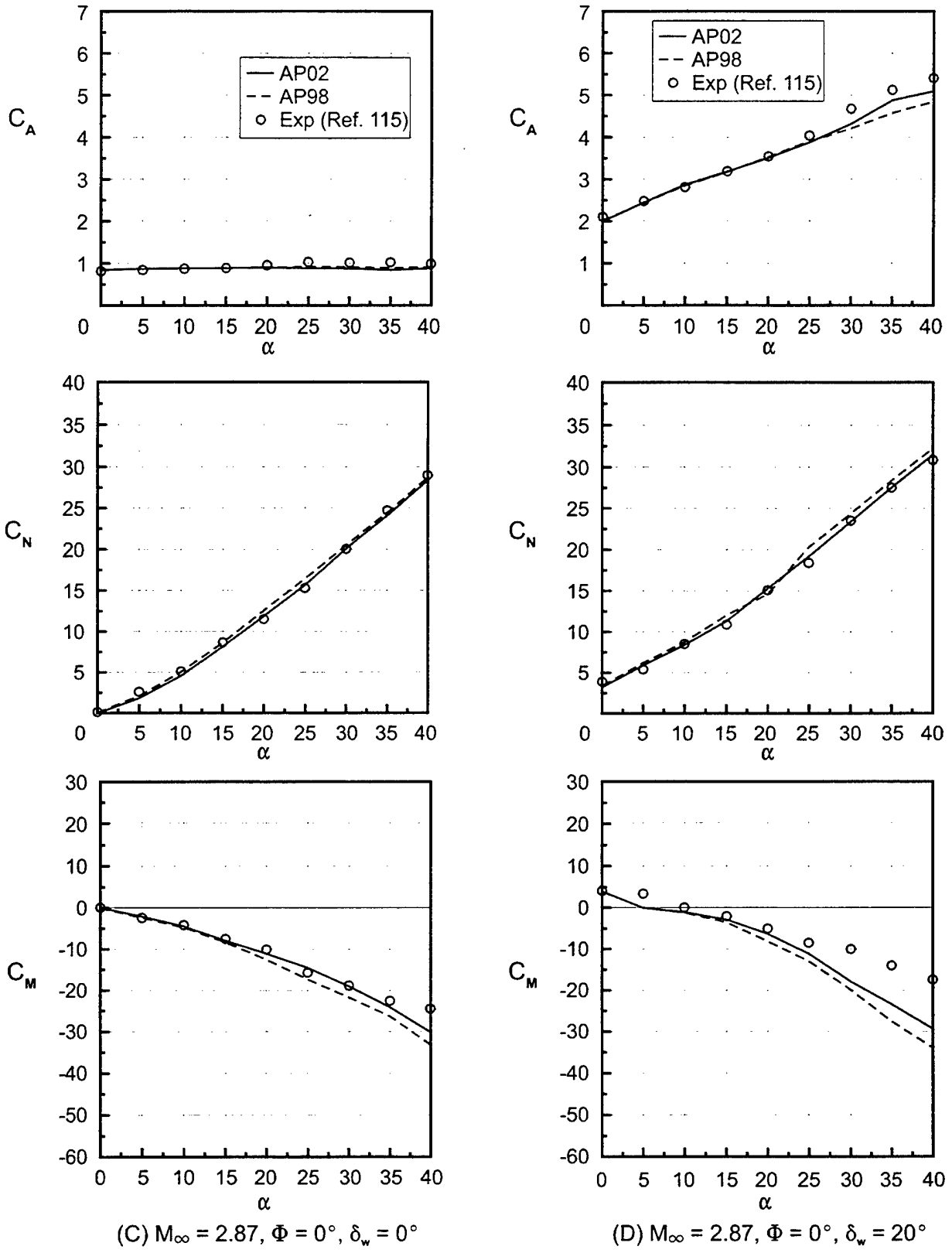

FIGURE 40. COMPARISON OF EXPERIMENT AND THEORY FOR C_A, C_N AND C_M FOR FIGURE 39 WING CONTROL CASE (Continued)

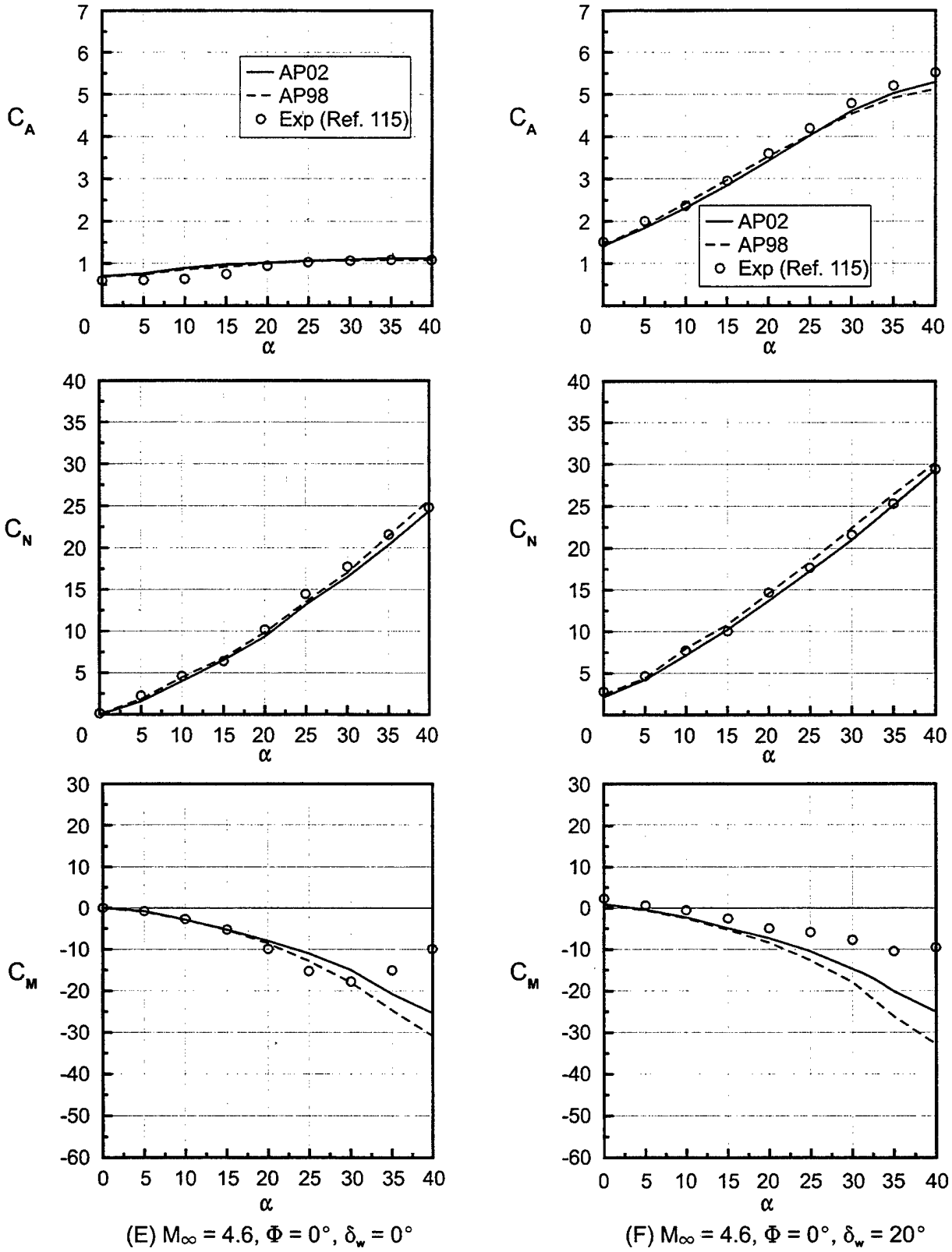

FIGURE 40. COMPARISON OF EXPERIMENT AND THEORY FOR C_A, C_N AND C_M FOR FIGURE 39 WING CONTROL CASE (Continued)

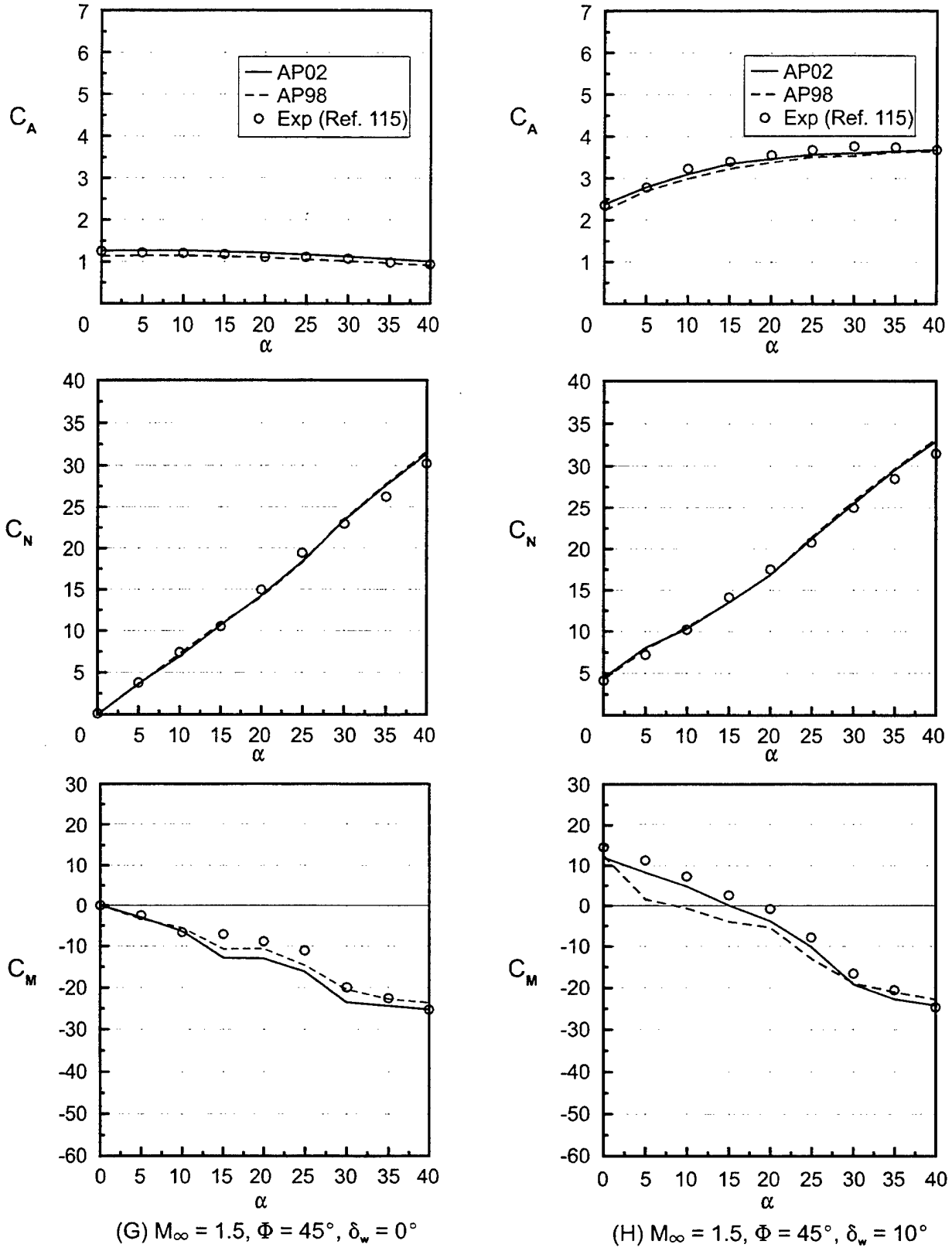

FIGURE 40. COMPARISON OF EXPERIMENT AND THEORY FOR C_A, C_N AND C_M FOR FIGURE 39 WING CONTROL CASE (Continued)

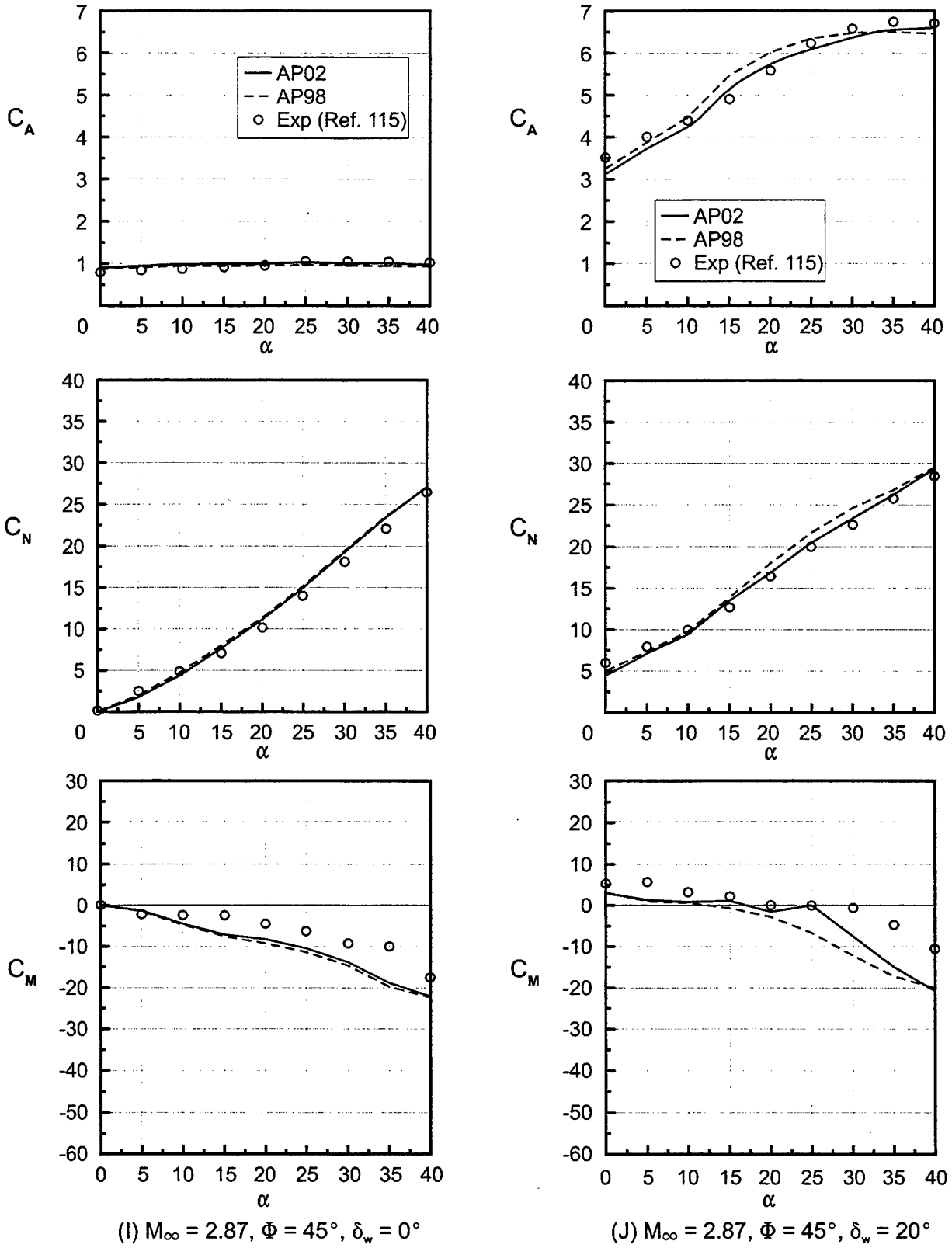

FIGURE 40. COMPARISON OF EXPERIMENT AND THEORY FOR C_A, C_N AND C_M FOR FIGURE 39 WING CONTROL CASE (Continued)

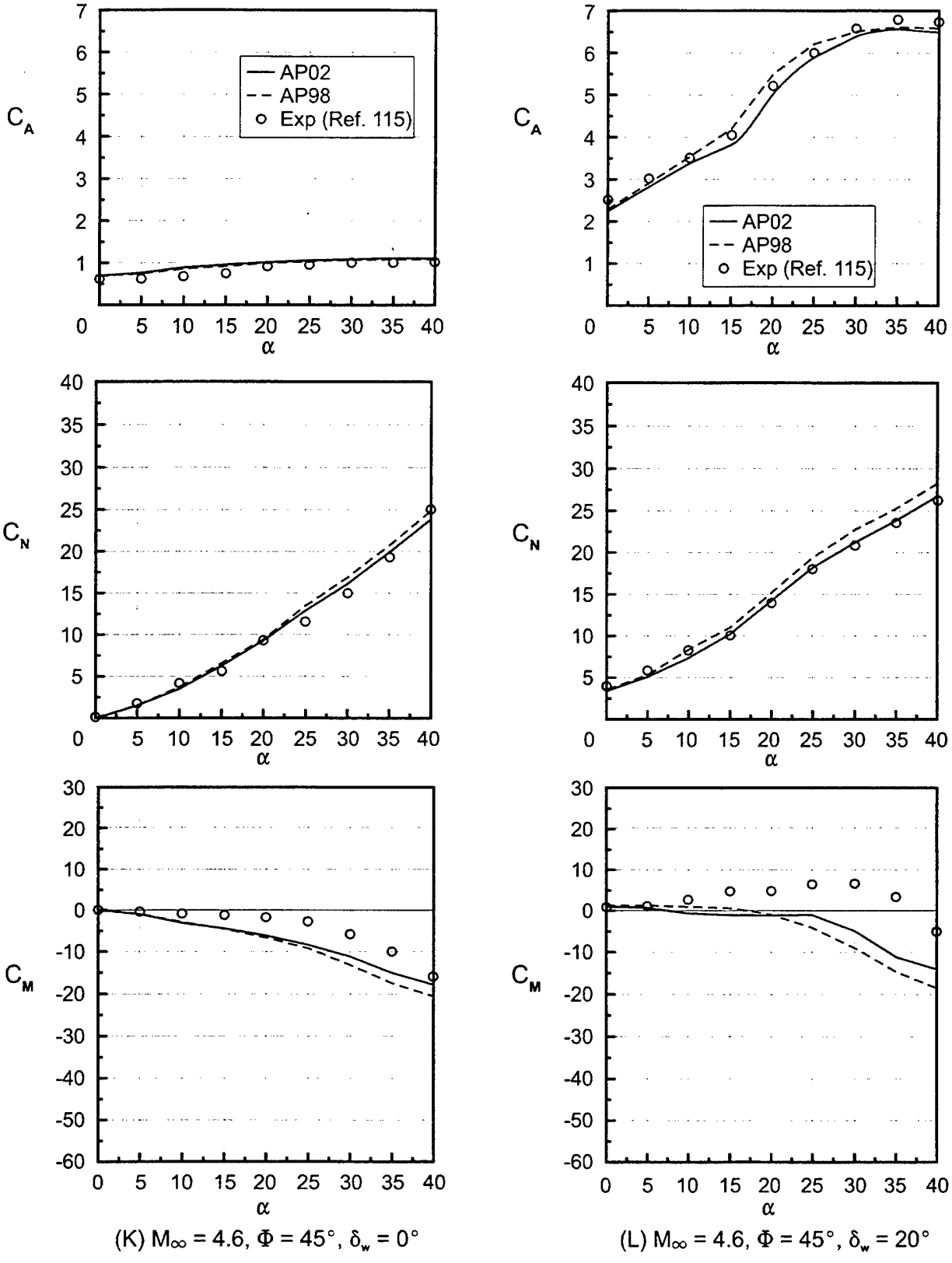

FIGURE 40. COMPARISON OF EXPERIMENT AND THEORY FOR C_A, C_N AND C_M FOR FIGURE 39 WING CONTROL CASE (Continued)

where the bow shock intersects the wing shocks. This nonlinear phenomenon is not modeled in the $\Phi = 0$ deg roll orientation at all. For the $\Phi = 45$ deg roll, the center of pressure shift partially accounts for this phenomenon, but not entirely. Center of pressure errors approach 0.6 caliber or 3 percent of the body length at $M_\infty = 4.6$ and $\alpha = 40$ deg. The other point is that the normal force predicted by the AP02 for combined α and δ_W is better than the AP98 at $M_\infty = 4.6$. The reason for this phenomenon has to do with the fact that the wing-alone normal force tables were decreased slightly at $\alpha = 60$ deg for the AP02.

Figures 40G and 40H present $M_\infty = 1.5$ results of theory compared to experiment for $\Phi = 45$ deg roll, again for the wing-controlled case of Figure 39. Figures 40G and 40H give C_A, C_N, and C_M for $M = 1.5$ and $\delta_W = 0$ and 10 deg. Figures 40I and 40J give similar results for $M_\infty = 2.87$ and $\delta_W = 0$ and 20 deg, and Figures 40K and 40L give results for $M_\infty = 4.6$ and $\delta_W = 0$ and 20 deg. Figure 40L shows the same phenomena as Figure 40F. That is, with the lowering of C_{N_W} at $\alpha = 60$ deg in Table 4C to be more in line with the Stallings data,[84] improvements in normal force coefficient prediction are realized. Note that reasonably good agreement is obtained between experimental data and both the AP98 and AP02 for all static aerodynamics at all three Mach numbers and for all control deflections. Here, the worst-case center of pressure error is less than 3 percent of the body length.

Figure 41 presents results for the Figure 39 configuration where the tail, versus the wing, is used for control. Here, only the $\delta_T = -10$ deg and -20 deg results are shown as the $\delta_T = 0$ deg control is basically the same as that in Figure 40 for $\delta_W = 0$ deg. Both the AP02 and AP98 give good results for C_A, C_N, and C_M. Note the good agreement of the AP02 and the AP98 with the data. Again, the worst case error on pitching moment results is a center of pressure error of less than 3 percent of the body length.

In general, for the configuration of Figure 39, the AP02 average errors show slight improvements over the AP98. This is primarily because the AP98 comparisons to data were already extremely good and the changes to the AP98 methodology based on the Reference 70 data base were minor for this configuration.

The second configuration is taken from Reference 116 and is a canard-body-tail missile configuration. It is 22.2 calibers in length, and the nose is hemispherical. The tail surfaces are fairly large, with aspect ratio 0.87, and fairly thick, with truncated trailing edges. The canards are aspect ratio 1.73. The configuration is shown in Figure 42A. The hangers which are on the wind tunnel model were not modeled by the APC. Tests were conducted for $M_\infty = 0.2$ to 4.63, AOA of 0 to 20 deg, control deflections of 0 to 20 deg, roll of 0 to 45 deg, R_N/ft of 2×10^6 for a model with boundary layer trips. Base pressure values as a function of M_∞ and AOA were given in Reference 116 and these values were added to the axial force information so total axial force values could be shown.

Figure 42B gives the comparison of theory and experiment for $\Phi = 0$ deg roll for both 0 and 20 deg control deflections. Results are shown in terms of C_A, C_N, and C_M versus Mach number for $\alpha = 20$ deg. Viewing Figure 42B, it is seen that the AP98 and AP02 both give good agreement to data. In comparing the AP02 to the AP98 and experiment, it is seen that the AP02

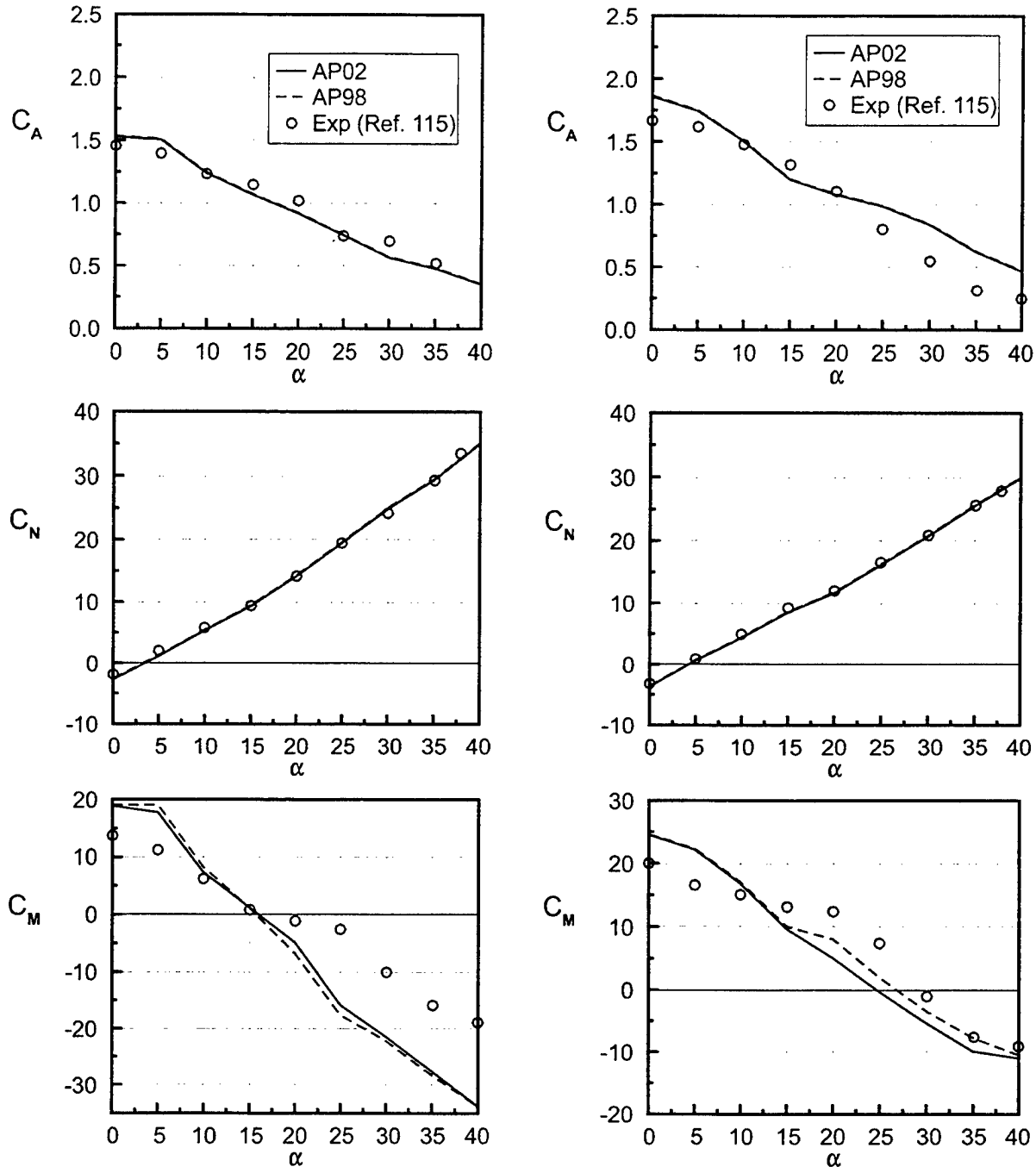

FIGURE 41. COMPARISON OF EXPERIMENT AND THEORY FOR C_A, C_N AND C_M FOR FIGURE 39 TAIL CONTROL CASE

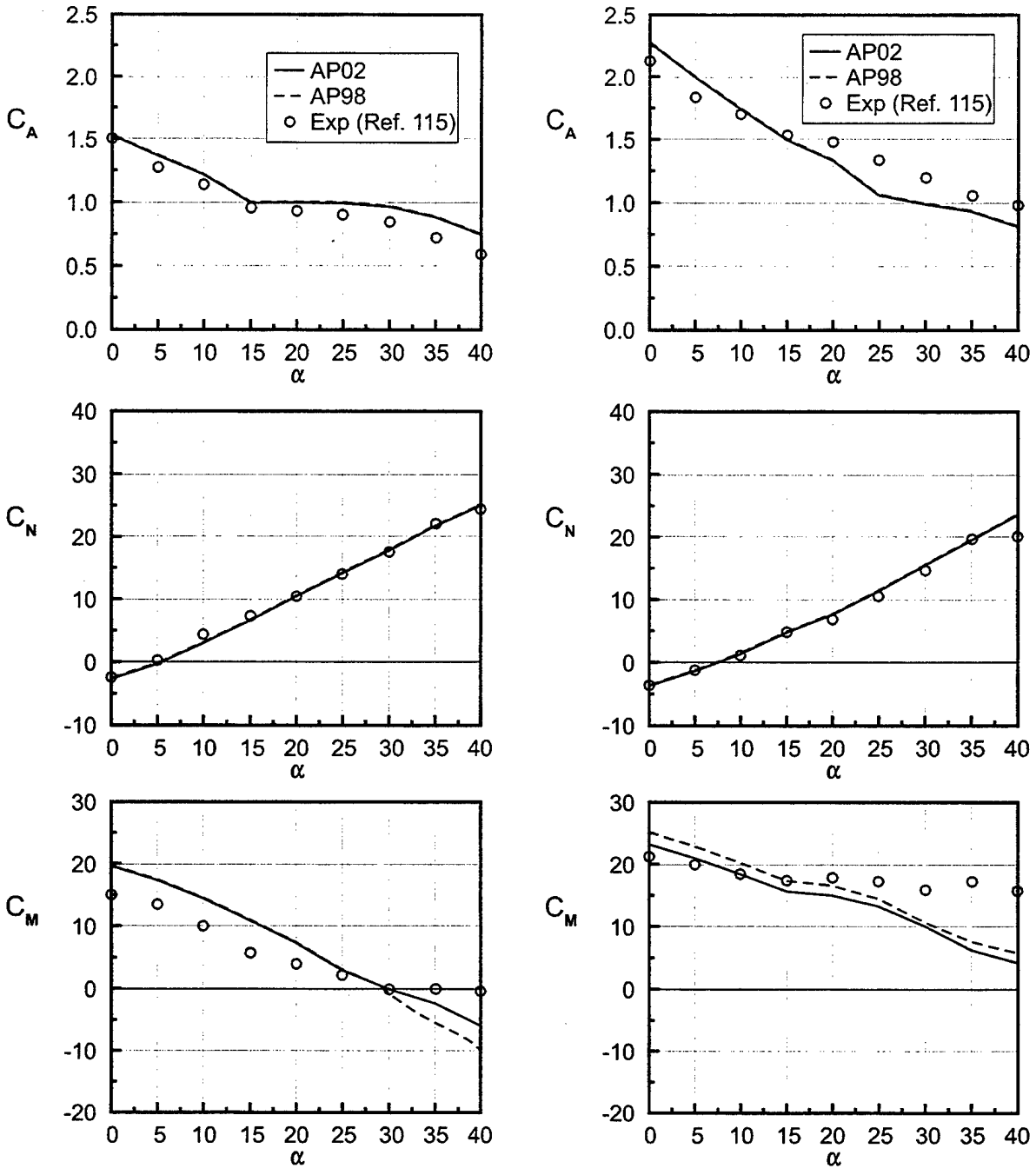

(C) $M_\infty = 2.87$, $\Phi = 0°$, $\delta_\tau = -20°$

(D) $M_\infty = 2.87$, $\Phi = 45°$, $\delta_\tau = -20°$

FIGURE 41. COMPARISON OF EXPERIMENT AND THEORY FOR C_A, C_N AND C_M FOR FIGURE 39 TAIL CONTROL CASE (Continued)

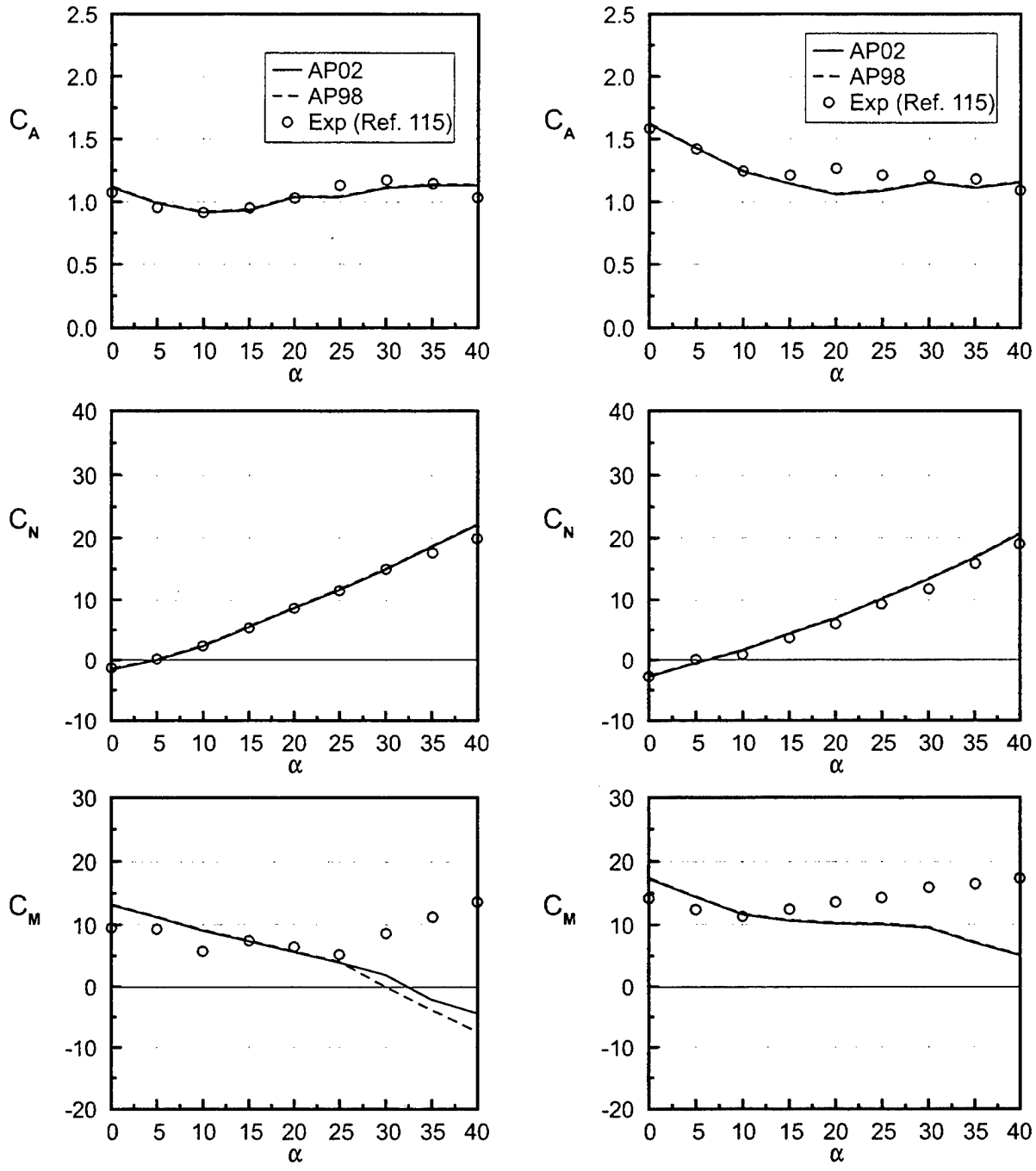

(E) $M_\infty = 4.6$, $\Phi = 0°$, $\delta_\tau = -20°$ (F) $M_\infty = 4.6$, $\Phi = 45°$, $\delta_\tau = -20°$

FIGURE 41. COMPARISON OF EXPERIMENT AND THEORY FOR C_A, C_N AND C_M FOR FIGURE 39 TAIL CONTROL CASE (Continued)

shows some improvement in prediction of normal force and pitching moment coefficients compared to the AP98 for the following conditions: (1) Mach numbers less than 0.9 and (2) Mach numbers greater than 2.1 for normal force coefficient. For the intermediate Mach numbers, prediction accuracy of the two versions of the APC is comparable. Axial force prediction accuracy for this configuration of the two codes also shows the AP02 to be slightly better than the AP98.

The $\Phi = 45$ deg roll comparisons of C_A, C_N, and C_M for $\alpha = 20$ deg and $\delta_C = 0$ and 20 deg are shown in Figure 42C. In general, the AP02 gives better normal force coefficient predictions compared to data than does the AP98. Pitching moment coefficients predicted by the AP02 are also slightly better than those predicted by the AP98, although the improvement is not as great as for the normal force coefficient. Again, slight improvement in axial force coefficient is also seen between the AP02 and AP98.

To summarize the second validation case considered, it is seen that the improvement in normal force prediction accuracy of the AP02 based on the more recent data base of Reference 70 carried over to the Figure 42A configuration. For the 56 data points of Figures 42B and 42C (14 Mach numbers, 2 roll orientations, and 2 control deflections), the average normal force error was reduced from 7.9 percent using the AP98 to 4.2 percent using the AP02. This is a reduction in the normal force prediction error of over 40 percent. Some slight

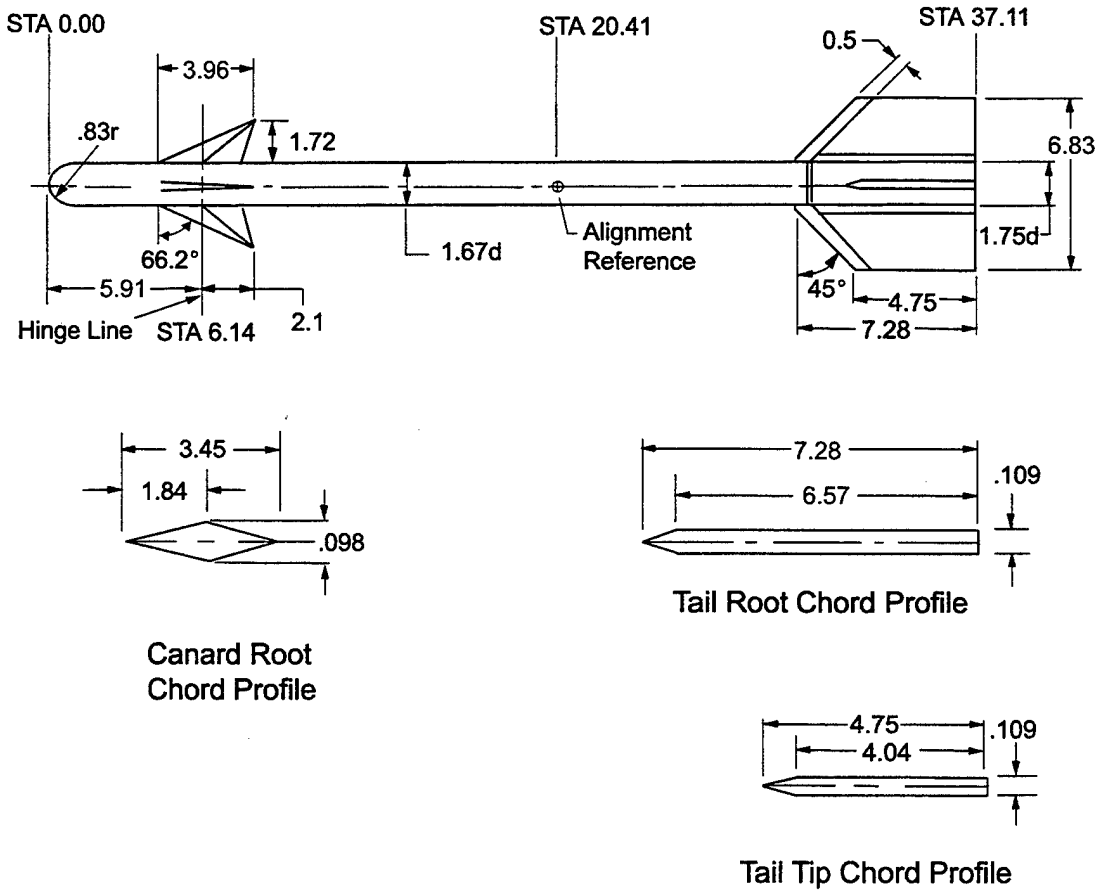

FIGURE 42A. CANARD-BODY-TAIL CONFIGURATION WITH HEMISPHERICAL NOSE[116]

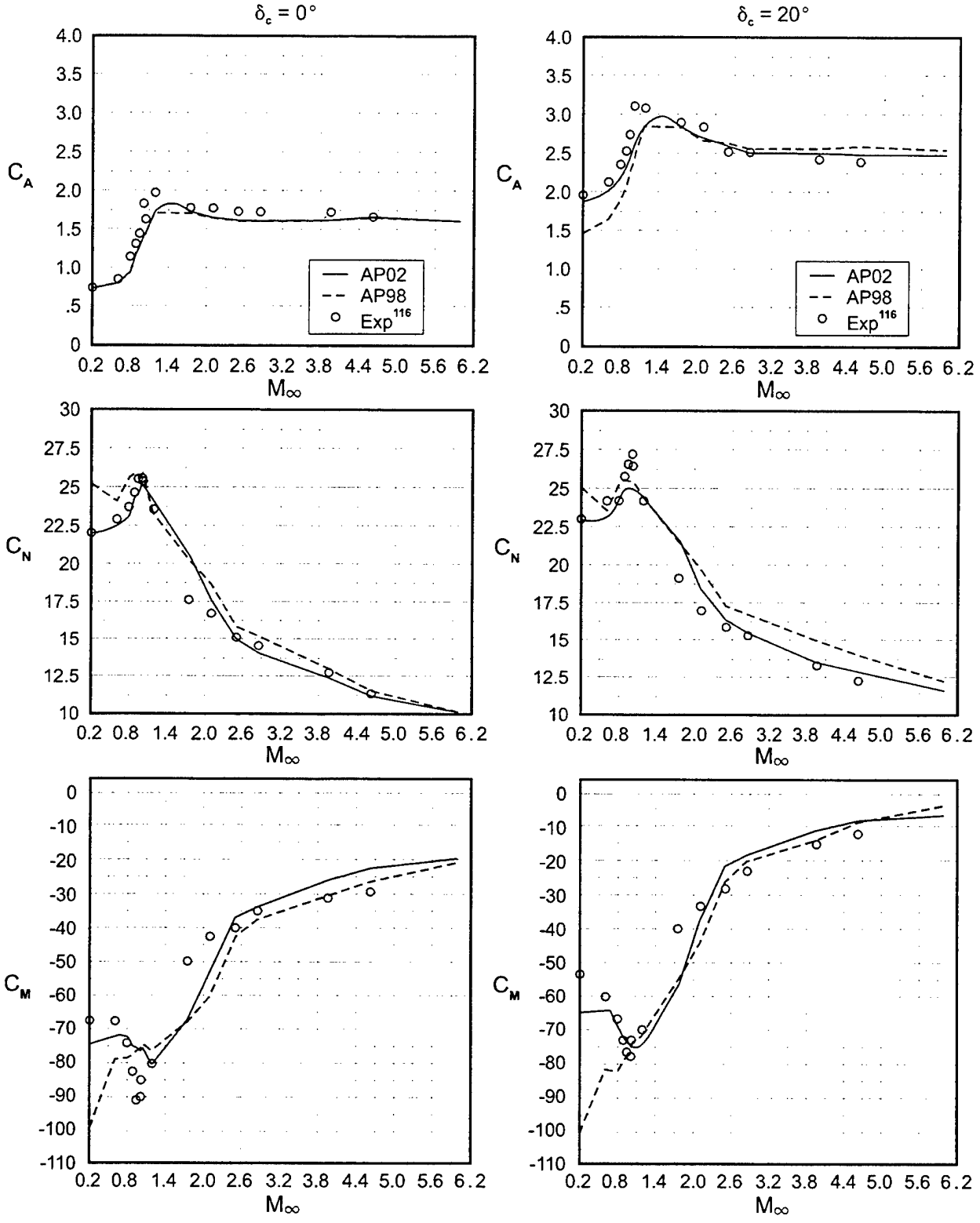

FIGURE 42B. C_A, C_N AND C_M VERSUS MACH NUMBER FOR CONFIGURATION OF FIGURE 42A ($\Phi = 0$, $\alpha = 20$ DEG)

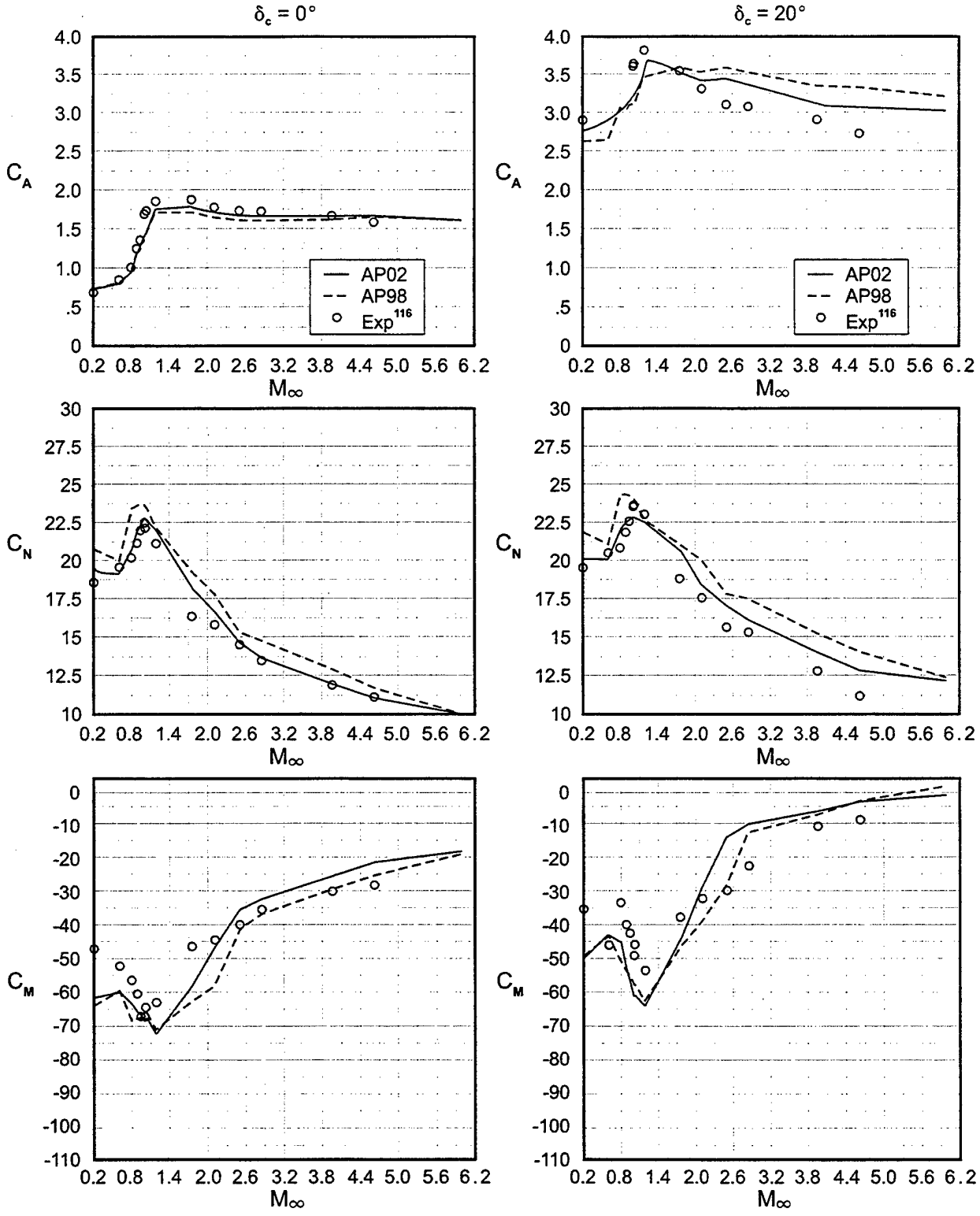

FIGURE 42C. C_A, C_N AND C_M VERSUS MACH NUMBER FOR CONFIGURATION OF FIGURE 42A ($\Phi = 45$, $\alpha = 20$ DEG)

improvement in pitching moment, center of pressure, and axial force was also observed for the AP02 compared to the AP98. However, these improvements were not as large as for normal force coefficient.

The third configuration was tested by Jorgensen.[117] The configuration is shown in Figure 43A and consists of a wing-body and wing-body-tail. Both the wings and tails are fairly large in surface area and aspect ratio. Figure 43B gives the normal force coefficient comparison between the AP98, the AP02, and experiment for the wing-body case at Mach numbers of 0.6, 0.9, 1.5, and 2.0 and AOA to 60 deg. The AP02 provides only slight overall average accuracy improvement over the AP98. Both predictions fall well within the average accuracy goal of ±10 percent. Figure 43C gives both the normal force and center of pressure comparisons for the wing-body-tail case of Figure 43A. Again, the AP02 shows only slight improvement over the AP98 compared to experiment.

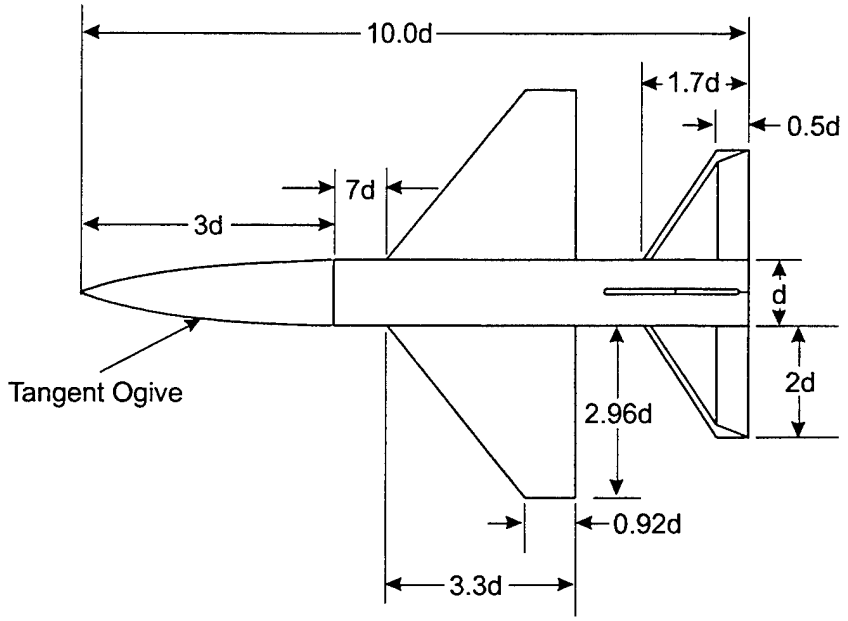

PARAMETERS

$(AR)_T = 3.64$ $\lambda_T = .29$ d = 2.6 in.
$(AR)_W = 2.81$ $\lambda_T = .28$

FIGURE 43A. WING-BODY AND WING-BODY-TAIL CONFIGURATIONS USED FOR COMPARING AP98 TO EXPERIMENT AND AP02

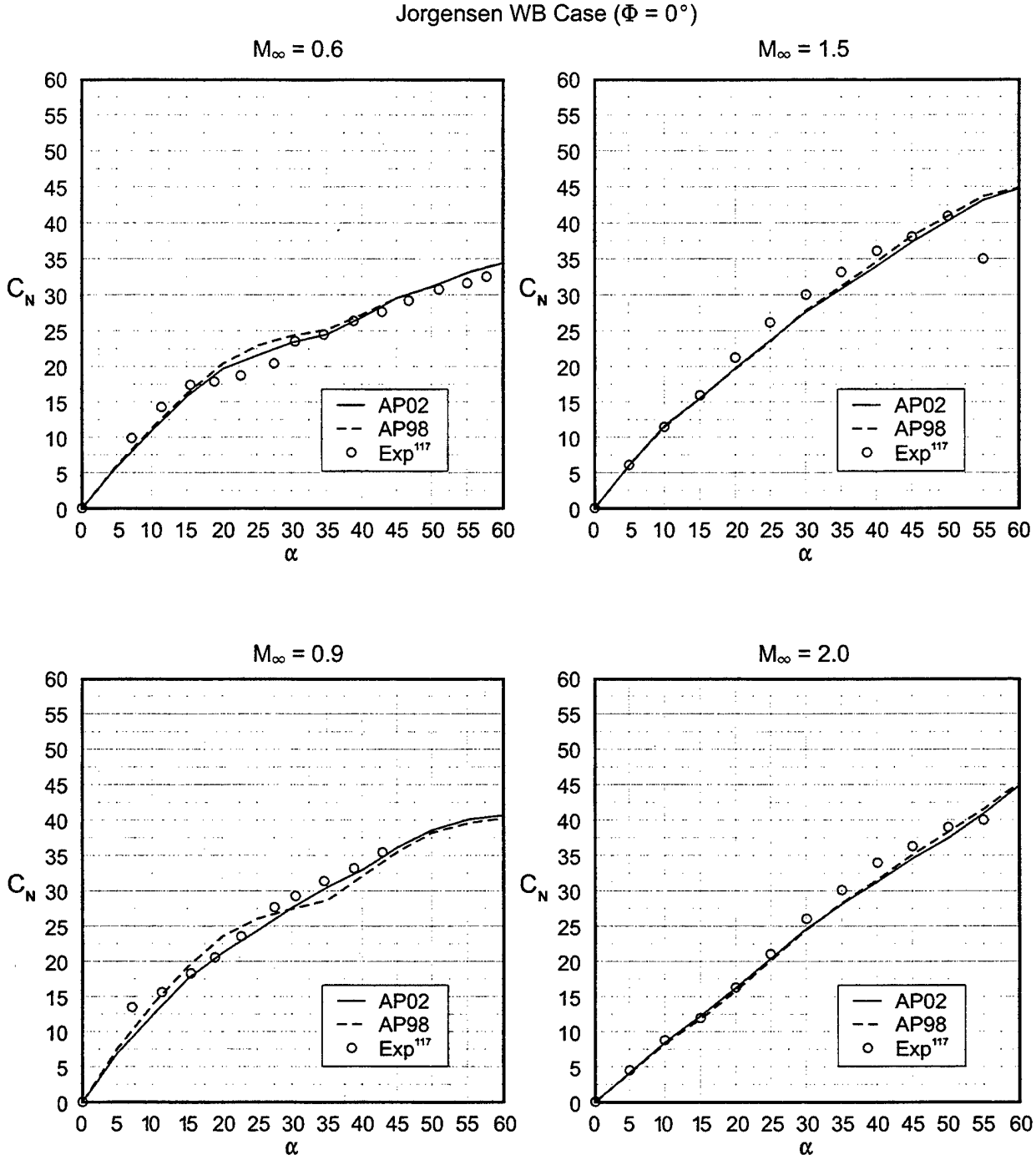

FIGURE 43B. NORMAL FORCE COEFFICIENT COMPARISONS FOR WING-BODY CONFIGURATION OF FIGURE 43A

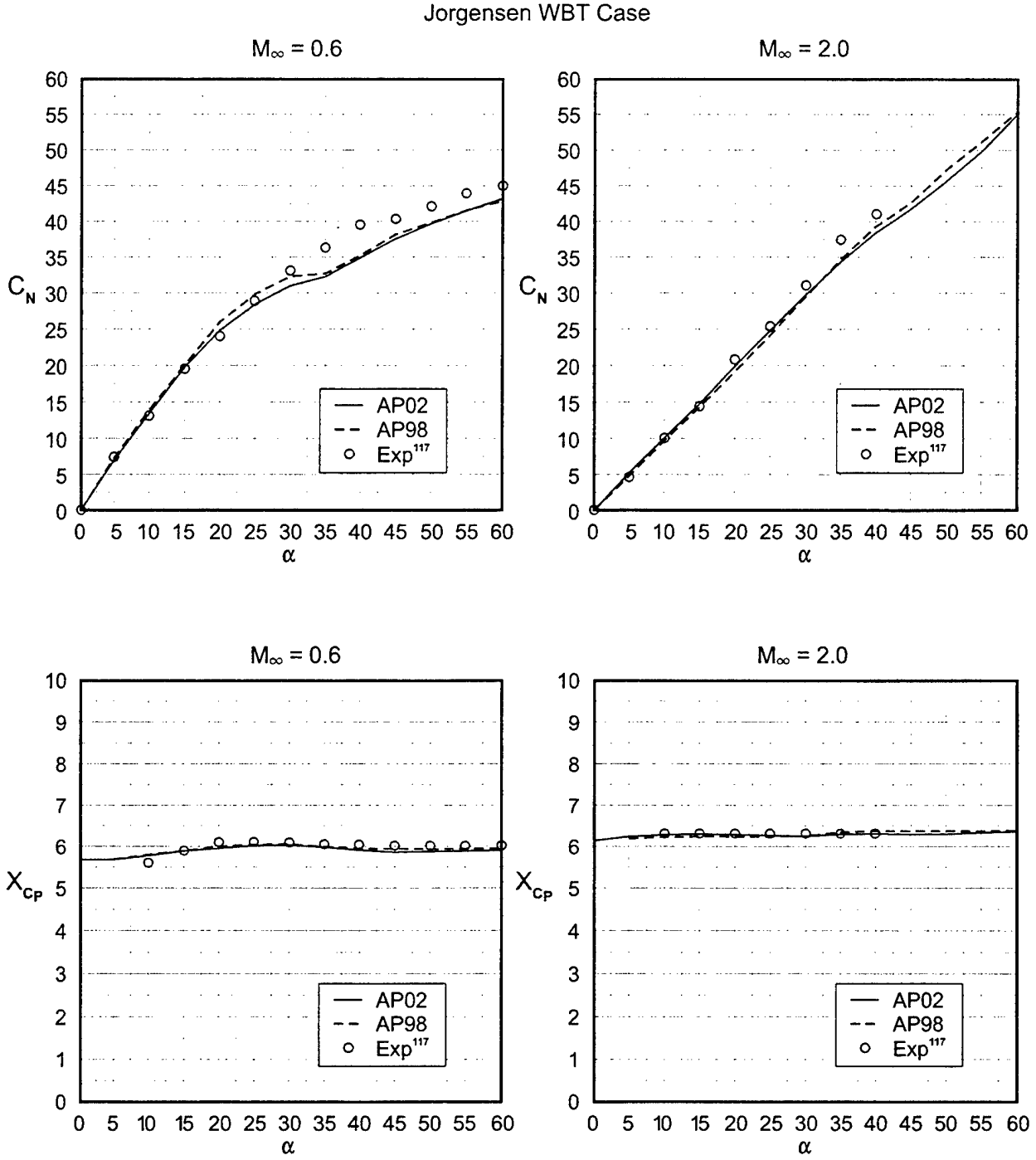

FIGURE 43C. NORMAL FORCE COEFFICIENT AND CENTER OF PRESSURE COMPARISONS FOR WING-BODY-TAIL CONFIGURATION OF FIGURE 43A

The fourth case considered in the evaluation of the improved empirical constants developed for the nonlinear aerodynamic terms of the normal force Equation (1) is taken from Reference 118 and is shown in Figure 44A. The wind tunnel model was about 22 calibers in length with a sharp nose of 2.25 calibers. The canards had an aspect and taper ratio of 2.0 and

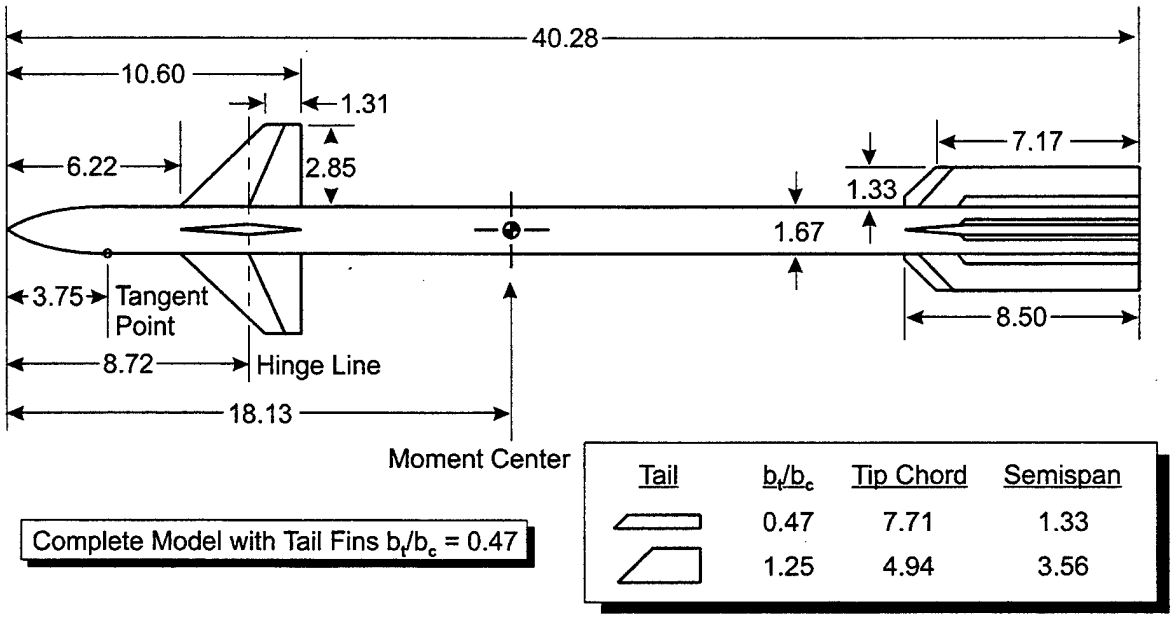

FIGURE 44A. CANARD-BODY-TAIL CONFIGURATION WITH VARYING TAIL SPAN (FROM REFERENCE 118 WITH ALL DIMENSIONS IN INCHES)

0.3, respectively. Various tail fin spans were considered. This model was tested at Mach numbers 1.6 to 3.5 at AOA to about 18 to 20 deg. It had a boundary layer trip present and was tested at a R_N/ft of 2.0×10^6. Reference 118 gave separate values of base axial force coefficient, which were added to the axial force values given in the reference to compare to the AP98 and AP02 computations. To compare the experimental data to theory, Mach numbers of 2.5 and 3.5 are selected at roll angle 45 deg. Also, values of the tail-to-canard semispan of 0.47 and 1.25 are considered. Figures 44B and 44C present the comparison of theory to experiment for b_t/b_c = 0.47 and b_t/b_c = 1.25 at Mach numbers of 2.5 and 3.5, respectively, for C_A, C_N, and C_M.

In examining Figures 44B and 44C, it is seen that the AP02 and AP98 both give excellent agreement with experiment for the b_t/b_c = 0.47 case. However, for the b_t/b_c = 1.25 case, the AP02 shows improvement over the AP98 in both C_N and C_M at both M = 2.5 and M = 3.5.

The next set of wind tunnel data considered for comparison purposes is taken from Reference 119. Body-alone, body-tail, and wing-body-tail configurations were all part of this test series. Figure 45A shows one of the configurations tested and considered here for validation of the AP02 results. The model is 13.5 calibers in length with a 1.5 caliber tangent ogive nose. The wing surfaces are fairly large, with thickness of t/c_r = 0.0178 and wedge angles of 15 deg on the leading and trailing edges. The tail surfaces have thickness of t/c_r = 0.05 and wedge angles of 20 deg. The tests were conducted at Mach numbers 0.7 to 3.08 with Reynolds number varying from about 2×10^6 to 4.6×10^6 per foot. The smooth model without boundary layer trip option was used for the AP02 and AP98 calculations. AOA to 25 deg were considered in the wind tunnel test. For comparison purposes, normal force and pitching moments are compared to

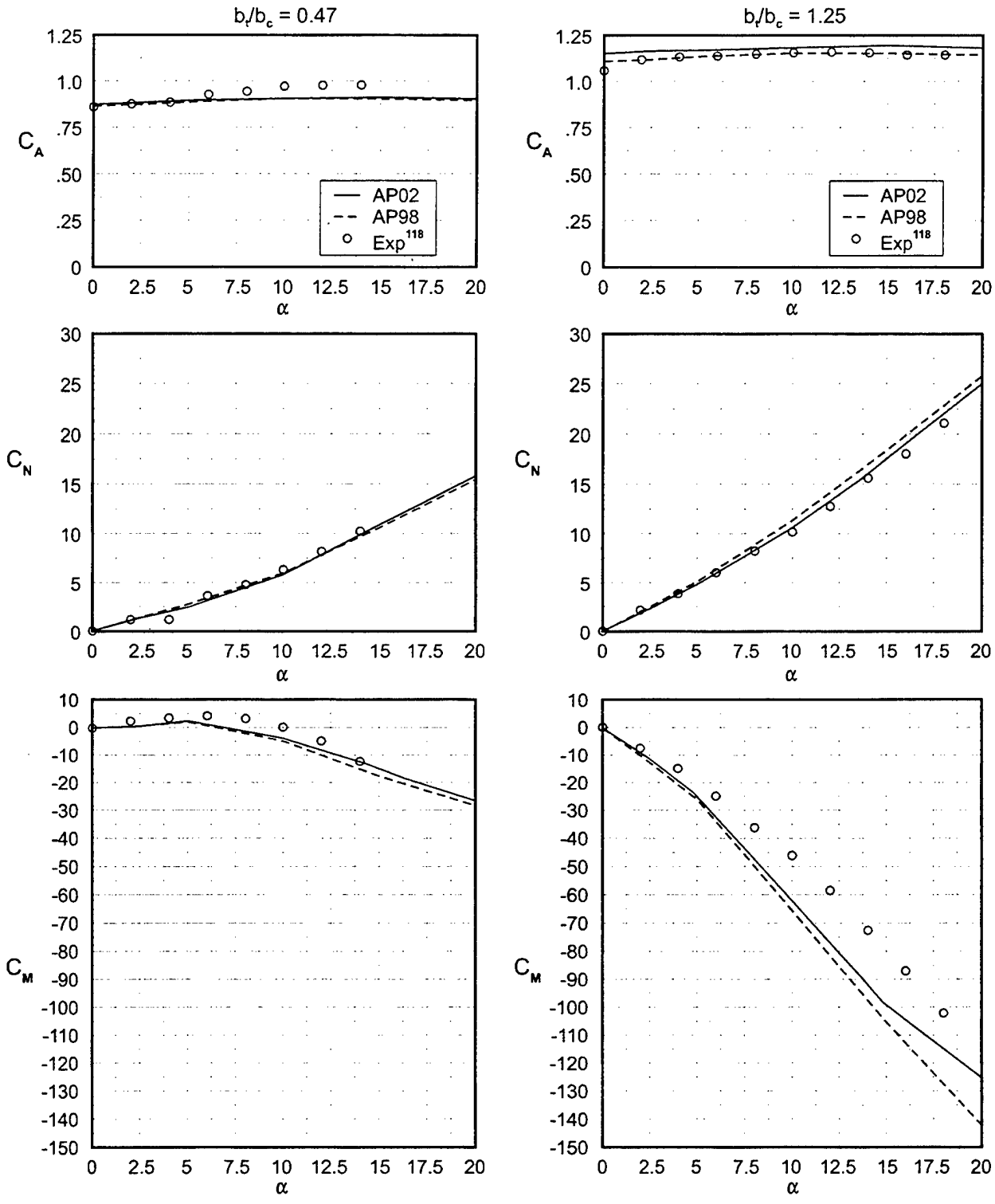

FIGURE 44B. COMPARISON OF THEORY AND EXPERIMENT FOR CONFIGURATIONS OF FIGURE 44A (Φ = 45 DEG, M_∞ = 2.5)

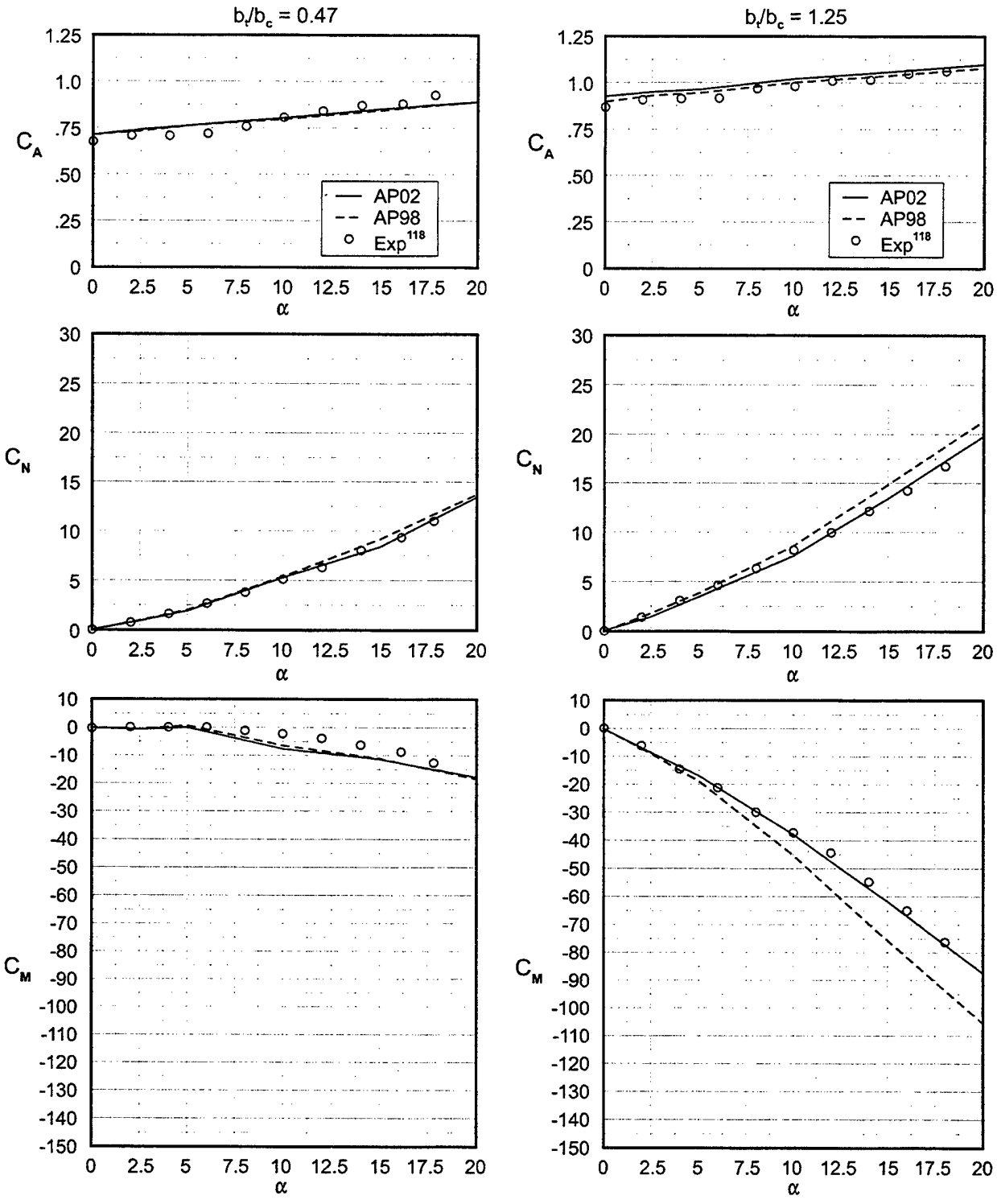

FIGURE 44C. COMPARISON OF THEORY AND EXPERIMENT FOR CONFIGURATIONS OF FIGURE 44A (Φ = 45 DEG, M_∞ = 3.5)

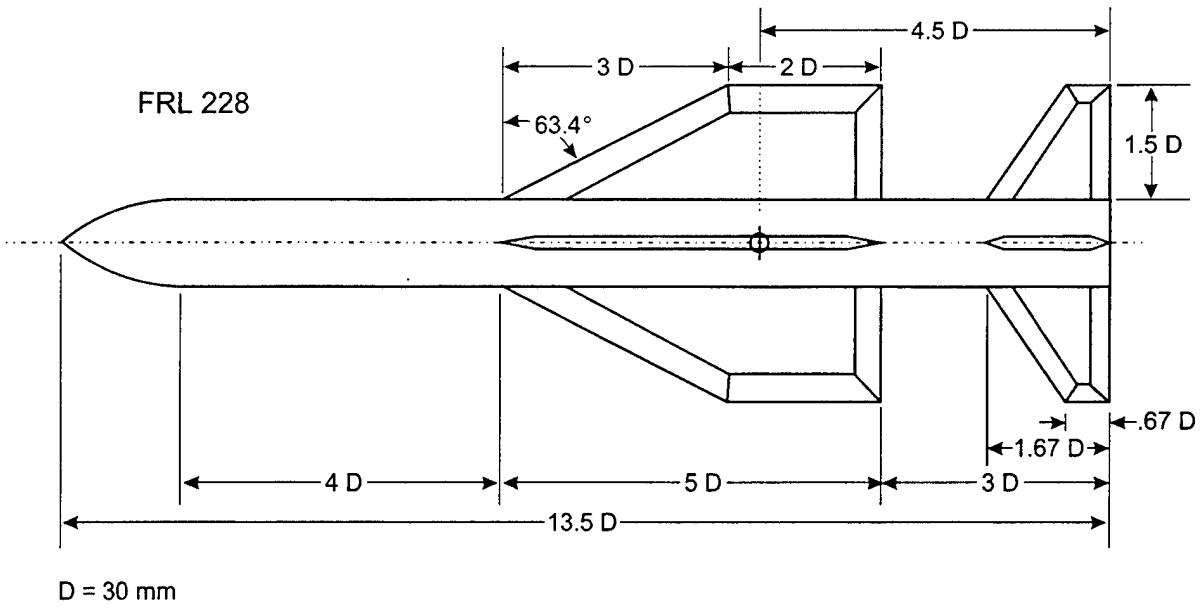

FIGURE 45A. WING-BODY-TAIL CONFIGURATION CONSIDERED FOR VALIDATION WITH AP02 AND AP98 (REFERENCE 119)

data at $M_\infty = 1.42$ and 3.08 for the $\Phi = 0$ deg roll orientation. Figure 45B presents these results. As seen in the figure, both the AP02 and AP98 give quite acceptable comparisons to data, with the AP02 giving slightly better comparisons for both the pitching moment and normal force coefficients. Both versions of the APC give aerodynamics well within the accuracy goals. Reference 119 also gives axial force information where the base pressure has been subtracted. Unfortunately, only a side camber tap was used, so the AOA information was not believed to be accurate. Hence, no axial force comparisons with AOA are shown.

The final case is shown in Figure 46 and the test data was given in a report by Howard and Dunn.[120] This configuration has dorsals that have an aspect ratio of 0.12 and tail surfaces that have an aspect ratio of 4.0. The exact configuration illustrated at the top of Figure 46 is not within the allowable constraints for fin planform required by the APC. Therefore, a modified version of the fin planforms is required, one that meets the constraints of the APC. This configuration is shown in the middle of Figure 46. Note that the parameters that were held constant for the fin planforms were area, aspect ratio, span, taper ratio, leading-edge sweep angle, and location of the geometric centroid of the planform area. The Howard and Dunn[120] work gave only normal force as a function of AOA. The AP02 and AP98 results are also shown at the bottom of Figure 46. Quite acceptable agreement is obtained with the AP02 compared to experiment, even at high AOA. The AP98 and AP02 are somewhat lower than the data suggests at high α. However, part of this underprediction is suspected to be the tendency of a base-mounted sting to give larger-than-true normal forces at subsonic Mach numbers. In making this statement, sting interference effects were assumed to be unaccounted for in Reference 120. Comparing the results of the AP02 to the AP98 in a quantitative sense, the average normal force error of the AP98 for 34 data points is 10.7 percent, whereas the average normal force error of the AP02 is 6.0 percent. This 6.0 percent error is based on 34 data points at both the $\Phi = 0$ and $\Phi = 45$ deg roll orientations.

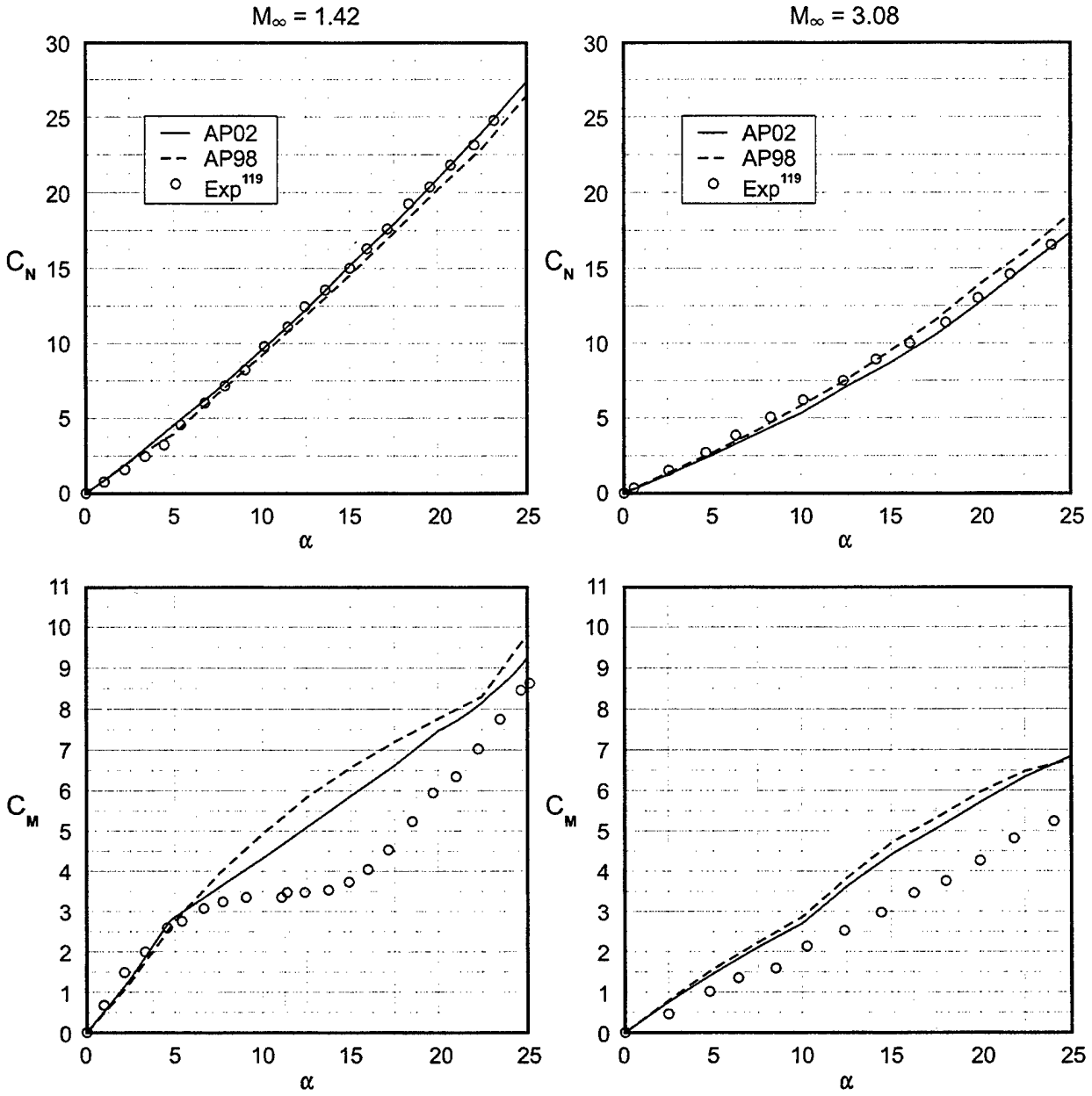

FIGURE 45B. NORMAL FORCE AND PITCHING MOMENT COEFFICIENT COMPARISONS OF THEORY AND EXPERIMENT FOR FIGURE 45A CONFIGURATION (Φ = 0 DEG)

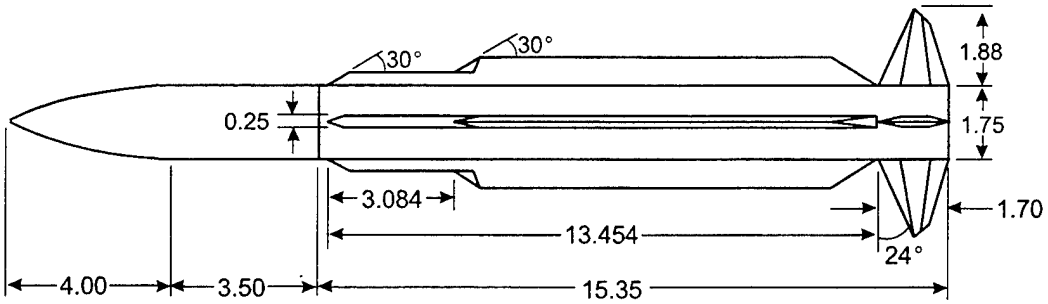

Configuration Tested in Wind Tunnel (From Reference 120)
(All Dimensions in Inches)

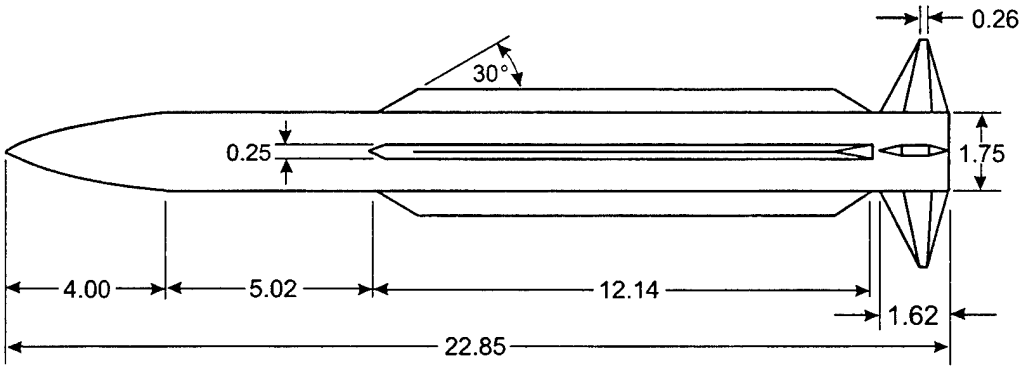

Modified Configuration Used in AP98 and AP02 Computations

Parameters For Both Models

$(AR)_T = 4.0$	$b_t = 3.76$ in.	$\lambda_T = 0.16$	$(\Lambda_{LE})_T = 24°$	$A_T = 3.54$ in.^{2}
$(AR)_D = 0.12$	$b_D = 1.32$ in.	$\lambda_D = 0.77$	$(\Lambda_{LE})_D = 60°$	$A_D = 14.2$ in.^{2}

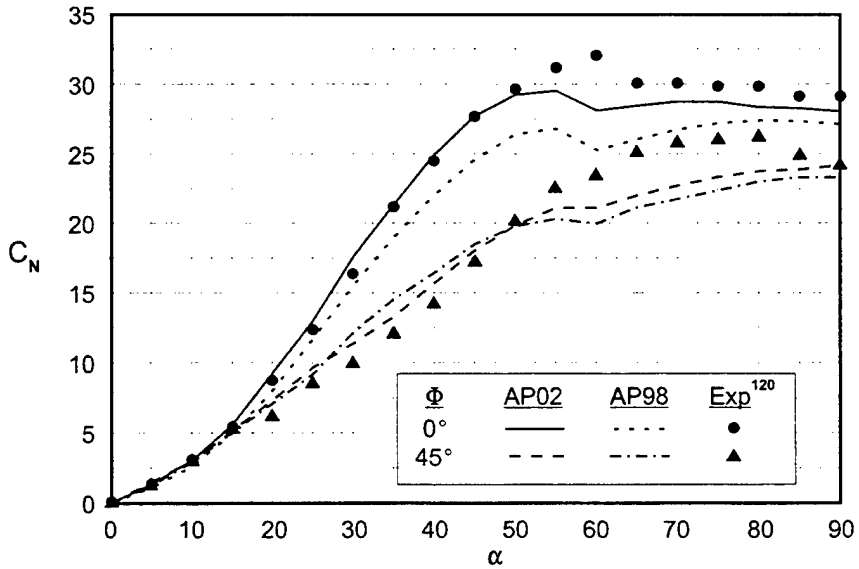

FIGURE 46. NORMAL FORCE COEFFICIENT COMPARISON OF THEORY AND EXPERIMENT ($M_\infty = 0.1$)

To summarize, the nonlinear empirical constants used in the APC to predict nonlinear normal force and pitching moments on missile configurations at high AOA have been refined based on a more recent missile-component, wind tunnel data base.[70] In comparing the new aerodynamic predictions of the revised code (AP02) to the latest released version of the APC (AP98), the following conclusions were drawn:

(1) The refined nonlinear empirical coefficients reduced the average normal force error of the AP02 compared to the AP98 for the NASA/MDAC[70] and NASA/Tri-Service[69] by about one third. Some improvement in center of pressure was also noted, but not quantified.

(2) In comparing the AP02 to the AP98 on six wing-body-tail configurations outside of the missile component data bases upon which the nonlinear empirical constants were derived, it was found that in general, the improvements in average normal force error of the AP02 were seen here as well. The average improvements range from only a slight improvement on one case to over 40 percent reduction in error for the best case. Overall, it is guessed that the average normal force error was reduced by about 20 to 25 percent from the AP98 to the AP02. Some improvement in both pitching moment, center of pressure, and axial force were also noted on several of the cases investigated.

4.2 MULTI-FIN WEAPON AERODYNAMICS

Multi-Fin here is meant 6 or 8 fins as the AP98 already has the capability to handle 2 and 4 fin cases in the computational process. Two cases will be considered in the validation process. Other cases can be found in Reference 67. The first case is an Army 6 fin projectile concept shown in Figure 47A and taken from References 90 and 121. The configuration of Figure 47A consists of a cone-cylinder-body and is 13.99 calibers in length with a diameter of 35.2 mm. The cone half-angle is 8 deg and the leading and trailing edges of the fins are blunt. For the AP02 computations, Reynolds number was computed based on sea level conditions and the body diameter as reference length. The "wind tunnel model with no boundary layer trip" option was used in the AP02 for viscous flow computations. Ballistic data was available over a Mach number range of 3.0 to about 4.5. CFD data was given from M_∞ = 3.0 to 5.5 and AP02 computations were performed over this same Mach number interval.

Comparisons for normal force coefficient and pitching moment coefficient slopes at zero AOA are shown in Figure 47B. The AP02 results at lower Mach numbers tend to be somewhat high compared to the CFD numbers in both cases, and both tend to lie above the range data. Figure 47B also shows the comparison for axial force coefficient. Good agreement is obtained throughout in this instance. The comparison for pitch damping coefficient is also shown in Figure 47B. Once again, the AP02 numbers are somewhat high relative to the CFD results and both tend to lie above the majority of the ballistic data.

A second set of data was available from the guided projectile wind tunnel tests of Reference 122. The model used is shown in Figure 48A. It consists of a circular body, approximately 12.26 calibers in length, with a 3-caliber Von Karman ogive nose. The body

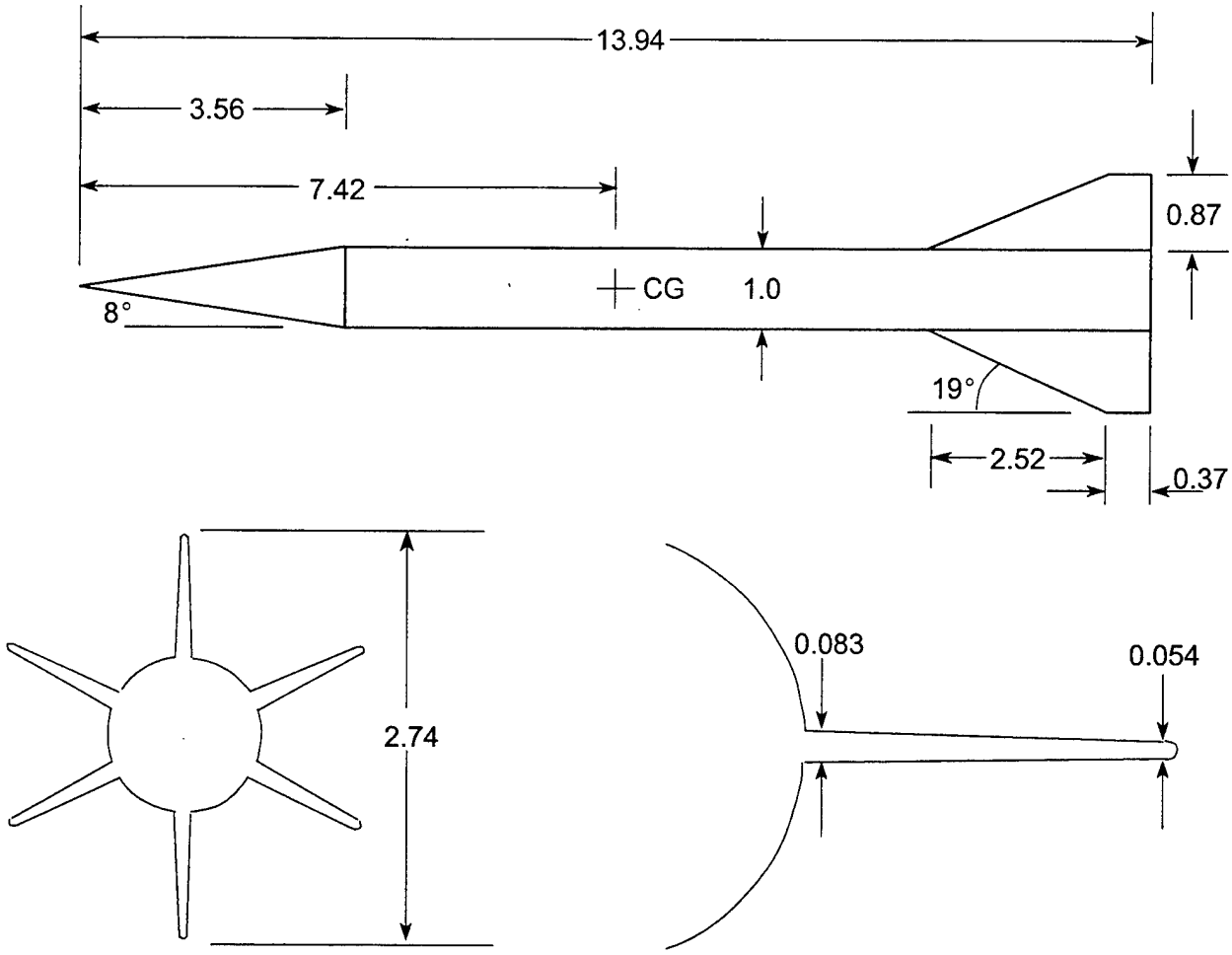

All Dimensions in Calibers (One Caliber = 35.2 mm)

FIGURE 47A. SCHEMATIC OF M735 PROJECTILE CONFIGURATION (FROM REFERENCE 121, 90)

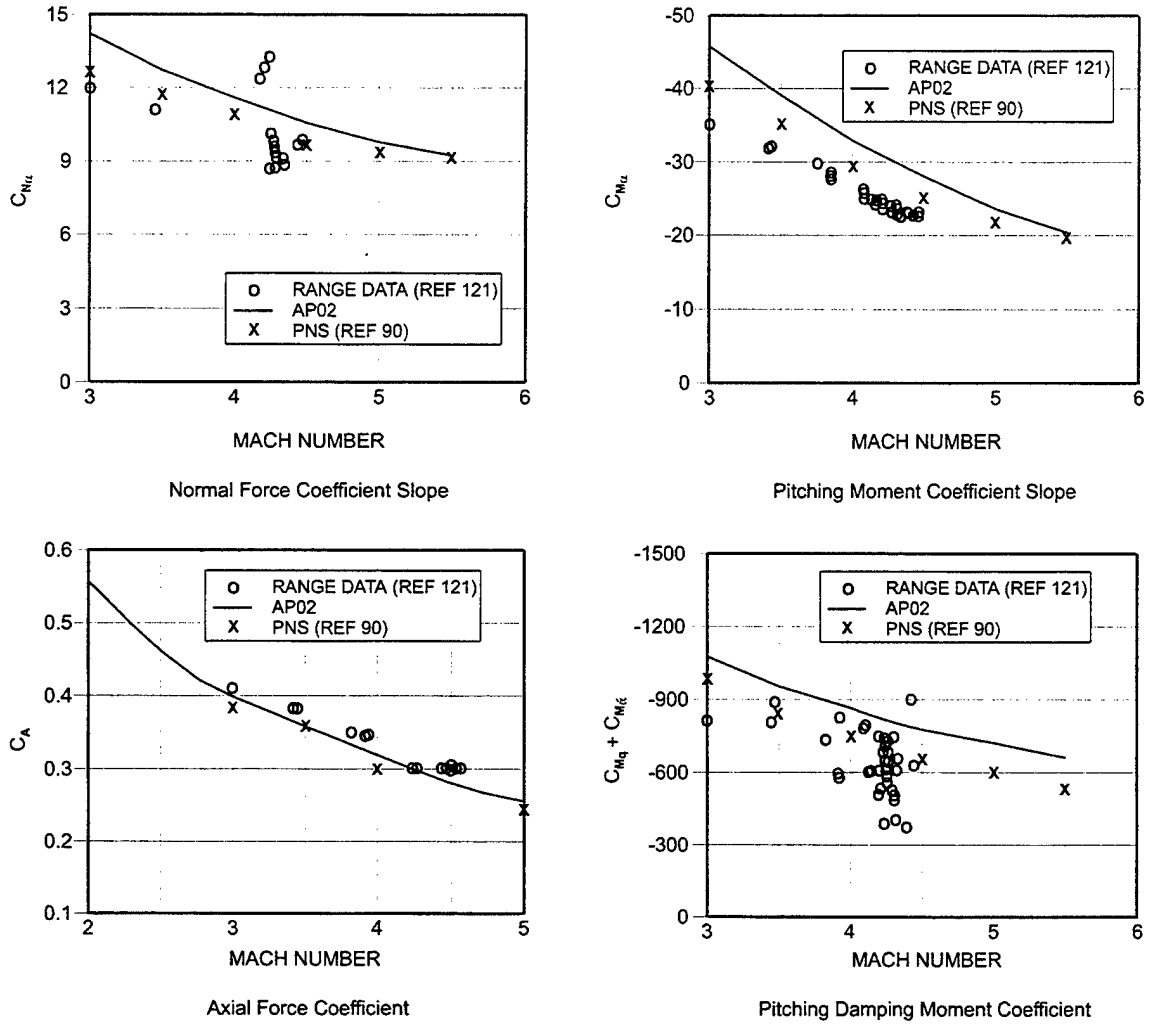

FIGURE 47B. COMPARISON OF NEW MULTIFIN METHOD TO CFD AND EXPERIMENT FOR FIGURE 47A CONFIGURATION

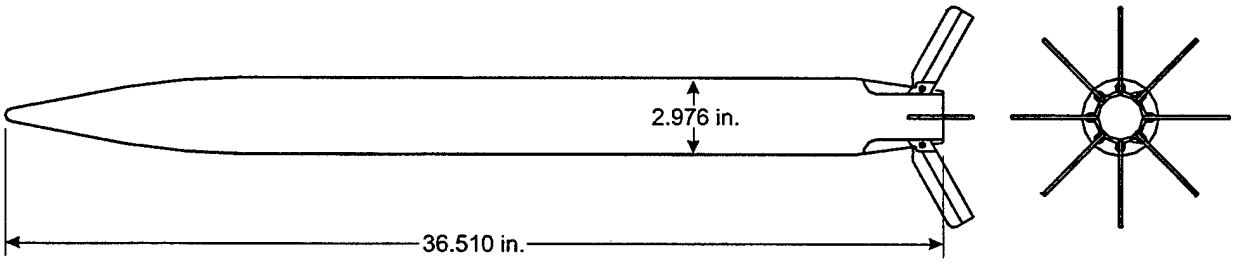

FIGURE 48A. SCHEMATIC OF EIGHT-FIN GUIDED PROJECTILE (FROM REFERENCE 122)

diameter is 2.976 inches. Eight small, high aspect ratio pop-out fins are located at the rear of a short boattail section. The model was also tested with four pop-out canards, but this configuration was not considered since the desire was to isolate the effects of the fins. It was

necessary to modify the fin geometry to conform to the input requirements of AP02. The equivalent fin has a trapezoidal planform with the same area, sweep angle, and aspect ratio as the original. AP02 runs were completed at the indicated Reynolds numbers for each case (which vary from 1.4 to 2.5 $\times$ 10^6 ft) and the "wind tunnel model with no boundary layer trip" option was used.

Wind tunnel data was available in this case for the body alone, so it was used to adjust for the effects of crossflow separation and reattachment. This adjustment is made in the AP02 by changing the critical crossflow Reynolds number and by shifting the value of crossflow Mach number at which the "drag bucket" starts. These two parameters are set to obtain a good fit to the experimental data at each Mach number and are then used for all further computations. The values that were determined are as follows:

M = 0.40: Critical Reynolds Number = 179000
Crossflow Mach Number Shift = −0.03

M = 0.80: Critical Reynolds Number = 333000
Crossflow Mach Number Shift = + 0.09

M = 0.95: Critical Reynolds Number = 333000
Crossflow Mach Number Shift = + 0.13

M = 1.05: Critical Reynolds Number = 333000
Crossflow Mach Number Shift = + 0.17

M = 1.10: Critical Reynolds Number = 333000
Crossflow Mach Number Shift = + 0.185

M = 1.30 Critical Reynolds Number = 2 $\times$ 10^6
Crossflow Mach Number Shift = + 0.25

M = 1.60 Critical Reynolds Number = 2 $\times$ 10^6
Crossflow Mach Number Shift = + 0.25

M = 2.00 Critical Reynolds Number = 2 $\times$ 10^6
Crossflow Mach Number Shift = + 0.25

The comparisons for total normal force for the full 8 fin configuration are shown in Figures 48B and 48C for Mach numbers 0.4, 0.8, 0.95, 1.05, 1.1, 1.3, 1.6, and 2.0, respectively. Angles of attack range up to 15 deg. In general, the comparisons are quite good. The body aerodynamics under these low Mach number conditions can be very sensitive to the subcritical or supercritical status of the flow in the leeward region, making accurate predictions difficult. The differences are related primarily to this effect rather than to the fin modeling.

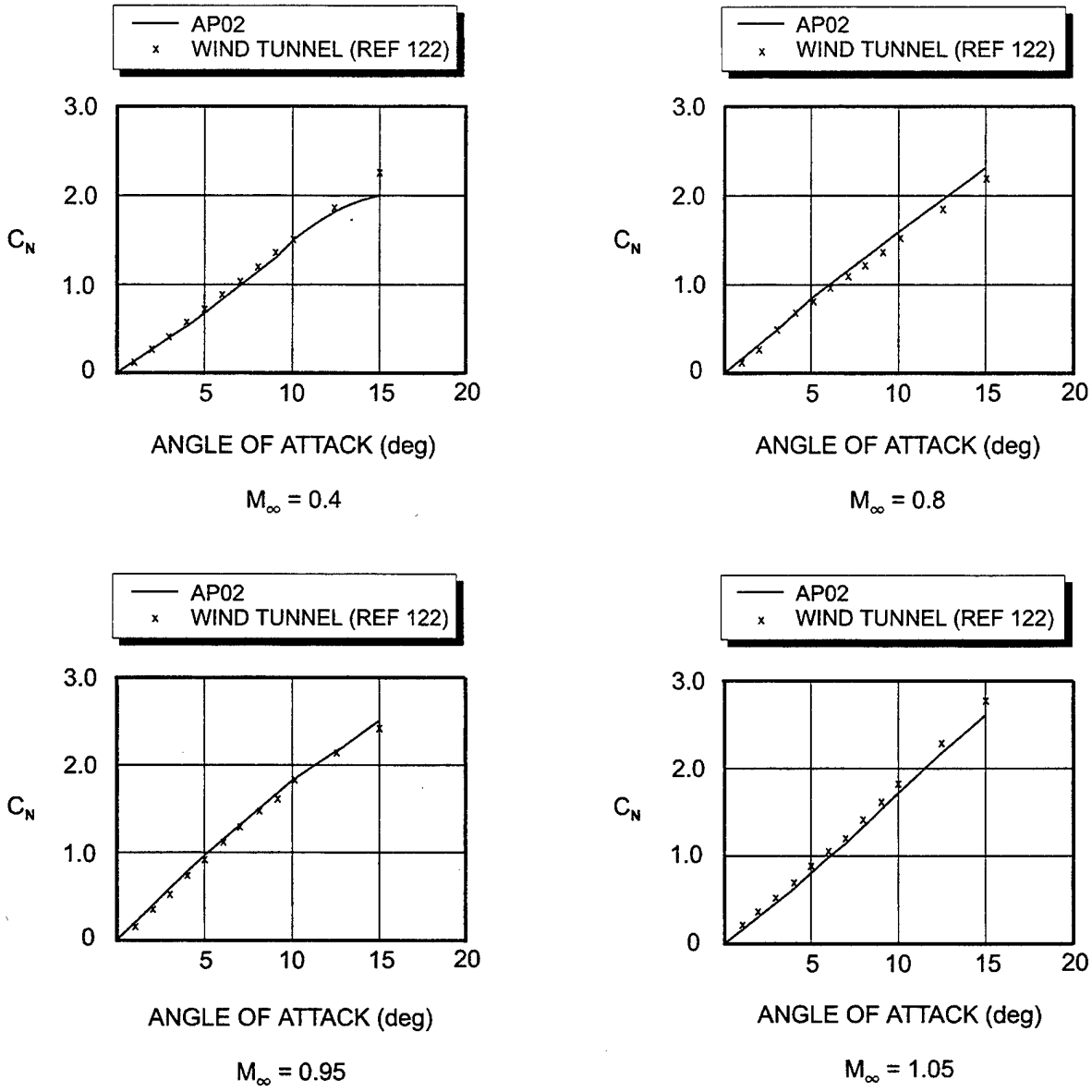

FIGURE 48B. NORMAL FORCE COEFFICIENT COMPARISONS FOR EIGHT-FIN GUIDED PROJECTILE OF FIGURE 48A

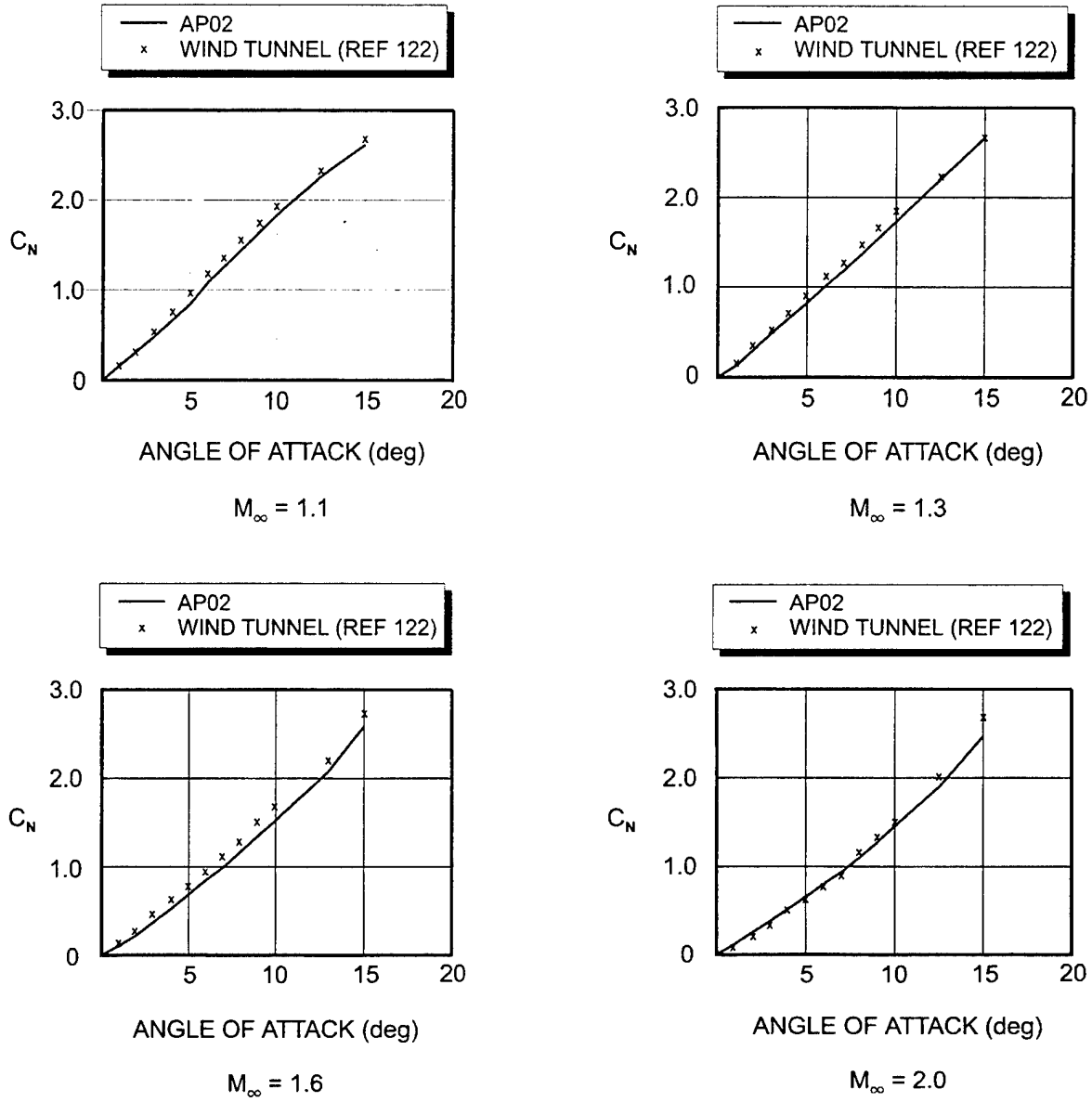

FIGURE 48C. NORMAL FORCE COEFFICIENT COMPARISONS FOR EIGHT-FIN GUIDED PROJECTILE OF FIGURE 48A

4.3 PITCH DAMPING IMPROVEMENTS

Several improvements were made to the AP98 that will be part of the AP02 with respect to pitch damping moment coefficient. These include improvements for body length, Mach number and in particular the addition of the flare (which was unaccounted for in AP98). Five cases will be shown to illustrate the results which will be part of the AP02. Additional cases are found in Reference 74. The AP02 results will be compared to the AP98, test data, and Navier Stokes computations (if available).

The first two cases are configurations without a flare. The first case is a secant ogive cylinder (SOC) configuration (see Figure 49). The ogive is three calibers in length and the afterbody varies in length from 2 to 4 to 7 calibers. The pitch damping coefficient results for each of these afterbody length cases is shown in Figure 49. The results are compared to parabolized Navier Stokes (PNS) computations of Reference 93. Note that as Mach number increases above 2, the AP02 gives results which are in much closer agreement to the PNS results than the AP98 computations.

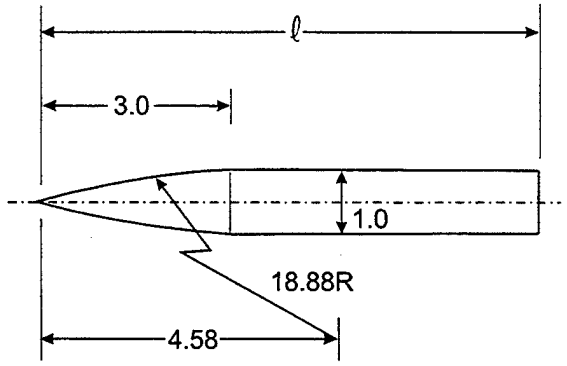

A. Schematic of the SOC Configuration[93]
(all dimensions in calibers)
(one caliber=57.2 mm)

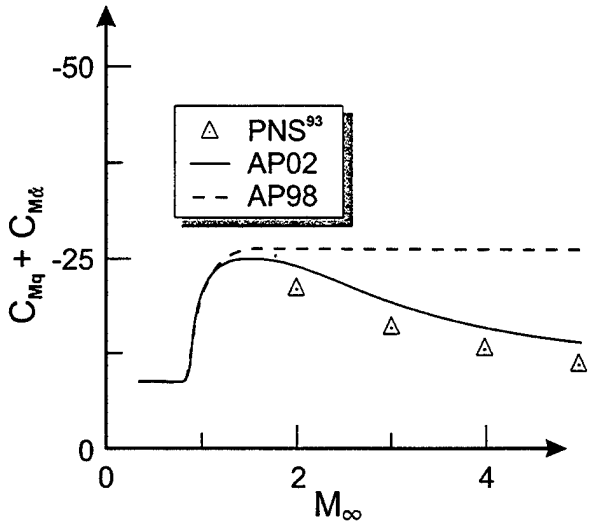

B. $\ell = 5, x_{CG} = 3$

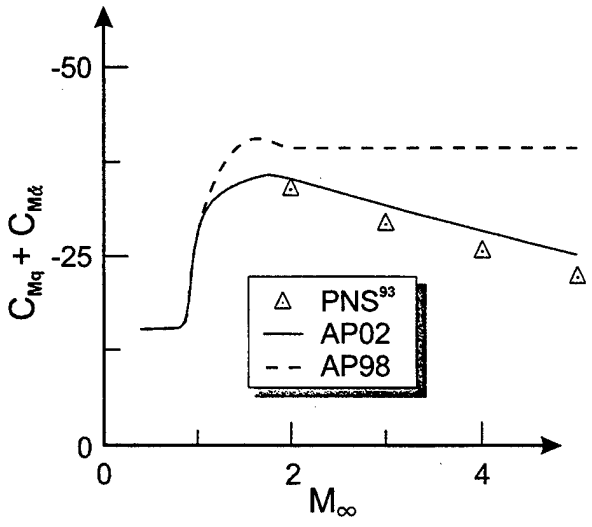

C. $\ell = 6, x_{CG} = 3.6$

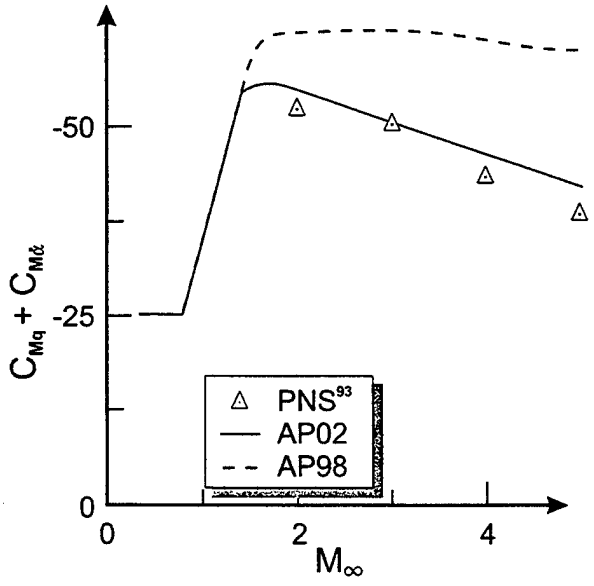

D. $\ell = 7, x_{CG} = 4.2$

FIGURE 49. PITCH DAMPING MOMENT COEFFICIENT PREDICTIONS FOR THE SOC CONFIGURATION

The second case considered is the Army-Navy-Spinner-Round (ANSR) shown in Figure 50. Test data and PNS computations are taken from References 93 and 94. Data is shown in Figure 50 for Mach number 0.8 to 2.5 along with AP02 and AP98 computations. Note that for these low Mach numbers, AP98 and AP02 are about the same and both agree with data and PNS results except for the 9 caliber case. For the 9 caliber case, there is a lot of scatter in the data, but both theories tend to be in the middle of most of the data.

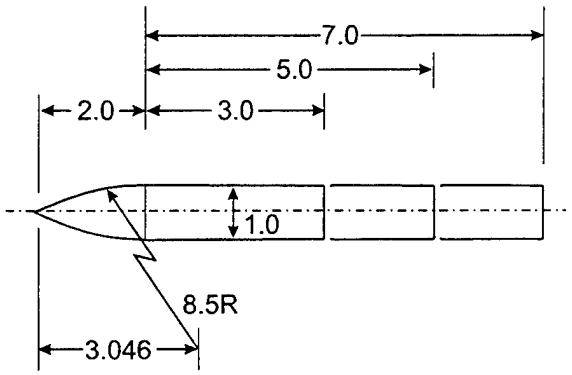

A. Schematic of the ANSR (all dimensions in calibers) (one caliber=20 mm)

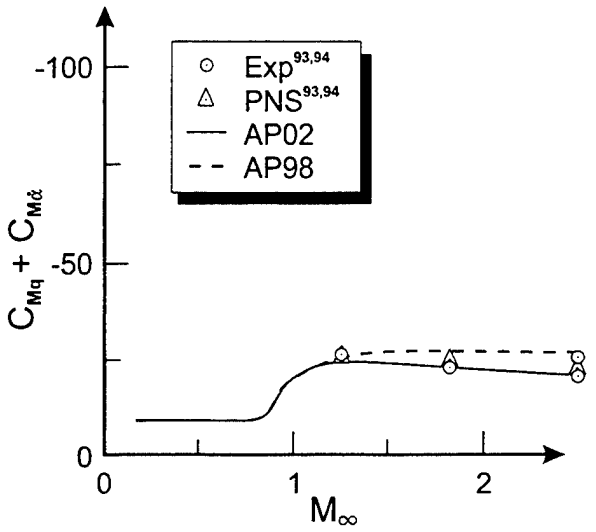

B. $\ell = 5$, $x_{CG} = 3$

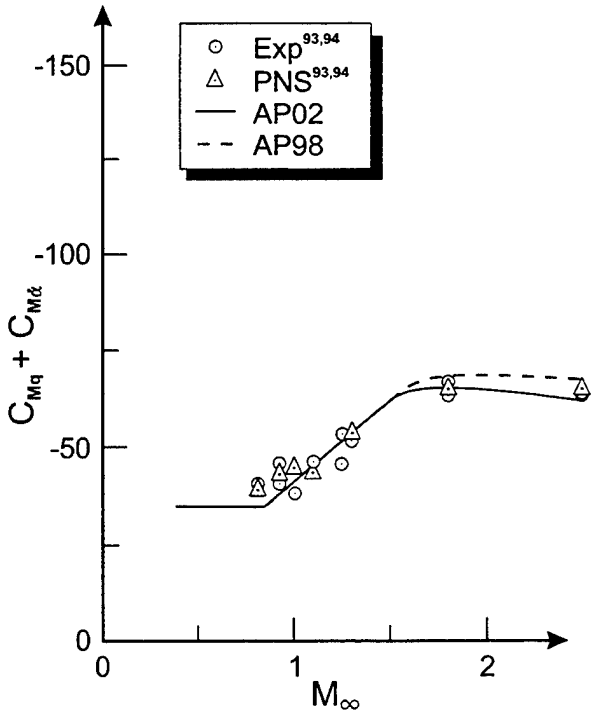

C. $\ell = 7$, $x_{CG} = 4.0$

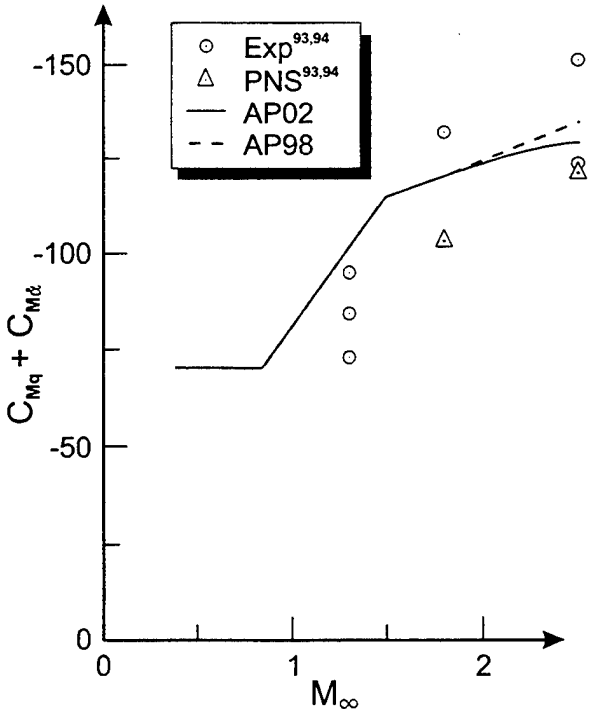

D. $\ell = 9$, $x_{CG} = 5.0$

FIGURE 50. PITCH DAMPING MOMENT COEFFICIENT PREDICTIONS COMPARED TO EXPERIMENT FOR ANSR

The next three cases are for flared projectile configurations. Figure 51 gives the first case considered. It is termed the CS-V4-1 configuration in Reference 91. This configuration consists of a blunt cone-cylinder-flare, where the flare angle is 6 deg and the flare length is 3.51 calibers. The overall configuration length is 15.36 calibers. The configuration of Figure 51 shows rifling grooves, but a smooth body was assumed in the PNS and aeroprediction calculations. Pitch damping results are shown in Figure 51 for Mach numbers 0.4 to 5.0 from the AP02 and AP98. PNS results are shown from M_∞ = 3 to 4.5 and ballistic range results are shown at M_∞ = 4.0. Note that the AP02 methodology agrees much closer to the experimental data and PNS results than does the AP98. The AP98 results are basically those of a cone-cylinder that is 15.36 calibers long.

Figure 52 shows pitch damping results for a configuration similar to that of Figure 51, except the flare is longer, 4.49 versus 3.51 calibers, and the overall Figure 52 configuration length is longer (16.34 versus 15.36 calibers) than that of Figure 51. Again, AP98 and AP02 results are shown for Mach number of 0.4 to 5 whereas PNS calculations were available for Mach number of 3 to 4.5 and ballistic range data was available for M_∞ = 4.0 only. The AP02 results match the PNS calculations adequately with the AP98, being much lower than the PNS results due to not accounting for the flare. The ballistic range data are somewhat lower than the PNS data and AP02 for this configuration, possibly due to the impact of the grooves on the pitch damping.

The final configuration considered was taken from Reference 90 and results are given in Figure 53. It consists of a 13.16 caliber cone-cylinder-flare where the flare angle varies from 4 to 14 deg. Only M_∞ = 4.4 data was given in Reference 90. Notice the good agreement of the AP02 to the CFD computations. Here the worst error of the AP02 compared to the CFD is under 6 percent for the θ_f = 14 deg case. Again, the AP98 gives unacceptable agreement to the CFD, except for small θ_f.

4.4 ENGINE-ON AND BASE BLEED EFFECTS ON BASE DRAG

Several cases will be used to show the improvements in the AP02 with respect to predicting base pressure when the rocket engine is on or when a projectile burns a small amount of propellant in the base region. We will consider the base bleed cases first.

The first base bleed case is shown in Figures 54 and 55. The case is for a condition where d_j/d_r = 0.31, T_j = 2150 °R. Figure 54 is for the M_∞ = 0.71 condition and Figure 55 is for M_∞ = 0.98. Base pressure ratio is shown as a function of the injection parameter I. As seen in both figures, excellent agreement of theory and experiment is seen.

The second case considered is shown in Figure 56. This case again shows a comparison of theory and experiment for M_∞ = 2.0, d_j/d_r = 0.2, and T_j = 5400 °R. Results are shown only up to values of I = .004. Good agreement of theory and experiment is seen.

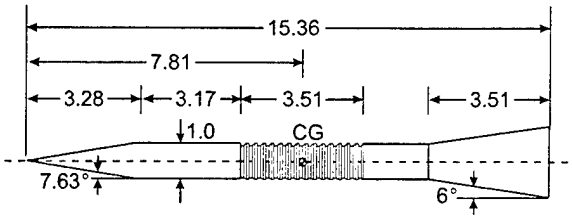

CS-V4-1 Flare Stabilized Projectile Geometry
(all dimensions in calibers)
(one caliber=8.28 mm)

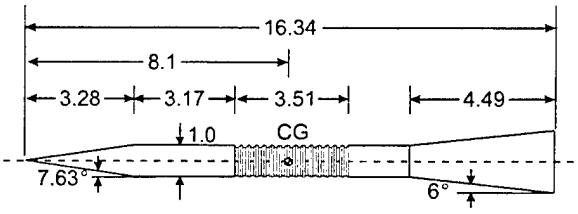

CS-V4-2 Flare Stabilized Projectile Geometry
(all dimensions in calibers)
(one caliber=8.28 mm)

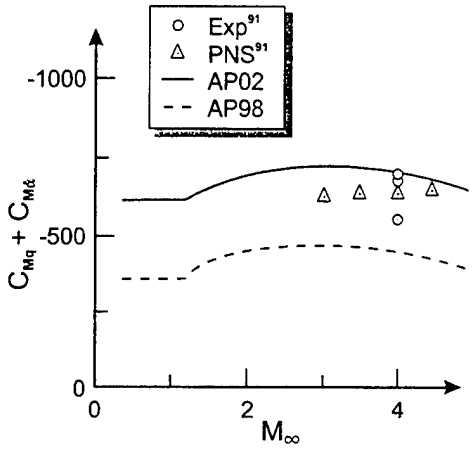

FIGURE 51. COMPARISON OF THEORY AND EXPERIMENT FOR PITCH DAMPING MOMENT COEFFICIENT OF CS-V4-1 CONFIGURATION

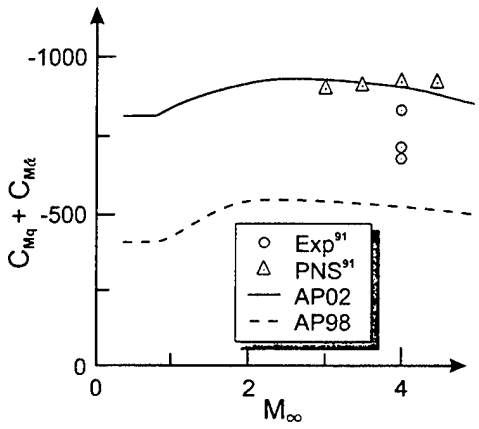

FIGURE 52. COMPARISON OF THEORY AND EXPERIMENT FOR PITCH DAMPING MOMENT COEFFICIENT OF CS-V4-2 CONFIGURATION

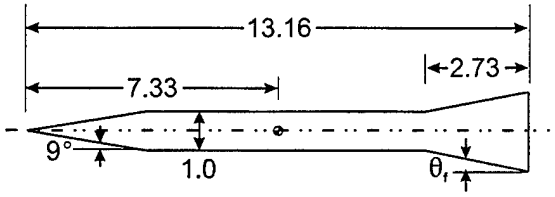

Control Projectile Configuration
(all dimensions in calibers)

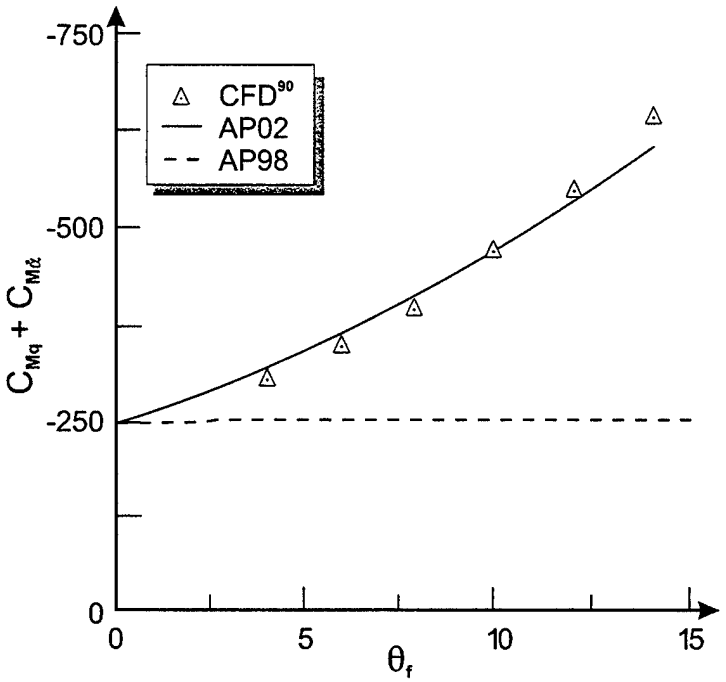

FIGURE 53. COMPARISON OF THEORETICAL PREDICTIONS OF PITCH DAMPING MOMENT COEFFICIENT FOR VARIOUS FLARE ANGLES ($M_\infty = 4.4$)

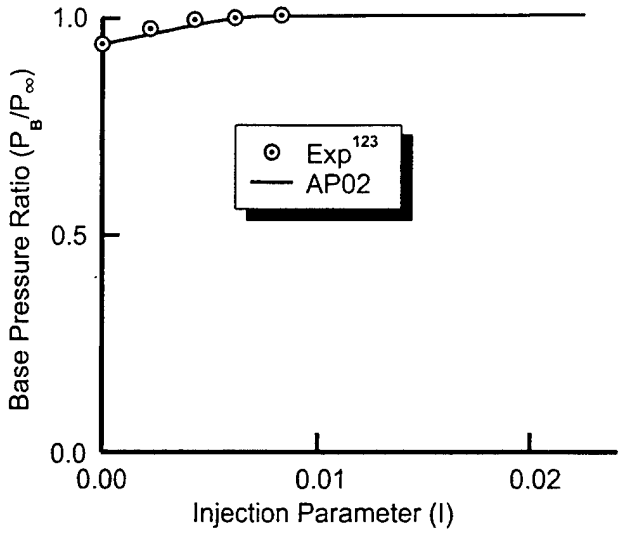

FIGURE 54. COMPARISON OF THEORY AND EXPERIMENT FOR BASE PRESSURE RATIO AT BASE BLEED CONDITIONS (M_∞ = 0.71; dj/dr = 0.31; Tj = 2150 °R)

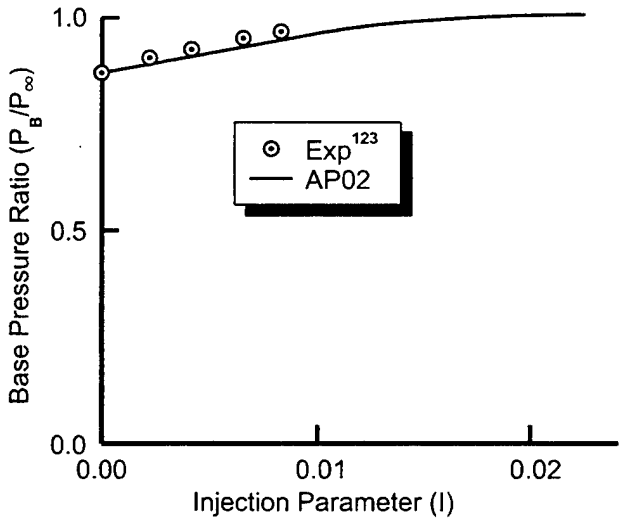

FIGURE 55. COMPARISON OF THEORY AND EXPERIMENT FOR BASE PRESSURE RATIO AT BASE BLEED CONDITIONS (M_∞ = 0.98; dj/dr = 0.31; Tj = 2150 °R)

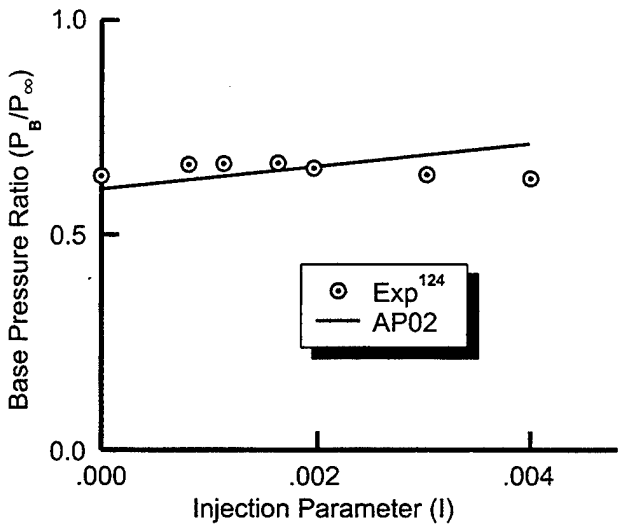

FIGURE 56. COMPARISON OF THEORY AND EXPERIMENT FOR BASE PRESSURE RATIO AT BASE BLEED CONDITIONS (M_∞ = 2.0; dj/dr = 0.2; Tj = 5400 °R)

The final base bleed example is a practical example taken from Reference 125 where NS calculations were performed on a cylindrical based afterbody at M_∞ = 1.7 and 2.5 for values of the mass injection parameter of 0 to 0.03. These NS results were then compared in Reference 125 to the experimental data of Schilling[126]. The AP02 computations for this same case at M_∞ = 1.7 and 2.5 are compared to both the experimental results of Schilling[126] and CFD results of Sahu[125] in Figure 57. At M_∞ = 1.7, the AP98 result for C_{A_B} at I = 0 is slightly higher than either the Reference 125 or 126 results. The decrease in C_{A_B} with increasing I is parallel to the experiment and CFD up to values of I of about 0.02 to 0.025 for this room temperature case. At M_∞ = 2.5, the AP02 agrees very well with the experimental data[126] and CFD[125] predictions up to values of I = 0.012 before the AP02 results depart from the more accurate theory or experimental results. Again, since the practical range of interest for I is generally 0.01 or less, this level of agreement with the data is viewed as being acceptable.

The first case to compare the present predictions of power-on base pressure are results taken from Reference 104 and correlated by Brazzel as a function of the Jet Momentum Flux parameter RMF. These results, shown in Figure 58, were for various jet to reference diameter ratios at $M_\infty = M_j$ = 2.0. Also shown in Figure 58 are the predictions of the Brazzel method (indicated by the AP98) for the low values of RMF computed from Equation (1) for various values of RMF assuming γ_j = 1.4 and x_j = 0. Since M_j = 2, $T_j / T_j^* = 0.67$ for Figure 58. Also shown in Figure 58 are the results for the improved method to be part of the AP02. As seen in Figure 58, both the Brazzel technique and the AP02 method predict base pressure slightly high compared to the Reference 104 data. This means base drag would be slightly low compared to the Reference 104 experimental data.

The next case considered is taken from Reference 127 and is for M_j = 2.5, M_∞ = 1.94, and d_j/d_r = 0.75. In addition to the experimental data of Reference 127, the data of Reference 102 is also shown in Figure 59. The AP02 compares fairly well with the Reference 102 data at lower

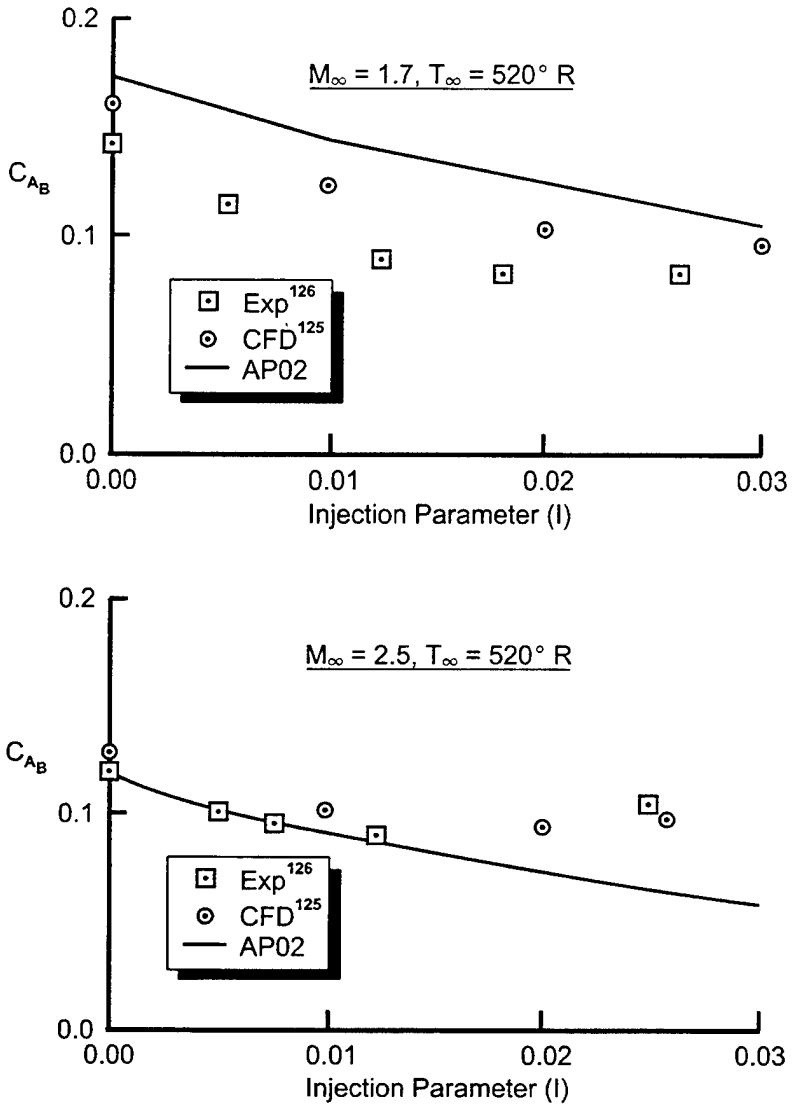

FIGURE 57. COMPARISON OF THEORY AND EXPERIMENT FOR BASE DRAG AS A FUNCTION OF MASS INJECTION PARAMETER

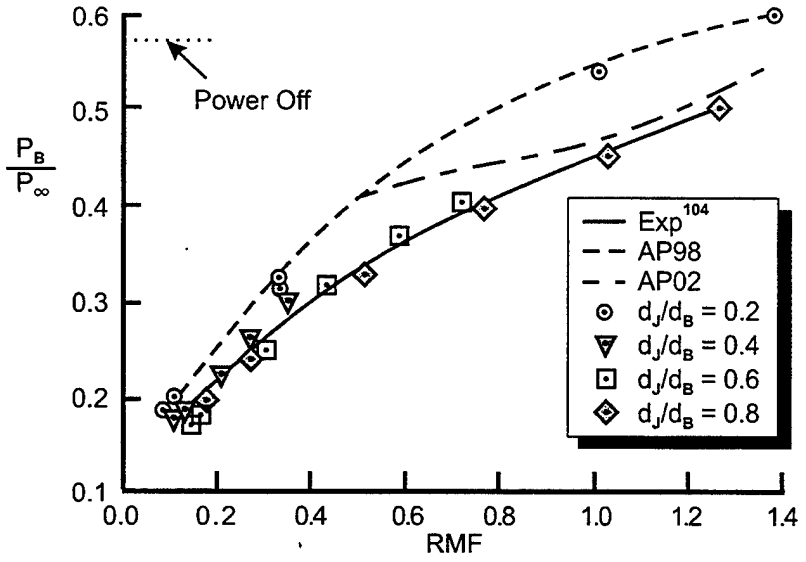

FIGURE 58. COMPARISON OF POWER-ON-BASE PRESSURE PREDICTION WITH EXPERIMENT (Mj = 2.0, M_∞ = 2.0)

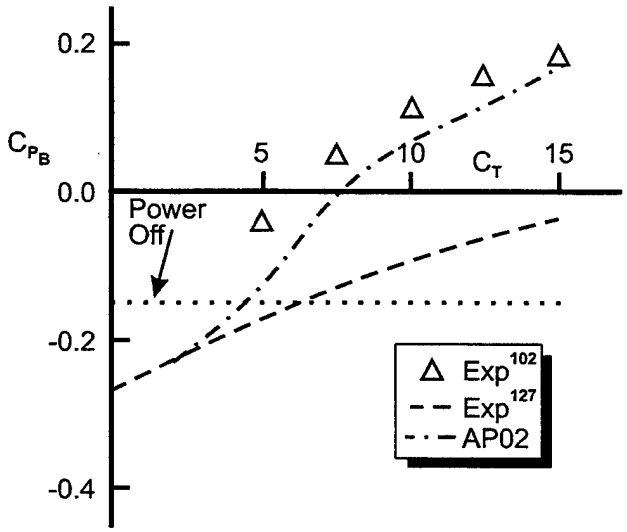

FIGURE 59. COMPARISON OF POWER-ON-BASE PRESSURE COEFFICIENT PREDICTION WITH EXPERIMENT (Mj = 2.5, M_∞ = 1.94, dj/dr = 0.75)

values of C_T and is in between the Reference 102 and Reference 127 data for higher values of C_T. Once again, the power-off base pressure coefficient is shown in Figure 59, illustrating that at very low values of thrust coefficient, power-on increases base drag, whereas for higher values of C_T, base drag is decreased.

Figure 60 illustrates results for jet exit Mach number of 3.5, where the other conditions (M_∞ = 1.94, d_j/d_r = 0.75) are the same as those in Figure 59. Again, the AP02 is in agreement

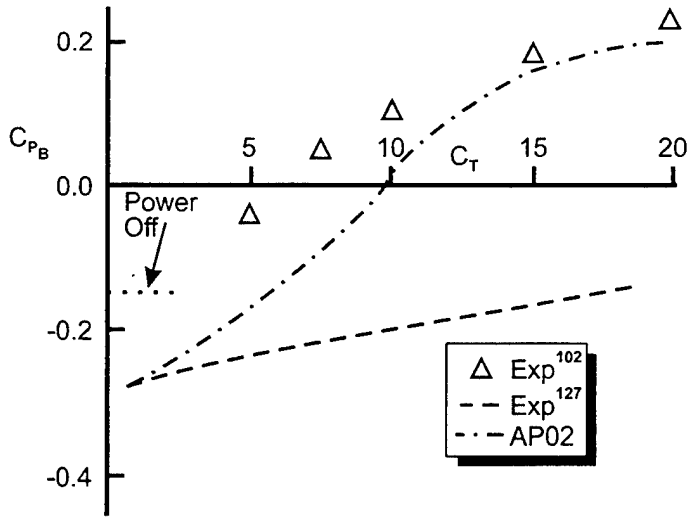

FIGURE 60. COMPARISON OF POWER-ON-BASE PRESSURE COEFFICIENT PREDICTION WITH EXPERIMENT (Mj = 3.5, M_∞ = 1.94, dj/dr = 0.75)

with the Reference 102 data at low values of C_T and is in between the Reference 127 and Reference 102 data for high values of C_T.

The next three examples are taken from the experimental database of Rubin.[128] Rubin measured power-on base drag in the transonic speed regime for cylindrical, flare, and boattail afterbodies at transonic Mach numbers. Figure 61 compares the semiempirical predictions to the data of Rubin for the cylindrical afterbody at M_∞ = 0.9, 1.0, and 1.2. Experimental data was based on M_j = 2.7 and d_j/d_B = 0.8 and 0.45. A conical nozzle was used with θ_j = 20 deg. The agreement between the experiment and theory at all three Mach numbers is reasonable. However, for M_∞ = 0.9 and $C_T < 4$, the experimental data shows P_b/P_∞ increasing. The present theory will not predict the minimum base pressure ratio. This increase in P_B/P_∞ will continue as C_T gets small until a maximum is reached at base bleed conditions, after which P_B/P_∞ will decrease to its power-off value.

Figure 62 presents the comparison of theory and experiment for the boattailed afterbody case. Results for the same three freestream Mach numbers (M_∞ = 0.9, 1.0, and 1.2) are shown in the figure. The boattail angle is 6.35 deg and the boattail length is 0.82 caliber. Again, reasonable agreement with experiment is seen except for M_∞ = 0.9 and 1.0 and for low values of C_T, where the minimum value of P_B/P_∞ has been reached.

Figure 63 presents the comparison of theory and experiment for the flare afterbody case. The flare angle is 6.54 deg and its length is 1.34 caliber. Good agreement between theory and experiment is seen, except for M_∞ = 0.9 and $C_T < 6$, where the base pressure is seen to start increasing after a minimum has been reached.

The last case considered is a boattailed configuration taken from the data of Craft and Brazzel.[101] Theory and experiment are shown in Figure 64 for M_∞ = 1.5 and 2.5. Again,

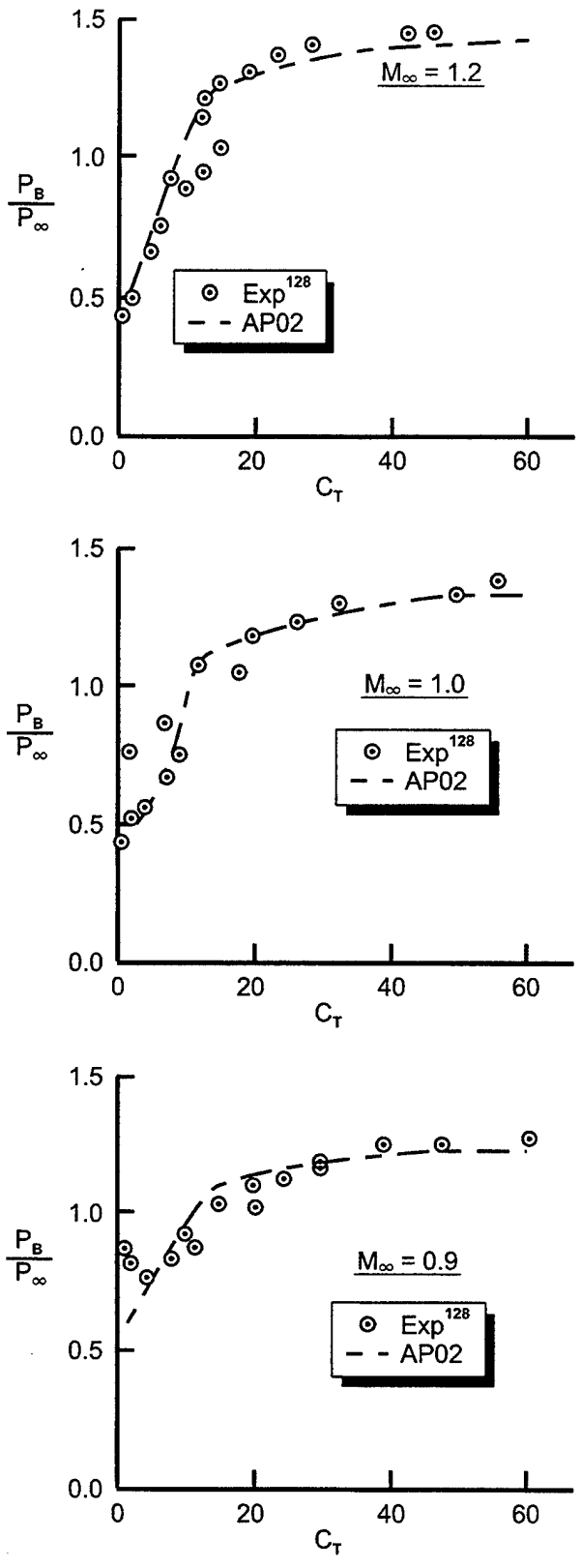

FIGURE 61. COMPARISON OF POWER-ON-BASE PRESSURE PREDICTION WITH EXPERIMENT FOR CYLINDRICAL AFTERBODY (Mj = 2.7; dj/d_B = 0.8, 0.45; θ_j = 20 DEG)

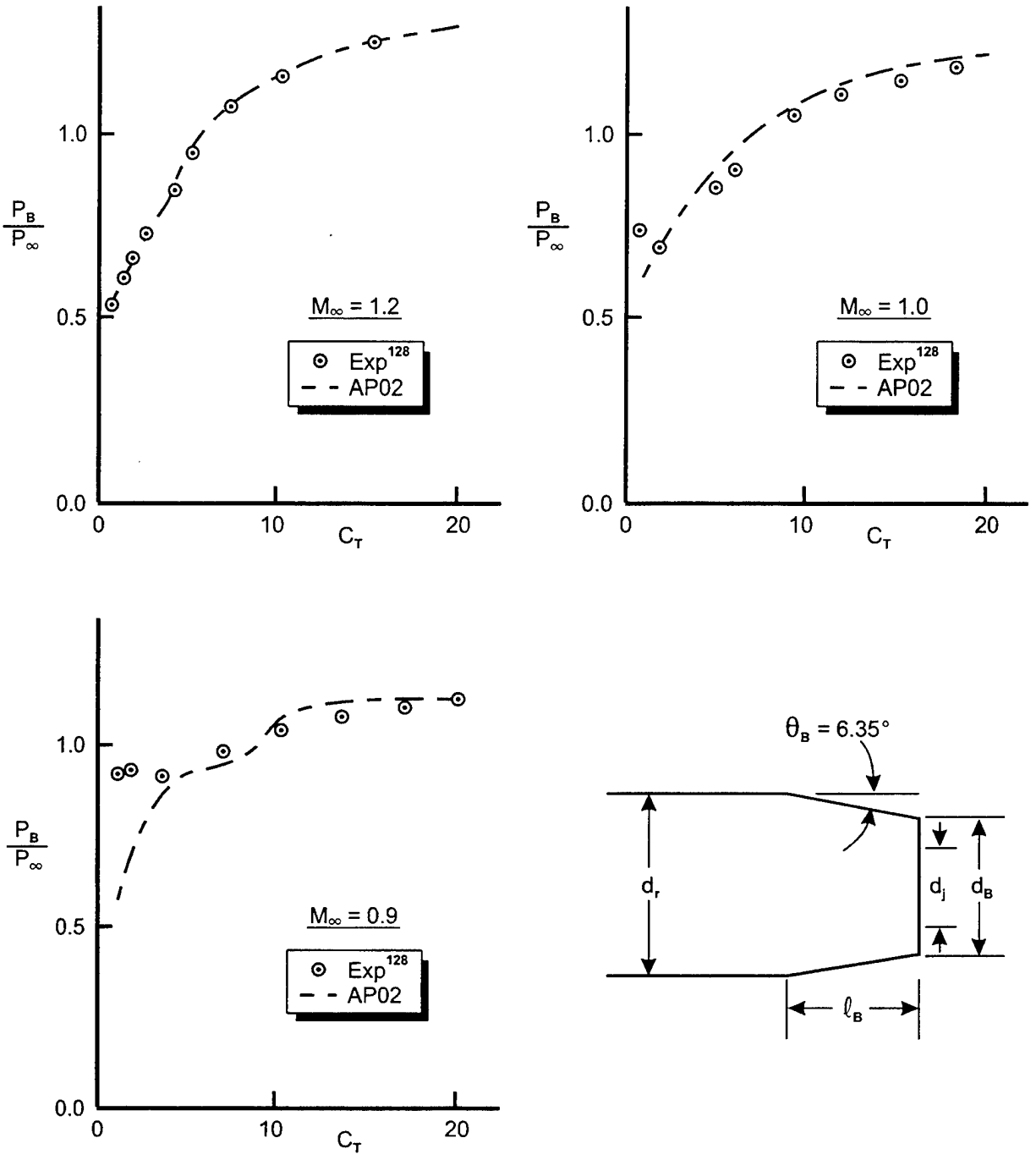

FIGURE 62. COMPARISON OF POWER-ON-BASE PRESSURE PREDICTION WITH EXPERIMENT FOR BOATTAIL AFTERBODY (dj/dr = 0.45; θj = 20 DEG; θ_B = 6.35 DEG; ℓ_B = 0.82 CAL; M_j = 2.7)

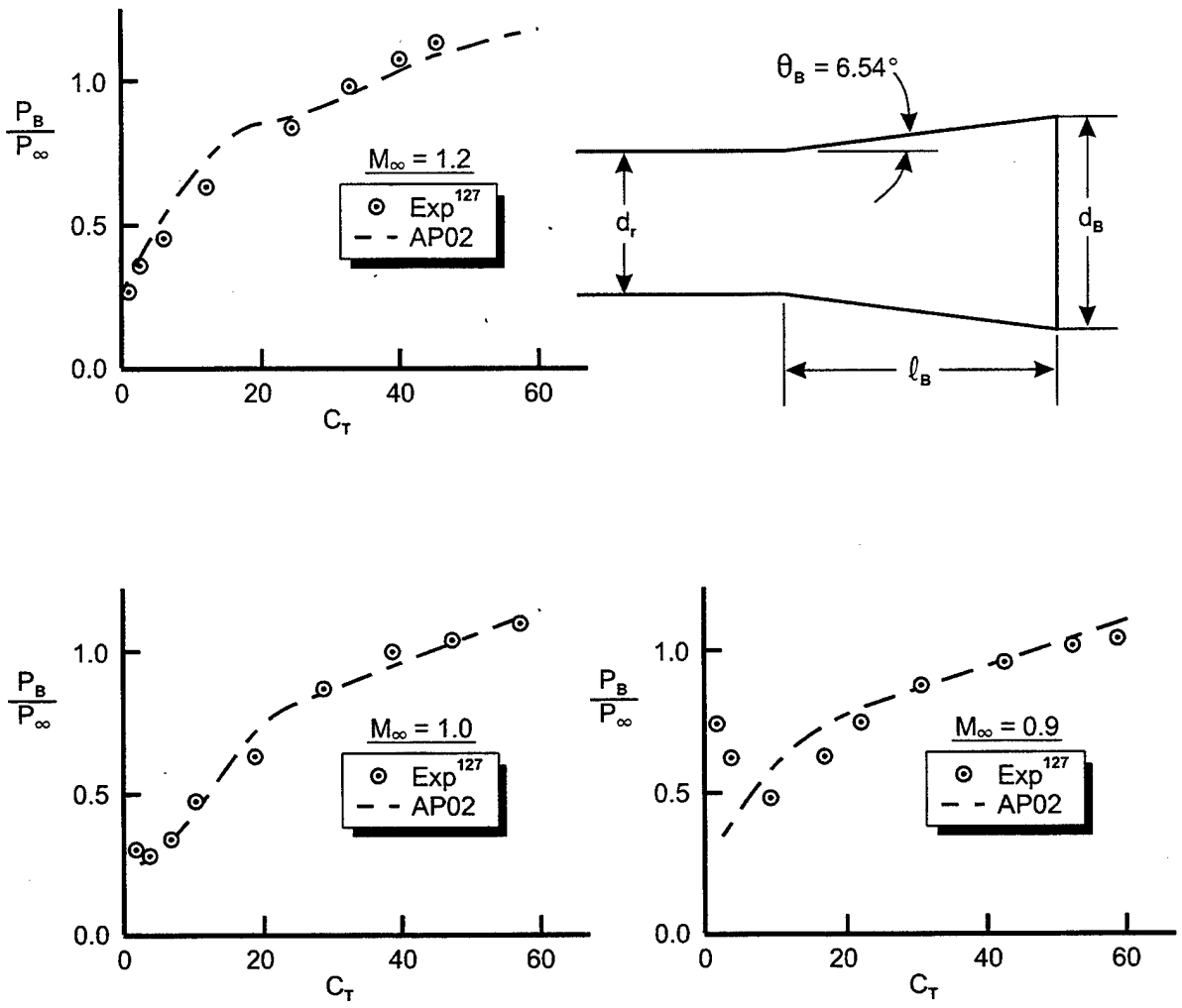

FIGURE 63. COMPARISON OF POWER-ON-BASE PRESSURE PREDICTION WITH EXPERIMENT FOR FLARE AFTERBODY (Mj = 2.7; dj/dr = 0.8; θj = 20 DEG; θ_B = 6.54 DEG; ℓ_B = 1.34 CAL)

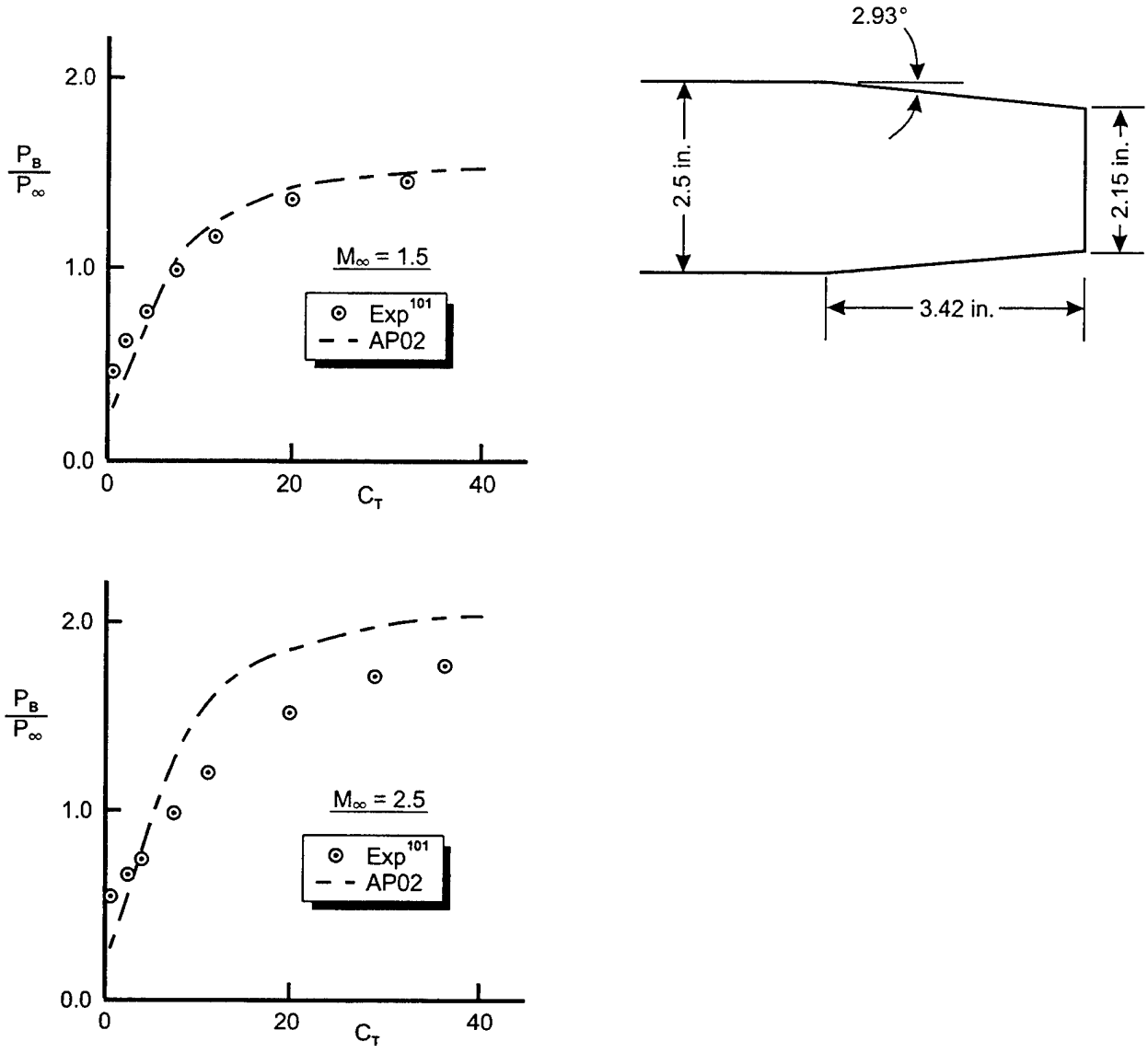

FIGURE 64. COMPARISON OF POWER-ON-BASE PRESSURE PREDICTION WITH EXPERIMENT FOR BOATTAILED AFTERBODY (Mj = 2.7; dj/dr = 0.45; θj = 20 DEG)

$M_j = 2.7$, $d_j/d_r = 0.45$, $\theta_j = 20$ deg, $\theta_B = 2.93$ deg, and $\ell_B = 1.37$ calibers. Very good agreement of theory and experiment is obtained at $M_\infty = 1.5$. However, for $M_\infty = 2.5$ the theory is about 10 to 30 percent too high for $C_T \geq 8$. The reason for the overprediction is not clear. However, it is suspected that the error is due to the Reference 102 data base being given more weight in the development of the present empirical model than the Reference 101 data base.

4.5 TRAILING-EDGE FLAP AERODYNAMICS

Equations (67) and (70) define the theoretical change in normal force and pitching moment coefficients due to a flap deflection. The value of $(\Delta C_N)_f$ computed by the theory is that value defined by

$$(\Delta C_N)_f = (C_N)_{\delta_{W=0}} - (C_N)_{\delta_{W\neq 0}} \tag{80A}$$

The value of δ_W in Equation (80A) is obtained from Equation (66) using the process defined earlier in the analysis section of this report. Using the values of δ_W from Equation (66) in the AP98, values of $(C_N)_{\delta_{W=0}}$ and $(C_N)_{\delta_{W\neq 0}}$ of Equation (80A) can be computed and then $(\Delta C_N)_f$ defined theoretically. This value of $(\Delta C_N)_f$ can then be compared to experimental data where $(\Delta C_N)_f$ is obtained using experimental data for $(C_N)_{\delta_{f=0}}$ and $(C_N)_{\delta_{f\neq 0}}$. That is

$$(\Delta C_N)_f = (C_N)_{\delta_{f=0}} - (C_N)_{\delta_{f\neq 0}} \tag{80B}$$

Likewise, experimentally measured values of $(\Delta C_M)_f$ can be defined as

$$(\Delta C_M)_f = (C_M)_{\delta_{f=0}} - (C_M)_{\delta_{f\neq 0}} \tag{81}$$

and compared to theoretical values computed from Equation (70). $(\Delta C_N)_f$ of Equation (70) comes from the theoretical values defined by Equation (80A). Thus, comparison of $(\Delta C_N)_f$ values obtained by Equations (80A) to (80B) and $(\Delta C_M)_f$ values obtained from Equations (70) to Equation (81) will allow us to determine the validity and accuracy of the new theory.

The first set of data we will consider is from Reference 111. The configuration tested in the wind tunnel is shown in Figure 33. Figures 65-67 compare theory and experiment for $(\Delta C_N)_f$ and $(\Delta C_M)_f$ at $\delta_f = -20$ deg and Mach numbers 1.5, 2.96, and 4.63. Results are plotted as a function of AOA up to 30 deg. For Mach number 1.5, experimental data was not available up to 30 deg AOA, so data was shown where available. As seen in the figures, the theory does a reasonable job in matching the data for both $(\Delta C_N)_f$ and $(\Delta C_M)_f$, except at $M_\infty = 4.63$ and $\alpha \geq 20$ deg. At these conditions, the theory somewhat overpredicts the normal force and pitching moment increments. However, since this region is beyond the anticipated practical range of usage ($M_\infty < 2.0$, $\alpha < 20$, $|\delta_f| < 30$ deg), no effort will be made to try to improve upon the theory at this condition.

Also shown on the $(\Delta C_M)_f$ portion of Figures 65-67 are the results of assuming the center of pressure of the flap is based on the flap in freestream flow and with the flap attached to the trailing edge. The flap attached to the trailing edge computations take into account the center of pressure shift shown in Figure 38. Note that at $M_\infty = 1.5$, no shift is shown so the Figure 65 pitching moment results show no change between the flap alone and the flap attached. However,

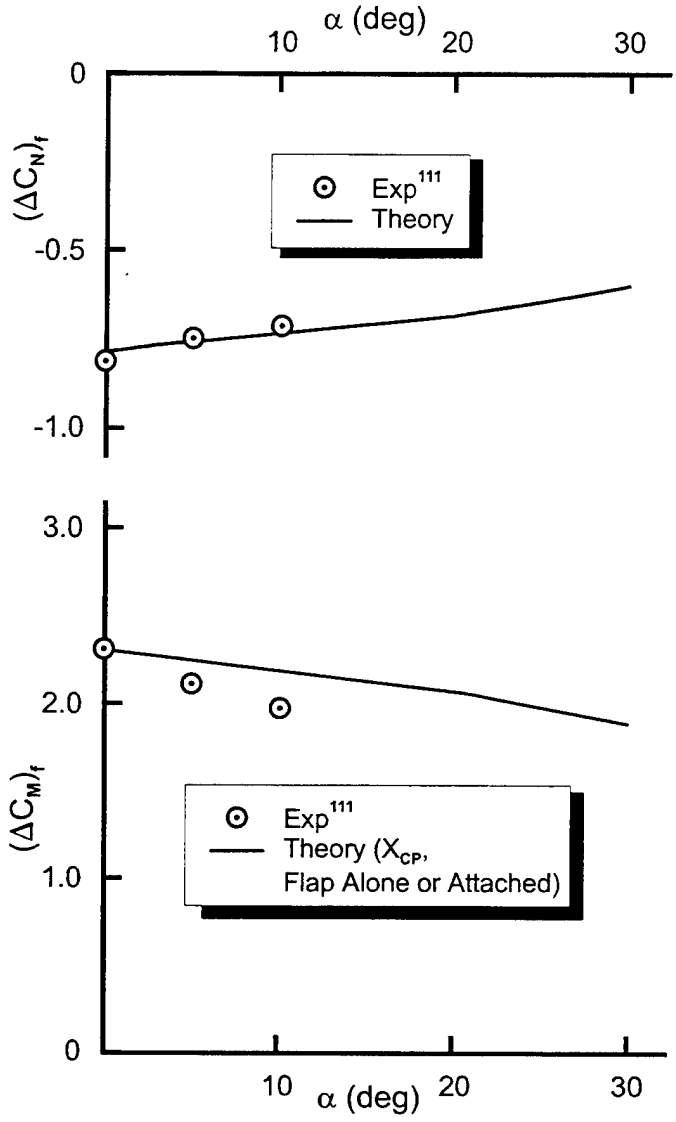

FIGURE 65. COMPARISON OF THEORY AND EXPERIMENT FOR NORMAL FORCE AND PITCHING MOMENT COEFFICIENTS OF TRAILING EDGE FLAPS ($M_\infty = 1.5$, $\delta_f = -20$ DEG)

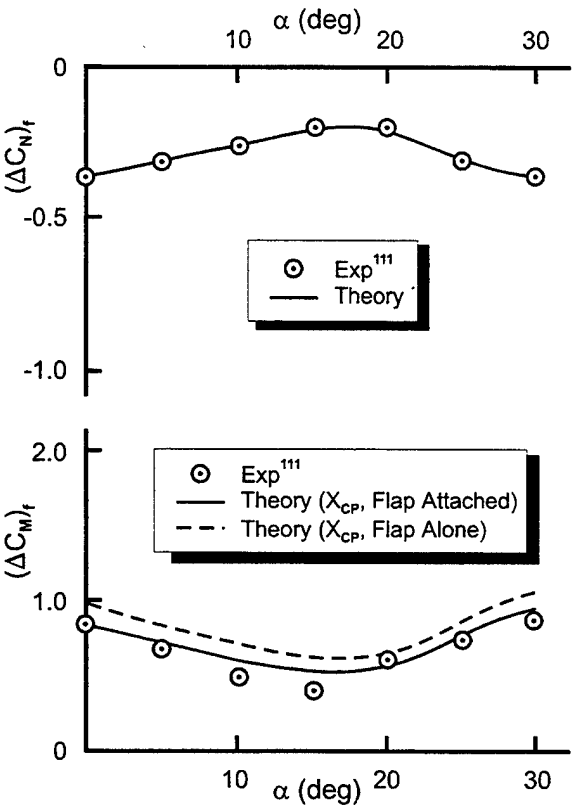

FIGURE 66. COMPARISON OF THEORY AND EXPERIMENT FOR NORMAL FORCE AND PITCHING MOMENT COEFFICIENTS OF TRAILING EDGE FLAPS ($M_\infty = 2.96$, $\delta_f = -20$ DEG)

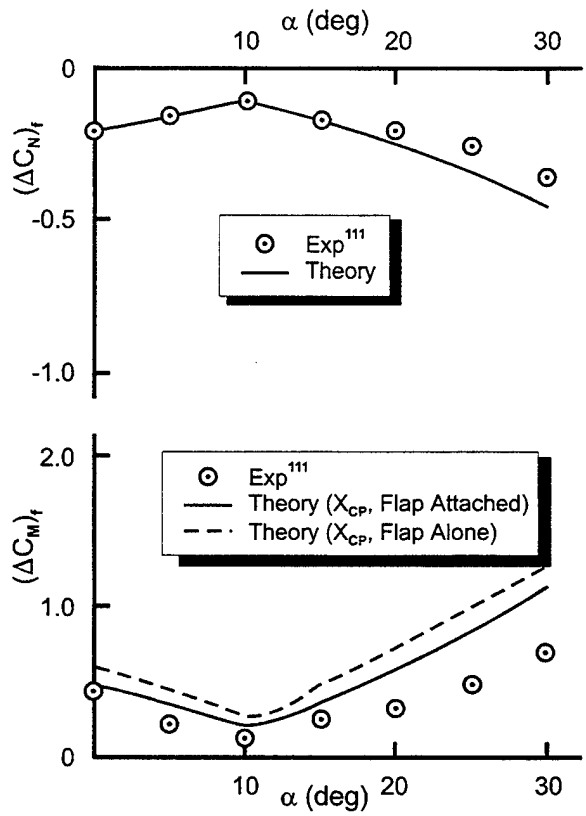

FIGURE 67. COMPARISON OF THEORY AND EXPERIMENT FOR NORMAL FORCE AND PITCHING MOMENT COEFFICIENTS OF TRAILING EDGE FLAPS ($M_\infty = 4.63$, $\delta_f = -20$ DEG)

Figures 66 and 67 show a change in pitching moment between flap alone and the flap attached. As seen in Figures 66 and 67, using the Figure 38 results tend to show an improvement in pitching moment calculations over assuming the flap alone.

It is also worthwhile to reemphasize the fact that all the theoretical calculations shown in Figures 65-67 (as well as the figures which will follow) were computed by using the AP02 in conjunction with Equation (66) as described in the Analysis Section of the report.

Reference 129 represents the only subsonic data base the author found in the literature. The configuration tested is shown in Figure 34. The ogive of the Figure 34 configuration can be either an elliptical or a circular cylinder tangent ogive. The case upon which the change in pitching moments and normal force coefficients were determined was based on an elliptical nose. However, since the data used was $(\Delta C_N)_f$ and $(\Delta C_M)_f$, it is expected the body shape will have little impact since the same body shape is used for the $\delta_f = 0$ case as well as the $\delta_f \neq 0$ case. Reference 129 has both positive and negative values of δ_f available. Unfortunately, $M_\infty = 0.4$ was the highest freestream Mach number considered, and AOA to 30 deg were also included in the test series.

Figure 68 compares the theory and experiment for $(\Delta C_N)_f$ and $(\Delta C_M)_f$ where δ_f is negative for α to 30 deg. Note that excellent agreement for $(\Delta C_N)_f$ is obtained between theory and experiment for both $\delta_f = -10$ deg and -30 deg cases. Good agreement between theory and experiment is obtained for $(\Delta C_M)_f$ for the $\delta_f = -10$ deg case up to α of about 20 to 25 deg, where the theory and experiment start to depart. For $\delta_f = -30$ deg, comparison of theory and experiment for $(\Delta C_M)_f$ is quite acceptable for α up to 20 deg. The trim AOA occurs at about 6 deg for $\delta_f = -10$ deg and at about 14.8 deg for $\delta_f = -30$ deg. In other words, good accuracy in both $(\Delta C_N)_f$ and $(\Delta C_M)_f$ can be obtained up to and slightly beyond the trim AOA, which is most critical. For α above the trim value, accuracy of $(\Delta C_N)_f$ and $(\Delta C_M)_f$ is not as important; therefore, no attempt was made to try to improve the theory for these conditions.

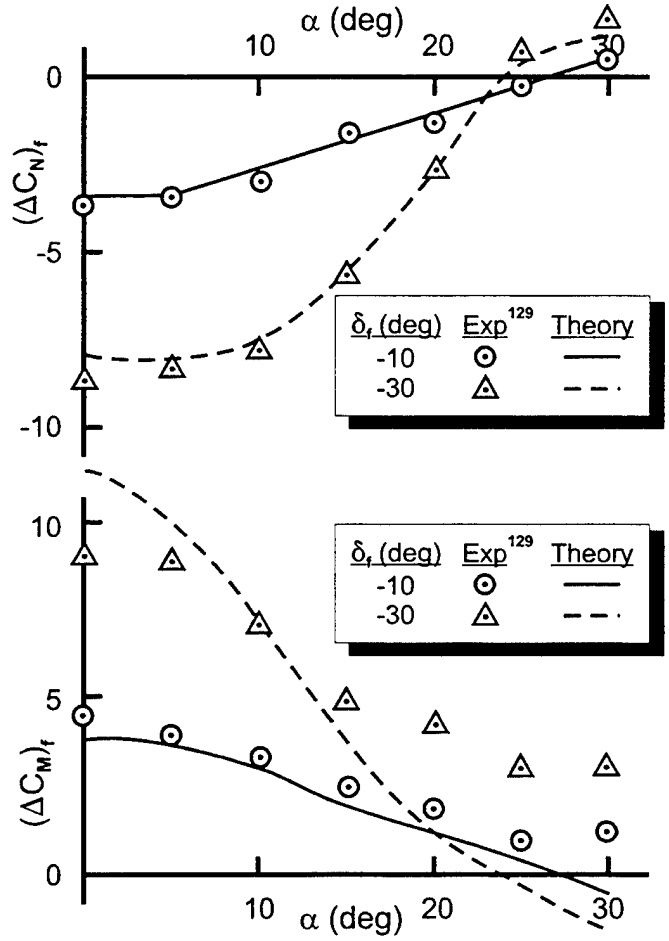

FIGURE 68. COMPARISON OF THEORY AND EXPERIMENT FOR NORMAL FORCE AND PITCHING MOMENT COEFFICIENTS OF TRAILING EDGE FLAPS ($M_\infty = 0.4$, δ_f NEGATIVE)

Figure 69 gives the complimentary results to the Figure 68 case except here δ_f is positive. While trim cannot occur due to the fact α and δ_f are of the same sign and the configuration is tail controlled, it is still of interest to see how well the theory compares to data for conditions where

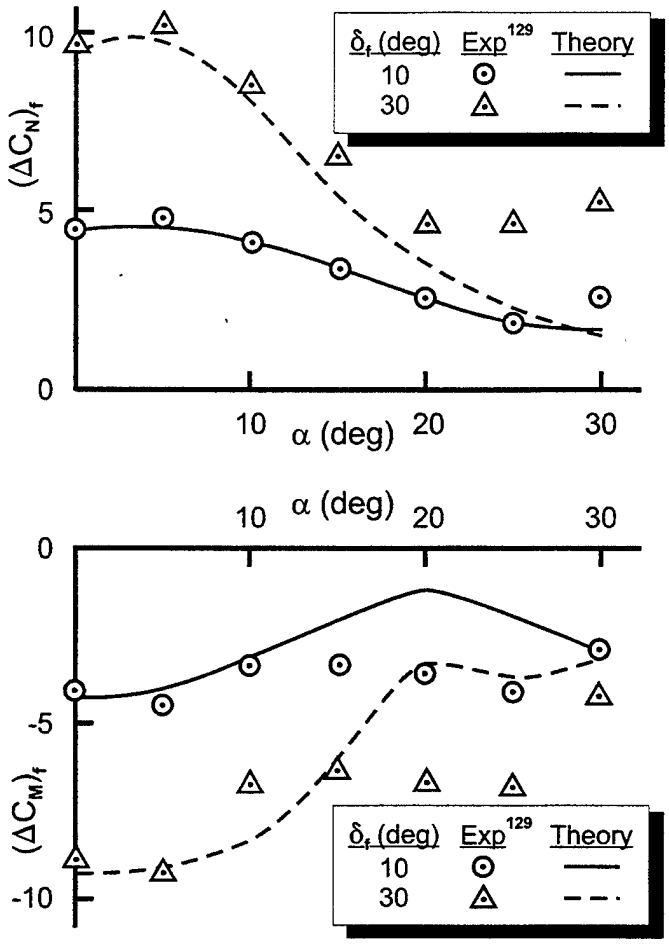

FIGURE 69. COMPARISON OF THEORY AND EXPERIMENT FOR NORMAL FORCE AND PITCHING MOMENT COEFFICIENTS OF TRAILING EDGE FLAPS ($M_\infty = 0.4$, δ_f POSITIVE)

trim is not possible. As seen in Figure 69, agreement between theory and experiment for both $(\Delta C_N)_f$ and $(\Delta C_M)_f$ is quite good up to an α of about 15 deg. Above α of 15 deg, both $(\Delta C_M)_f$ and $(\Delta C_N)_f$ deviate from experiment at most conditions. Again, since this is not a practical set of conditions for trim, no effort has been made to improve $(\Delta C_N)_f$ and $(\Delta C_M)_f$ for α above 15 deg and δ_f is positive.

Figure 70 compares the theory and experiment for axial force coefficient where the trailing edge flap has been deflected −10 deg and −30 deg, respectively. The equivalent value of δ_W corresponding to $\delta_f = -10$ deg and −30 deg, respectively, is shown at the top of Figure 70 as a function of freestream Mach number. Note that δ_W is only a small fraction of δ_f. The wing area is 8.67 times that of the trailing edge flap. At the bottom of Figure 70 is the axial force coefficient based on the AP02 calculations plus the value defined by Equation (71). Two cases are shown for the theory: where the wind tunnel model has a boundary layer trip and where no boundary layer trip is present. The Reynolds number for the tests was 2.5×10^6. According to Reference 111, a boundary layer trip was present. Based on comparison of theory and experiment, it appears the boundary layer trip was effective in producing a turbulent boundary

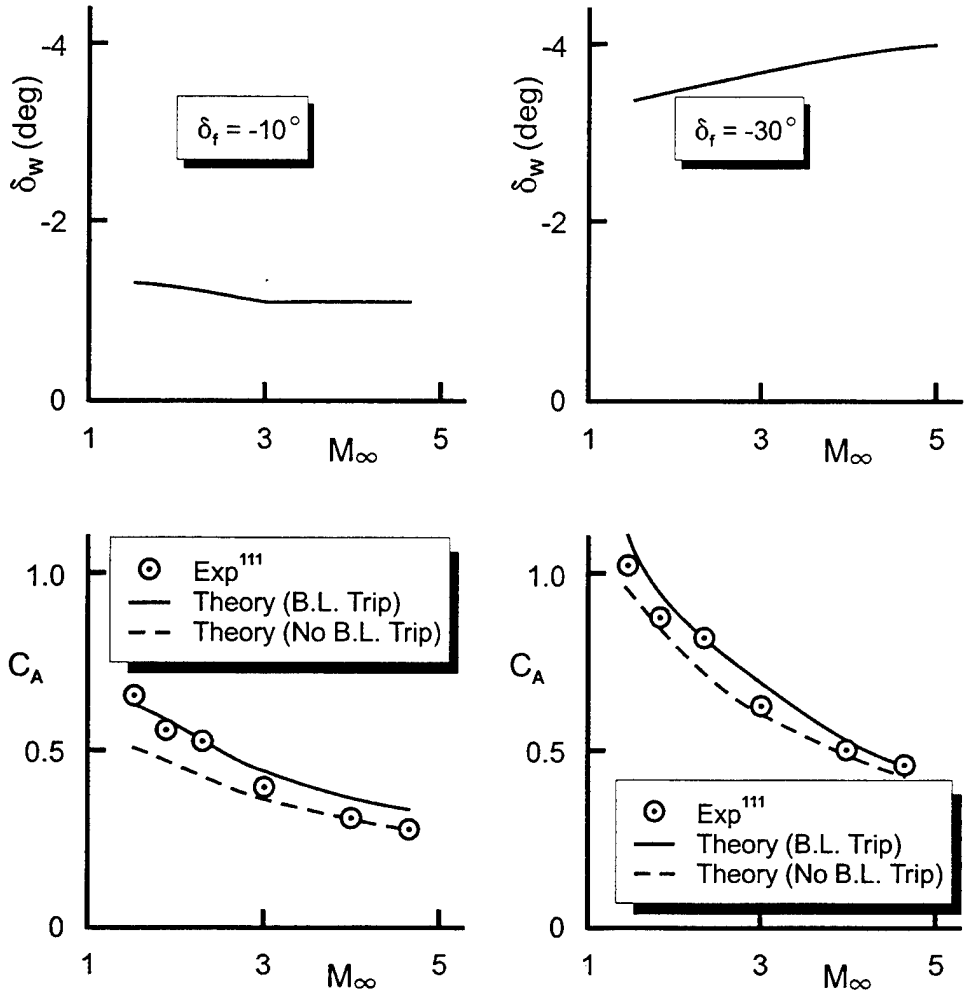

FIGURE 70. COMPARISON OF THEORY AND EXPERIMENT FOR AXIAL FORCE COEFFICIENT AT VARIOUS VALUES OF FLAP DEFLECTION AND AS REPRESENTED BY AN EQUIVALENT DEFLECTION OF ENTIRE WING AT $\alpha = 0$ DEG (R_N/ft = 2.5 x 10^6)

layer over the surface at the lower supersonic Mach numbers. However, at the higher supersonic Mach numbers, it appears that the flow partially transitions back to laminar over much of the body and large wing for the $\delta = -10$ deg case. This relaminarization of the flow is speculated to be the reason the theory with no boundary layer trip option agrees closer to the wind tunnel data at high supersonic Mach number than does the theory which assumes turbulent flow over the entire surface of the model at all Mach numbers. If the above hypothesis of relaminarization of the flow is correct, the theory predicts the experimental data quite well. If this hypothesis is not correct, then the theory is high for Mach numbers 3.0 and greater.

The Reference 129 data base also contained axial force data. Unfortunately, the base drag term was subtracted, only one fin was deflected and the numbers for no fin deflection were small and irregular. As a result, it was believed an accurate value of experimental data for the axial force would be difficult to obtain; therefore, no comparisons of axial force coefficient will be shown at subsonic Mach numbers.

4.6 IMPROVED AXIAL FORCE FOR NONAXISYMMETRIC BODIES

While the improvement explicitly made to improve the aerodynamics of nonaxisymmetric bodies was the wave drag component of the axial force coefficient, the improvement in the nonlinear aerodynamic terms discussed in Section 4.1 could also have an impact. Therefore, we will investigate three cases to see if the improvements made to the AP02 also show improvement in predicting aerodynamics of nonaxisymmetric bodies. The first case considered is based on the data base of Jorgensen[108] and the configurations tested are shown in Figure 71.

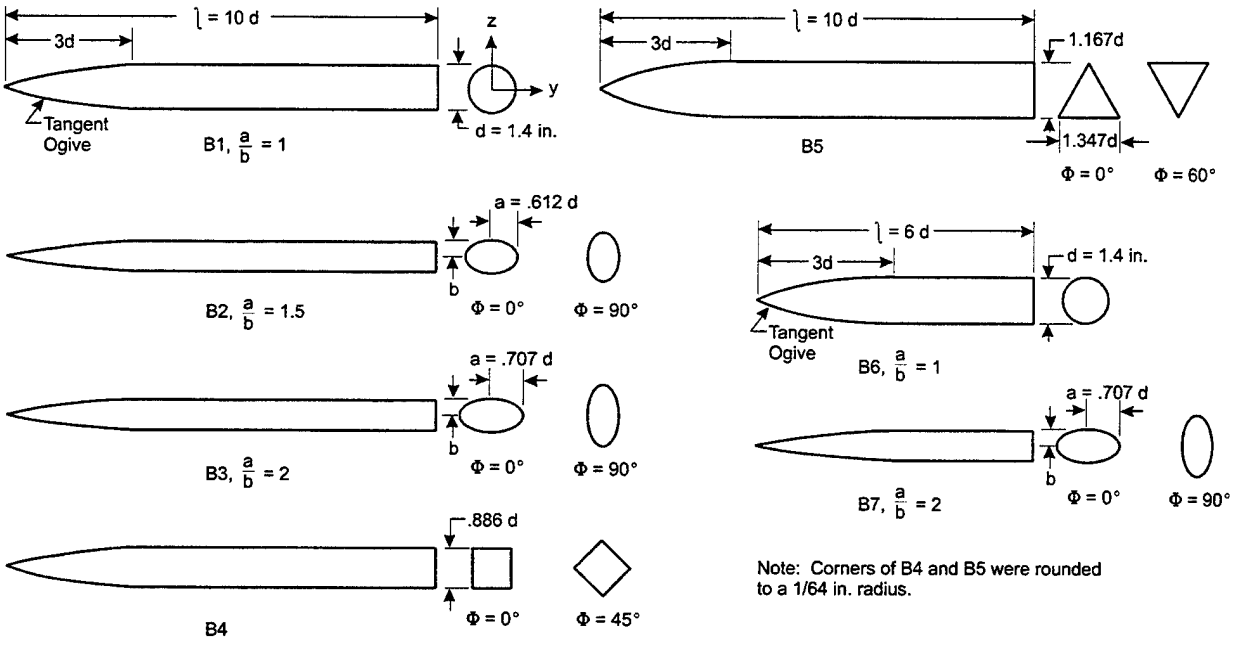

FIGURE 71. BODY ALONE CONFIGURATIONS[108] WITH ELLIPTICAL, SQUARE, DIAMOND, TRIANGULAR, AND INVERTED TRIANGULAR SHAPES

Included in the Figure 71 configurations are two circular bodies, 1.4 inch in diameter, with 3.0-caliber tangent ogive noses, and either a 7.0-caliber or 3.0-caliber cylindrical afterbody, giving l/d (length/diameter) ratios of 10 and 6. The critical Reynolds number parameters were adjusted using these bodies, and optimal settings were found to be $R_{N_C} = 330000$ and $\Delta M_{N_C} = -0.2$. The noncircular bodies in the data set are squares, diamonds (squares at a 45 deg roll position), triangles, inverted triangles (triangles at a 60 deg roll position), and ellipses with axis ratios of 2:1, 1.5:1, 0.67:1 (1.5:1 at 90 deg roll), and 0.5:1 (2:1 at 90 deg roll). All bodies have the same cross sectional area as the circle, and the distribution of that area along the longitudinal axis is the same as for the circle. The squares, diamonds, triangles, and inverted triangles have very small corner radii and were assumed to have a value of k equal to 0. All noncircular bodies are identical in length to the l/d = 10 circular cylinder except for a 2:1 ellipse and a 0.5:1 ellipse, which have the same length as the l/d = 6 cylinder. Mach numbers were 1.98 and 3.88.

Figures 72A through 72C show the results of the AP02 computations for lift coefficient, lift to drag ratio, and center of pressure location (referenced to the nose tip in this and all future cases) compared to the experimental data for the l/d = 10 ellipses at M = 1.98. The circular body results are shown in each figure for reference. In most cases, the lift coefficient comparisons, found in Figure 72A, are quite good, with the computed values tending to be somewhat low at the higher angles of attack. This is especially true of the 0.5:1 axis ratio case. Since the circular body values tend to be lower than the data in this region, this trend is not surprising. The noncircular computations rely on the circular results as a starting point and are thus influenced by their behavior. The lift to drag ratios and the center of pressure locations for the 2:1 ellipse, found in Figures 72B and 72C, respectively, are in very good agreement with experimental data. These comparisons for the 0.5:1 ellipse, while not as good as for the 2:1 ellipse, are within the accuracy limits of the code. Figures 73A through 73C show the same comparisons for the 2:1 and the 0.5:1 ellipse at M = 3.88. For the lift coefficients, found in Figure 73A, the 0.5:1 ellipse compares with data well, but the 2:1 ellipse tends to be high at α = 10 and above. As can be seen from the circular body results shown on the same plot, this is to some degree a carryover effect. The lift to drag ratios and the center of pressure comparisons are shown in Figures 73B and 73C. The lift to drag ratios are in reasonable agreement with the wind tunnel results with the greatest discrepancies coming for the 0.5:1 ellipse. The center of pressure locations agree well with experiment in all instances. It should be pointed out that the drag of Figures 72B and 73B does not contain the base drag term, thereby somewhat falsely increasing all the lift to drag ratios.

Figure 74A - 74C show the lift coefficient, lift to drag ratio, and center of pressure comparisons for the squares and diamonds at M = 1.98. Once again, the circular body values are shown for reference. For lift coefficient, found in Figure 74A, the square results are quite good, being just a little high at the higher angles of attack. The diamond values tend to follow the same pattern as the ellipses, being low above α = 12 deg. The lift to drag ratios are shown in Figure 74B and are in very good agreement with the wind tunnel results. The center of pressure locations are presented in Figure 74C and are well within the accuracy limits of the code. The results for these cross sections at M = 3.88 are presented in Figures 75A - 75C. In this case, the lift coefficient results in Figure 75A are seen to be high for both cross sections. A comparison to the circular body results, which are also shown, indicates that they are in large part following the established trend. A look at Figure 75B shows that the code does well predicting lift to drag ratio for these conditions with the exception of a few low α instances. It should be noted that with angles of attack of 2 or 4 deg, it can be difficult to measure drag accurately in the wind tunnel, so some disagreement in this region could be attributed to experimental uncertainty. The center of pressure results, shown in Figure 75C, agree well with the experimental data.

Results for the triangles and inverted triangles at M = 1.98 are shown in Figures 76A - 76C. Overall, the lift coefficient comparisons, presented in Figure 76A, are not as good as for the other body cross sections, with most values being too low. This is partially a reflection of the circular body results, but also indicates some uncertainty in the modeling of triangles and inverted triangles because of a scarcity of data. On the other hand, the lift-to-drag and center-of-pressure results shown in Figures 76B and 76C are in very good agreement with the wind tunnel results. The M = 3.88 comparisons for these cross sections are shown in Figures 77A - 77C. Here, the lift coefficient values, found in Figure 77A, tend to be somewhat high above α = 8 deg, but this is in agreement with the circular body results. The lift-to-drag ratio comparisons in

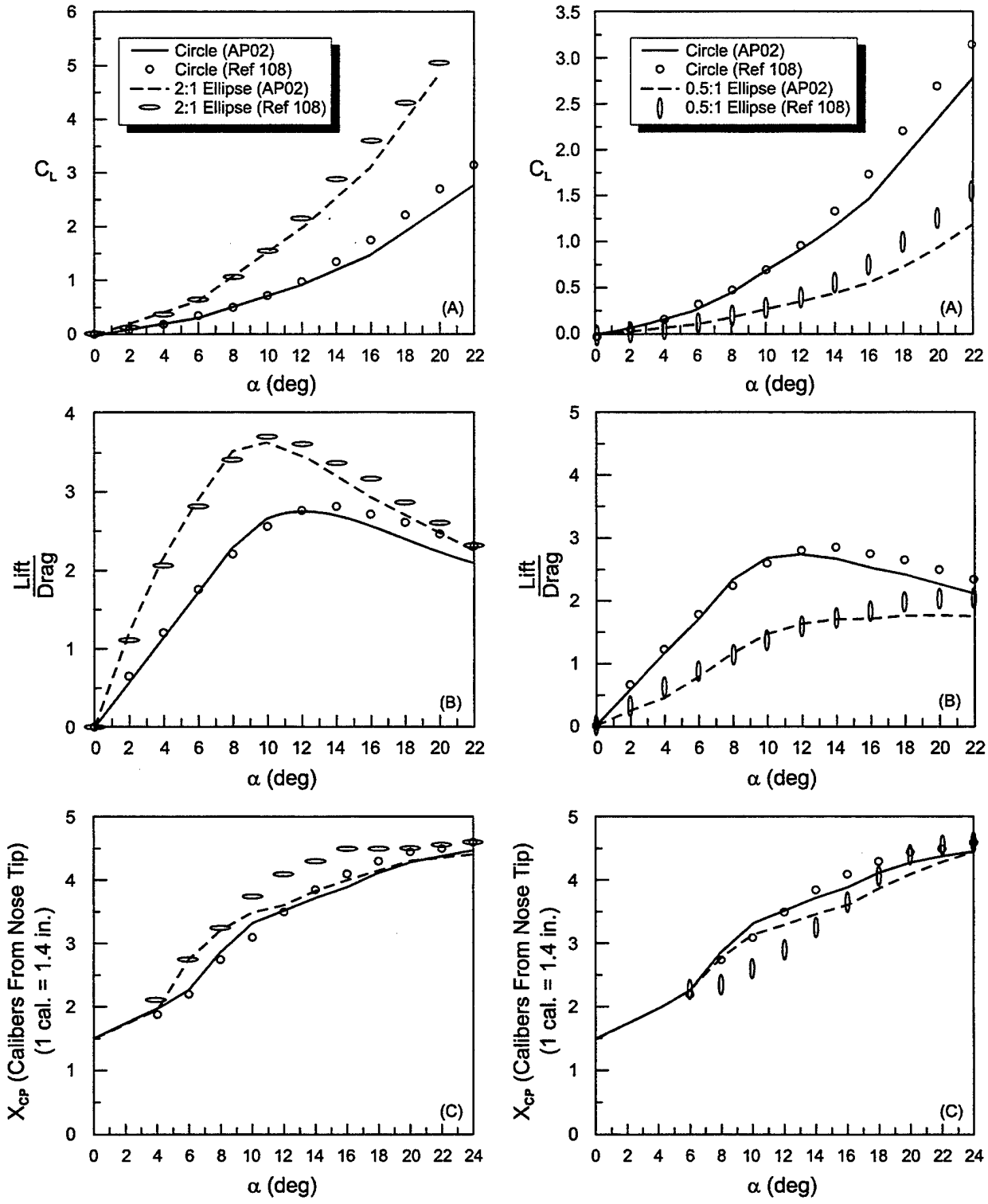

FIGURE 72. AERODYNAMIC DATA OF 2:1 AND 0.5:1 ELLIPSES OF FIGURE 71 COMPARED TO CIRCULAR BODY AND AP02 RESULTS AT M = 1.98 (L/D = 10): (A) LIFT COEFFICIENT, (B) LIFT TO DRAG RATIO, (C) CENTER OF PRESSURE

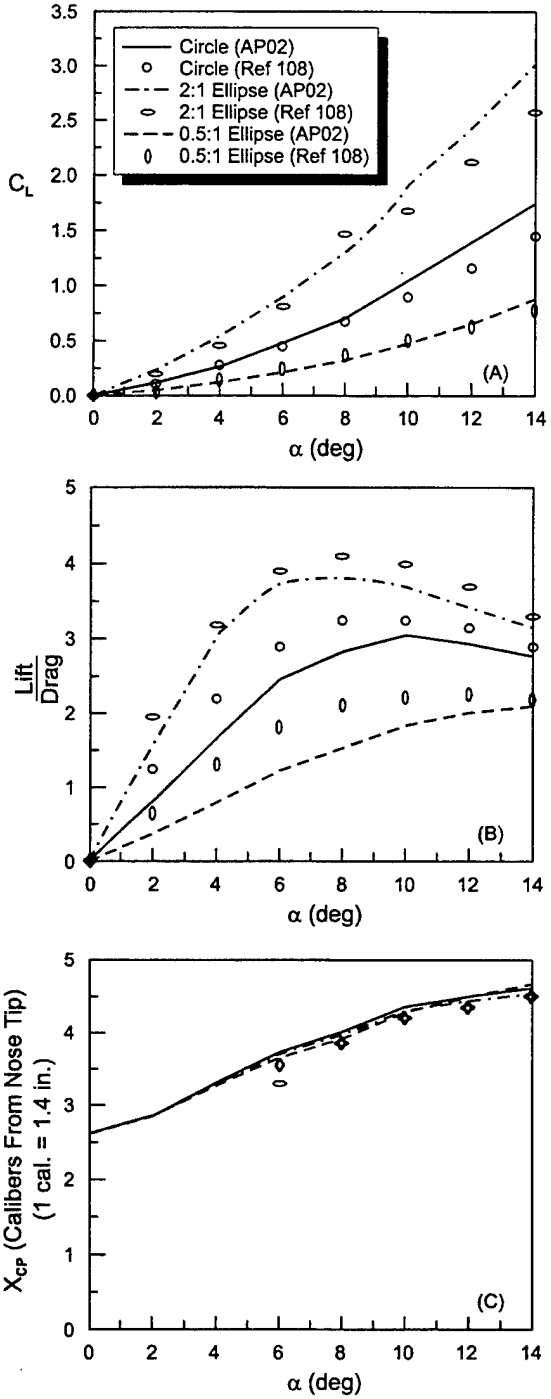

FIGURE 73. AERODYNAMIC DATA OF 2:1 AND 0.5:1 ELLIPSES OF FIGURE 71 COMPARED TO CIRCULAR BODY AND AP02 RESULTS AT M = 3.88 (L/D = 10): (A) LIFT COEFFICIENT, (B) LIFT TO DRAG RATIO, (C) CENTER OF PRESSURE

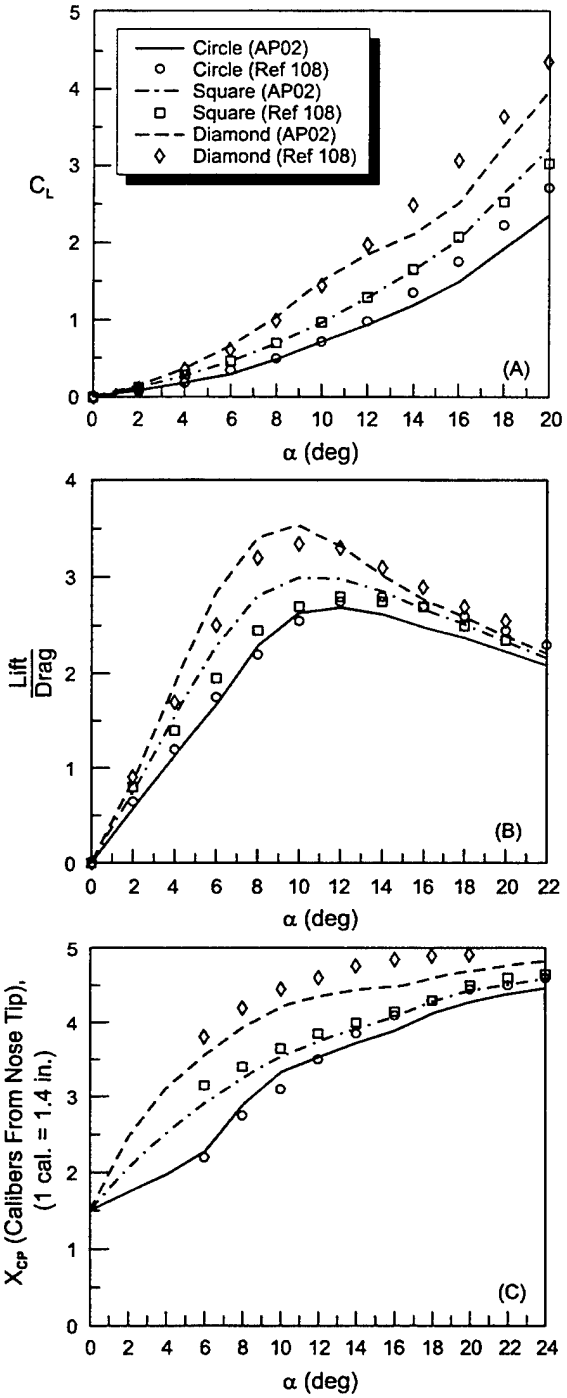

FIGURE 74. AERODYNAMIC DATA OF SQUARES (k = 0.0) AND DIAMONDS (k = 0.0) OF FIGURE 71 COMPARED TO CIRCULAR BODY AND AP02 RESULTS AT M = 1.98 (L/D = 10): (A) LIFT COEFFICIENT, (B) LIFT TO DRAG RATIO, (C) CENTER OF PRESSURE

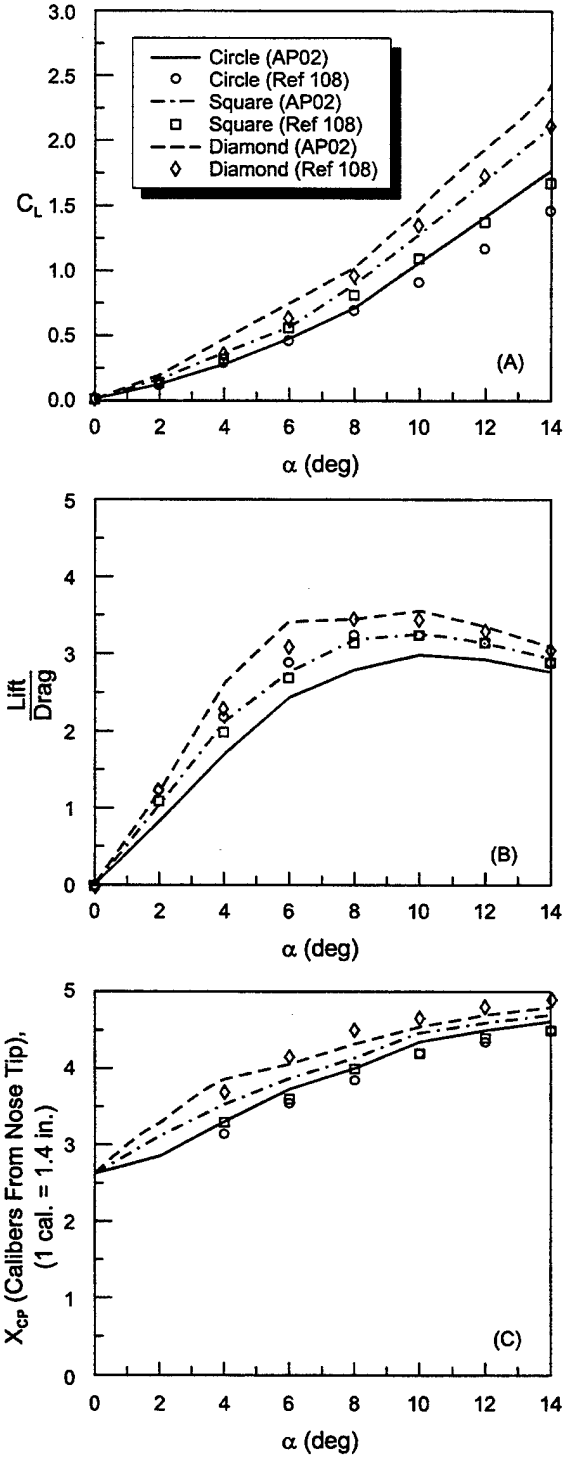

FIGURE 75. AERODYNAMIC DATA OF SQUARES (k = 0.0) AND DIAMONDS (k = 0.0) OF FIGURE 71 COMPARED TO CIRCULAR BODY AND AP02 RESULTS AT M = 3.88 (L/D = 10): (A) LIFT COEFFICIENT, (B) LIFT TO DRAG RATIO, (C) CENTER OF PRESSURE

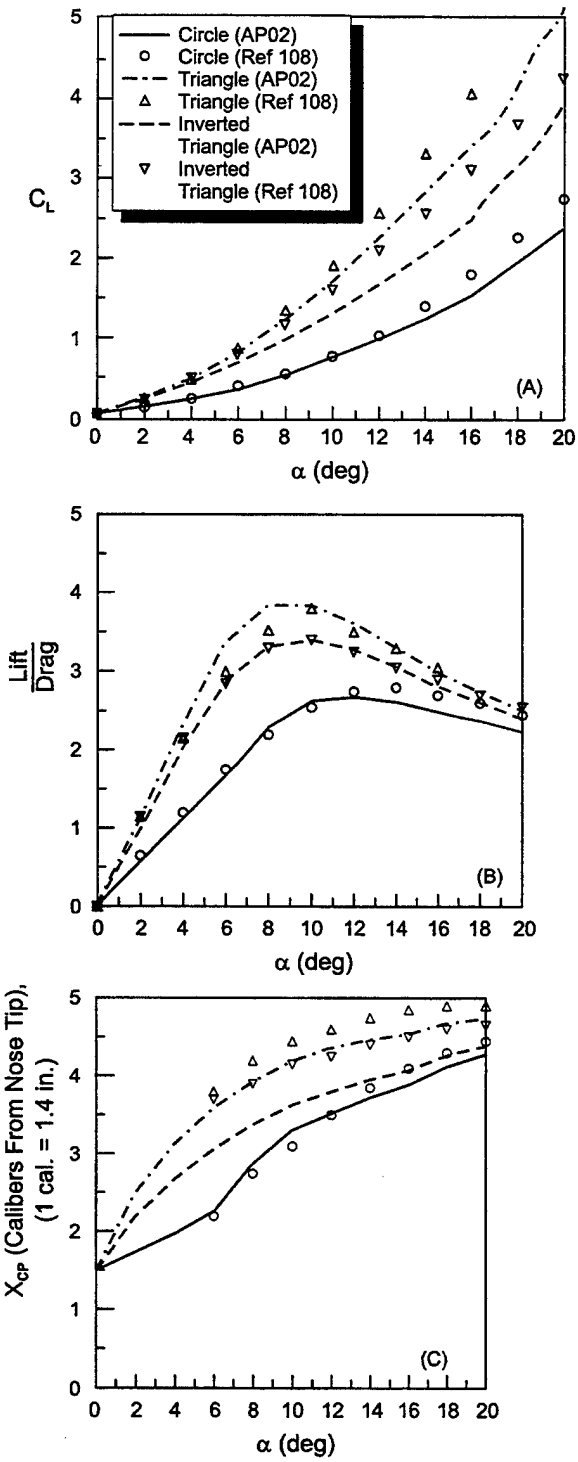

FIGURE 76. AERODYNAMIC DATA OF TRIANGLES (k = 0.0) AND INVERTED TRIANGLES (k = 0.0) OF FIGURE 71 COMPARED TO CIRCULAR BODY AND AP02 RESULTS AT M = 1.98 (L/D = 10): (A) LIFT COEFFICIENT, (B) LIFT TO DRAG RATIO, (C) CENTER OF PRESSURE

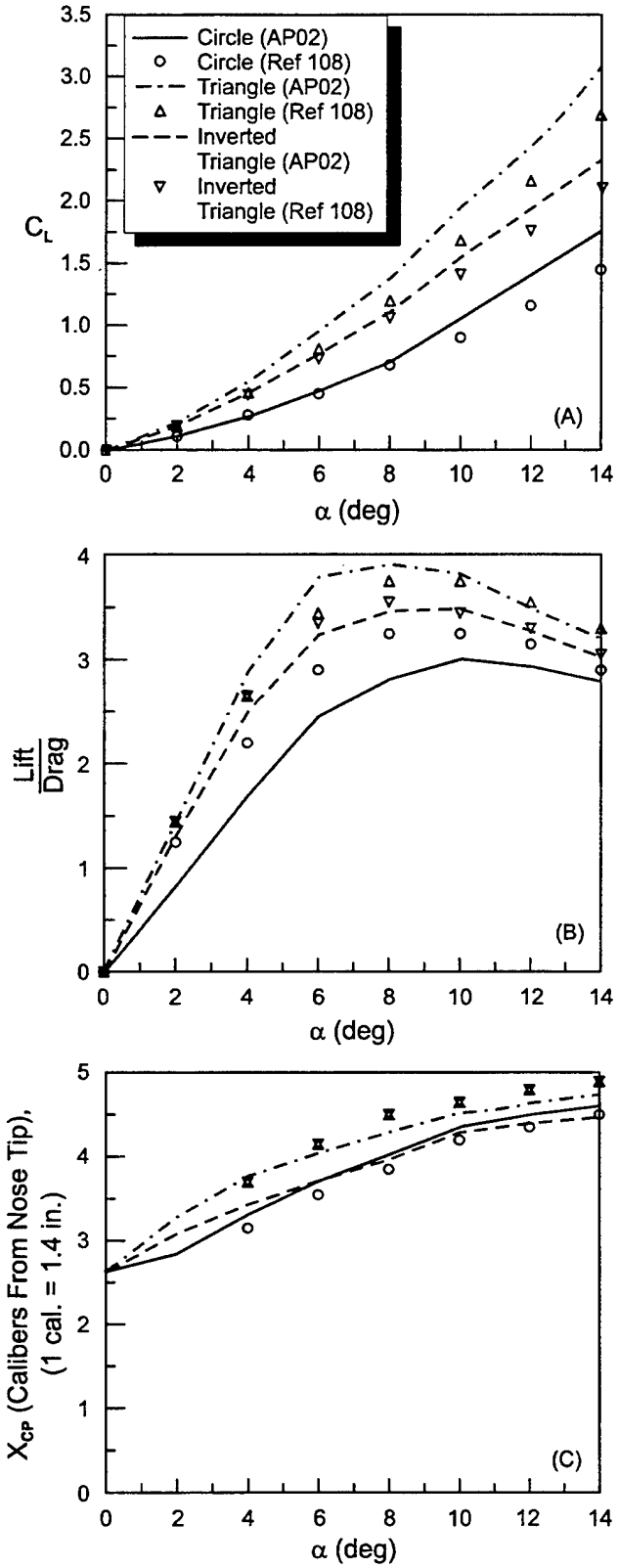

FIGURE 77. AERODYNAMIC DATA OF TRIANGLES (k = 0.0) AND INVERTED TRIANGLES (k = 0.0) OF FIGURE 71 COMPARED TO CIRCULAR BODY AND AP02 RESULTS AT M = 3.88 (L/D = 10): (A) LIFT COEFFICIENT, (B) LIFT TO DRAG RATIO, (C) CENTER OF PRESSURE

Figure 77B are fairly good, with some discrepancies at lower α, especially for the circle. As mentioned before, this situation could be attributed to the difficulty of measuring drag at low angles of attack. The center of pressure results in Figure 77C compare favorably with the wind tunnel measurements for triangles, but are slightly outside the accepted range for inverted triangles. If it is assumed that the AP02 will be allowed slightly more leeway in modeling noncircular bodies, then these results are certainly acceptable.

The AP98 results are not shown in Figures 72-77 for clarity. However, in comparing the AP98 results from Reference 55 with those of the AP02 shown in Figures 72-77, it was seen that the AP02 gave some slight improvement in predictions over the AP98. These improvements are probably due to the improved nonlinear aerodynamics methodology discussed in Section 4.1.

The second case considered is also a data base by Jorgensen[117]. He tested circular and elliptical bodies with high aspect ratio wings and tails at Mach numbers 0.6 to 2.0. The elliptical cross section shapes are illustrated in Figure 78.

Each configuration of Figure 78 has a 2:1 elliptical body. One has a large wing mounted near mid-body and the other has the same wing but, in addition, a vertical-horizontal tail assembly mounted at the rear of the body. The wind tunnel tests were conducted at Mach numbers of 0.6 and 2.0 with corresponding Reynolds numbers based on equivalent body diameter of 430000 and 380000. For the AP02 computations, R_{N_C} was set to 330000 and ΔM_{N_C} to -0.1. The comparisons for the normal force coefficients for the wing-body configuration are shown for both Mach numbers in Figure 79A and for the wing-body-tail configuration in Figure 80A. In both cases, the agreement is very good. Center of pressure predictions for these two configurations are shown in Figures 79B and 80B. As for the normal force coefficients, agreement with experimental data is very good. Also, the AP02 and AP98 results (although not shown for clarity) are almost identical for this case.

The final configuration considered is the recent data base at the Aeroballistic Research Facility at Eglin Air Force Base described in Reference 78. The configurations tested are shown in Figure 26. Zero lift axial force coefficient comparisons of the AP02 and experimental data were given in Figures 27-30. The square body results of Reference 78 are chosen as a comparison of the AP02 computations. Normal force and pitching moment coefficient derivatives, along with pitch damping, are selected from the Reference 78 data set. The AP02 square body results with fins at $\Phi = 45$ deg roll orientation and the AP02 diamond body with the fins at $\Phi = 0$ roll are compared to the ARF results. The ARF results are when the body is allowed to roll freely so an average of the square and diamond configurations will be obtained. However, the AP02 computations for these two configurations will be slightly different. Results of the AP02 computations compared to experiment are shown in Figure 81. The AP02 results for C_{N_α} compare quite nicely to the range data. Theoretical predictions of pitching and pitch damping moments are slightly high, particularly at supersonic speeds.

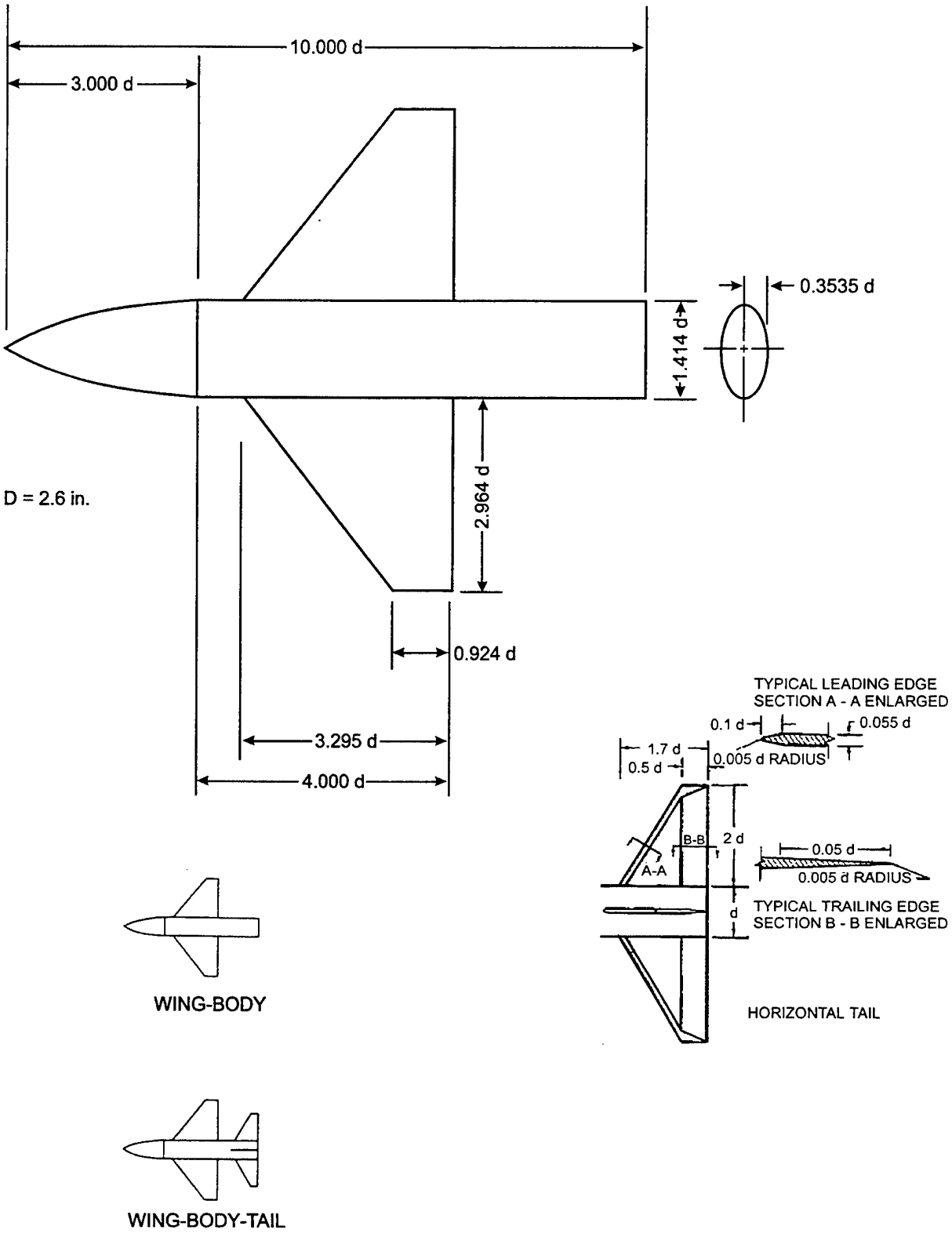

FIGURE 78. GEOMETRY OF THE WING-BODY AND WING-BODY-TAIL CONFIGURATIONS WITH 2:1 ELLIPTICAL BODIES

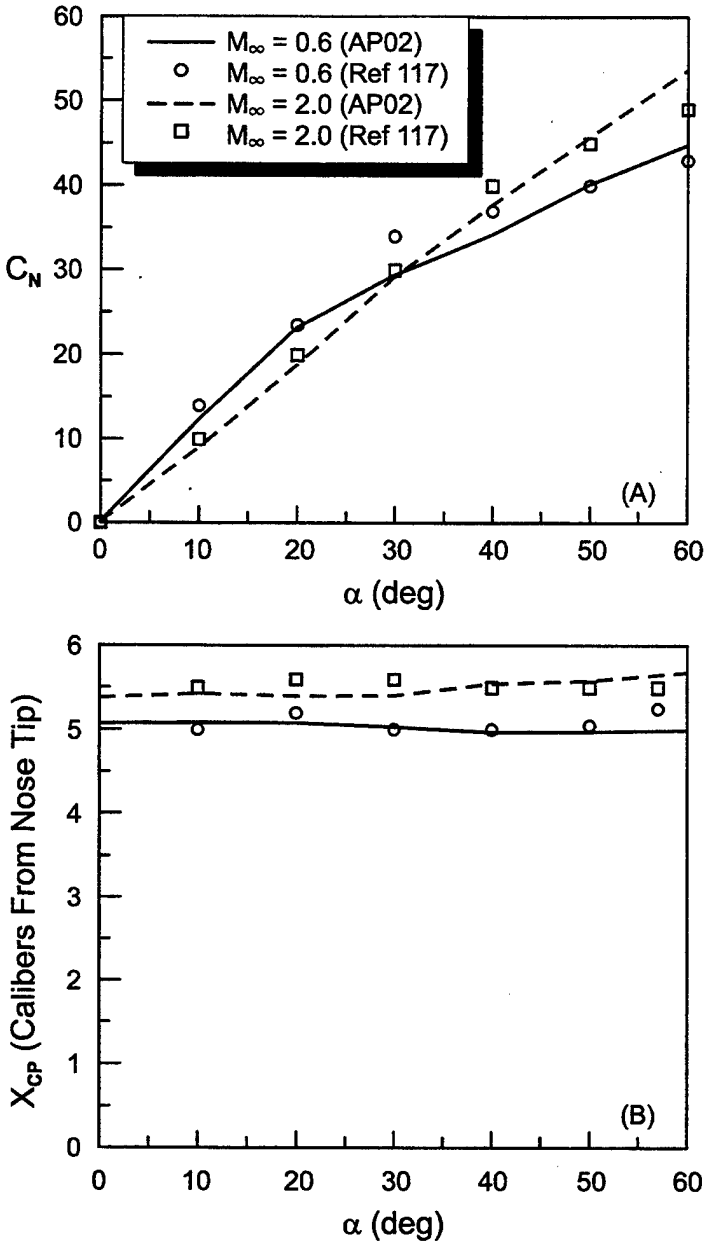

FIGURE 79. AERODYNAMIC DATA FOR THE WING-BODY CONFIGURATION OF FIGURE 78 WITH A 2:1 ELLIPTICAL CROSS SECTION BODY: (A) NORMAL FORCE COEFFICIENT, (B) CENTER OF PRESSURE

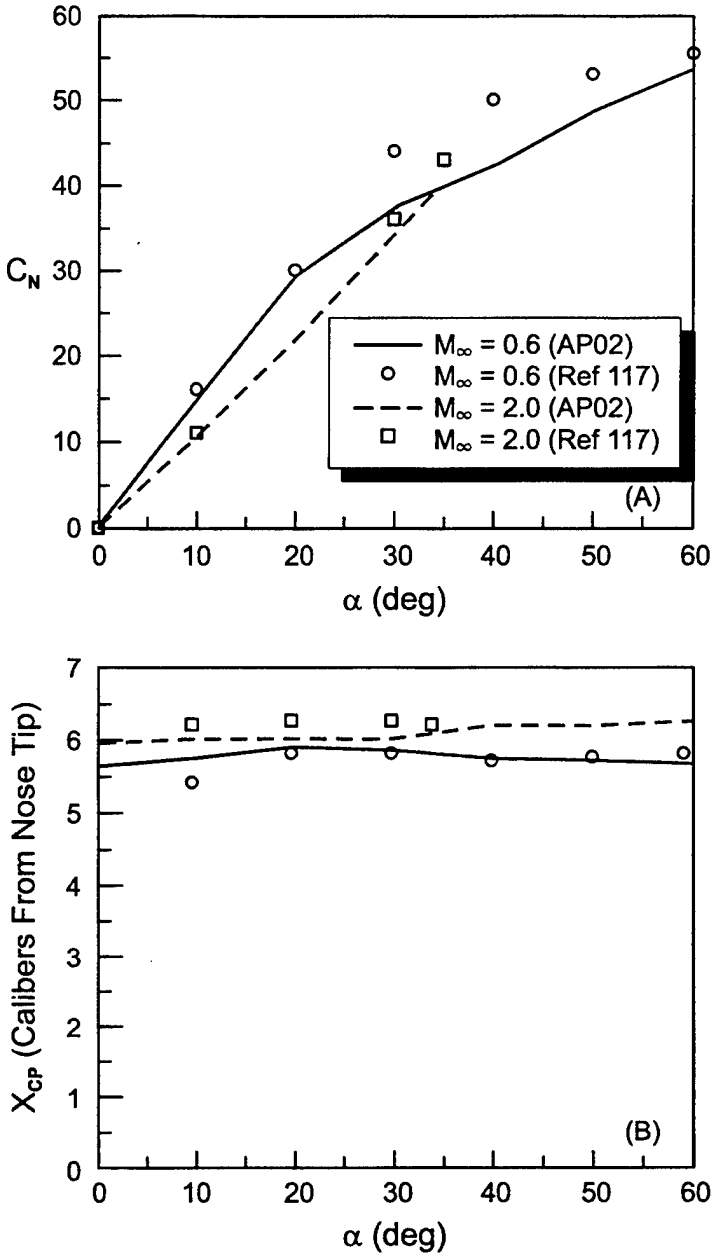

FIGURE 80. AERODYNAMIC DATA FOR THE WING-BODY-TAIL CONFIGURATION OF FIGURE 78 WITH A 2:1 ELLIPTICAL CROSS SECTION BODY: (A) NORMAL FORCE COEFFICIENT, (B) CENTER OF PRESSURE

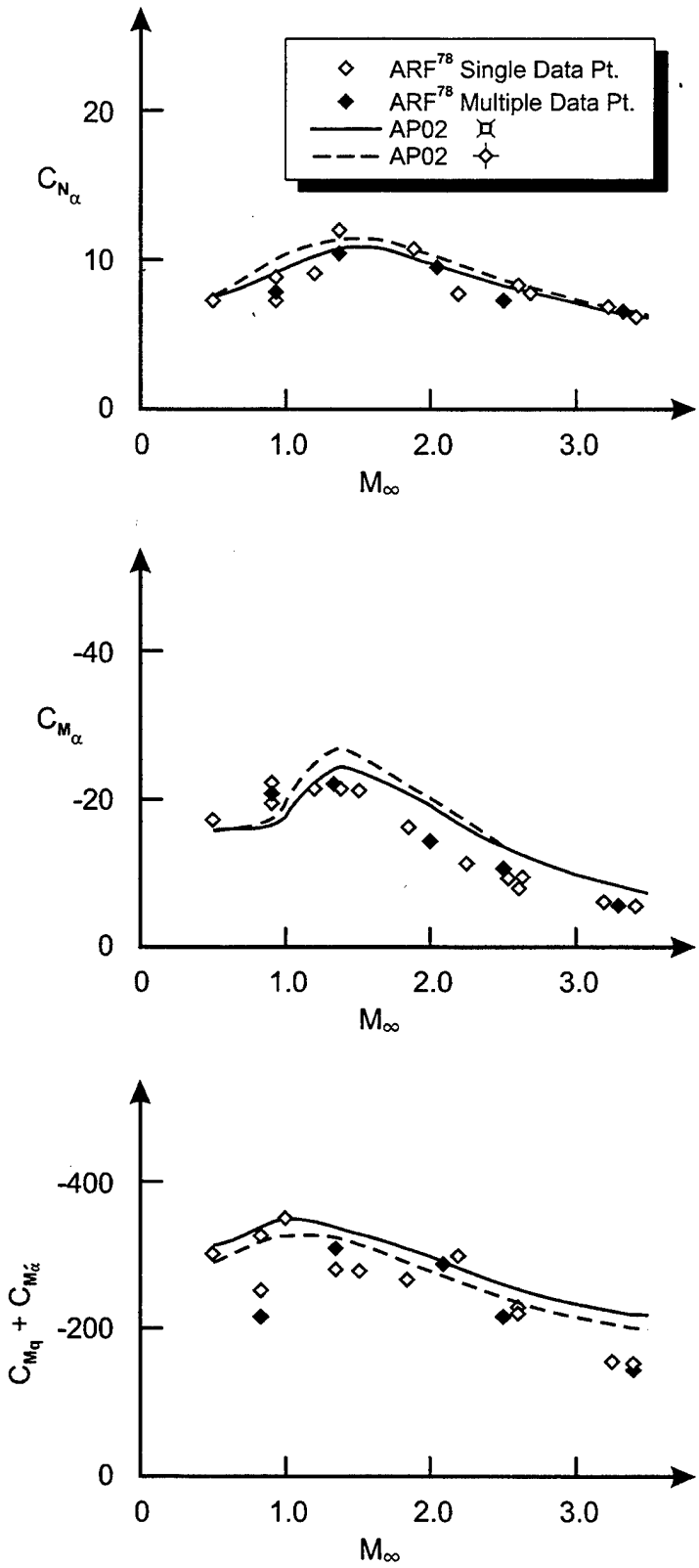

FIGURE 81. COMPARISON OF AP02 PREDICTIONS TO ARF SQUARE BODY TEST RESULTS (SEE FIGURE 26)

In general, the AP02 predictions for aerodynamics of nonaxisymmetric bodies are as good as or slightly better than those of the AP98. In general, the aerodynamic predictions of the AP02 for nonaxisymmetric bodies is not quite as good as axisymmetric bodies. This is as expected, due to approximating the nonaxisymmetric body by an equivalent axisymmetric body.

4.7 TRAJECTORY EXAMPLES

Two examples will be chosen to illustrate the new capability that will be part of the AP02 to not only compute aerodynamics, but to predict range as well. The first case will be a ballistic round typical of an unguided projectile. The second case will be a fin stabilized round that will utilize the trim performance model to predict range.

4.7.1 Ballistic Example

Figure 82A shows the configuration that will be considered for range computations. It is a 5 inch diameter round, 26 inches in length with a 3 caliber tangent ogive nose. The nose has a meplat diameter of 0.5 inches, typical of most fuze designs. The round also has a 1 caliber boattail with a 7 deg boattail angle. The Figure 82A configuration is assumed to weigh 65 lb and to have an initial velocity of 3000 ft/sec. We will first consider the range of this configuration when launched at an elevation angle of 50 deg. The free flight boundary layer option will be used for the aerodynamic computations since we are computing range.

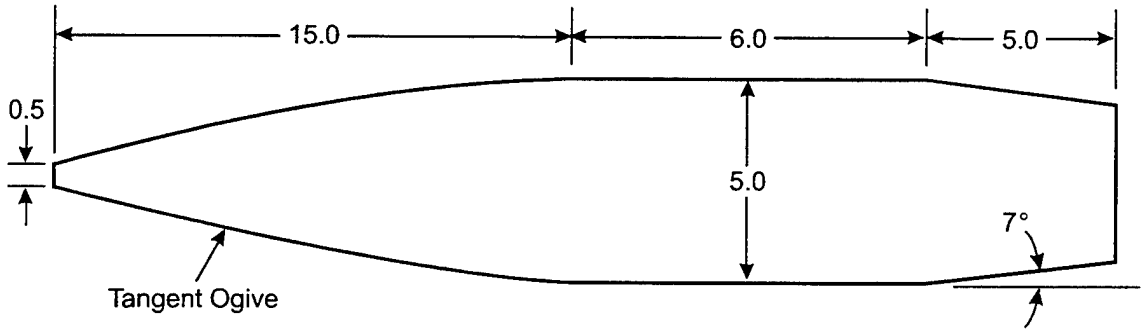

FIGURE 82A. TYPICAL SPIN STABILIZED PROJECTILE (DIMENSIONS IN INCHES)

Figure 82B shows the axial force coefficient versus Mach number for an AOA 1 deg. Figures 82C - 82E show some of the many plots available in the AP02 interface. Figure 82C gives the altitude versus range, Figure 82D provides the Mach number versus time of flight, and Figure 82E gives the drag coefficient versus time of flight. Notice the round travels just under 90,000 ft (29,967 yards to be exact), with about 75 percent of the flight time between M_∞ of 1.2 and 0.9.

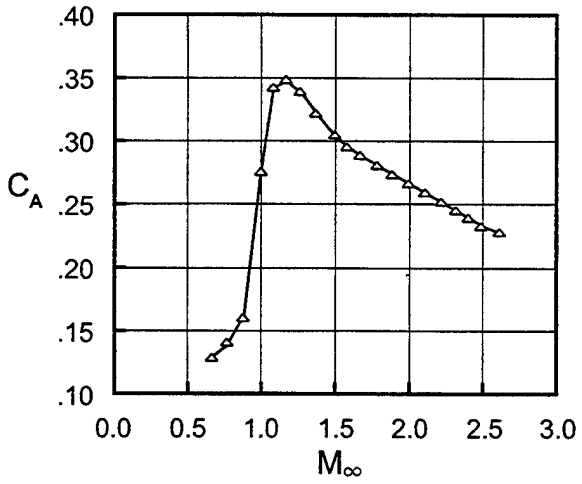

FIGURE 82B. AXIAL FORCE COEFFICIENT VERSUS MACH NUMBER FOR FIGURE 82A CONFIGURATION (α = 1 DEG)

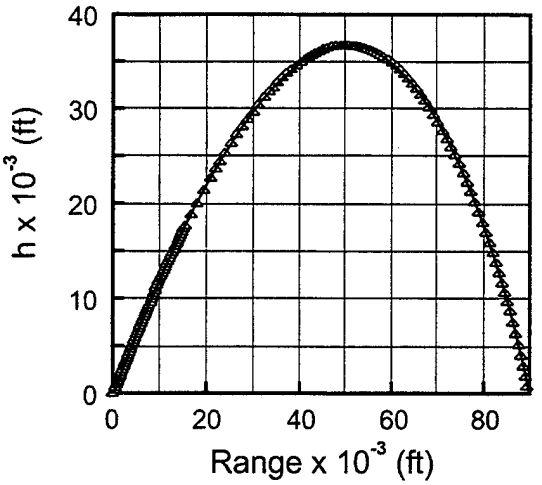

FIGURE 82C. ALTITUDE VERSUS RANGE FOR FIGURE 82A CONFIGURATION (QE = 50 DEG)

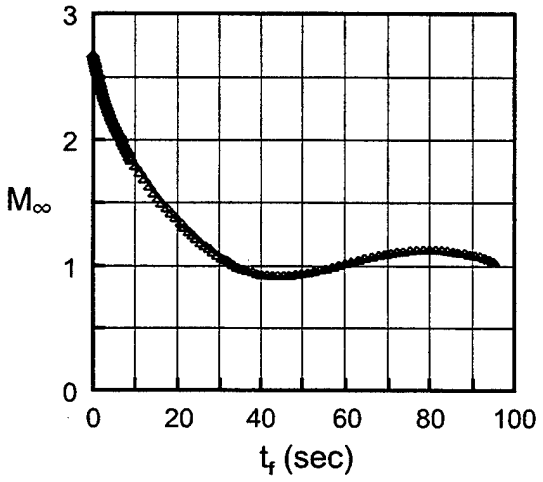

FIGURE 82D. MACH NUMBER VERSUS TIME OF FLIGHT FOR FIGURE 82A CONFIGURATION (QE = 50 DEG)

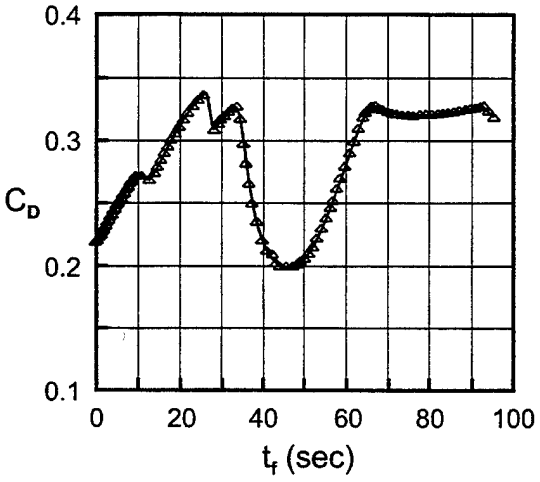

FIGURE 82E. DRAG COEFFICIENT VERSUS TIME OF FLIGHT FOR FIGURE 82A CONFIGURATION (QE = 50 DEG)

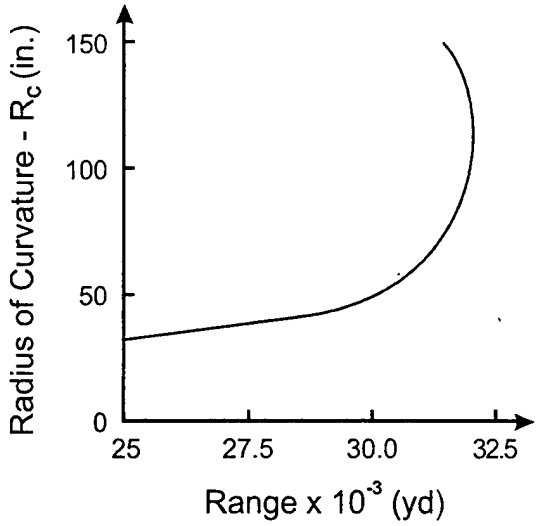

FIGURE 83A. RADIUS OF CURVATURE VERSUS RANGE FOR FIGURE 82A CASE WITH SECANT OGIVE (W = 65 LB, IV = 3000 f/sec, QE = 50 DEG)

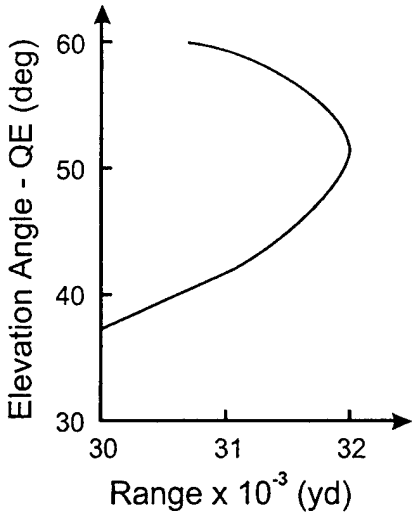

FIGURE 83B. ELEVATION ANGLE VERSUS RANGE FOR FIGURE 82A CASE WITH SECANT OGIVE (W = 65 LB, IV = 3000 f/sec, R_c = 120 IN.)

To illustrate a typical design application of the new trajectory package that has been integrated with the aerodynamics module of the AP02, consider the following. We would like to compare a secant ogive to the tangent ogive of the Figure 82A nose for possible range improvement. We would then like to determine the elevation angle for maximum range with the best secant ogive nose shape. Figure 83A compares the range of the secant ogive versus the radius of curvative of the ogive. Figure 83A assumes the same initial conditions as those used for Figure 82A (W = 65 lb, IV = 3000 ft/sec, QE = 50 deg). Figure 83A shows the maximum range is obtained for a radius of curvature of 120 inches. On the other hand, if one wants slightly more volume with little range penalty, a radius of curvature of 80 to 120 inches could be selected. Also noteworthy is the fact that the 120 inches radius of curvature secant ogive gives a 1971 yard range increase over the tangent ogive shape of Figure 82A (31938 versus 29967). This amounts to a 6.6 percent range increase, which is quite substantial just by changing the ogive type. Figure 83B gives the range for various elevation angles using the optimum radius of curvature of 120 inches for the Figure 82A case where the tangent ogive is replaced by a secant ogive. Note from Figure 83B, the maximum range is obtained at a QE of 52 deg. The maximum range obtained is 31,999 yards.

Figures 82 and 83 are just one example of a design tradeoff and elevation angle study. Other design studies could also be conducted. A few of these would examine other ogive shapes for minimum drag and maximum range, boattail length versus range, nose tip shape (sharp, blunt, or truncated) versus range, or nose tip bluntness ratio versus range just to name a few. Any of these design studies can now be performed by a single person in a matter of a few hours using the AP02.

4.7.2 Trim Performance Model Example

The second example to be illustrated using the new trajectory models uses the trim performance model. The configuration chosen is a simple body tail with a 3 caliber secant ogive (see Figure 84). The tail has an aspect ratio of 0.67. The parameters used in the trajectory analysis are provided in Table 39. Table 39A is for a configuration that has a 40 percent propellant to total weight ratio, whereas Table 39B is for a 50 percent propellant to total weight ratio. The initial thrust to weight ratio for both options in Table 39 is 7.4. Table 39A allows for a burn time of 10 sec whereas Table 39B has a burn time of 12.5 sec due to the 25 percent larger mass of propellant. Both Tables 39A and 39B assume a maximum tail fin deflection of ±30 deg, have a structural limit of 60 g's, and are launched from a surface launcher with an exit velocity of 100 ft/sec at an elevation angle of 45 deg. Figure 85 illustrates the results of flying the Figure 84 configuration using Table 39A parameters in a purely ballistic mode. As seen in the figure, a maximum Mach number of about 2.5 is obtained as the engine burns out after 10 sec. The vehicle attains an altitude of about 20,000 ft and a range of about 100,000 ft using the set of conditions in Table 39A and the drag curve provided internally within the AP02.

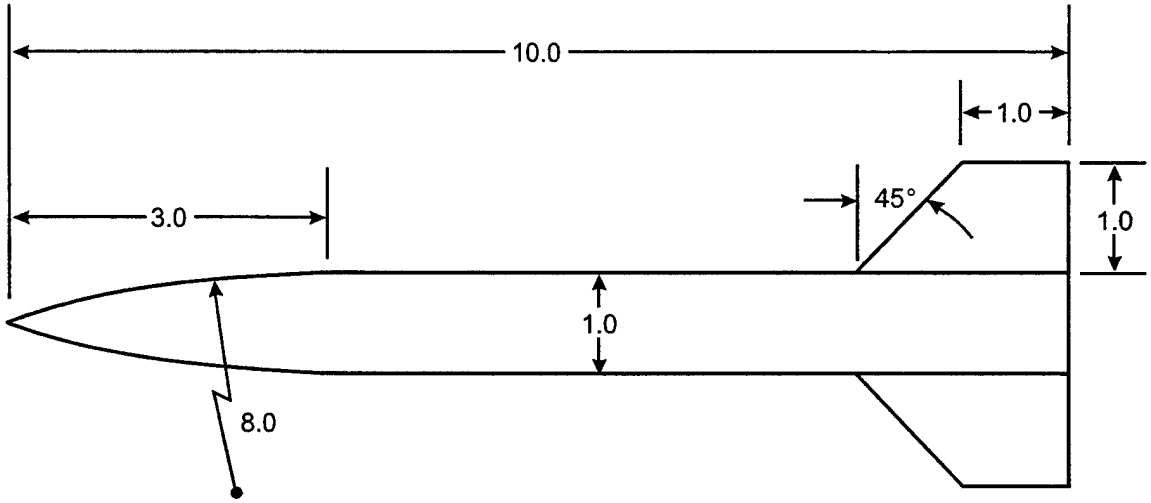

FIGURE 84. BODY-TAIL MISSILE CONCEPT USED IN TRAJECTORY ANALYSIS (ALL DIMENSIONS IN FT)

Figure 86 then takes the very same conditions for Figure 85 except a guidance mode is selected in the trim model that allows the vehicle to fly a maximum lift to drag ratio trajectory. For this case, the minimum Mach number is lower than Figure 85A due to the fin deflection and AOA. However, the altitude is slightly higher and a range increase to 125,000 ft is realized due to the maximum L/D trajectory.

The final option is shown in Figure 87. This case is also for a maximum L/D trajectory, except the parameters of Table 39B are used to fly the Figure 84 configuration. Notice that a 25 percent increase in propellant produces a 40 percent increase in maximum Mach number (Figure 87A compared to Figure 86A) and a 45 percent increase in maximum range (Figure 87B compared to Figure 86B).

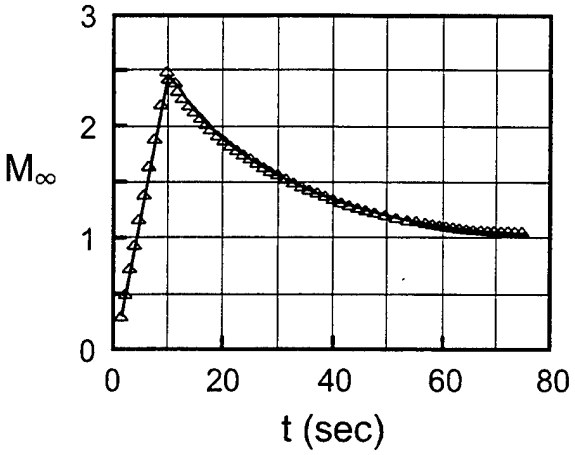

FIGURE 85A. MACH NUMBER PROFILE FOR BALLISTIC TRAJECTORY FOR FIGURE 84 CONFIGURATION WITH TABLE 39A PARAMETERS

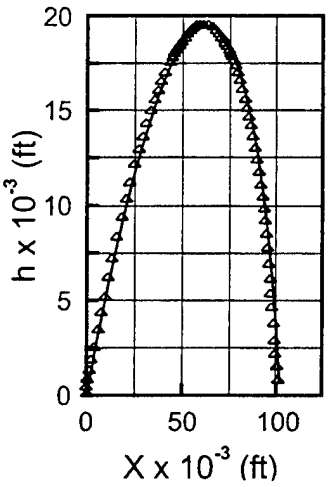

FIGURE 85B. ALTITUDE VERSUS RANGE FOR BALLISTIC TRAJECTORY FOR FIGURE 84 CONFIGURATION WITH TABLE 39A PARAMETERS

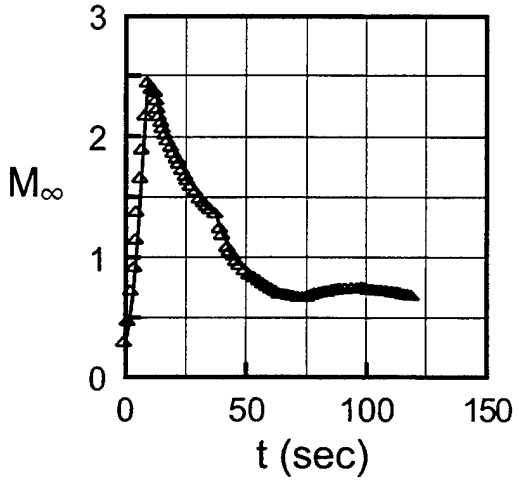

FIGURE 86A. MACH NUMBER PROFILE FOR MAXIMUM L/D TRAJECTORY FOR FIGURE 84 CONFIGURATION WITH TABLE 39A PARAMETERS

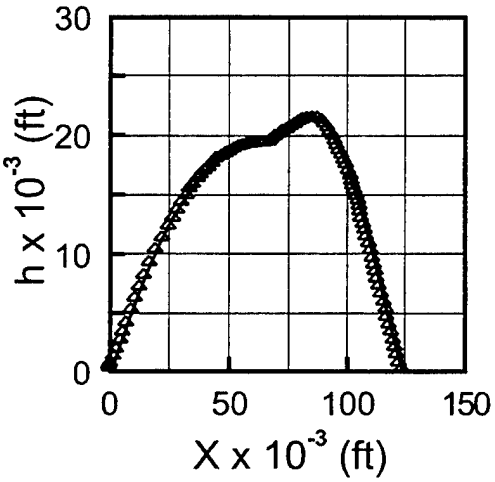

FIGURE 86B. ALTITUDE VERSUS RANGE FOR MAXIMUM L/D TRAJECTORY FOR FIGURE 84 CONFIGURATION WITH TABLE 39A PARAMETERS

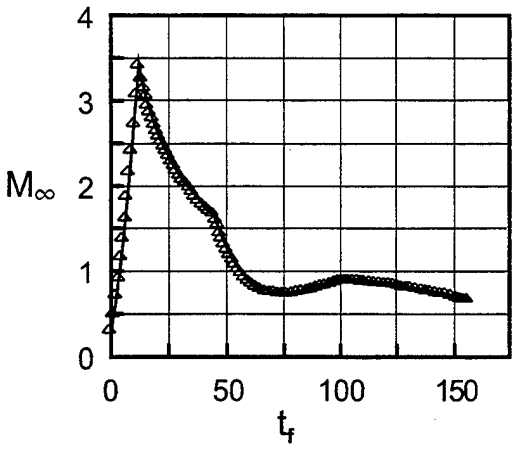

FIGURE 87A. MACH NUMBER PROFILE FOR MAXIMUM L/D TRAJECTORY FOR FIGURE 84 CONFIGURATION WITH TABLE 39B PARAMETERS

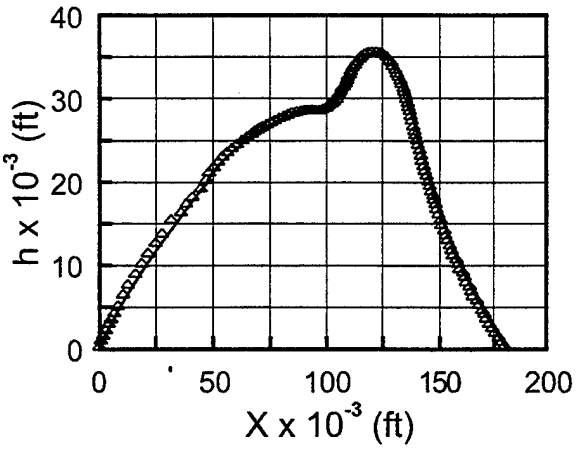

FIGURE 87B. ALTITUDE VERSUS RANGE FOR MAXIMUM L/D TRAJECTORY FOR FIGURE 84 CONFIGURATION WITH TABLE 39B PARAMETERS

TABLE 39. PARAMETERS USED IN TRAJECTORY ANALYSIS FOR FIGURE 84 CONFIGURATION

A. 600 lb Propellant	B. 750 lb Propellant
W_O = 1500 LB	W_O = 1500 LB
W_{BO} = 900 LB	W_{BO} = 750 LB
t_{BO} = 10 sec	t_{BO} = 12.5 sec
CG = 5.5 ft at t = 0	CG = 5.5 ft at t = 0
CG = 5.0 ft at t ≥ 10 sec	CG = 4.83 ft at t ≥ 12.5 sec
T_1 = 11100 lb for 10 sec	T_1 = 11100 lb for 12.5 sec
T_2 = 0 for t > 10 sec	T_2 = 0 for t > 12.5 sec
δ_{max} = ± 30 deg	δ_{max} = ± 30 deg
g limit = 60 g's	g limit = 60 g's
IV = 100 ft/sec	IV = 100 ft/sec
QE = 45 deg	QE = 45 deg

Figures 85 - 87 illustrate just one application of the trim performance model. One could examine variations in thrust, weight, center of gravity, or various other configuration design options very easily using the AP02 with a single person as opposed to the AP98 and all prior versions requiring an illustration process with two people. Other design options include various guidance modes including proportional navigation, explicit and a user defined option as well. Initial launch conditions are allowed from a surface or air vehicle and target parameters can be fairly general as well.

In summary, the new ballistic and trim performance models that will be part of the AP02 will allow the user to rapidly determine the effect of a given airframe or weapon system parameter on the overall performance of the vehicle. This new model will save many hours and many dollars through the provided productivity improvements.

5.0 SUMMARY

In summary, new technology has been developed that will allow the APC to treat weapons in a more robust and accurate manner in the aerodynamic calculation process. The latest version of the APC will be referred to as the AP02. Some of these new technologies include the capability to consider configurations with 6 and 8 fins in addition to the present (2 and 4 fin options), improved nonlinear aerodynamics for higher AOA, improved dynamic derivatives with particular emphasis on pitch damping, improved power-on base drag prediction for rockets, a new base bleed capability for projectiles, improved axial force prediction of nonaxisymmetric bodies, and new technology that allows trailing edge flap aerodynamics to be calculated. In addition to the new aerodynamics technology developed, several other improvements and productivity enhancements have been integrated into the APC. These include an aerodynamic smoother for the aerodynamics, ballistic and 3 DOF trajectory models, many additional plots in the post processor for APC output, alternative reference length and area options in the pre-processor for the APC inputs. Many of the new technologies integrated into the AP98 which form the AP02 were driven by advanced projectile concepts.

In comparing the new technology to predict the nonlinear aerodynamics to both the AP98 and experimental data, it was seen that the AP02 reduces the average AP98 normal force coefficient prediction errors by about 25 percent. Both the AP98 and AP02 give average normal force and axial force errors within the ± 10 percent goal of the APC. Some slight improvement in axial force, pitching moment, and center of pressure predictions were also seen using the AP02, but were not quantified.

In comparing the new multi-fin aerodynamic prediction capability of the AP02 and experimental data on a limited number of cases, it was seen that acceptable accuracy was obtained for static and dynamic aerodynamic coefficients. Additional multi-fin data would be desirable, particularly for 8 fin cases, in order to allow additional validation of the multi-fin capability.

The pitch damping improvements added to the APC code were seen to improve the pitch damping moment coefficient derivative accuracy compared to experiment for body-alone and bodies with flares. While not shown, the body-alone improvements will also improve the predictions of pitch damping for wing-body or body-tail cases as well.

The modified engine on base pressure prediction was seen to be as accurate or slightly more accurate than the AP98 predictions, while being much more robust in terms of input options. The new base bleed capability was seen to compare well to a range of experimental data for both cold and hot exhaust data.

Comparison of normal force, pitching moment, and axial force coefficients of the AP02 trailing-edge flap predictions to limited experimental data showed predictions to give acceptable accuracy. However, additional data for validation purposes would be desirable.

The aerodynamics of nonaxisymmetric bodies are seen to be slightly improved using the AP02 compared to the AP98. These improvements in aerodynamic prediction accuracy are due to the improvements added for axial force coefficient and the improved nonlinear aerodynamics discussed earlier.

Finally, the ballistic and 3 DOF trajectory options available as part of the APC were seen to improve cost effectiveness of aerodynamic design as well as performance assessment of conceptual design tradeoffs. The cost reductions were due to the single person, versus two people with the AP98, being able to make design changes and examine the effect of the design changes on performance in a very rapid manner.

In general, it is believed the AP02 is by far the most robust, as well as the most accurate, of all prior versions of the APC. As such, the AP02 will be a significant capability for engineers in the conceptual and preliminary design phase of weapon development. The AP02 will also find use among personnel involved in numerical code calculations, since the AP02 will approximate total aerodynamics one should expect from the numerical code.

6.0 REFERENCES

1. Pitts, W. C,; Nielsen, J. N.; and Kaatari, G. E., *Lift and Center of Pressure of Wing-Body-Tail Combinations at Subsonic, Transonic, and Supersonic Speeds*, NACA TR 1307, 1957.

2. Douglas Aircraft Co. Inc., *USAF Stability and Control DATCOM*, Revisions by Wright Patterson Air Force Base, OH, 2 Vols., Jul 1963.

3. Whyte, R. E., *Spinner – A Computer Program for Predicting the Aerodynamic Coefficients of Spin Stabilized Projectiles*, General Electric Class 2 reports, 1969.

4. Saffell, B. F., Jr.; Howard, M. L.; and Brooks, E. N., Jr., *A Method for Predicting the Static Aerodynamic Characteristics of Typical Missile Configurations for Angles of Attack to 180 Degrees*, NSRDC Report 3645, 1971 (Bethesda, MD).

5. Moore, F. G., *Body Alone Aerodynamics of Guided and Unguided Projectiles at Subsonic, Transonic, and Supersonic Mach Numbers*, NWL TR-3796, Nov 1972.

6. Moore, F. G., "Aerodynamic Drag and Lift of General Body Shapes at Subsonic, Transonic, and Supersonic Mach Numbers," AGARD Conference Preprint No. 124 on Aerodynamic Drag, Paper No. 2, 1973.

7. Moore, F. G. and McKerley, C. W., *Aerodynamics of Guided and Unguided Weapons: Part I – Theory and Application*, NWL TR-3018, Dec 1973.

8. Moore, F. G. and McKerley, C. W., *Aerodynamics of Guided and Unguided Weapons: Part II – Theory and Application*, NWL TR-3036, Jan 1974.

9. Moore, F. G., "Static Aerodynamics of Missile Configurations for Mach Number Zero to Three," AIAA Paper No. 74-538, Jun 1974 and Journal of Aircraft, Vol. 12, No. 10, pp. 797-806, Oct 1975.

10. Graff, G. and Moore, F. G., *The Effect of Boattail Shape on Magnus*, NSWCDL TR-3581, Dec 1976.

11. Graff, G. and Moore, F. G., "Empirical Method for Predicting the Magnus Characteristics of Spinning Shells," AIAA Journal, Vol. 15, No. 10, pp. 1379-1380, Oct 1977.

REFERENCES (Continued)

12. Moore, F. G. and Swanson, C., *Aerodynamics of Tactical Weapons to Mach Number 3 and Angle of Attack 15 Degrees: Part I – Theory and Application*, NSWCDL TR-3584, Feb 1977.

13. Swanson, C. and Moore, F. G., *Aerodynamics of Tactical Weapons to Mach Number 3 and Angle of Attack 15 Degrees: Part II – Computer Program and Usage*, NSWCDL TR-3600, Mar 1977.

14. Moore, F. G. and Swanson, C., "Dynamic Derivatives for Missile Configurations to Mach Number Three," *Journal of Spacecraft and Rockets*, Vol. 15, No. 4, 1978.

15. Devan, L.; Sun, J.; and Moore, F. G., "Aerodynamic Prediction for Tactical Weapons," AIAA Paper 79-0361, 17th Aerospace Sciences Meeting, New Orleans, LA, 15-17 Jan, 1979.

16. DeJarnette, F. R., Ford, C. P.; and Young, D. E., "Calculation of Pressures on Bodies at Low Angles of Attack in Supersonic Flow," AIAA Article No. 79-1552, *JSR*, Vol. 17, No. 6, pp. 529-536, Nov-Dec 1980.

17. Chaussee, D. S., *Improved Transonic Nose Drag Estimates for the NSWC Missile Aerodynamic Computer Program*, Nielsen Engineering Contractor Report Prepared for NSWC as NSWC/DL TR-3830, Apr 1978.

18. Devan, L., *Aerodynamics of Tactical Weapons to Mach Number 8 and Angle of Attack 180 °: Part I, Theory and Application*, NSWC TR 80-346, Oct 1980.

19. Devan, L. and Mason, L., *Aerodynamics of Tactical Weapons to Mach Number 8 and Angle of Attack 180 Degrees; Part II, Computer Program and Users Guide*, NSWC TR-81-358, Sep 1981.

20. Mason. L.; Devan, L.; Moore, F.; and McMillan, D., *Aerodynamic Design Manual for Tactical Weapons*, NSWC TR-81-156, Jul 1981.

21. Devan, L.; Mason, L.; and Moore, F. G., "Aerodynamics of Tactical Weapons to Mach Number 8 and Angle-of-Attack 180 Degrees," AIAA Paper 82-0250, AIAA 20th Aerospace Sciences Meeting, 11-14 Jan 1982.

22. Moore, F. G.; Armistead, M.; Rowles, S.; and DeJarnette, F. R., *Second-Order Shock Expansion Theory Extended to Include Real Gas Effects*, NAVSWC TR 90-683, Feb 1992.

REFERENCES (Continued)

23. Moore, F. G.; Armistead, M.; Rowles, S.; and DeJarnette, F. R., "A New Approximate Method for Calculating Real Gas Effects on Missile Configurations," AIAA paper No. 92-4637, AFM Conference, Aug 1993, Also JSR Vol. 30, No. 1, pp. 22-31, Jan-Feb 1993.

24. Moore, F. G.; Hymer, T.; and Devan, L., *New Methods for Predicting Nonlinear Lift, Center of Pressure, and Pitching Moment on Missile Configurations*, NSWCDD/TR-92/317, Jul 1992.

25. Moore, F. G.; Devan. L.; and Hymer, T,. "A New Semiempirical Method for Computing Nonlinear Angle-of-Attack Aerodynamics on Wing-Body-Tail Configurations," AIAA Paper No. 93-0034 presented at 31st Aerospace Sciences Meeting, 1993.

26. McInville, R. M. and Moore, F. G., *Incorporation of Boundary Layer Heating Predictive Methodology into the NAVSWC Aeroprediction Code*, NSWCDD TR-93/29, Apr 1993.

27. Moore, F. G.; Wilcox, F.; and Hymer, T., *Improved Empirical Model for Base Drag Prediction on Missile Configurations Based on New Wind Tunnel Data*, NSWCDD TR-92-509, Oct 1992.

28. Moore, F. G.; Wilcox, F.; and Hymer, T., "Base Drag Predictions of Missile Configurations," AIAA Paper No. 93-3629 presented at AIAA Atmospheric Flight Mechanics Conference in Monterey, CA, Aug 1993. (Also Journal of Spacecraft and Rockets, Sep-Oct 1994, Vol. 31, No. 5, pp. 759-765.)

29. Moore, F. G.; Hymer, T.; and McInville, R., *Improved Aeroprediction Code: Part I – Summary of New Methods and Comparison with Experiment*, NSWCDD TR-93/91, May 1993.

30. Moore, F. G.; McInville, R.; and Hymer, T., *Improved Aeroprediction Code: Part II – Computer Program User's Guide and Listing*, NSWC TR-93/241, Aug 1993.

31. Moore, F. G.; Devan, L.; and Hymer, T., "A New Semiempirical Method for Computing Nonlinear Missile Aerodynamics," *AIAA Journal of Spacecraft and Rockets*, pp. 696-706, Nov-Dec 1993.

32. Moore, F. G., *State-of-the-Art Engineering Aeroprediction Methods with Emphasis on New Semiempirical Techniques for Predicting Nonlinear Aerodynamics on Complete Missile Configurations*, NSWCDD/TR-93/551, Nov 1993.

33. Moore, F. G., "Engineering codes: State-of-the-Art and New Methods," AGARD Paper No. 2 on Missile Aerodynamics Given at Brussels, Belgium, and Ankora, Turkey, Jun 1994.

REFERENCES (Continued)

34. McInville, R. M., and Moore, F. G., "Incorporation of Boundary Layer Heating Predictive Methodology into the NAVSWC Aeroprediction Code," AIAA Paper No. 2001, presented at the 6th AIAA/ASME Joint Thermo Physics and Heat Transfer Conference, Colorado Springs, CO, Jun 1994.

35. Moore, F. G.; McInville, R. M.; and Hymer, T. C., "An Improved Version of the Naval Surface Warfare Center Aeroprediction Code (AP93)," Journal of Spacecraft and Rockets, Vol. 31, No. 5, pp. 783-791, Sep-Oct 1994.

36. Moore, F. G.; McInville, R.; and Hymer, T. C., "Planar Nonlinear Missile Aeroprediction Code for All Mach Numbers," AIAA paper No. 94-0026, 32nd Aerospace Sciences Meeting, Reno, NV, Jan 1994.

37. Hymer, T. C.; Downs, C.; and Moore, F. G., *A Interactive, User-Friendly, Personal Computer Version of the Aeroprediction Code*, NSWCDD/TR-94/107, Jun 1994.

38. Moore, F. G. and McInville, R. M., *A Method for Calculating Wing Alone Aerodynamics to Angle of Attack 180 Degrees*, NSWCDD/TR-94/3, Mar 1994.

39. Moore, F. G.; McInville, R. M.; and Hymer, T. C., *The 1995 Version of the NSWC Aeroprediction Code: Part I – Summary of New Theoretical Methodology*, NSWCDD/TR-94/379, Feb 1995.

40. Moore, F. G.; McInville, R. M.; and Hymer, T. C., *The 1995 Version of the NSWC Aeroprediction Code: Part II – Computer Program Users Guide and Listing*, NSWCDD/TR-94, Mar 1995.

41. Moore, F. G. and McInville, R. M., "Calculation of Wing-Alone Aerodynamics to High Angles of Attack," *Journal of Spacecraft and Rockets*, Vol. 32, No. 1, pp. 187-189, Jan-Feb 1995.

42. Moore, F. G. and McInville, R. M., A New Method for Calculating Wing Alone Aerodynamics to Angle of Attack 180 Degrees," AIAA paper 95-0757, presented at 33 Aerospace's Sciences Meeting, Reno, NV, 9-12 Jan 1995.

43. Moore, F. G.; McInville, R. M.; and Hymer, T. C., "Extension of the NSWCDD Aeroprediction Code Above Angle of Attack Thirty Degrees," Paper No. 96-0065, 34th Aerospace Sciences Meeting, Reno, NV, 15-18 Jan 1996.

44. Moore, F. G.; McInville, R. M.; and Hymer, T. C., "An Aeroprediction Code for Angles of Attack Above Thirty Degrees, *JSR*, Vol. 33, No. 3, May-Jun 1996.

REFERENCES (Continued)

45. Moore, F. G. and McInville, R. M., "A New Semiempirical Model for Wing-Tail Interference," AIAA paper 96-3393, AFM Conference, San Diego, CA, 29-31 Jul.

46. Moore, F. G. and McInville, R. M., *Extension of the NSWCDD Aeroprediction Code to the Roll Position of 45 Degrees*, NSWCDD/TR-95/160, Dec 1995.

47. Moore, F. G., Invited AIAA AFM Workshop on "Semiempirical Aeroprediction Methods," San Diego, CA, 30 Jul 1996.

48. McInville, R. M.; Moore, F. G.; and Housh, C., *Nonlinear Structural Load Distribution Methodology for the Aeroprediction Code*, NSWCDD/TR-96/133, Sep 1996.

49. Moore, F. G. and McInville, R. M., "Nonlinear Aeroprediction Methodology for Roll Positions of 0 and 45 Degrees," paper presented at Session 6B of AIAA Missile Sciences Conference, Monterey, CA 3-5 Dec 1996 (Papers archived at DTIC/OCP, 8725 John Ray Kingman Road, Suite 0944, Fort Belvoir, VA 22060-6218).

50. Moore, F. G. and McInville, R. M., "New Semiempirical Model for Wing Tail Interference, *JSR*, Vol. 34, No. 1, pp. 48-53, Jan-Feb 1977.

51. Moore, F. G. and McInville, R. M. "Nonlinear Aeroprediction Methodology for Roll Position of 45 Degrees," *JSR*, Vol. 34, No. 1, pp. 54-61, Jan-Feb 1997.

52. Moore, F. G. and Hymer, T. C., *An Improved Method for Predicting Axial Force at High Angle of Attack*, NSWCDD/TR-96/240, Feb 1997.

53. Moore, F. G., "Current Status and Future Plans of the Aeroprediction Code," invited AIAA Paper No. 97-2279, 1997 AIAA Applied Aerodynamics Conference, Atlanta, GA, 24 Jun 1997.

54. Moore, F. G.; McInville, R. M.; and Housh, C., "Methods for Distributing Semiempirical, Nonlinear, Aerodynamic Loads on Missile Components," AIAA Paper No. 97-1969, 28th AIAA Fluid Dynamics Conference, Snowmass Village, CO, 30 Jun-2 Jul 1997 (Also *JSR*, Vol. 34, No. 6, pp. 744-752, Nov-Dec 1997).

55. Moore, F. G.; McInville, R. M.; and Hymer, T. C., *An Improved Semiempirical Method for Calculating Aerodynamics of Missiles with Noncircular Bodies*, NSWCDD/TR-97/20, Sep 1997.

56. Moore, F. G. and Hymer, T. C., "Improved Methodology for Axial Force Prediction at Angle of Attack," AIAA paper 98-0579, Jan 1998 (Also *JSR*, Vol. 35, No. 2, pp. 132-139, Mar-Apr 1998).

REFERENCES (Continued)

57. Moore, F. G.; McInville, R. M.; and Hymer, T. C., "A Robust Method for Calculating Aerodynamics of Noncircular-Cross Section Weapons," AIAA Paper 98-4270, presented at AIAA AFM Conference, Boston, MA, pp. 323-340, Aug 1998.

58. Moore, F. G.; McInville, R. M.; and Hymer, T. C., "Review and Extension of Computational Methods for Noncircular-Cross Section Weapons, *JSR*, Vol. 35, No. 5, pp. 584-600, Sep-Oct 1998.

59. Moore, F. G.; McInville, R. M.; and Hymer, T. C., *The 1998 Version of the NSWC Aeroprediction Code: Part I – Summary of New Theoretical Methodology*, NSWCDD/TR-98/1, Apr 1998.

60. Moore, F. G.; McInville, R. M.; and Hymer, T. C., *The 1998 Version of the NSWCDD Aeroprediction Code: Part II – Program Users Guide and Source Code Listing*, NSWCDD/TR-98/73, Aug 1998.

61. Hymer, T. C.; Downs, C.; and Moore, F. G., *Users Guide for an Interactive Personal Computer Interface for the 1998 Aeroprediction Code (AP98)*, NSWCDD/TR-98/7, Jun 1998.

62. Moore, F. G.; McInville, R. M.; and Hymer, T. C., "a Review of Some Recent New and Improved Semi-empirical Aeroprediction Methods," paper presented to the Applied Vehicle Technology Panel of NATO in Sorrento, Italy, 11-15 May 1998.

63. Moore, F. G.; McInville, R. M.; and Hymer, T. C., "The 1998 Version of the Aeroprediction Code," AIAA Paper 99-0762, AIAA 37th Aerospace Science Meeting, Reno, NV, Jan 1999.

64. Moore, F. G.; McInville, R. M.; and Hymer, T. C., "Application of the 1998 Version of the Aeroprediction Code," *JSR*, Vol. 36, No. 5, pp. 633-645, Sep-Oct 1999.

65. Moore, F. G., "The NSWCDD Aeroprediction Code: Past, Present, and Future Plans," *NSWCDD Technical Digest*, 1998 Issue, Nov 1998.

66. Moore, F. G., "Approximate Methods for Weapon Aerodynamics," *AIAA Progress in Astronautics and Aeronautics*, Vol. 186, Aug 2000.

67. Moore, F. G.; McInville, R. M.; and Robinson, D. I., *A Simplified Method for Predicting Aerodynamics of Multi-Fin Weapons*, NSWCDD/TR-99/19, Mar 1999.

68. Moore, F. G.; McInville, R. M.; and Robinson, D. I., "A Semiempirical Method for Predicting Multi-fin Weapon Aerodynamics," AIAA 2000-0766, 38th Aerospace Science Meeting, Jan 2000.

REFERENCES (Continued)

69. NASA Langley Research Center Tri-Service Missile Data Base, transmitted from NASA/LRC Jerry M. Allen to NSWCDD, 5 Nov 1991 (formal documentation of data base in process).

70. Allen, J. M.; Hemsch, M. J.; Burns, K. A.; and Peters, K. J., *Parametric Fin-Body and Fin-Alone Data Base on a Series of 12 Missile Fins*, NASA/LRC TM in publication, (data base transmitted from Jerry Allen to NSWCDD in May 1996).

71. Moore, F. G. and McInville, R. M., *Refinements in the Aeroprediction Code Based on Recent Wind Tunnel Data*, NSWCDD/TR-99/116, Dec 1999.

72. Moore, F. G.; McInville, R. M.; and Hymer, T. C., "Modifications to the Aeroprediction Code Based on Recent Test Data," AIAA Paper 2000-4195, Atmospheric Flight Mechanics Conference, Denver, CO, Aug 2000.

73. Moore, F. G.; McInville, R. M.; and Hymer, T. C., "Evaluation and Improvements to the Aeroprediction Code Based on Recent Test Data," *JSR*, Vol. 37, No. 6. pp. 720-730, Nov-Dec 2000.

74. Moore, F. G. and Hymer, T. C., *Improvement in Pitch Damping for the Aeroprediction Code with Particular Emphasis on Flare Configurations*, NSWCDD/TR-00/009, Apr 2000.

75. Moore, F. G. and Hymer, T. C., "Semiempirical Prediction of Pitch Damping Moments for Configurations with Flares," AIAA Paper 2001-0101, Reno, NV, Jan 2001 (also JAS, Vol. 38, No. 2, pp. 150-158, Mar-Apr 2001).

76. Moore, F. G. and Hymer, T. C., *Improved Power-on, Base Drag Methodology for the Aeroprediction Code*, NSWCDD/TR-00/67, May 2001.

77. Moore, F. G. and Hymer, T. C., "An Improved Semiempirical Method for Power-on Base Drag Prediction," AIAA Paper 2001-4328, Aug 2001 (also JSR article to be published).

78. Hathaway, W. H.; Kruggel, B.; Abate, G.; Winchenbach, G.; and Krieger, J., *Aeroballistic Range Tests of Missile Configurations with Non-circular Cross Sections*, AFRL-MN-EG-TR-2001-7082, Sep 2001 (Air Force Research Laboratory Munitions Directorate, Eglin Air Force Base, FL 32542).

79. Moore, F. G. and Hymer, T. C., *A Semiempirical Method for Predicting Aerodynamics of Trailing Edge Flaps*, NSWCDD/TR-01/30, Oct 2001.

80. Nielsen, J. N., *Missile Aerodynamics*, NEAR, Inc. Mountain View, CA, 1988.

REFERENCES (Continued)

81. Bryson, A. E., "Stability Derivatives for a Slender Missile with Application to a Wing-Body-Tail Configuration," *Journal of Aeronautical Sciences*, Vol. 20, No. 5, 1953.

82. Wardlaw, A. B. and Davis, S., *A Second-Order-Gudonov Method for Supersonic Tactical Missiles*, NSWC TR 86-506, 1986.

83. Walters, R. W.; Slack, D. C.; Cimmella, P.; Applebaum, M. P.; and Frost, C., "A Users Guide to GASP," Virginia Polytechnic Institute and State University, Department of Aerospace and Ocean Engineering, Blacksburg, VA, Nov 1990.

84. Stallings, R. L., Jr. and Lamb, M. L., *Wing-Alone Aerodynamic Characteristics for High Angles of Attack at Supersonic Speeds*, NASA TP 1989, Jul 1981.

85. Baker, W. B., Jr., *Static Aerodynamic Characteristics of a Series of Generalized Slender Bodies With and Without Fins at Mach Numbers from 0.6 to 3.0 and Angles of Attack from 0 to 180°*, Arnold Engineering Development Center, TR-75-124, Vols. 1 and 2, Tullahoma, TN, May 1976.

86. Lesieutre, D. J.; Love, J. F.; and Dillenius, M. F., *M3HAX Aerodynamic Analysis for Finned Vehicles with Axisymmetric Bodies*, NEAR TR 493-D, Feb 1996 (NEAR, Inc., 526 Clyde Ave., Mountain View, CA 94043-2212).

87. Vukelich, S. R. and Jenkins, J. E., "Missile DATCOM: Aerodynamic Prediction on Conventional Missiles Using Component Build-up Techniques," AIAA Paper 84-0388, Reno, NV, 1984.

88. Washington, W. D. and Spring, D. J., "An Experimental Investigation of Wing-Tail Interference for a Typical Supersonic Missile," AIAA Paper 82-1339, AIAA 9th Atmospheric Flight Mechanics Conference, San Diego, CA, 9-11 Aug 1982.

89. Aiello, G. F. and Bateman, M. C., *Aerodynamic Stability Technology for Maneuverable Missiles, Vol. I – Configuration Aerodynamic Characteristics*, AFFDL-TR-76-55, Vol. 1 (Contractor: Martin Marietta Corporation, Orlando, FL), Mar 1979.

90. Sturek, W. B., Nietubicz, C. J., Sahu, J.; and Weinacht, P., *Recent Applications of CFD to the Aerodynamics of Army Projectiles*, ARL-TR-22, U.S. Army Research Laboratory, Aberdeen Proving Ground, MD, Dec 1992.

91. Weinacht, P., *Navier-Stokes Predictions of Pitch-Damping for a Family of Flared Projectiles*, ARL-TR-591, U.S. Army Research Laboratory, Aberdeen Proving Ground, MD, Oct 1994.

REFERENCES (Continued)

92. Qin, N., Ludlow, D. K., Shaw, S. T., Edwards, J. A., and Dupuis, A., "Calculation of Pitch Damping Coefficients for Projectiles," AIAA Paper No. 97-0405, 35th Aerospace Sciences Meeting, Jan 1997.

93. Weinacht, P., Sturek, W. B., and Schiff, L. B., *Navier-Stokes Predictions of Pitch-Damping for Axisymmetric Shell Using Steady Coning Motion*, ARL-TR-575, U.S. Army Research Laboratory, Aberdeen Proving Ground, MD, Sep 1994.

94. Weinacht, P., "Prediction of Pitch-Damping of Projectiles at Low Supersonic and Transonic Velocities," AIAA Paper No. 98-0395, 36th Aerospace Sciences Meeting, Reno, NV, Jan 1998.

95. Wu, J. M. and Aoyoma, K., *Transonic Flow-Field Calculation Around Ogive Cylinders by Nonlinear – Linear Stretching Method*, U.S. Army Missile Command Technical Report No. RD-TR-70-12, April 1970. Also AIAA 8th Aerospace Sciences Meeting, AIAA Paper 70-189, Jan 1970.

96. Ames Research Staff, *Equations, Tables, and Charts for Compressible Flow*, NACA Report 1135, 1953.

97. Whyte, R. H., *Spinner – A Computer Program for Predicting the Aerodynamic Coefficients of Spin Stabilized Projectiles*, General Electric Class 2 Reports, 1969.

98. Chin, S. S., *Missile Configuration Design*, McGraw Hill Book Company, Inc., New York, NY, 1961, pp. 134-138

99. Brazzel, Charles E. and Henderson, J. H., "An Empirical Technique for Estimating Power-On Base Drag of Bodies-of-Revolution With a Single Jet Exhaust," Proceedings of a Specialists' Meeting Sponsored by the AGARD Fluid Dynamics Panel, held in Melhouse, France, 5-8 Sep 1966.

100. Danberg, J. E., *Analysis of the Flight Performance of the 155 mm M864 Base Burn Projectile*, BRL-TR-3083, Apr 1990.

101. Craft, J. C. and Brazzel, C. E., *An Experimental Investigation of Base Pressures on a Body of Revolution at High Thrust Levels and Freestream Mach Numbers of 1.5 to 2.87*, U.S. Army Missile Command, Redstone Arsenal, AL, Report No. RD-TM-70-6, Jul 1970.

102. Henderson, J. H., *An Investigation for Modeling Jet Plume Effects on Missile Aerodynamics*, TR RD-CR-82-25, U.S. Army Missile Command, Redstone Arsenal, AL 35809, Jul 1982.

REFERENCES (Continued)

103. Deep, R. A.; Henderson, J. H.; and Brazzel, C. E.; *Thrust Effects on Missile Aerodynamics*, RD-TR-71-9, U.S. Army Missile Command, Huntsville, AL 35809, May 1971.

104. Reid, J. and Hastings, R. C.; *The Effect of a Central Jet on the Base Pressure of a Cylindrical Afterbody in a Supersonic Stream*, Royal Aircraft Establishment Report No. Aero 2621, Dec. 1959 (Farnborough, England).

105. Bowman, J. E. and Clayden, W. A., "Cylindrical Afterbodies in Supersonic Flow with Gas Injection," AIAA Journal, Vol. 5, No. 8, pp.1524-1525, Aug 1967.

106. Mathur, T. and Dutton, J. C., "Base Bleed Experiments with a Cylindrical Afterbody in Supersonic Flow," AIAA 95-0062, 33RD Aerospace Science Meeting, Reno, NV, 9-12 Jan 1995.

107. Kayser, L. D., "Effects of Base Bleed and Supersonic Nozzle Injection on Base Pressure," Memorandum Report No. 2456, USA Ballistic Research Laboratories, Aberdeen Proving Ground, MD, Mar 1975. (AD B 003442L)

108. Jorgensen, L. H., "Inclined Bodies of Various Cross Sections at Supersonic Speeds," NASA Memo 10-3-58A, 1958.

109. Moore, F. G. and Hymer, T. C., *A Semiempirical Method for Predicting Aerodynamics of Trailing Edge Flaps*, NSWCDD/TR-01/30, Oct 2001.

110. Goin, K. L., *Equations and Charts for the Rapid Estimation of Hinge-Moment and Effectiveness Parameters for Trailing-Edge Controls Having Leading and Trailing Edges Swept Ahead of the Mach Lines*, NACA TR 1041, 1951.

111. Triscott, C. D., Jr., *Longitudinal Aerodynamic Characteristics at Mach 1.50 to 4.63 of a Missile Model Employing Various Canards and a Trailing-Edge Flap Control*, NASA TM X-2367, Oct 1971.

112. Hughes, S. V. and Jones, H. J., *A Point Mass Trajectory Model (TRAMOD) with Exterior Ballistic Analysis Enhancements*, NSWCDD/MP-98/41, Apr 1998.

113. Phillips, C., *Standard Missile – 2 (SM-2) Block IV Midcourse Engineering Model Formulation*, NSWC/TR-89/39, Feb 1989.

114. Hymer, T. C. and Moore, F. G., *Integration of the Aeroprediction Code with a Point Mass Ballistic Model (TRAMOD) with a Trim Three-Degree-of-Freedom Model (MEM)*, NSWCDD/TR-00/77, Aug 2000.

REFERENCES (Continued)

115. Monta, W. J., *Supersonic Aerodynamic Characteristics of a Sparrow III Type Missile Model With Wing Controls and Comparison With Existing Tail-Control Results*, NASA TP 1078, Nov 1977.

116. Graves, E. B. and Fournier, R. H., *Stability and Control Characteristics at Mach Numbers From 0.20 to 4.63 of a Cruciform Air-to-Air Missile With Triangular Canard Controls and a Trapezoidal Wing*, NASA TMX-3070, May 1974.

117. Jorgensen, L. H., *Predictions of Static Aerodynamic Characteristics for Slender Bodies Alone and With Lifting Surfaces to Very High Angles of Attack*, NASA TR R-474, Sep 1977.

118. Blair, A. B., Jr.; Allen, J. M.; and Hernandez, G., *Effect of Tail-Fin Span on Stability and Control Characteristics of a Canard Controlled Missile at Supersonic Mach Numbers*, NASA TP 2157, Jun 1983.

119. Gudmundson, S. E. and Torngren, L., *Supersonic and Transonic Wind Tunnel Tests on Slender Ogive-Cylinder Body Single and in Combination With Cruciform Wings and Tails of Different Sizes*, Technical Note FFA AU-772, Apr 1972 (The Aeronautical Research Institute of Sweden, Aeronautics Department, Stockholm, Sweden).

120. Howard, R. M. and Dunn, A., "Missile Loads at High Angles of Attack," Engineering Note in Journal of Spacecraft and Rockets, Vol. 28, No. 1, Jan-Feb 1991.

121. Guidos, B. J., *Static Aerodynamics CFD Analysis for 120 MM Hypersonic KE Projectile Design*, ARL-MR-84, U.S. Army Research Laboratory, Aberdeen Proving Ground, MD, Sep 1984.

122. DTRA/SAIC Projectile Development and Test Wind Tunnel Data, Defense Threat Reduction Agency, Alexandria, VA. Received through Darryl W. Hall, Science Applications International Corporation. (Unpublished)

123. Ding, Z.; Liu, Y.; and Chen, S., "A Study of Drag Reduction by Base Bleed at Subsonic Speeds," First International Symposium on Special Topics in Chemical Propulsion: Base Bleed, Athens, Greece, 23-25 Nov 1988.

124. Bowman, J. E. and Clayden, W. A., "Cylindrical Afterbodies at $M_\infty = 2$ with Hot Gas Ejection," AIAA Journal, Vol. 6, No. 12, pp. 2429-2431, Dec 1968.

125. Sahu, J., *Supersonic Flow Over Cylindrical Afterbodies with Base Bleed*, BRL Technical Report TR-2742, Aberdeen, MD, Jun 1986.

REFERENCES (Continued)

126. Schilling, H., "Experimental Investigation on the Base-Bleed-Effect for Body-Tail-Combinations," Proceedings of the 8th International Symposium on Ballistics, Amsterdam, Holland, 1984.

127. Martin, T. A. and Brazzel, C. E., *Investigation of the Effect of Low Thrust Levels on the Base Pressure of a Cylindrical Body at Supersonic Speeds*, USAMC, Redstone Arsenal, USA, RD-TR-70-11, May 1970.

128. Rubin, D. V.; *A Transonic Investigation of Jet Plume Effects on Base and Afterbody Pressures of Boattail and Flare Bodies of Revolution*, U.S. Army Missile Command Report RD-TR-70-10, Redstone Arsenal, AL, Oct 1970.

129. Baldwin, A. W. and Adamczak, D. W., *Experimental Evaluation of Aerodynamic Control Devices for Control of Tailless Fighter Aircraft*, WL-TM-92-318, Flight Dynamics Directorate, Wright Laboratory, Wright Patterson AFB, OH 45433-6553, Apr 1992.

7.0 SYMBOLS AND DEFINITIONS

AOA	Angle of Attack
APC	Aeroprediction Code
AP72, AP74, AP77, AP81, AP93, AP95, AP98, AP02	Various versions of the APC and the year produced
AR	Aspect Ratio = b^2/A_W
CFD	Computational Fluid Dynamics
DOF	Degrees of freedom
LT	Linear Theory
NASA/LRC	National Aeronautics and Space Administration/Langley Research Center
NSWCDD	Naval Surface Warfare Center, Dahlgren Division
SB, SBT	Slender Body, Slender-body Theory
SOSE, SOVD	Second-Order-Shock-Expansion and Second-Order-Van Dyke
A_{eq}	Cross-sectional area of circular cylinder equal to that of body with noncircular cross section
A_P	Planform area of the body in the crossflow plane (ft^2)
A_{REF}	Reference area (maximum cross-sectional area of body, if a body is present, or planform area of wing, if wing along)(ft^2)
A_t	Area of rocket motor nozzle throat cross-section
A_W	Planform area of wing in crossflow plane (ft^2)
a,b	Semimajor and semiminor axis, respectively, of ellipse

B	Conditions at body base
b	Wing span (not including body)(ft)
C	Conditions in rocket motor chamber
C_A	Axial force coefficient
$C_{A_B}, C_{A_F}, C_{A_W}$	Base, skin-friction, and wave components, respectively, of axial force coefficient
C_{A_O}	Axial force coefficient at 0 deg AOA
$C_{A_{SF}}$	Axial force coefficient of a single fin
$(\Delta C_A)_f, (\Delta C_N)_f, (\Delta C_M)_f$	Change in axial, normal and pitching moment coefficients, respectively, due to a flap deflection δ_f
C_{d_c}	Crossflow drag coefficient
C_D	Drag coefficient
Cir	Circumference of body (ft)
C_L	Lift coefficient
C_ℓ	Roll moment coefficient
C_{ℓ_P}	Roll damping moment coefficient
C_M	Pitching moment coefficient (based on reference area and body diameter, if body present, or mean aerodynamic chord, if wing alone)
C_{M_f}	Pitching moment coefficient of flare
C_{M_L}	Linear component of pitching moment coefficient
$C_{M_{NL}}$	Nonlinear component of pitching moment coefficient
$C_{M_q} + C_{M_{\dot\alpha}}$	Pitch damping moment coefficient $[C_M(q)/(qd/2V_\infty) + C_M(\dot\alpha)/(\dot\alpha d/2V_\infty)]$

C_N	Normal force coefficient
C_{N_B}	Normal force coefficient of body alone
$C_{N_{B(V)}}$	Negative afterbody normal-force coefficient due to canard or wing-shed vortices
$C_{N_{B(W)}}, C_{N_{B(T)}}$	Normal-force coefficient on body in presence of wing or tail
C_{N_f}	Normal force coefficient of flare
C_{N_L}	Linear component of normal-force coefficient
$C_{N_{NL}}$	Nonlinear component of normal-force coefficient
$(C_{N_\alpha})_W, (C_{N_\alpha})_T, (C_{N_\alpha})_f, (C_{N_\alpha})_C$	Normal force coefficient slope of wing, tail, flare, or cone, respectively
$C_{N_{T(V)}}$	Negative normal-force coefficient component on tail due to wing or canard-shed vortex
C_{N_W}	Normal force coefficient of wing alone
$C_{N_{W(B)}}, C_{N_{F(B)}}$	Normal-force coefficient of wing or fin in presence of body
C_{N_α}	Normal-force coefficient derivative
C_P	Pressure coefficient $\left(\frac{p - p_\infty}{1/2\rho_\infty V_\infty^2}\right)$
C_{P_B}	Base pressure coefficient
c, sq, tr	Circle, square, triangle
c_r	Rood chord (ft)
c_{r_w}, c_{r_f}	Root chord of wing and flap, respectively (ft)
C_T	Thrust coefficient
c_t	Tip chord (ft)

D	Drag (lb)
d_{ref}	Reference body diameter (ft)
$\frac{dK_{W(B)}}{d\alpha}, \frac{dK_{B(W)}}{d\alpha}$	Rate at which $K_{W(B)}$ or $K_{B(W)}$ decreases
deg	Degree(s)
F_6, F_8	Empirical factors used to represent aerodynamics of 6 and 8 fins based on 4 fin aerodynamics
g	Acceleration due to gravity (32.2 f/sec^2)
I	Nondimensional base bleed injection parameter
i	Tail interference factor
j	Conditions at nozzle exit
k, k_1	Parameters used to define corner radius for squares and triangles ($k = r_n/W_M$; $k_1 = r_n/W$)
$K_{B(W)}$, $K_{B(T)}$	Ratio of additional body normal-force coefficient in presence of wing, or tail to wing, or tail alone normal-force coefficient at $\delta = 0$ deg
$k_{B(W)}$, $k_{B(T)}$	Ratio of additional body normal-force coefficient due to presence of wing or tail at a control deflection to that of wing or tail alone at $\alpha = 0$ deg
$[K_{B(W)}]_{MIN}$	Minimum value of $K_{B(W)}$ as percent of slender-body theory value
$K_{W(B)}$, $K_{T(B)}$	Ratio of normal-force coefficient of wing or tail in presence of body to that of wing or tail alone at $\delta = 0$ deg
$k_{W(B)}$, $k_{T(B)}$	Ratio of wing or tail normal-force coefficient in presence of body due to a control deflection to that of wing or tail alone at $\alpha = 0$ deg
ΔK	Nonlinear component of wing-body or body-wing interference
$[\Delta K_{W(B)}]_{\alpha=0}$ and $[\Delta K_{B(W)}]_{\alpha=0}$	Amount that the experimental values of $K_{W(B)}$ and $K_{B(W)}$ exceed slender body theory at $\alpha = 0$ deg
ℓ, ℓ_n, ℓ_a, ℓ_B, ℓ_f	Total, nose, afterbody, and boattail or flare length, respectively (ft)
ℓ_{ref}	Reference length (ft)

m	Cotangent of leading edge sweep angle; also mass when used in equations of motion
$\dot{m}$	Mass rate of flow (ρAV)
M_N	Mach number normal to body = $M_\infty \sin \alpha$
M_∞	Freestream Mach number
NC	Noncircular
N_f	Normal force of trailing edge flap (lb)
p	Pressure (lb/ft^2)
Q	Dynamic pressure (lb/ft^2)
r	Local body radius (ft)
r_{eq}, d_{eq}	Radius and diameter, respectively, of a circular cross-section body which has same cross-sectional area as that of noncircular cross-section body
RMF	Jet momentum flux ratio
r_n	Corner radius of a rounded corner on square or triangle
R_{N_T}	Reynolds number where flow transitions from laminar to turbulent conditions
r_W, r_T, r_C	Radius of body at wing, tail, or canard locations
s	Wing or tail semispan plus the body radius in wing-body lift methodology
T	Temperature (°R) or thrust (lbs)
V	Velocity (ft/sec)
V_∞	Freestream velocity (ft/sec)
V_N	Velocity normal to body
V_t	Velocity at time t (ft/sec)
W	Length of one side of a triangle or square
W_x, W_y, W_z	Wind velocity in x, y, and z directions (ft/sec)

W_m	Maximum diameter of a triangle or square as measured normal to the velocity vector
X_{CG}, X_C, X_T	Distance to center of gravity, canard, or tail leading edge, respectively (ft)
X_{CP}	Center of pressure (in feet or calibers from some reference point that can be specified) in x direction
$(X_{CP})_L$, $(X_{CP})_{NL}$	Center of pressure of linear and nonlinear terms of normal force
X_{LE}	Distance from nose tip to leading edge of canard or wing
$\dot{x}$, $\dot{y}$, $\dot{z}$	Velocity in x, y, and z directions (ft/sec)
$\ddot{x}$, $\ddot{y}$, $\ddot{z}$	Acceleration in x, y, and z directions (ft/sec)
x_T	Range at termination of flight
x_t	Range at time t
x_o	Reference location
α	Angle of attack (deg)
α_C	Angle of attack where wing-body interference factor starts decreasing (deg)
α_D	Angle of attack where the wing-body interference factor reaches a minimum (deg)
α_M	Angle of attack where $K_{W(B)}$ reaches a constant value
α_{TR}	Trim angle of attack (deg)
α_W, α_T	Local angle of attack of wing or tail ($\alpha_W + \delta$ or $\alpha_T + \delta$, respectively, in degrees)
α_1, α_2	Angles of attack used in nonlinear model for $K_{B(W)}$
γ	Ratio of specific heats
δ	Control deflection (deg), positive leading edge up
δ_f	Control deflection (deg) of trailing edge flap, positive trailing edge down
δ_W, δ_T	Deflection of wing or tail surfaces (deg), positive leading edge up

η	Parameter used in viscous crossflow theory for nonlinear body normal force (in this context, it is the normal force of a circular cylinder of given length-to-diameter ratio to that of a cylinder of infinite length)
η_0	Value of η at $M_N = 0$
ρ	Density (slugs/ft^3)
Φ	Roll position of missile fins (Φ = 0 deg corresponds to fins in the plus (+) orientation. Φ = 45 deg corresponds to fins rolled to the cross (×) orientation).
Λ	Earths rotational speed (rad/sec)
Λ_{LE}	Leading edge sweepback angle of fin (deg)
λ	Taper ratio of a lifting surface = c_t/c_r
ϕ	Roll position of point on body with ϕ = 0 deg being the leeward plane
θ	Local surface slope of body with respect to body axis
θ_f	Flare angle (deg)
θ_L	Latitude at firing point (deg)
θ_e	Line of fire (deg)
∞	Freestream conditions

Superscript

*	Indicates conditions where M = 1.0

DISTRIBUTION

DOD ACTIVITIES (CONUS)

		Copies
ATTN	CODE 35 (ZIMET)	1
	CODE 351 (GRAFF)	1
	CODE 351 (MORRISON)	1
	CODE 332FD (LEKOUDIS)	1

CHIEF OF NAVAL RESEARCH
BALLSTON CENTRE TOWER ONE
800 NORTH QUINCY ST
ARLINGTON VA 22217-5660

ATTN	CODE 474T60D (LOFTUS)	1
	CODE 4732H0D (SMITH)	1
	CODE 47H000D (BOSS)	1
	CODE 473C00D (MCMANIGAL)	1
	CODE 473110D (HOUSH)	1
	CODE 473110D (GLEASON)	1
	CODE 4722E0D (JETER)	1
	TECHNICAL LIBRARY	1

COMMANDER
NAVAL AIR WARFARE CENTER
WEAPONS DIVISION
1 ADMINISTRATION CIRCLE
CHINA LAKE CA 93555-6001

ATTN	TECHNICAL LIBRARY	1
	G RUDACILLE PMS 38012 7	1

COMMANDER
NAVAL SEA SYSTEMS COMMAND
2531 JEFFERSON DAVIS HWY
ARLINGTON VA 22242-5160

ATTN	TECHNICAL LIBRARY	1

COMMANDER
NAVAL AIR SYSTEMS COMMAND
47122 LILJENCRANTZ ROAD UNIT 7
PATUXENT RIVER MD 20670-5440

ATTN	T C TAI	1
	M J MALIA	1
	TECHNICAL LIBRARY	1

COMMANDER
NSWC
CARDEROCK DIVISION
WASHINGTON DC 20034

ATTN	R M HOWARD	1
	TECHNICAL LIBRARY	1

SUPERINTENDENT
NAVAL POSTGRADUATE SCHOOL
1 UNIVERSITY CIRCLE
MONTEREY CA 93943-5001

ATTN	HEAD WEAPONS DEPT	1
	HEAD SCIENCE DEPT	1

SUPERINTENDENT
UNITED STATES NAVAL ACADEMY
121 BLAKE RD
ANNAPOLIS MD 21402-5000

ATTN	DIAG DT 4T (PAUL MURAD)	1

DIRECTOR
DEFENSE INTELLIGENCE AGENCY
WASHINGTON DC 20301

ATTN	BRENT WAGGONER	1

CODE 4072 BLDG 2540
NAVAL WEAPONS SUPPORT CENTER
CRANE IN 47522-5000

ATTN	W T RITTER	1

DEPT OF AIR FORCE
846TH TEST SQUADRON TGTM
1521 TEST TRACK RD
HOFFMAN AFB NM 88330-7847

DISTRIBUTION (Continued)

	Copies
ATTN CODE 5252P (KRAUSE)	1
TECHNICAL LIBRARY	1
COMMANDER	
INDIAN HEAD DIVISION	
NAVAL SURFACE WARFARE CENTER	
101 STRAUSS AVE	
INDIAN HEAD MD 20640-5035	
ATTN TECHNICAL LIBRARY	1
COMMANDING GENERAL	
MARINE CORPS COMBAT	
DEVELOPMENT COMMAND	
2048 SOUTH ST	
QUANTICO VA 22134-5129	
ATTN E SEARS	1
L E LIJEWSKI	1
C COTTRELL	1
TECHNICAL LIBRARY	1
AFATL (ADLRA) (DLGC)	1
EGLIN AFB FL 32542-5000	
ATTN TECHNICAL LIBRARY	1
USAF ACADEMY	
COLORADO SPRINGS CO 80912	
ATTN B BLAKE (BLD 146)	1
J JENKINS (BLD 146)	1
TECHNICAL LIBRARY	1
COMMANDING OFFICER	
AFSC	
2210 8TH STREET	
WRIGHT PATTERSON AFB OH 45433	
ATTN JIM SIMON	1
NAIC TANW	
HQ NAIC TANW	
4180 WATSON WAY	
WPAFB OH 45433-5623	
ATTN J USSELTON	1
W B BAKER JR	1
TECHNICAL LIBRARY	1
ARNOLD ENGINEERING DEVELOPMENT CENTER USAF	
TULLAHOMA TN 37389	

	Copies
ATTN H HUDGINS	1
G FRIEDMAN	1
AMSTA-AR-WEL-TL	1
COMMANDER	
US ARMY TACOM-ARDEC	
BUILDING 59 PHIPPS ROAD	
PICATINNY ARSENAL NJ 07806-5000	
ATTN R PUHALLA JR	1
W STUREK	1
C NIETUBICZ	1
A MIKHAIL	1
P PLOSTINS	1
TECHNICAL LIBRARY	1
COMMANDING GENERAL	
BALLISTIC RESEARCH LABORATORY	
ABERDEEN PROVING GROUND	
ABERDEEN MD 21005-5066	
ATTN DIRECTOR	1
INTERCEPTOR TECHNOLOGY	
BALLISTIC MISSILE DEFENSE OFFICE	
THE PENTAGON	
WASHINGTON DC 20350	
ATTN SFAE SD ASP	1
SFAE SD HED	1
DEPUTY COMMANDER	
US ARMY STRATEGIC DEFENSE COMMAND	
P O BOX 1500	
HUNTSVILLE AL 35807-3801	
ATTN D WASHINGTON	1
W WALKER	1
R KRETZSCHMAR	1
D FERGUSON JR	1
COMMAND GENERAL	
US ARMY AVIATION AND MISSILE COMMAND	
AMSAM RD SS AT	
REDSTONE ARSENAL AL 35898-5252	
DEFENSE TECHNICAL INFORMATION CENTER	
8725 JOHN J KINGMAN ROAD	
SUITE 0944	
FORT BELVOIR VA 22060-6218	2

DISTRIBUTION (Continued)

	Copies
DIRECTOR DEFENSE PRINTING SERVICE BLDG 176 WASHINGTON NAVY YARD 901 M ST E WASHINGTON DC 20374-5087	1
ATTN CODE A76 TECHNICAL LIBRARY COMMANDING OFFICER CSSDD NSWC 6703 W HIGHWAY 98 PANAMA CITY FL 32407-7001	1
ATTN DR P WEINACHT AERODYNAMICS BRANCH PROPULSION AND FLIGHT DIV WTD AMSRL WT PB US ARMY RESEARCH LAB ABERDEEN PROVING GROUND MD 21005-5066	1
ATTN GREGG ABATE US AIR FORCE WRIGHT LABORATORY WL MNAA 101 W EGLIN BLVD STE 219 EGLIN AFB FL 32542-5000	1
ATTN JOHN GRAU US ARMY ARDEC COMMANDER US ARMY ARDEC AMSTA AR FSF T BLDG 382 PICATINNY ARSENAL NJ 07806-5000	1
ATTN FRANK MACDONALD NAWC CHINA LAKE COMMANDER CODE 473120D NAVAIRWARCENNSDNDIV CHINA LAKE CA 93555	1
ATTN MARK LAMBERT NAWC CODE 4732HOD CHINA LAKE CA 93555	1
ATTN MICHAEL MUSACHIO DIRECTOR OFFICE OF NAVAL INTELLIGENCE 4251 SUITLAND ROAD (ONI 2321) WASHINGTON DC 20395	1
ATTN DR ALAN NICHOLSON MSC 5B DEFENSE INTELLIGENCE AGENCY MISSILE AND SPACE INTELLIGENCE CTR REDSTONE ARSENAL AL 35898-5500	1
ATTN EDWARD HERBERT US ARMY MISSILE COMMAND AMSMI RD MG GA BLDG 5400 ROOM 250 REDSTONE ARSENAL AL 35898	1
ATTN PAUL KOLODZIEJ NASA AMES RESEARCH CENTER MS 234 1 MOFFETT FIELD CA 94035	1
ATTN LCDR T HARTLINE USNR R NR ONI 2109 NAVAL RESERVE UNIT 112 CRESTVIEW CIRCLE MADISON AL 35758	1
ATTN CODE 4732HOD DAVID HALL PROPULSION PERFORMANCE OFFICE NAVAL AIR WARFARE CTR WEAPONS DIV 1 ADMINISTRATIVE CIR CHINA LAKE CA 93555-6001	1
ATTN DONALD SHEREDA WL FIMA BLDG 450 2645 FIFTH ST STE 30 WRIGHT PATTERSON AFB OH 45433-7936	1
BMDO AQS 1725 JEFFERSON DAVIS HWY STE 809 ARLINGTON VA 22202	1
ATTN JEFFREY RANDORF US ARMY SPACE AND STRATEGIC DEFENSE COMMAND P O BOX 1500 CSSD-BC-SS 106 WYNN DRIVE HUNTSVILLE AL 35807-3801	1
ATTN EDWARD ELLISON WHITE SANDS MISSILE RANGE NRO DA F WHITE SANDS MISSILE RANGE NM 88002	1

DISTRIBUTION (Continued)

	Copies
ATTN MATT THOMAS	1
LAMAR M AUMAN	1
US ARMY AVIATION AND MISSILE COMMAND	
AMSAM RD SS AT	
REDSTONE ARSENAL AL 35898-5252	
ATTN JEFF OBERMARK	1
US ARMY AVIATION AND MISSILE COMMAND	
ASAM AR E S W	
BLDG 5681 ROOM 223	
REDSTONE ARSENAL AL 35898-5000	
ATTN BILL SCHOENFELD	1
USAF AFMC 46TG 846TS TGTM	
846TH TEST SQUADRON TGTM	
1521 TEST TRACK RD	
HOLLOMAN AFB NM 88330-7847	
ATTN RAYMOND TROHANOWSKY	1
TACOM ARDEC DEPT OF ARMY	
BUILDING 382 SOUTH	
PICATINNY ARSENAL NJ 07806-5000	
ATTN MICHAEL ADAMS	1
CIA	
5N01 NHB	
WASHINGTON DC 20505	
ATTN HUGO GONZALEZ	1
NAV AIR (AIR 4 3 2 2)	
AERODYNAMICS PERFORMANCE	
NAVAIRSYSCOM	
48110 SHAW RD UNIT 5	
PATUXENT RIVER MD 20670-1906	
ATTN LT KATHERINE D GARON	1
AFRL MNAV EGLIN AFB	
101 W EGLIN SUITE 332	
FORT WALTON BEACH FL 32542-6810	
ATTN DAVID TASSIA CODE 4410	1
NSWCIHD BLDG 301	
101 STRAUSS AVE	
INDIAN HEAD MD 20640-5035	

	Copies
ATTN KENNARD WATSON	1
NSWC COASTAL SYSTEMS STATION	
CODE R11	
6703 W HWY 98	
PANAMA CITY FL 32407-7001	
ATTN FRANK J REGAN	1
NSWCDD	
NAVAL SECURITY STATION	
3801 NEBRASKA AVE	
WASHINGTON DC	

NON-DOD ACTIVITIES (CONUS)

NICHOLS RESEARCH CORPORATION	
MS 912	
P O BOX 400002	
4040 S MEMORIAL PKWY	
HUNTSVILLE AL 35815-1502	1
THE CNA CORPORATION	
P O BOX 16268	
ALEXANDRIA VA 22302-0268	1
GIDEP OPERATIONS OFFICE	
CORONA CA 91720	1
ATTN TECHNICAL LIBRARY	1
NASA AMES RESEARCH CENTER	
MOFFETT CA 94035-1099	
ATTN C SCOTT	1
D CURRY	1
NASA JOHNSON SPACE CENTER	
HOUSTON TX 77058	
ATTN TECHNICAL LIBRARY	1
NASA	
WASHINGTON DC 20546	
ATTN B HENDERSON	1
D MILLER	1
J ALLEN	1
F WILCOX	1
TECHNICAL LIBRARY	2
NASA LANGLEY RESEARCH CENTER	
HAMPTON VA 23365	

DISTRIBUTION (Continued)

	Copies
ATTN TECHNICAL LIBRARY LAWRENCE LIVERMORE NATIONAL LABORATORY EARTH SCIENCES DIVISION UNIVERSITY OF CALIFORNIA P O BOX 808 LIVERMORE CA 94551	1
ATTN DR F MOORE AEROPREDICTION INC 12341 MILLBANK RD KING GEORGE VA 22485	3
ATTN W RUTLEDGE (1635) R LAFARGE R EISLER TECHNICAL LIBRARY SANDIA NATIONAL LABORATORY P O BOX 5800 ALBUQUERQUE NM 87185-5800	1 1 1 1
ATTN WALT GUTIERREZ SANDIA NATIONAL LABORATORIES MAIL STOP 0825 P O BOX 5800 ALBUQUERQUE NM 87185-0825	1
ATTN ASSISTANT DEFENSE COOPERATION ATTACHE EMBASSY OF SPAIN WASHINGTON DC 20016	1
DE/AVT DEFENSE EQUIPMENT STAFF BRITISH EMBASSY 3100 MASSACHUSETTS AVE NW WASHINGTON DC 20008-3688	1
ATTN ASO LO IS ISRAEL AIR FORCE LIAISON OFFICER 700 ROBBINS AVE PHILADELPHIA PA 19111	1
ATTN GERMAN MILITARY REP US OA GMR TRAFFIC AND TRANSPORTATION DIVISION 10 SERVICES ROAD DULLES INTERNATIONAL AP WASHINGTON DC 20041	1
ATTN PROF F R DEJARNETTE NORTH CAROLINA STATE UNIVERSITY DEPT OF MECHANICAL AND AEROSPACE ENGINEERING BOX 7921 RALEIGH NC 27695	1
ATTN PROF J A SCHETZ VIRGINIA POLYTECHNIC AND STATE UNIVERSITY DEPT OF AEROSPACE ENGINEERING BLACKSBURG VA 24060	1
ATTN J M WU C BALASUBRAMAYAN TECHNICAL LIBRARY THE UNIVERSITY OF TENNESSEE SPACE INSTITUTE TULLAHOMA TN 37388	1 1 1
ATTN R NELSON TECHNICAL LIBRARY UNIVERSITY OF NOTRE DAME DEPT OF AEROSPACE AND MECHANICAL ENGINEERING BOX 537 NOTRE DAME IN 46556	1 1
ATTN PROF F NELSON DEPT OF MECH AND AERO ENG UNIVERSITY OF MISSOURI ROLLA ROLLA MO 65401	1
ATTN ROBERT ENGLAR GEORGIA TECH RESEARCH INSTITUTE AEROSPACE SCIENCE AND TECHNOLOGY LAB ATLANTA GA 30332	1
ATTN E LUCERO D FROSTBUTTER L PERINI TECHNICAL LIBRARY APPLIED PHYSICS LABORATORY JOHNS HOPKINS UNIVERSITY JOHNS HOPKINS ROAD LAUREL MD 20723-6099	1 1 1 1

DISTRIBUTION (Continued)

	Copies
ATTN B BROOKS	1
R STANCIL	1
R ELKINS	1
LORAL VOUGHT SYSTEMS	
P O BOX 650003	
M S EM 55	
DALLAS TX 75265-0003	
ATTN TECHNICAL LIBRARY	1
HUGHES MISSILE SYSTEMS COMPANY	
P O BOX 11337 BLDG 802 MS A1	
OLD NOGALES HWY	
TUCSON AZ 83734-1337	
ATTN M DILLENIUS	1
NIELSEN ENGINEERING AND	
RESEARCH INC	
526 CLYDE AVE	
MOUNTAIN VIEW CA 95043	
ATTN J WILLIAMS	1
S VUKELICH	1
J FIVEL	1
R GERBSCH (CODE 1111041)	1
TECHNICAL LIBRARY	1
MCDONNELL DOUGLAS	
ASTRONAUTICS CO (EAST)	
BOX 516	
ST LOUIS MO 63166-0516	
ATTN TECHNICAL LIBRARY	1
UNITED TECHNOLOGIES	
NORDEN SYSTEMS	
NORWALK CT 06856	
ATTN T LUNDY	1
D ANDREWS	1
TECHNICAL LIBRARY	1
LOCKHEED MISSILES AND SPACE CO INC	
P O BOX 1103	
HUNTSVILLE AL 35807	
ATTN W CHRISTENSON	1
D WARNER	1
ALLIANT TECHSYSTEMS INC	
600 SECOND ST NE	
HOPKINS MN 55343	

	Copies
ATTN TECHNICAL LIBRARY	1
B SALEMI	1
J BOUDREAU	1
RAYTHEON COMPANY	
MISSILE SYSTEMS DIVISION	
P O BOX 1201	
TEWKSBURY MA 01876-0901	
ATTN JOSEPH ANDRZEJEWSKI	1
MEVATEC CORP	
1525 PERIMETER PARKWAY	
SUITE 500	
HUNTSVILLE AL 35806	
ATTN DR G S SCHMIDT	1
LORAL DEFENSE SYSTEMS	
1210 MASSILLON ROAD	
AKRON OH 44315-0001	
ATTN TECH LIBRARY	1
AEROJET ELECTRONIC SYSTEMS	
P O BOX 296 III	
AZUSA CA 91702	
ATTN P REDING	1
G CHRUSCIEL	1
TECHNICAL LIBRARY	1
LOCKHEED MISSILES AND SPACE CO INC	
P O BOX 3504	
SUNNYVALE CA 94088	
ATTN K C LEE	1
AEROTHERM CORP	
580 CLYDE AVE	
MOUNTAIN VIEW CA 94043	
ATTN TECH LIBRARY	1
FMC NAVAL SYSTEMS DIV	
4800 E RIVER ROAD	
MINNEAPOLIS MN 55421-1402	
ATTN JAMES SORENSON	1
VINCENT ALLEN	1
ORBITAL SCIENCES	
3380 SOUTH PRICE ROAD	
CHANDLER AZ 85248	

DISTRIBUTION (Continued)

	Copies
ATTN RON EFROMSON MIT LINCOLN LABORATORY 244 WOOD STREET LEXINGTON MA 02173-0073	1
ATTN BRIAN WALKUP ALLIANT TECH SYSTEMS 210 STATE ROUTE 956 ROCKET CENTER WV 26726-3548	1
ATTN DR T LIN TRW ELECTRONICS AND DEFENSE SECTOR BLDG 527/RM 706 P O BOX 1310 SAN BERNADINO CA 92402	1
ATTN G VINCENT SPARTA INC 4901 CORPORATE DR HUNTSVILLE AL 35805	1
ATTN M S MILLER N R WALKER DYNETICS INC P O BOX 5500 HUNTSVILLE AL 35814-5050	1 1
ATTN H A MCELROY GENERAL DEFENSE CORP P O BOX 127 RED LION PA 17356	1
ATTN ENGINEERING LIBRARY ARMAMENT SYSTEMS DEPT GENERAL ELECTRIC CO BURLINGTON VT 05401	1
ATTN TECHNICAL LIBRARY OAYNE AERONAUTICAL 2701 HARBOR DRIVE SAN DIEGO CA 92138	1
ATTN BRIAN EST THE BOEING COMPANY P O BOX 516 ST LOUIS MO 63166-0516	1
ATTN WILLIAM FACINELLI ALLIED SIGNAL P O BOX 22200 MS 1207 3B TEMPE AZ 85285	1
ATTN DR T P SHIVANANDA TRW BMD P O BOX 1310 SAN BERNADINO CA 92402-1313	1
ATTN T R PEPITONE AEROSPACE TECHNOLOGY INC P O BOX 1809 DAHLGREN VA 22448	1
ATTN ERIC MOORE MAIL STOP MER 24 1281 LOCKHEED SANDERS P O BOX 868 NASHUA NH 03061	1
ATTN DR BRIAN LANDRUM RI BLDG E33 PROPULSION RESEARCH CENTER UNIVERSITY OF ALABAMA HUNTSVILLE AL 35899	1
ATTN JIM ROBERTSON RESEARCH SOUTH INC 555 SPARKMAN DRIVE SUITE 818 HUNTSVILLE AL 35816-3423	1
ATTN BOB WHYTE ARROW TECH ASSOCIATES INC 1233 SHELBURNE ROAD D8 SO BURLINGTON VT 05403	1
ATTN JUAN AMENABAR SAIC 4001 NORTH FAIRFAX DRIVE STE 800 ARLINGTON VA 22209	1
ATTN DR KIRIT PATEL SVERDRUP TECHNOLOGY INC TEAS GROUP BLDG 260 P O BOX 1935 EGLIN AFB FL 32542	1

DISTRIBUTION (Continued)

	Copies
ATTN FRANK LANGHAM MICRO CRAFT TECHNOLOGY 740 4TH ST MS 6001 ARNOLD AFB TN 37389	1
ATTN LAURA AYERS DELTA RESEARCH INC 315 WYNN DRIVE SUITE 1 HUNTSVILLE AL 35805	1
ATTN BRIAN BENNETT MCDONNELL DOUGLAS MC 064 2905 P O BOX 516 ST LOUIS MO 63166-0516	1
ATTN THOMAS FARISS LOCKHEED SANDERS P O BOX 868 MER24 1206 NASHUA NH 03061-0868	1
ATTN JEFFREY HUTH KAMAN SCIENCES CORPORATION 2560 HUNTINGTON AVE ALEXANDRIA VA 22303	1
ATTN WILLIAM JOLLY KAMAN SCIENCES 600 BLVD SOUTH SUITE 208 HUNTSVILLE AL 35802	1
ATTN STEPHEN MALLETTE KBM ENTERPRISES 15980 CHANEY THOMPSON RD HUNTSVILLE AL 35803	1
ATTN DONALD MOORE NICHOLS RESEARCH CORPORATION 4040 SOUTH MEMORIAL PARKWAY P O BOX 400002 MS 920C HUNTSVILLE AL 35815-1502	1
ATTN NANCY SWINFORD LOCKHEED MARTIN MISSILES AND SPACE CO P O BOX 3504 ORG E5-40 BLDG 1575E SUNNYVALE CA 94088-3504	1
ATTN DAVID RESSLER TRW BALLISTIC MISSILES DIV MS 953 2420 P O BOX 1310 SAN BERNARDINO CA 92402	1
ATTN LEROY M HAIR COLEMAN RESEARCH CORP 6820 MOQUIN DRIVE HUNTSVILLE AL 35806	1
ATTN SCOTT ALLEN ALLEN AERO RESEARCH 431 E SUNNY HILLS RD FULLERTON CA 92635	1
ATTN DARRYL HALL SAIC 1100 FIRST AVENUE SUITE 300 KING OF PRUSSIA PA 19406	1
ATTN BARRY LINDBLOM ALLIANT DEFENSE ELECTRONICS SYSTEMS INC P O BOX 4648 CLEARWATER FL 34618	1
ATTN DR SHIN CHEN THE AEROSPACE CORP M4 964 P O BOX 92957 LOS ANGELES CA 90009	1
ATTN EUGENE HART SYSTEM PLANNING CORP 1000 WILSON BLVD ARLINGTON VA 22209-2957	1

DISTRIBUTION (Continued)

	Copies
ATTN ELAINE POLHEMUS ROCKWELL AUTONETICS & MISSILE SYSTEMS DIVISION D611 DL21 1800 SATELLITE BLVD DULUTH GA 30136	1
ATTN MICHAEL GLENN TASC 1992 LEWIS TURNER BLVD FT WALTON BEACH FL 32547	1
ATTN STEVEN MARTIN SYSTEMS ENGINEERING GROUP INC 9841 BROKEN LAND PARKWAY SUITE 214 COLUMBIA MD 21046-1120	1
ATTN C W GIBKE LOCKHEED MARTIN VOUGHT SYSTEMS MS SP 72 P O BOX 650003 DALLAS TX 75265-0003	1
ATTN CHRIS HUGHES EDO GOVERNMENT SYSTEMS DIV 1500 NEW HORIZONS BLVD AMITYVILLE NY 11701-1130	1
ATTN DANIEL LESIEUTRE NIELSEN ENGINEERING & RES INC 526 CLYDE AVENUE MOUNTAIN VIEW CA 94043-2212	1
ATTN THOMAS LOPEZ COLEMAN RESEARCH CORP 990 EXPLORER BLVD HUNTSVILLE AL 35806	1
ATTN JENNIE FOX LOCKHEED MARTIN VOUGHT SYSTEMS P O BOX 650003 MS EM 55 DALLAS TX 75265-0003	1
ATTN JOHN BURKHALTER AUBURN UNIVERSITY 211 AEROSPACE ENGR BLDG AUBURN UNIVERSITY AL 36849	1
ATTN DR MAX PLATZER NAVAL POSTGRADUATE SCHOOL DEPT OF AERONAUTICS & ASTRONAUTICS CODE AA PL MONTEREY CA 93943	1
ATTN MIKE DANGELO MIT LINCOLN LABORATORY 1745 JEFFERSON DAVIS HWY 1100 ARLINGTON VA 22202	1
ATTN RICHARD HAMMER JOHNS HOPKINS APPLIED PHYSICS LAB JOHNS HOPKINS ROAD LAUREL MD 20723-6099	1
ATTN STEVE MULLINS SIMULATION AND ENGINEERING CO INC 4935 CENTURY ST NW HUNTSVILLE AL 35816-1901	1
ATTN ROBERT BRAENDLEIU KAISER MARQUARDT 16555 SATICOY ST VAN NUYS CA 91406-1739	1
ATTN LAWRENCE FINK BOEING AIRCRAFT AND MISSILES P O BOX 3707 MC 4A 36 SEATTLE WA 98124-2207	1
ATTN ROY KLINE KLINE ENGINEERING CO INC 27 FREDON GREENDELL RD NEWTON NJ 07860-5213	1
ATTN THOMAS KLAUSE TRW P O BOX 80810 ALBUQUERQUE NM 87198	1
ATTN DAN PLATUS THE AEROSPACE CORPORATION P O BOX 92957 LOS ANGELES CA 90009	1

DISTRIBUTION (Continued)

	Copies
ATTN DR REX CHAMBERLAIN TETRA RESEARCH CORPORATION 2610 SPICEWOOD TR HUNTSVILLE AL 35811-2604	1
ATTN PERRY PETERSEN NORTHROP GRUMMAN CORP DEPT 9B51 MAIL ZONE XA 8900 EAST WASHINGTON BLVD PICO RIVERA CA 90660-3783	1
ATTN DR JAMES HAUSER AERO SPECTRA INC 2850 KENYON CIRCLE P O BOX 3006 BOULDER CO 80307	1
ATTN DARRELL AUSHERMAN TRW SPACE AND DEFENSE ONE SPACE PARK MAIL STATION R1-1062 REDONDO BEACH CA 90278-1071	1
ATTN JAY EBERSOHL ADVATECH PACIFIC INC 2015 PARK AVENUE SUITE 8 REDLANDS CA 92373	1
ATTN PAUL WILDE ACTA INC 2790 SKYPARK DR SUITE 310 TORRANCE CA 90505-5345	1
ATTN DR MICHAEL HOLDEN CALSPAN UB RESEARCH CENTER P O BOX 400 BUFFALO NY 14225	1
ATTN RICHARD GRABOW SPACE VECTOR CORP 17330 BROOKHURST ST SUITE 150 FOUNTAIN VALLEY CA 92708	1
ATTN BRENT APPLEBY DRAPER LABORATORY 555 TECHNOLOGY SQ MS77 CAMBRIDGE MA 02139	1
ATTN JAMES JONES SPARTA INC 1901 N FORT MYER DR SUITE 600 ARLINGTON VA 22209	1
ATTN SCOTT HOUSER PHOENIX INTEGRATION 1872 PRATT DRIVE SUITE 1835 BLACKSBURG VA 24060	1
ATTN S ROM MURTY TELEDYNE BROWN ENGINEERING MS 200 300 SPARKMAN DRIVE HUNTSVILLE AL 35807	1
ATTN STUART COULTER SVERDRUP TECHNOLOGY 673 2ND ST MS4001 ARNOLD AIR FORCE BASE TULLAHOMA TN 37389-4001	1
ATTN DR RICHARD HOWARD NAVAL POSTGRADUATE SCHOOL DEPT OF AERONAUTICS AND ASTRONAUTICS CODE AA HO NPS MONTEREY CA 93943	1
ATTN J BRENT RUMINE MIT LINCOLN LABORATORY 244 WOOD STREET BUILDING S ROOM 52-327 LEXINGTON MA 02173-9185	1
ATTN ANDY MOORE SVERFRUP TECHNOLOGY INC AEDC GROUP 740 FOURTH ST MS 6001 ARNOLD AFB TN 37389-6001	1
ATTN MICHAEL A GLENN TASC 1992 LEWIS TURNER BLVD FORT WALTON BEACH FL 32547-1255	1

DISTRIBUTION (Continued)

	Copies
ATTN CARLOS RUIZ (MP 135) LOCKHEED MARTIN ELECTRONICS AND MISSILES 5600 SAND LAKE RD ORLANDO FL 32819-8907	1
ATTN ERIC GRABOW SPACE VECTOR CORPORATION 9223 DEERING AAVE CHATSWORTH CA 91311	1
ATTN S R MURTY TELEDYNE BROWN ENGINEERING MS 200 300 SPARKMAN DRIVE HUNTSVILLE AL 35807	1
ATTN STEVE JOHNSON DELTA RESEARCH INC 315 WYNN DR SUITE 1 HUNTSVILLE AL 35805	1
ATTN EDWARD ZABRENSKY TRW MAIL CODE SBCA 971 P O BOX 1310 SAN BERNARDINO CA 92402	1
ATTN CARMEN J PEZZONE JR SYSTEMS ENGINEERING GROUP INC 9861 BROKEN LAND PARKWAY SUITE 350 COLUMBIA MD 21046	1
ATTN GORDON S SCHMIDT LOCKHEED MARTIN TACTICAL DEFENSE SYSTEMS 1210 MASSILLON RD AKRON OH 44315-0001	1
ATTN DANIEL B CORBETT DELTA RESEARCH INC 315 WYNN DR SUITE 1 HUNTSVILLE AL 35805	1
ATTN JAMES W JOBE THE BOEING COMPANY BOEING INFORMATION DEFENSE AND SPACE SYSTEMS 20403 68TH AVE SO MS 8Y 69 KENT WA 98032	1
ATTN BRIAN K BENNETT BOEING MAIL CODE 5221 1350 P O BOX 516 ST LOUIS MO 63166	1
ATTN DARRELL E GILLETTE COALESCENT TECHNOLOGIES CORP 7061 UNIVERSITY BLVD WINTER PARK FL 32792	1
ATTN SAL MICELI LOCKHEED MARTIN ASTRONAUTICS P O BOX 179 DENVER CO 80201	1
ATTN MINH DANG ITT SYSTEMS AND SCIENCES CORP 600 BOULEVARD SO SUITE 208 HUNTSVILLE AL 35802-2104	1
ATTN FRANCIS J PRIOLO MILLENNIUM ENG AND INTEG CO CRYSTAL PARK 3 2231 CRYSTAL DRIVE SUITE 711 ARLINGTON VA 22202	1
ATTN KENNETH V CHAVEZ SANDIA NATIONAL LAB P O BOX 5800 ALBUQUERQUE NM 87185-0825	1
ATTN MARK A JANTSCHER ALLIANT TECH SYSTEMS INC 600 2ND ST NE MAIL STATION MN11 2626 HOPKINS MN 55343	1
ATTN DR DANNY LIU ZONA TECHNOLOGY INC 7430 E STETSON DR STE 205 SCOTTSDALE AZ 85251	1

DISTRIBUTION (Continued)

	Copies
ATTN LES WIGGINS THE BOEING COMPANY 499 BOEING BLVD MS JN 67 P O BOX 240002 HUNTSVILLE AL 35824-6402	1
ATTN KENNETH M ELLIOT III APPLIED ORDNANCE TECHNOLOGY INC P O BOX 899 5254 POTOMAC DRIVE STE E DAHLGREN VA 22448	1
ATTN DARRELL GILLETTE MICHAEL CEBULA COALESCENT TECHNOLOGIES 10640 CHARLES CIRCLE CYPRESS CA 90630	1 1
ATTN DR RICHARD KROEGER NICHOLS RESEARCH 4040 SOUTH MEMORIAL PARKWAY MAIL STOP 912 HUNTSVILLE AL 35802	1
ATTN DAVID REINBOLD ORBITAL SCIENCES CORP 3380 S PRICE RD CHANDLER AZ 85248	1
ATTN RALPH H KLESTADT RAYTHEON MISSILE SYSTEMS P O BOX 11337 BLDG 801 MS C6 TUCSON AZ 85739-1337	1
ATTN RONALD W GREEN SANDIA NATIONAL LAB P O BOX 5800 MS 0303 ALBUQUERQUE NM 87185-0303	1
ATTN WAYNE HATAWAY ARROW TECH ASSOCIATES 1233 SHELBURNE RD SUITE D8 SOUTH BURLINGTON VT 05403	1
ATTN KEITH ODELL THIOKOL MS 251 P O BOX 707 BRUGGAM CITY NT 84302-0707	1
ATTN PAUL D THORNLEY ITT INDUSTRIES SYSTEMS DIV P O BOX 15012 COLORADO SPRINGS, CO 80935-5012	1
ATTN NICHOLAUS BONAFEDE NORTHROP GRUMMAN RYAN AERONAUTICAL CENTER P O BOX 85311 SAN DIEGO CA 92186-5311	1
ATTN KARL L BRUNSON SAIC SCIENCE APPLICATIONS INTERNATIONAL CORP 1901 N FORT MYER DR STE 301 ARLINGTON VA 22209	1
ATTN JAMES Q TALLEY GENERAL DYNAMICS ARMAMENT SYS LAKESIDE AVE ROOM 1305 BURLINGTON VT 05401	1
ATTN DANIEL SHEDD SCIENCE APPLICATIONS INTL 1710 GOODRIDGE DR MS 188 MCLEAN VA 22102	1
ATTN SEAN GEORGE CHARLES S DRAPER LAB 555 TECHNOLOGY SQUARE MS 23 CAMBRIDGE MA 02139	1
ATTN DARK T EDQUIST APPLIED RESEARCH ASSOC INC 5941 S MIDDLEFIELD RD STE 100 LITTLETON CO 80123	1
ATTN KENNETH SCHROEDER COLEMAN AEROSPACE COMPANY 7675 MUNICIPAL DR ORLANDO FL 32819	1

DISTRIBUTION (Continued)

	Copies
ATTN GARY DON VINCENT SPARTA INC 6000 TECHNOLOGY DR BLDG 3 HUNTSVILLE AL 35805-1955	1
ATTN DR JOHN L PORTER SVERDRUP TECHNOLOGY INC P O BOX 1935 BLDG 260 EGLIN AFB FL 32542	1
ATTN STEVE BROWN LOCKHEED MARTIN MISSILE AND FIRE CONTROL 9500 GODWIN DRIVE MANASSAS VA 20108	1
ATTN AL HASTINGS HASTINGS CHARIOTS 6280 SOUTH VALLEY VIEW BLVD UNIT 108 LAS VEGAS NV 89118-3814	1
ATTN GERALD SOLOMON PRIMEX TECH WARHEAD SYSTEMS 4565 COMMERCIAL DRIVE STE A NICEVILLE FL 32578	1
ATTN LAWRENCE FINK BOEING P O BOX 3707 MC 4A 45 SEATTLE WA 98124-2207	1
ATTN KAREN Y EVANS AEROJET 1100 WEST HOLLYVALE STREET BLDG 160 1 D8320 AZUSA CA 91702	1
ATTN JONATHAN KATZ THIOKOL PROPULSION ELKTON DLV OPERATIONS 55 THIOKOL ROAD ELKTON MD 21921	1
ATTN JIM HURRELL SAIC 14 EAST WASHINGTON STREET ORLANDO FL 32801-2320	1
ATTN JAHN DYVIK UNITED DEFENSE M170 4800 EAST RIVER RD MINNEAPOLIS MN 55421	1
ATTN PROF DOYLE KRUGHT RUTGERS UNIVERSITY DEPT OF MECH AND AERO ENG 98 BRETT RD PISCATAWAY NJ 08855	1
ATTN RICHARD A HAMMER JOHNS HOPKINS APPLIED PHYSICS LAB 11100 JOHNS HOPKINS RD LAUREL MD 20723-6099	1
ATTN DR BARTLEY L CARDON MIT LINCOLN UNIVERSITY 244 WOOD STREET LEXINGTON MA 02173-9108	1
ATTN DEWEY H HODGES GEORGIA INSTITUTE OF TECH SCHOOL OF AEROSPACE ENGNR ATLANTA GA 30332-0150	1
ATTN DR DEAN WILKENING STANFORD UNIV CENTER FOR INTERNATINAL SECURITY AND COOPERATION ENCINA HALL STANFORD CA 94305-6165	1
ATTN WILLIAM H MASON VIRGINIA TECH DEPT OF AEROSPACE AND OCEAN ENGINEERING MC 0203 BLACKSBURG VA 24061-0203	1
NON-DOD ACTIVITIES (EX-CONUS)	
ATTN A BOOTH BRITISH AEROSPACE DEFENCE LTD MILITARY AIRCRAFT DIVISION WARTON AERODROME WARTON PRESTON LANCASHIRE PR4 1AX UNITED KINGDOM	1

DISTRIBUTION (Continued)

	Copies
ATTN R CAYZAC GIAT INDUSTRIES 7 ROUTE DE GUERCY 18023 BOURGES CEDEX FRANCE	1
ATTN MAJ F DE COCK ECOLE ROYALE MILITAIRE 30 AV DE LA RENAISSANCE 1040 BRUXELLES BELGIUM	1
ATTN J EKEROOT BOFORS MISSILES 691 80 KARLSKOGA SWEDEN	1
ATTN M HARPER BOURNE DEFENCE RESEARCH AGENCY Q134 BUILDING RAE FARNBOROUGH HAMPSHIRE QU14 6TD UNITED KINGDOM	1
ATTN A H HASSELROT FFA P O BOX 11021 161 11 BROMMA SWEDEN	1
ATTN B JONSSON DEFENCE MATERIAL ADMINISTRATION MISSILE TECHNOLOGY DIVISION 115 88 STOCKHOLM SWEDEN	1
ATTN P LEZEAUD DASSAULT AVIATION 78 QUAI MARCEL DASSAULT 92214 SAINT CLOUD FRANCE	1
ATTN J LINDHOUT N L R ANTHONY FOKKERWEG 2 1059 CM AMSTERDAM THE NETHERLANDS	1
ATTN A MICKELLIDES GEC MARCONI DEFENCE SYSTEMS LTD THE GROVE WARREN LANE STANMORE MIDDLESEX UNITED KINGDOM	1
ATTN K MOELLER BODENSEEWERK GERAETETECHNIK GMBH POSTFACH 10 11 55 88641 UBERLINGEN GERMANY	1
ATTN RIBADEAU DUMAS MATRA DEFENSE 37 AV LOUIS BREGUET BP 1 78146 VELIZY VILLACOUBLAY CEDEX FRANCE	1
ATTN R ROGERS DEFENCE RESEARCH AGENCY BLDG 37 TUNNEL SITE CLAPHAM BEDS MK 41 6AE UNITED KINGDOM	1
ATTN S SMITH DEFENCE RESEARCH AGENCY Q134 BUILDING RAE FARNBOROUGH HAMPSHIRE QU14 6TD UNITED KINGDOM	1
ATTN J SOWA SAAB MISSILES AB 581 88 LINKOPING SWEDEN	1
ATTN D SPARROW HUNTING ENGINEERING LTD REDDINGS WOOD AMPTHILL BEDFORDSHIRE MK452HD UNITED KINGDOM	1

DISTRIBUTION (Continued)

	Copies
ATTN P STUDER DEFENCE TECHNOLOGY AND PROCUREMENT AGENCY SYSTEMS ANALYSIS AND INFORMATION SYSTEMS DIVISION PAPIERMUEHLESTRASSE 25 3003 BERNE SWITZERLAND	1
ATTN J M CHARBONNIER VON KARMAN INSTITUTE 72 CHAUSSEE DE WATERLOO 1640 RHODE SAINT GENESE BELGIUM	1
ATTN P CHAMPIGNY DIRECTION DE L AERONAUTIQUE ONERA 29 AV DE LA DIVISION LECLERC 92320 CHATILLON SOUS BAGNEUX CEDEX FRANCE	1
ATTN DR P HENNIG DEUTSCHE AEROSPACE (DASA) VAS 414 ABWEHR AND SCHUTZ POSTFACH 801149 8000 MUENCHEN 80 GERMANY	1
ATTN PETER CAAP HD FLIGHT SYS DEPT FAA AERONAUTICAL RESEARCH INST OF SWEDEN BOX 11021 BROMMA SWEDEN 16111	1
ATTN DAVE BROWN WEAPON SYSTEMS DIVISION AERONAUTICAL AND MARITIME RESEARCH LABORATORY P O BOX 1500 SALISBURY SOUTH AUSTRALIA 5108	1
ATTN PROF JOHN EDWARDS BLD A23 FORT HALSTEAD SEVEN OAKS KENT TN147BP UNITED KINGDOM	1
ATTN DR ERDAL OKTAY ROKETSAN MISSILE INDUSTRIES INC 30 ELMADAG 06780 ANKARA, TURKEY TURKEY	1

INTERNAL

		Copies
B		1
B04		1
B04	(ZIEN)	1
B05	(STATON)	1
B10		1
B10	(HSIEH)	1
B51	(ARMISTEAD)	1
B60	(TECHNICAL LIBRARY)	3
C		1
D		1
G		1
G02		1
G20		1
G205		1
G21		1
G21	(COOK)	1
G22		1
G23		1
G23	(CHISHOLM)	1
G23	(HANGER)	1
G23	(HARDY)	1
G23	(HYMER)	50
G23	(JONES)	1
G23	(KNIESS)	1
G23	(OHLMEYER)	1
G23	(MALYEVAC)	1
G23	(PHILLIPS)	1
G23	(ROWLES)	1
G23	(WEISEL)	1
G24		1
G24	(VAVRICK)	1
G30		1
G305		1
G31	(RINKO)	1

DISTRIBUTION (Continued)

		Copies
G32	(DAY)	1
G33	(FRAYSSE)	1
G33	(LUU)	1
G33	(RINALDI)	1
G50		1
G50	(SOLOMON)	1
G60		1
G70		1
G72		1
G72	(CHEPREN)	1
K		1
K40		1
K44	(DAVIS)	1
N		1
N92	(AMBROSE)	1
N92	(PIERCE)	1
T		1
T13	(ALEXOPOULOS)	1
T13	(CARSOLA)	1
T406		1